

Magnetic drug delivery: Iron oxide nanoparticles as a drug carrier for the antimicrobial peptide lasioglossin

Chiara Maria Turrina

Vollständiger Abdruck der von der TUM School of Engineering and Design der Technischen Universität München zur Erlangung einer
Doktorin der Naturwissenschaften (Dr. rer. nat.)
genehmigten Dissertation.

Vorsitz: Prof. Dr.-Ing. Andreas Kremling

Prüfer*innen der Dissertation:

1. Prof. Dr. rer. nat. Sonja Berensmeier
2. Assistant Prof. Dr. rer. nat. Sebastian Schwaminger
3. Assoc. Prof. Dr. Martin Himly

Die Dissertation wurde am 17.04.2023 bei der Technischen Universität München eingereicht und durch die TUM School of Engineering and Design am 06.10.2023 angenommen.

"I am among those who think that science has great beauty."

Marie Curie

Acknowledgments

First and foremost, I would like to thank my supervisor, Ass. Prof. Sebastian Schwaminger. I am grateful for everything you have taught me and for the necessary freedom to learn and work on my project. I always felt encouraged and supported with plenty of ideas. Even though we mostly worked in different countries and time zones, you always found time for discussion and had a sympathetic ear for me. I could not have wished for a better supervisor.

I thank Prof. Sonja Berensmeier for the chance to do my doctorate at your research family and the freedom I had to follow my ideas and learn from them. It was a pleasure to work and learn in this interdisciplinary group.

Thank you, Prof. Martin Himly, for your expertise and immediate willingness to be my examiner. It is an honor for me.

Further, thanks go to Prof. Patricia Dankers for hosting me in her laboratory and introducing me to supramolecular engineering and cellular work. I really learned a lot during my time in Eindhoven. Special thanks to Riccardo Bellan, who supported me with Cryo TEM measurements and Nile red assay.

I want to thank all the people who helped me during my thesis. Thank you Maria Müller for the kind introduction to XRD system. Thank you, Dr. Carsten Peters, for all the time and support during TEM measurements. I want to thank Dr. Jennifer Cookman that made beautiful micrographes with HAADF-STEM combined with iDPC and with low-dose TEM of my nanoparticles. I am very grateful for Matthias Opel's help with SQUID measurements. Thanks to Diana Rojas Gonzalez for the effort of testing the nanoparticles for their cytocompatibility.

My further thanks go to all my colleagues from STT and SBT for a great time, valuable discussions, and support. I would like to thank Stefan Rauwolf and Alexander Zanker, who helped me with their work experience and ideas, especially in the beginning. Eva Krolitzki, Lea Martin, and Leonie Wittmann, thank you for sharing an office with me, for your consistent motivation, and for being there when needed. For similar reasons, I would like to thank Dr. Paula Fraga Garcia, Yasmin Kaveh Baghbaderani, Tatjana Trunzer, Michael Schobesberger, Lucía Abarca-Cabrera, Tobias Stegmüller, Dennis Röcker, Patrick Muschak, Marko Tesanovic, Gregor Essert, and Ines Zimmermann. I want to thank Stefan Darchinger for his enthusiasm to keep the lab running and help with many small problems. You all made this time special for me. Further, thanks to Tobias and Tatjana for giving me feedback on my final manuscript.

A special thanks goes to all my students who were involved and contributed to my research significantly. Thank you Davide Milani, Anna Klassen, Anne Oppelt, and Michaela Mitzkus. You have helped me with hours of work in the laboratory and your joy of discussion. I enjoyed working with every single one of you.

Finally, I thank my family, friends, and my partner Lukas for their everlasting support and help under all circumstances.

Thanks to everybody who accompanied and shaped my time during my doctorate. I will keep these years in good memory.

Table of content

Acknowledgments	I
Table of content	III
Abbreviations	VI
Symbols	X
1. Introduction	1
1.1. Iron oxide nanoparticles	2
1.1.1. Synthesis of iron oxide nanoparticles	3
1.1.2. Coatings of iron oxide nanoparticles	4
1.1.3. Properties and characterization of iron oxide nanoparticles	8
1.2. Nanomedicine	14
1.2.1. Diagnostics	14
1.2.2. Therapeutics	16
1.2.3. Drug Delivery	17
1.2.4. Designing nanoparticles for their application in drug delivery	19
1.3. Antimicrobial resistance and cancer	24
1.3.1. Antimicrobial peptides	25
1.3.2. Lasioglossin	26
2. Motivation	29
3. Publications	1
3.1. Bare iron oxide nanoparticles as drug delivery carrier for the short cationic peptide lasioglossin	1
3.2. Silica-coated superparamagnetic iron oxide nanoparticles: New insights into the influence of coating thickness on the particle properties and lasioglossin binding	19
3.3. Carboxymethyl-dextran coated superparamagnetic iron oxide nanoparticles for drug delivery: Influence of coating thickness on the particle properties	28
3.4. Iron oxide nanoparticles with supramolecular ureidopyrimidinone coating	50
3.5. Iron oxide nanoparticles with supramolecular ureido-pyrimidinone coating for antimicrobial peptide delivery	55

3.6. Superparamagnetic iron oxide nanoparticles for their application in the human body: Influence of the surface	72
4. Discussion.....	87
4.1. Drug Delivery System	87
4.2. Stability and Agglomeration.....	92
5. Summary & Outlook	95
6. References	98
7. Appendix	115
7.1. Supporting information	115
7.1.1. Bare iron oxide nanoparticles as drug delivery carrier for the short cationic peptide lasioglossin	115
7.1.2. Silica-coated superparamagnetic iron oxide nanoparticles: New insights into the influence of coating thickness on the particle properties and lasioglossin binding.....	122
7.1.3. Carboxymethyl-dextran coated superparamagnetic iron oxide nanoparticles for drug delivery: Influence of coating thickness on the particle properties.....	126
7.1.4. Iron Oxide Nanoparticles with Supramolecular Ureido-Pyrimidinone Coating for Antimicrobial Peptide Delivery.....	141
7.1.5. Superparamagnetic iron oxide nanoparticles for their application in the human body: Influence of the surface.....	144
References	148
7.2. List of publications	149
7.3. Permissions.....	151
7.3.1. Bare iron oxide nanoparticles as drug delivery carrier for the short cationic peptide lasioglossin	151
7.3.2. Silica-coated superparamagnetic iron oxide nanoparticles: New insights into the influence of coating thickness on the particle properties and lasioglossin binding.....	151
7.3.3. Carboxymethyl-dextran coated superparamagnetic iron oxide nanoparticles for drug delivery: Influence of coating thickness on the particle properties.....	152
7.3.4. Iron oxide nanoparticles with supramolecular ureidopyrimidinone coating.....	152
7.3.5. Superparamagnetic iron oxide nanoparticles for their application in the human body: Influence of the surface	152

7.3.6. Iron oxide nanoparticles with supramolecular ureido-pyrimidinone coating for antimicrobial peptide delivery 153

Abbreviations

Abbreviation	Description
ADH	Alcohol dehydrogenases
ads	adsorbed
ADP3	Antimicrobial peptide database
AEF	Artificial endosomal fluid
Ala	Alanine
ALF	Artificial lysosomal fluid
AMP	Antimicrobial peptide
AMR	Antimicrobial resistance
ANUC	Analytical ultracentrifugation
Asn	Asparagine
a.u.	Arbitrary units
APTS	(3-Aminopropyl)triethoxysilan
ATR	Attenuated total reflectance
ATP	Adenosine triphosphate
BET	Brunauer-Emmett-Teller
BION	Bare iron oxide nanoparticle
<i>B. subtilis</i>	<i>Bacillus subtilis</i>
BSA	Bovine serum albumin
C	BET constant
CD	Charge distribution
CMD	Carboxymethyl dextran
cov	Covalently bound
CT	Computed tomography
D	Dimensional
dd	Double-distilled
Dartbac	Dutch Antimicrobial Resistance Technology development and Biofilm Assessment Consortium
DDS	Drug delivery system
Dex	Dextran
DFG	German Research Foundation
DMSA	3-dimercaptosuccinic acid
DOI	Digital object identifier
DOX	Doxorubicin

DLS	Dynamic light scattering
DLVO	Derjagun, Landau, Verwey, and Overbeek
DNA	Desoxyribunucleic acid
EDC	N-ethyl-N'-(3-(dimethylamino)propyl)carbodiimide
<i>E. coli</i>	<i>Escherichia coli</i>
ECR	Electron coupling reagent
e.g.	Exempli gratia
EMA	European Medicines Agency
EPR	Enhanced permeability and retention
<i>et al.</i>	<i>Et alii</i> or <i>et aliae</i> (Latin for and others)
Eq.	Equivalents
Eq.	Equation
FCS	Fetal calf serum
FDA	Food and drug administration
FMS	Field magnet system
FT	Fourier-transform
FWHM	Full width at half maximum
GFP	Green fluorescent protein
Glu	L-glutamic acid
Gly	Glycine
HAADF-STEM	High-angle annular dark field scanning transmission electron microscopy
HeLa S3	Human cervix carcinoma
HK-2	Human kidney cells
HL-60	Human promyelocytic leukemia
HS	Human serum
HP	Human plasma
HUASMCs	Human umbilical artery smooth muscle cells
iDPC	Integrated differential contrast
IC ₅₀	Half maximal inhibitory concentration
IEP	Isoelectric point
IGSSE	International Graduate School of Science and Engineering
Ile	Isoleucine
IPTG	Isopropyl- β -D-thiogalactopyranoside
IR	Infrared spectroscopy

ION	Iron oxide nanoparticles
k	thousand
k_b	Boltzmann constant
<i>K. pneumoniae</i>	<i>Klebsiella pneumoniae</i>
L1210	Mouse lymphocytic leukemia
Leu	Leucine
LL	Lasioglossin
Lys	Lysine
M	Molar concentration
M9	Minimal Medium
Mo	Molybdenum
MIC	Minimal inhibitory concentration
MNP	Magnetic nanoparticle
MPI	Magnetic particle imaging
MPS	Mononuclear phagocyte system
MRI	Magnetic resonance imaging
MRXI	Magnetorelaxometry imaging
n	Nano (unit prefix denoting a division by 1000000000)
NdFeB	Neodymium boron ferrite
NHS	N-hydroxysuccinimide
n_m	Monolayer capacity
NMR	Nuclear magnetic resonance
NR	Nile Red
NP	Nanoparticle
OD	Optical density
OECD	Organisation for economic co-operation and development
<i>P. aeruginosa</i>	<i>Pseudomonas aeruginosa</i>
PBS	Phosphate buffered saline
PC 12	Pheochromocytoma of the rat adrenal medulla
PEG	Polyethylene glycol
PET	Positron emission tomography
PGA	Polyglutaraldehyde
pH	Negative logarithm to base 10 of activity of hydrogen ions

pK	Negative base-10 logarithm of the acid dissociation constant
PLA	Poly(lactic acid)
PLGA	Poly(lactic-co-glycolic acid)
PVA	Poly(vinyl alcohol)
PVP	Poly(vinylpyrrolidone)
rpm	Revolutions per minute
RT	Room temperature
ROS	Reactive oxygen species
<i>S. aureus</i>	<i>Staphylococcus aureus</i>
SI	Supporting information
siRNA	small interfering ribonucleic acid
SBF	Simulated body fluid
STEP	Space and time-resolved extinction profiles
SW480	Human colon adenocarcinoma
SQUID	Superconducting quantum interference device
TEM	Transmission electron microscopy
TEOS	Tetraethyl orthosilicate
TGA	Thermogravimetric analysis
THP-1	Tamm-Horsfall Protein 1
Trp	Tryptophan
UPy	Ureidopyrimidinone
UV	Ultraviolet
Val	Valine
VSM	Vibrating sample magnetometer
wt	weight
XRD	X-ray diffraction
XTT	2,3-bis-(2-methoxy-4-nitro-5-sulfophenyl)-2H-tetrazolium-5-carboxanilide

Symbols

Symbol	Description	Unit
η	Viscosity	$\text{m}^2 \text{s}^{-1}$
Δ	Difference	
%	Percent	
Å	Ångström	
λ	X-ray wavelength	nm
ρ	Density	kg m^{-3}
θ	Crystallographic measuring angle	°
amu	Atomic mass unit	Da
c	Concentration	g mol^{-1}
C	Conductivity	mS cm^{-1}
d	Diameter	m
D	Diffusion coefficient	$\text{m}^2 \text{s}^{-1}$
d_H	Hydrodynamic diameter	nm
emu	Electromagnetic unit	10^{-3} A m^2
G	Electric conductance	S
H	Magnetic field strength	Oe
I	Electric current	A
K	Shape factor	ft
L	Length/ Particle size	nm
m	Mass	g
M	Molar concentration	mol L^{-1}
n	Amount of substance	mol
n_a	Adsorbed amount of gas	L
n_m	Monolayer capacity	L
p	Pressure	Pa
p_0	Saturation pressure	kPa
t	Time	h
T	Temperature	°C
U	Voltage	V
V	Volume	L

1. Introduction

The term ‘nano’ is derived from the greek word νόμος [nános], meaning dwarf. One nanometer (1 nm) is a billionth meter (10^{-9} m). A comparison can be made to visualize the size of one nanometer. If the diameter of a walnut is compared to the earth's diameter, the ratio is similar to comparing a fullerene (1nm) with a walnut (3.5 cm, Figure 1.1).

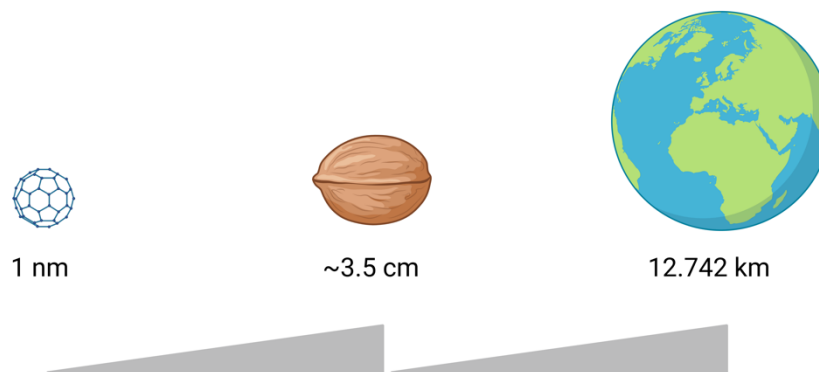


Figure 1.1: Schematic visualization of the size ratio between a fullerene, a walnut, and the earth. It was created with BioRender.com.

The origin of many life-threatening diseases is at the nanoscale level. The malfunction or miscommunication of cells can be caused by bacteria, viruses, misfolded proteins, and mutated genes. Biological barriers at nanometer size protect small specific harmful molecules or infectious agents. Nanomaterials are at the same scale and can be designed to have several sizes, shapes, and functionalizations. In nanomedicine, nanomaterials with ideal biological, chemical, and physical properties are used to improve the diagnosis and treatment of diseases on a molecular level [1]. The Nobel physicist Richard P. Feynman laid the cornerstone of contemporary nanomedicine in his renowned 1959 talk: “There’s Plenty of Room at the Bottom.” He proposed to make machine tools so small that they reach the atomic level [2]. This idea of using nanomachines, nanodevices, and nanorobots for manufacturing and instrumentation is the basis of nanotechnology. The concept of nanomedicine is built up by this idea. It proposes to design and build nanorobots that could be introduced into the human body to perform cellular repairs at the molecular level [3]. Drexler and Freitas were important voices from the 1980s to the 1990s in the field of nanomedicine [3–5]. However, Feynman and Albert R. Hibbs already knew that nanotechnology has potential for medicine. Their idea to treat heart diseases was the following: “Although it is a very wild idea, it would be interesting in surgery if you could swallow the surgeon. You put the mechanical surgeon inside the blood vessel, which goes into the heart and looks around. It finds out which valve is faulty and takes a little knife and slices it out. Other small machines might be permanently incorporated in the body to assist some inadequately functioning organ [2,3].” Today nanomedicine already provides miniaturized tools that are sensitive and specific, highly controllable, versatile, reliable, and cost-efficient. Nanostructured materials range from dendrimers, fullerenes, micelles, hydrogels, liposomes, quantum dots, nanoemulsions, nanoparticles, nanofibers, and

nanoshells [3]. Iron oxide-based nanoparticles are used in all areas of nanomedicine, including diagnostic, therapeutic, drug delivery, and regenerative medicine [14].

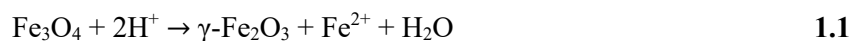
1.1. Iron oxide nanoparticles

Iron oxides are chemical compounds consisting of iron and oxide [15]. Depending on the natural conditions, dissolved iron ions can form multiple iron oxides or hydroxides with different iron ion content and oxidation state [16]. Overall, sixteen species exist, applied in various areas ranging from pigments to thermite (Table 1.1) [15,16].

Table 1.0: List of the sixteen different iron oxides and oxyhydroxides [16].

Oxides	Hydroxides	Oxide/hydroxides
<ul style="list-style-type: none"> • iron (II) oxide, wüstite, FeO • iron (II,III) oxide, magnetite, Fe₃O₄ • iron (III) oxide, Fe₂O₃ <ul style="list-style-type: none"> ○ α-phase, hematite ○ β-phase ○ γ-phase, maghemite ○ ϵ-phase 	<ul style="list-style-type: none"> • iron (II) hydroxide, Fe(OH)₂ • iron (III) hydroxide, bernalite, Fe(OH)₃ 	<ul style="list-style-type: none"> • goethite, α-FeOOH • akaganéite, β-FeOOH • lepidocrocite, γ-FeOOH • feroxyhyte, δ-FeOOH • ferrihydrite, Fe₅HO₈4H₂O • high-pressure FeOOH • schwertmannite, Fe₈O₈(OH)₆(SO)_nH₂O

In nanotechnology, particles are classified regarding their size. Fine particles range from 2500 nm to 100 nm, while nanoparticles (NP) are categorized between 100 nm and 1 nm. NPs can have specific size-related properties that strongly deviate from fine particles of the same material [15,17]. Semiconducting nano-materials are the research focus due to their exceptional properties [15]. The three iron oxide nanoparticles (IONs), hematite, magnetite, and maghemite, are particularly interesting and are most commonly used. Hematite (α -Fe₂O₃) is the most stable ION and an *n*-type semiconductor. Its rhombohedral lattice is an almost ideal hexagonal close-packed oxygen lattice. The Fe³⁺ ions occupy two-thirds of the octahedral sites. Magnetite (Fe₃O₄) has the lowest resistivity, containing iron (II) and (III) with a stoichiometry of Fe²⁺/Fe³⁺ = 1/2, and can be both an *n*-type and a *p*-type semiconductor. It has a centered cubic spinel lattice structure. Maghemite (γ -Fe₂O₃) is fully oxidized magnetite and an *n*-type semiconductor with a cubic close-packed array (Eq. 1.1) [18–22].



All three IONs are ferromagnetic at room temperature (RT). Magnetite and maghemite can show a saturation magnetization of up to 92 emu g⁻¹, while hematite has a comparable low saturation magnetization of < 1 emu g⁻¹ [23]. If the particle size is < 15 nm, the IONs become superparamagnetic (at RT) because the anisotropy energy barrier of a single ION can overcome the thermal energy [21]. A superparamagnetic curve is characterized by having no coercive force and no hysteresis loop

compared to the ferromagnetic one (Figure 1.2). The particles are magnetic only in the presence of an external magnetic field [24].

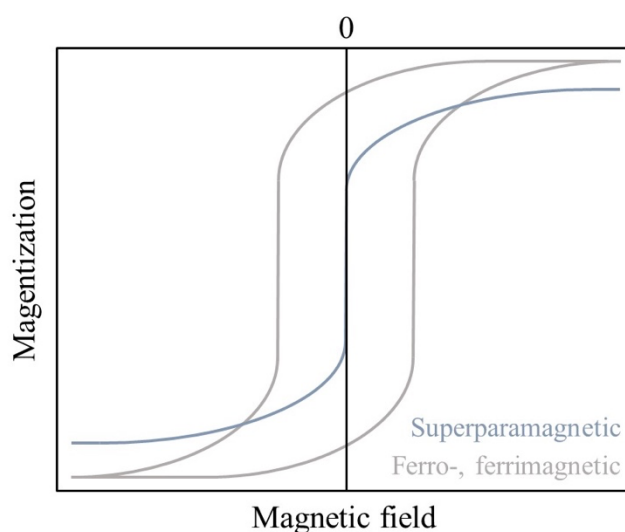


Figure 1.2: Schematic illustration of ferro-, ferrimagnetic and superparamagnetic materials in an applied magnetic field.

1.1.1. Synthesis of iron oxide nanoparticles

Due to their relatively high saturation magnetization, superparamagnetic behavior, low toxicity, high surface-to-volume ratio, and simple and affordable synthesis techniques, magnetite and maghemite-based IONs are the subject of research for a variety of applications [25]. Co-precipitation, thermal decomposition, hydrothermal and solvothermal syntheses, sol-gel synthesis, microemulsion, ultrasound irradiation, and biological synthesis are just a few of the established synthetic pathways. The different synthesis methods can influence typical properties such as shape, morphology, size, and biocompatibility [21,26–29]. This work focuses on the chemical co-precipitation method according to the Massart process [21,22,30]. It is a fast, inexpensive, reproducible method with a high yield and allows being influenced towards particle size and magnetization. As described by Eq 1.2, IONs form when iron (II/III) ions salts in an aqueous solution are added to an alkaline solution (Eq. 1.2) [21,22,29,31].



When the iron ion concentration reaches supersaturation, seeds form that nucleate and grow upon an equilibrium. Small IONs with a sharp size distribution form when fast nucleation is followed by a short growth phase [32,33]. The size, composition, and morphology of the magnetite nuclei formed depend on many factors, including $\text{Fe}^{3+}/\text{Fe}^{2+}$ ratio, dosing rate, temperature, ionic strength, pH, synthesis time, and stirring speed [26,27,33,34]. The particle size generated by co-precipitation is in the range of 3 – 17 nm [26,29]. Roth et al. have shown that a high saturation magnetization can be caused by using high iron salt concentrations with a $\text{Fe}^{3+}/\text{Fe}^{2+}$ ratio $< 2:1$. Bigger particles can be synthesized with high iron salt concentration and adjusting the $\text{OH}^-/\text{Fe}^{3+/2+}$ balance to 1.4:1 [26]. Stoichiometric

ratios form goethite and lepidocrocite instead of magnetite [26]. The stirring rate is indirectly proportional to the ION size, as it induces the nucleation process [28,35].

To prevent the oxidation from magnetite to maghemite, as described above, the synthesis and storage of the IONs should occur under a nitrogen atmosphere [29,31]. The oxidation expands from the particle surface to its core and decreases the saturation magnetization. Furthermore, oxidation can change the surface reactivity of IONs [8,29]. Bare IONs (BIONs) tend to agglomerate with time due to energy reduction. This effect reduces the dispersibility and the usable surface area and impedes its application in biomedical fields [21,29,36,37]. BIONs are also known for their non-specific interactions with blood proteins, which reduce the half-life of the particles in the body due to opsonization and subsequent rapid removal from the bloodstream [31,38–40].

1.1.2. Coatings of iron oxide nanoparticles

A solution to these problems of BIONs is surface functionalization. Coating with organic (dextran (Dex), carboxymethyl-dextran (CMD), polyvinyl alcohol (PVA), polyethylene glycol (PEG), polylactide-co-glycolide (PLGA)) or inorganic polymers (silica, carbon, gold), bioactive molecules, supramolecular structures or organic surfactants (oleic acid, lauric acid, alkyl sulfonic acid) counteract agglomeration and oxidation (Figure 1.3) [29,31].

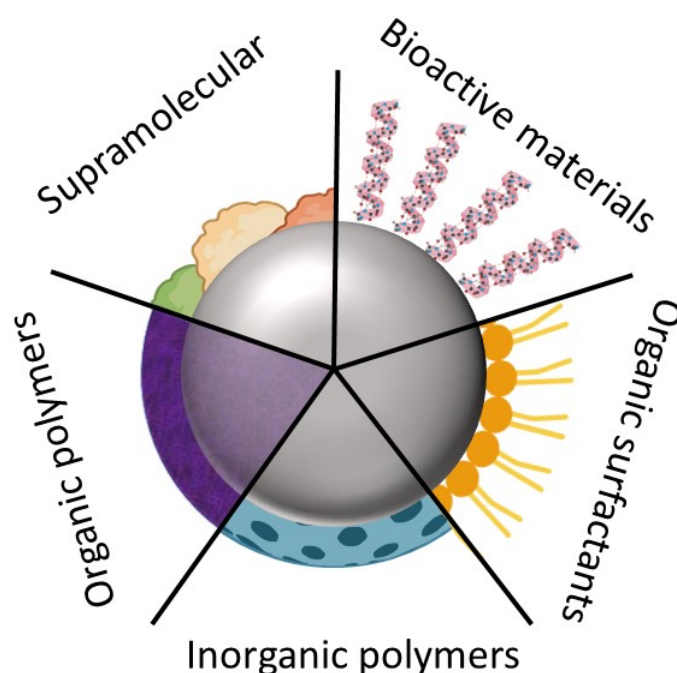


Figure 1.3: Schematic illustration of different particle coatings, including supramolecular structures, bioactive materials, inorganic polymers, organic polymers, and organic surfactants. It was created with BioRender.com.

One coating method is the generation of a core-shell structure. The IONs are enclosed in a coating, stabilizing them while maintaining their flexibility [22]. The coatings can either be synthesized around the ION core or already formed in situ during the particle synthesis [31]. Surfactants like oleic acid can

comprise particles with a lipid bilayer by bidentate coordination of the carboxyl group [41]. Roth et al. showed that increasing the oleate bilayer leads to a decrease of the isoelectric point from pH 7.4 to 4.3 and, therefore, a steric and electrostatic stabilization of IONs [41]. Wang et al. used oleic acid-stabilized monodisperse nanoparticles for an efficient phase transfer from hexane to an aqueous cyclodextrin solution [42]. Even though good colloidal stability is desirable, the IONs are more susceptible to Brownian motion the smaller the agglomerates are. Higher magnetic fields are required for controlled separation or guidance of the particles because this effect reduces magnetic interaction [43]. Furthermore, due to their hydrophobicity, organic surfactants can be challenging to apply *in vivo* [42,44].

As coatings, bioactive molecules like proteins, peptides, and lipids obtain material magnetization [21,31,45]. Jahanban-Esfahlan et al. used desolvation to bind various serum albumins on magnetic nanoparticles [46]. Nosratie et al. generated bovine serum albumin (BSA) coated particles as biocompatible curcumin carriers for anticancer therapy [46,47]. The negative surface charge of these IONs prevents electrostatic interaction with negatively charged plasma proteins or blood cells, which keeps them stable in biological media [31,47].

Inorganic and organic coating compounds can, apart from enhancing stability, significantly increase the range of applications of IONs [31]. One of the most widely used inorganic coatings is the bioinspired material silica [21,31]. It is an acid-stable material that improves the dispersion of IONs in aqueous solutions and leads to better durability [22,48]. The inert silica shell stabilizes the magnetic core by shielding the magnetite-dipole interactions, and the negative surface charge increases the Coulomb repulsion [29]. The Stöber process can generate the silica coating by hydrolysis and condensation reaction of tetraethoxysilane (TEOS, Figure 1.4 A) [49,50].

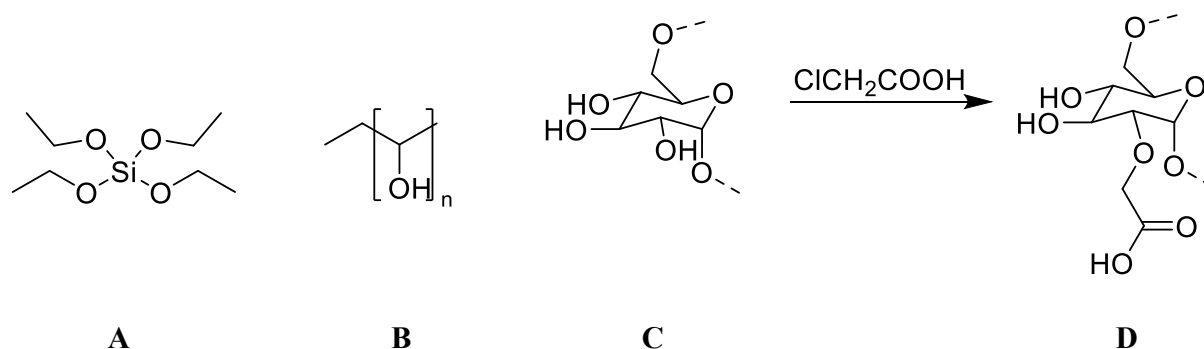


Figure 1.4: Structure of TEOS (A) and PVA (B). Synthesis of CMD (D) by reaction of Dex (C) with monochloric acid under alkaline conditions.

Silanol groups on the surface of IONs reduce toxicity and lead to colloidal stability at physiologic pH values. These effects make silica-coated IONs applicable in molecular biology and medicine [45,51,52]. In nanomedical applications, silica coating delays the degradation of particles in the human body, and its easy functionalization facilitates cellular uptake or drug loading [22,48,53,54]. The enhanced reactivity and specificity of the silica surface allow enhanced binding of organic molecules and

biological ligands by electrostatic interaction or covalent binding [29,55]. Differently synthesized and functionalized ION@Silica have been analyzed in recent years for multiple applications like contrast agents for magnetic resonance imaging, adsorption of BSA or pyridine, drug delivery of doxorubicin (DOX) or mycophenolic acid, or nanowarming [56–62].

Organic polymers are advantageous due to their good biocompatibility and water solubility [31,63]. Many of them, e.g., PEG, PVA, polyvinylpyrrolidone (PVP), chitosan, Dex, or CMD, can prolong the circulation of IONs in blood [63–67]. PVA is a hydrophilic, non-toxic, biodegradable, synthetic polymer prepared by hydrolysis of polyvinyl acetate (Figure 1.4 B) [68]. A base-catalyzed transesterification mainly guides the conversion of polyvinyl esters with ethanol [69]. The number of hydroxy groups in the polymer defines its physiochemical and mechanical properties [70]. PVA is approved by the food and drug administration (FDA) and is an established protective agent for ION stabilization [29,71]. Commonly ION@PVA are synthesized by the addition of the polymer to the co-precipitation [72]. PVA adsorbs on the ION surface and can form hydrogen bonding with the hydroxylated and protonated surface of the iron oxide [73]. The interaction is influenced by the polymer concentration, molecular weight, pH, ionic strength, and surface charge [74]. The polymer surface interaction leads to steric stabilization and prevents agglomeration of IONs. ION@PVA, which are stabilized both physically and chemically, have the ability to form agglomerates ≤ 100 nm in size. This makes it a promising candidate for biomedical applications, where hydrodynamic diameters less than 200 nm are considered optimal. [73]. Kayal et al. demonstrated that ION@PVA is a potential drug carrier of DOX for magnetically controlled drug delivery with a size distribution of 10-15 nm [75]. Ebadi et al. showed good binding and high release of the hydrophobic drug sorafenib for tumor treatment with hydrophilic PVA/layered double hydroxide-coated IONs [76]. Another often used organic polymer is the water-soluble, biopolysaccharide Dex (10-50000 kDa, Figure 1.4 C). It can be produced from sucrose by *Leuconostoc* bacteria [77]. The FDA already approves Dex-coated IONs for ferumoxytol and Feridex IV drug delivery to treat anemia and as a contrast agent in magnetic resonance imaging (MRI) [78–81]. Unterweger et al. and Peng et al. also investigated Dex-coated particles as a drug delivery system (DDS) of DOX or hypericin in cancer therapy [82,83]. The chemotherapeutic efficacy of DOX could be improved by loading on the ION@Dex in *in vitro* and *in vivo* experiments [82]. Dex can be functionalized with carboxymethyl side chains by adding monochloric acid at a basic pH value (Figure 1.4 D) [81]. Carboxymethyl dextran (CMD) is increasingly used as a coating because of its high density of free carboxyl groups [84,85]. ION@CMD can be synthesized in a one-step process or by carboxymethyl-activated cross-linking to ION@Dex [84,86]. Ayala et al. showed, based on ION@CMD with different amounts of carboxymethyl-substitution, that the cellular uptake in CaCo-2 human colon cancer cells could be increased with a rising negative charge [84]. The negative surface charge leads to slower clearance of the particles from the bloodstream and fewer fouling activities [85,87]. The carboxyl groups have cross-linked the particles to anti-BSA antibodies or alcohol dehydrogenases [88,89]. Das

et al. showed that ION@CMD have a high potential as a robust contrast agent for MRI mapping the cerebral blood volume [90].

Supramolecular polymers as a coating for IONs find a minor biomedical application yet but can induce many tunable properties to the system. Supramolecular nanoparticle systems enable the incorporation of different hydrophilic or hydrophobic drugs, photosensitizers, radiosensitizers, and biological therapeutics [91]. However, research has increased in the last five years [91–93]. Li et al. have designed a magnetically controllable, non-viral gene delivery system composed of a cationic star polymer forming supramolecular complexes with surface oleyl groups on IONs. The star polymer exists of oligoethylenimine chains on an α -cyclodextrin core [92]. Philip et al. report a new stabilizing supramolecular β -cyclodextrin coating with antibacterial and antifungal activity [93]. The innovative combination of IONs and hydrogels has drawn considerable interest as an emerging delivery system, electronics, catalysis, and biosensing. Hydrogels (pluronic F127, hyaluronic acid, alginate, hemicellulose) are hydrophilic, three-dimensional network gels of water and cross-linked polymers [94–98]. They can swell and retain significant water content, which provides excellent biocompatibility [94,99]. Hydrogels can be categorized as conventional hydrogels that are insensitive to environmental changes or environmentally sensitive hydrogels that can be stimulated by the external environment (e.g., temperature (T), pH, light, pressure, electricity). Especially for controlled drug release, stimuli-responsive hydrogels are of significant interest [99]. Combining IONs and hydrogels can lead to synergistic property enhancement of the components, e.g., a reduced agglomeration of IONs due to the mechanical strength of hydrogels and magnetic responsive hydrogels [99,100]. IONs can be encapsulated in hydrogels (core-shell), embedded in a hydrogel matrix, or synthesized in situ during the gelation process [99]. Gonçalves et al. synthesized mercaptosuccinic acid-modified IONs that can bind and release nitric oxide and incorporated them in pluronic F127 hydrogel. The system could find usage in topical applications such as nitric oxide delivery in the human skin for improved wound healing [101]. Zhang et al. synthesized multifunctional hydrogels consisting of folate/polyethyleneimine-conjugated poly(organophosphazene) polymers, encapsulating small interfering ribonucleic acid (siRNA) and Au-IONs, forming a nanocapsule structure. The nanocapsules show potential for prolonged blood circulation, magnetically controlled drug delivery, and near-infrared hyperthermia [20]. Most methods are a time-consuming, expensive multi-step synthesis of IONs and encapsulation by the hydrogel, drug loading, washing, and drying. This limits large-scale production [102]. In contrast to the methods mentioned above, Zhao et al. developed an easy one-pot synthesis for stimuli-responsive hemicellulose-based magnetic hydrogels. IONs were in situ formed during covalent crosslinking of O-acetylgalactoglucomannan. The system doesn't need tedious purification and has excellent potential to be used for controlled drug release of BSA [102]. Hydrogels can improve drug biocompatibility and bioavailability, prevent ION aggregation and oxidation, and keep drugs from degrading prematurely. The majority of this field's research is conducted in vitro and in vivo on mice. Human study results are still lacking [20,102,103].

Depending on their application, IONs must meet specific criteria. Therefore a good and entire characterization is inevitable.

1.1.3. Properties and characterization of iron oxide nanoparticles

Composition, surface properties, magnetization, size, including agglomeration, and cytocompatibility, are essential parameters that need to be known for applying IONs in nanomedicine (Figure 1.5, Table 1.2).

The particle composition can for example, be analyzed by Fourier-transform infrared (FT-IR), thermogravimetric analysis (TGA), Raman spectroscopy, and X-ray diffraction (XRD). FT-IR spectroscopy is a tool to analyze the organic and inorganic composition of bare and coated IONs. It can determine qualitatively if a coating or an adsorption/desorption was successful. Every molecule has a unique FT-IR spectrum [104,105]. IR active molecules need at least two atoms to form a molecular bond and allow a dipole moment. IR light is absorbed by molecules and converted into molecular symmetrical or asymmetrical vibrations or rotations. [106,107]. The absorption bands formed can be assigned to existing atom bonds, and thus the sample composition and their functional groups can be determined [106].

Raman spectroscopy detects a substance's polarization using visible, near-infrared, or near-ultraviolet laser light. The molecule doesn't need a permanent dipole moment. Therefore, water can be used as a solvent [108]. The Raman effect relies upon inelastic scattering. The induced energy shift determines the vibrational modes of the molecule [109–111]. IR and Raman spectroscopy give related yet complementary information. Raman indicates the covalent character of a molecule, while FT-IR is usable to describe the ionic character [108]. Raman spectroscopy has been used to analyze the oxidation process from magnetite to maghemite of IONs [8]. A potential alternative for analyzing the oxidation state of IONs is Mössbauer spectroscopy. It is based on the Mössbauer effect and can differentiate between divalent and trivalent iron ions [8].

Thermogravimetric analysis (TGA) is a quantitative technique for determining the amount of coating material, adsorbed components, or moisture and their characteristic decomposition temperatures [112]. It calculates the mass loss of a material as a function of temperature and time while it is heated in a controlled environment. Steps in the TGA curve can indicate mass changes caused by evaporation, drying, desorption or adsorption, sublimation, or thermal decomposition. It is a powerful tool for analyzing ION surface coatings when combined with FT-IR, mass spectrometry, or gas chromatography [113].

Table 0.1: Summary of different analytical tools for the characterization of IONs [6–13].

Analytical tool	Basis	Analyzed properties	Determines	Limits
FT-IR	Light absorption, change in dipolmoment	Composition, surface properties	Successful coating, surface functionalization, ionic character, binding, adsorption, desorption	Water as solvent not possible
TGA	Mass change	Composition	Quantifies amount of coating, bound components, moister	Expensive
Raman	Light scattering, change in polarizability	Composition	Oxidation state, successful coating, covalent character	Expensive
Mössbauer spectroscopy	Mössbauer effect	Composition	Oxidation state	Time-consuming
XRD	Angle of scatter radiation, Bragg's law	Composition, size	Crystallinity, phase purity, diameter	Sample must be crystallin
TEM	Transmitted primary electron signal	Composition, size	Size, shape, surface topography, diameter	Expensive
DLS	Brownian motion, backscattered light intensity	Size, agglomeration	Hydrodynamic diameters, size distribution	Sedimentation, material properties
ANUC	Sedimentation velocity	Size, agglomeration	Hydrodynamic diameters, size distribution	Time-consuming
Zeta potential	Electrophoretic light scattering, electrical double layer	Surface properties	Colloidal stability, IEP	High agglomeration
BET	BET adsorption isotherm	Surface properties	Specific surface area	Time-consuming, dried samples are necessary
SQUID	Superconducting loop, changes in the magnetic flux	Magnetical behavior	Saturation magnetization	Expensive
STEP	Lambert-Beer law, magnetically induced sedimentation velocity	Magnetical behavior	Magnetophoresis	Low throughput, reproducibility
VSM	Homogeneous magnetic field, relaxation processes	Magnetical behavior	Magnetic moment	Efficiency is affected by temperature

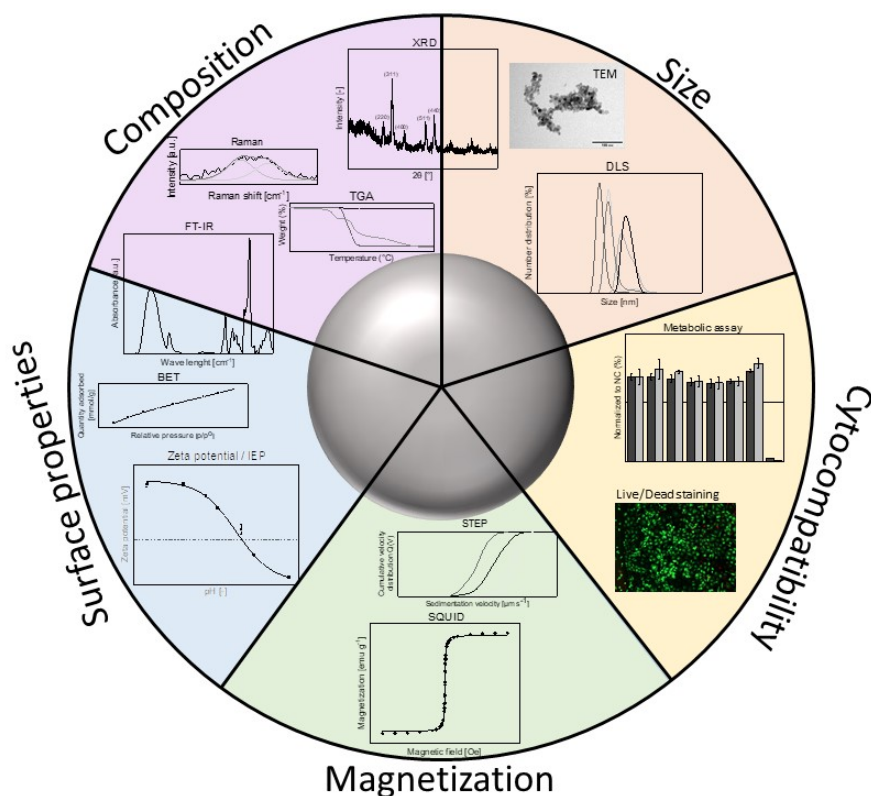


Figure 1.5: Illustration of different particle characterization methods regarding their size, composition, surface properties, magnetization, and cytocompatibility. It was created with BioRender.com.

X-ray diffraction (XRD) allows for determining a material's crystallinity and phase purity. Therefore it is a standard method to analyze the crystal type. Magnetite or maghemite, e.g., have an inverse and distorted spinel crystal lattice, respectively [31,114]. X-rays are scattered by the electron shell of an atom producing elastic scattering. Significant diffraction is created when the spacing between the scatters is comparable to the wavelength of the radiation. A regular arrangement of atoms in the lattice produces a regular diffraction array of spherical waves. This diffracted radiation forms interferences with reflection having a distinct Bragg angle [115–118]. Additional to the crystal structure, the size of nanoparticles can be determined by XRD. The size can be determined by changes in the Bragg reflection due to higher defect rates in nanomaterials. Using the Scherrer equation (Eq. 1.3), the crystalline particle size (L) can be calculated using the shape factor (K) with a value of 0.89, the X-ray wavelength (λ), the Bragg angle (θ), and the broadening of the half maximum intensity (FWHM) after the subtraction of the instrumental broadening ($\Delta 2\theta$) [119,120].

$$L = \frac{0.89 \cdot \lambda}{\Delta 2\theta \cdot \cos(\theta)} \quad 1.3$$

Transmission electron microscopy is an alternative method for imaging the size, shape, and surface topography of IONs in high resolution (TEM). This technique is frequently used to examine microstructures, nanostructures (particles, fibers), and atom imaging [121,122]. An electron gun in a

high vacuum produces electrons (200-300 keV) [122]. When the electron beam hits the probe prevalent, primary, secondary electrons, and X-rays are emitted from the specimen. The transmitted primary electron signal is used for TEM and detected by charge-coupled device cameras. The arrangement of atoms can be examined using high-resolution TEM [121].

Dynamic light scattering (DLS) is an optical method to analyze the hydrodynamic size of IONs. DLS is an essential tool for improving the knowledge of IONs before application as their agglomeration depends on the concentration, T, pH, and medium composition. When a light beam collides with the particles, it is scattered in all directions due to the different refraction indices. Backscattered light intensity is measured over time. Particle movement, according to Brownian motion, causes changes in intensity. Attraction, repulsion, and sedimentation can all influence the measurement. According to the Stokes-Einstein law, smaller particles move faster than bigger ones (Equation 1.4) [123]. The hydrodynamic diameter (d_H) can be calculated with the diffusion coefficient (D), the Boltzmann constant (k_b), T, and the viscosity (η) [124,125].

$$D = \frac{k_b \cdot T}{6 \cdot \pi \cdot \eta \cdot d_H} \quad 1.4$$

Analytical ultracentrifugation (ANUC) is an alternative quantitative method for determining hydrodynamic diameters. Unlike DLS, it relies on sedimentation velocity analysis and is more time-consuming. However, ANUC offers several advantages, including the ability to analyze a wide range of sample types, high accuracy, and the ability to directly measure the molecular weight of the sample. [9,126].

The surface properties can be characterized by zeta potential and Brunauer-Emmett-Teller (BET) measurements. The zeta potential is used to analyze colloidal dispersive systems' electrokinetic potential and stability by electrophoretic light scattering (Table 1.3) [127]. Particles suspended in a specific medium adsorb ions in a double layer. Different models of the electrical double layer exist. An advanced concept is the stern model, combining a static layer (Helmholtz plane) with a diffuse layer. It consists of the surface charge of the particles that interact with oppositely charged ions.

Table 1.3: Coherence of zeta potential and the stability of a colloidal dispersive system [127].

Stability	Zeta potential (mV)
Rapid coagulation or flocculation	0 to ± 5
Incipient instability	± 10 to ± 30
Moderate stability	± 30 to ± 40
Good stability	± 40 to ± 60

The inner layer includes adsorbed ions, and the outer layer, called the slipping plane, consists of diffusely arranged ions dependent on electrical forces and temperature (Figure 1.6). The net electrical charge of this outer area causes the zeta potential. The zeta potential measurement indicates the degree

of electrostatic repulsion [128–130]. The zeta potential can be used to confirm a coating, determine potential adsorption and desorption properties and the isoelectric point (IEP). It is mainly influenced by the ionic strength, pH, functional groups, and particle concentration [29,131].

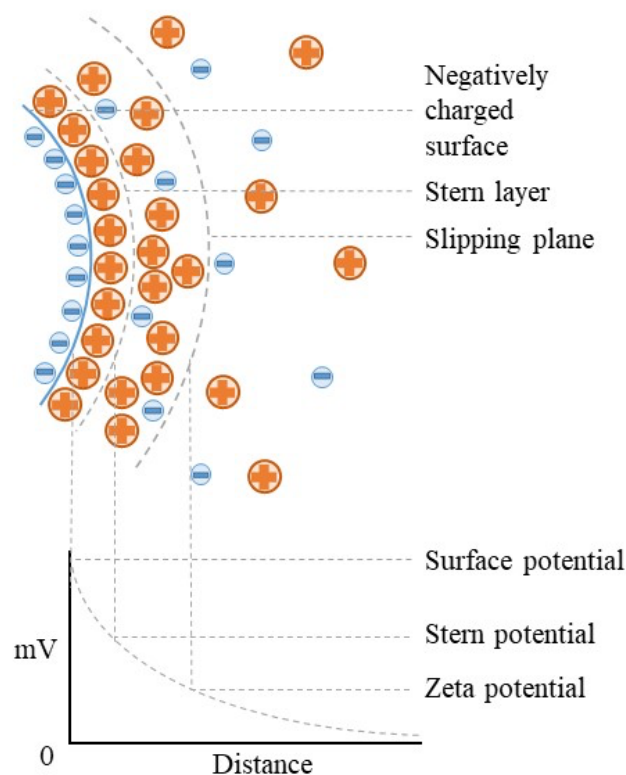


Figure 1.6: Schematic illustration of the surface charge and the surrounding diffuse double layer with stern layer and slipping plane. Adapted from Lunardi et al. [131].

The DLVO theory (named after Derjagun, Landau, Verwey, and Overbeek) describes the colloidal stability based on attractive and repulsive forces between dispersed particles, e.g., Van-der-Waals, sterical, and electrostatic interactions. It is assumed that the electrochemical double layers of particles overlap when they get closer. The repulsive force range is bigger than the Van-der-Waals force, which stabilizes particle dispersions electrostatically. Agglomeration occurs if no stability maxima is reached at a specific distance between two particles. [132,133]. A further theory is the charge distribution model (CD) model, where surface complexes are treated as spatial distribution, and the surface structure is included [134]. An alternative is combining the dissociative electrical double layer model (DEDL) and Lubetkin-Middleton-Ottwil (LMO), which uses Maxwellian electrostatics with linear distribution laws. Compared to the DLVO theory, larger coulombic forces and no universal Van-der-Waals adhesion are predicted [135].

The specific surface area can be determined with BET measurements. A specific amount of gas (often nitrogen) is adsorbed in a monolayer on the material depending on the surface and pore area. Adsorption is measured in equilibrium with the adsorptive gas pressure and plotted against the relative pressure p/p_0 . The adsorbed amount of gas (n_a) at a specific pressure (p) is described by the linear BET adsorption

isotherm (Eq. 1.5). Further parameters are the BET constant (C), the monolayer capacity (n_m), and the saturation pressure (p_0). This equation can determine the specific surface area [10,136,137].

$$\frac{p/p_0}{n_a \cdot (1 - \frac{p}{p_0})} = \frac{1}{n_m \cdot C} \cdot \frac{C-1}{n_m \cdot C} \cdot p/p_0 \quad 1.5$$

The magnetical behavior of IONs can be determined with a superconducting quantum interference device (SQUID) and Space-and-Time-resolved Extinction Profiles (STEP) technology. SQUID is a sensitive technique that can analyze the ferromagnetic properties and the saturation magnetization of nanoparticles. It uses a superconducting loop interrupted by Josephson contacts. An external magnetic field leads to a decreased potential at these contacts. The responding qualities of SQUID are linearized by a flow control loop that allows for the detection of minimal changes in the magnetic flux [11,138,139]. An alternative method using periodic vibrations in a homogeneous magnetic field is a vibrating sample magnetometer (VSM) [140].

The magnetophoretic behavior of the particles can be determined by STEP technology. Sensors analyze the transmission profile in dependence on the distance, and the Lambert-Beer law determines the magnetically induced sedimentation velocity. The resilience counteracts gravity and magnetophoretic behavior. The efficient magnetophoretic speed depends on the change in the height of the IONs at a particular time. The agglomeration behavior and the magnetophoretic separation of IONs are highly influenced by pH, salt concentration, and viscosity [12,141].

Especially for the application in medicine, the cytocompatibility of IONs is essential. It can be analyzed by calorimetric cell viability assays for eukaryotic cell activity, like XTT (2,3-bis(2-methoxy-4-nitro-5-sulphophenyl)-5-[(phenylamino) carbonyl]-2H-tetrazolium hydroxide)-assay or Resazurin assay [142]. By metabolic activity, XTT is converted to colored formazan due to flavoprotein oxidases, mitochondrial succinoxidase, and cytochrome P450 system [143]. Watersoluble formazan can be measured in the cellular supernatant [144]. Viable cells can reduce the cell-permeable resazurin into pink fluorescent resorufin. Both dyes are quantitatively proportional to the number of viable cells. The resazurin reduction assay is slightly more sensitive compared to the tetrazolium reduction [145]. Live/dead viability staining is an alternative approach. Live cells are colored green, commonly with Calcein AM, a membrane-permeable dye metabolized with viable cells. Esterases cleave it to cytoplasmic green fluorescence that can be visualized by microscopy [146]. Propidium iodide colors dead cells red-fluorescent. It can only penetrate disrupted cell membranes and is excluded from viable cells [147]. The fluorescent of the nucleic acid stain gets enhanced 20-30 fold when bound to desoxyribonucleic acid (DNA) [148]. The live/dead ratio can be analyzed by counting [146].

1.2. Nanomedicine

Nanotechnology is used in a variety of sectors, including pigments, energy, and the environment, as well as catalysis, biology, and sensors [16,149–156]. Yet nanotechnology has an enormous potential to transform medicine and healthcare in the following years. New ideas and solutions have been developed to improve diagnosis, therapeutics, drug delivery, and regenerative medicine (Figure 1.7). In the future, nanomedicine could lead to a faster diagnosis, treatment, and prevention of diseases like cancer or antibiotic-resistant infections at a cellular level [14,156,157]. Nanomedicine is “the comprehensive examination, control, development, repair, resistance, and enhancement of all human natural frameworks, working from the atomic dimension, utilizing designed nano-devices and nanostructures” [14].

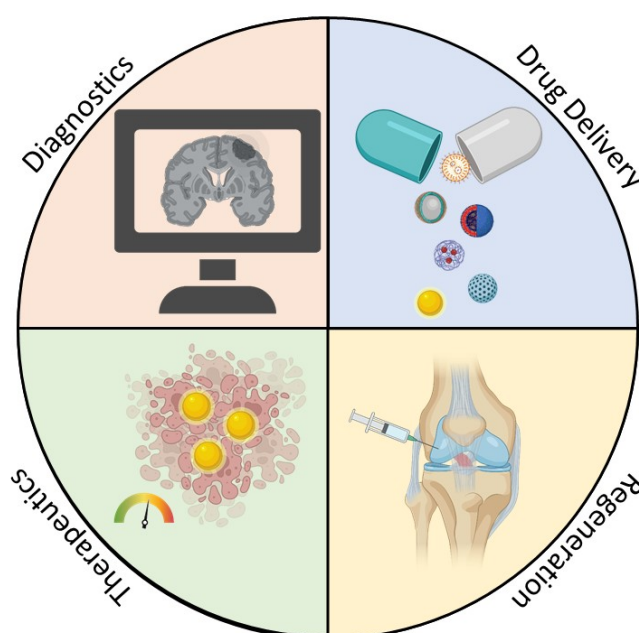


Figure 1.7: Illustration of the four main fields in nanomedicine: diagnostics, therapeutics, drug delivery, and regenerative medicine. It was created with BioRender.com.

1.2.1. Diagnostics

Diagnostics aims to detect diseases as early as possible under the given conditions. At the cellular and subcellular levels, nanotechnology enables early detection and prevention. It enables efficient and accurate clinical diagnostics *in vitro* and *in vivo* [158]. Especially cancer diagnosis and treatment can be improved by nanotechnology. The use of antibody-functionalized gold nanoparticles for biopsy diagnostics *in vitro* is a potential application. They bind epidermal growth factor receptors, which are abundant on malignant growth cells. When attached, they emit a characteristic light spectrum that indicates the presence of harmful cells [14,159]. Molecular imaging allows for non-invasive imaging of diseases *in vivo*. Once the stage of the disease has been determined, effective image-guided treatment can follow [14]. Nanoparticles can improve the imaging of biological processes in cells by acting as a contrast agent. They require unique characteristics to facilitate accumulation at a target and imaging

[160]. Materials that are electron-dense, fluorescent, radioactive, paramagnetic, or superparamagnetic can boost contrast generation. Therefore noble metal nanoparticles, quantum dots, and magnetic nanoparticles are focused [161]. Magnetic resonance imaging (MRI) creates spatial, anatomic, high-resolution images using nuclear magnetic resonance (NMR) active nuclei. Magnetic dipoles align under a strong magnetic field and revert to their original orientation at varying speeds and relaxation durations. T1 and T2 contrast agents can enhance contrast by altering the relaxation time. T1 contrast agents (lanthanides as gadolinium compounds) are paramagnetic and can shorten the longitudinal recovery, resulting in a lighter spot. T2 contrast agents (iron oxides) are superparamagnetic and increase the transverse decay rate leading to a darker signal [162–164]. Most approved MRI contrast agents are based on gadolinium. Due to the toxic side effects of Gd^{3+} ions, the European Medicines Agency (EMA) restricted the use of most linear Gd^{3+} agents for body scans in 2017, while macrocyclic gadolinium compounds are still allowed [165–167]. This restriction leads to a clinical need for safe MRI contrast agents. Unterweger et al. demonstrated the potential of new dextran-coated superparamagnetic IONs as a biocompatible and safe contrast agent. Their ultra-small IONs (30 nm) showed no hypersensitivity reactions, irritation potential, and no internalization by non-phagocytic cells [168]. IONs can find application in further quantitative imaging techniques called magnetic particle imaging (MPI) and magnetorelaxometry imaging (MRXI). MPI is a new, non-invasive imaging method based on superparamagnetic ION tracers established in 2005 by Philips [169]. MPI systems use particular changing magnetic fields to generate a single field-free point that can move through the sample. The applied magnetic tracers create a signal without a background [170]. Usually, electrical coils are used to generate fast-moving gradient fields, but Vogel et al. demonstrated a concept utilizing mechanically rotating permanent magnets (Halbach rings) [171,172]. This method needs no electrical power and can improve the signal-to-noise ratio [172]. MPI has high potential in cardiology, visualizing blood flow in real-time or the heart's pumping motion [169]. Solid tumors could be detected within rats after accumulation of the IONs in the tumor-induced by enhanced permeability and retention effect [173]. For MRXI, a net magnetic moment is generated by the alignment of superparamagnetic IONs in an external magnetic field. The relaxation of the net magnetic moment can be monitored by sensitive magnetometers like SQUID, fluxgates, or optically pumped magnetometers [174–176]. The method can quantify the spatial ION distribution in the body, which is essential for developing magnetic hyperthermia or magnetic drug targeting. Jaufenthaler et al. quantified the iron amounts to 6 μg and generated a high-precision 1D and 2D imaging setup [177]. Nanoparticle contrast agents can enhance the contrast of computed tomography (CT) measurements. Therefore, the exposure time of the x-ray radiation can be reduced [14]. Functionalized gold nanoparticles have been used to improve the visibility of small breast tumors or differentiate between cancerous or inflamed tissue [178]. Due to their physiochemical properties, biocompatibility, and non-toxicity, gold nanoparticles are used as tags, nucleic acid probes, or to bind DNA for diagnostic purposes [179]. Positron emission tomography (PET) uses positron-emitting radionucleotides as radiotracers to visualize metabolic processes and detect

tumors early. It can be improved by using radiolabeled nanoparticles and is often combined with MRI or CT [180,181]. PET can further be used for image-guided therapy and drug delivery of nanomaterials with real-time monitoring [181]. Thorek et al. used ^{89}Zr ferumoxytol-labeled superparamagnetic IONs for a high-resolution PET/MR investigation of deep-tissue lymph nodes. IONs can bind isotopes (radioarsenic, germanium-69) that can not be labeled with traditional chelator-based routes [182]. Liposomes and polymeric micelles have great potential to load positron-emitting radionucleotides for contrast imaging and use for cancer detection and combination with drug delivery [183].

1.2.2. Therapeutics

Nanotechnology-based therapeutics have the potential to significantly improve antimicrobial or anticancer treatment. Antimicrobial activity is high in nanocrystals or nanoparticles made of silver, zinc oxide, or antibiotic-coated nanoparticles. Silver nanocrystals can emit silver ions from their surface for up to seven days. Silver ions exhibit antibacterial properties against a variety of species, including vancomycin-resistant enterococci and methicillin-resistant staphylococci [14,184]. Silver nanoparticles' antibacterial activity is based on a variety of mechanisms, including a breakdown of the cell wall by Ag^+ or reactive oxygen species (ROS), denaturation of the membrane or ribosomes, interruption of adenosine triphosphate (ATP) generation, and interference with DNA replication [185]. Hyperthermia is an alternate, risk-free cancer therapy method. While cancer cells are more heat-sensitive than healthy cells, controlled heating can eradicate them without causing injury to surrounding tissue. Hyperthermia treatment raises the body temperature to $40\text{ }^\circ\text{C}$ - $43\text{ }^\circ\text{C}$. The therapy is most effective when the cancer tissue is heated at $41\text{ }^\circ\text{C}$ for one hour [186,187]. Hyperthermia has been used to treat liver, breast, and prostate cancer and glioblastoma [187,188]. Although many ideas exist to heat cancer cells ranging from microwaves or ultrasound to infrared radiators, the most promising technique seems to be nanosystems [186,188]. These systems are based on carbon nanotubes, graphene, gold, iron oxide, or silica [186]. Therefore, the nanosystems can be injected directly into subcutaneous tumors or targeted at cancer by surface modification, antibodies, or magnetic guidance [187]. Von Maltzahn et al. used long-circulating PEG-coated gold nanorods for irradiating tumors in mice by computational therapy. Near-infrared light is absorbed by the nanorods, leading to an oscillation of the electron cloud and creating heat [189]. Superparamagnetic IONs can be magnetically guided to cancer after injection (Figure 1.8A). An alternating magnetic field creates magnetic hysteresis of IONs. The heat generated by Brownian rotation and Néel's rotation depends on the nanoparticles' size and the magnetic moment (Figure 1.8B) [186].

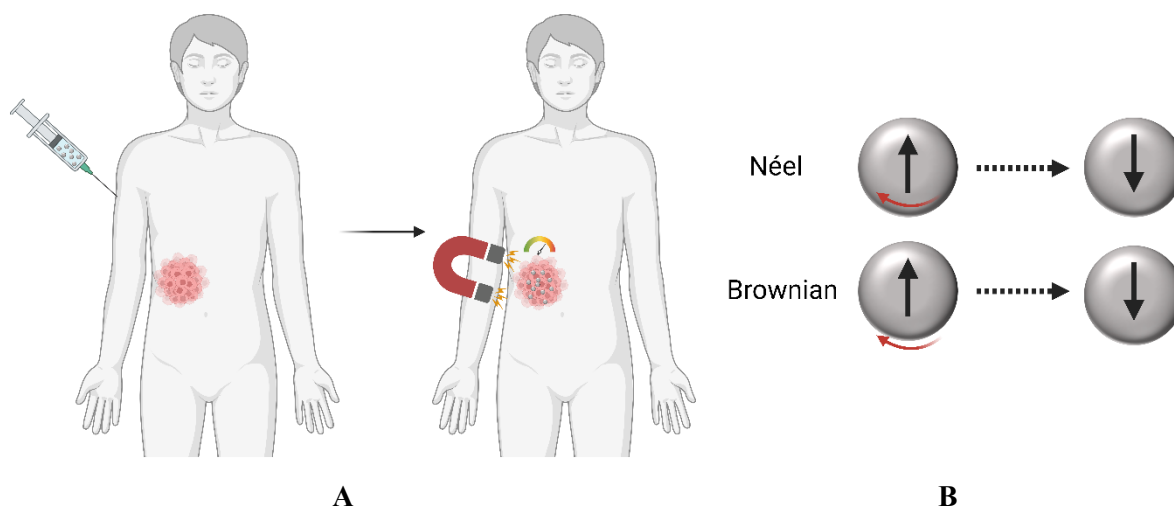


Figure 1.8: **A** Illustration of steps for magnetic hyperthermia treatment. **B** Scheme of Néel or Brownian relaxation of IONs. It was created with BioRender.com.

Magnetic IONs can enhance membrane permeability and lead to microtubule or protein damage, improving anticancer treatment. The therapy induces apoptosis and necrosis and inhibits cell growth [186,188]. Jang et al. used magnesium-doped $\gamma\text{-Fe}_2\text{O}_3$ superparamagnetic nanoparticles for massive magnetic heat induction. They showed hyperthermia effects and complete tumor killing with *in vitro* and *in vivo* studies [190]. Hemery et al. could induce 80% glioblastoma cell death with PEGylated multicore IONs by hyperthermia treatment [191].

1.2.3. Drug Delivery

Drugs frequently fail clinical trials due to inaccuracy in delivery or cytotoxicity. As a result, novel strategies for effective drug delivery are being investigated. Conventional drug delivery is frequently hampered by the medication's poor solubility or stability, as well as its low specificity or therapeutic index. Furthermore, due to the short half-life and high distribution throughout the body, a high pharmacological dose is required, resulting in side effects and limited patient compliance [192]. Nanoparticles, with their high surface area-to-volume ratio, are ideal for targeted drug delivery. They can carry a high drug dose directly to a target, like cancer cells or inflamed tissue. With a targeted delivery, the overall drug amount can be reduced, and side effects to healthy cells are minimized. This specific efficient treatment and reduced drug consumption decrease the general patient cost [186,193]. Recent progression in nanotechnology led to various drug-binding carriers, ranging from gold or iron oxide nanoparticles to fullerenes, liposomes, micelles, or dendrimers [186]. Combining drugs with nanoparticle carriers helps reduce toxicity, protect the drug from degradation or clearance, and improve temporal and spatial presentation. A high drug loading can be achieved by incorporating it during the nanoparticle formation or adsorbing afterward. The ideal mechanism depends on the material and drug properties. Commonly high binding efficiencies for macromolecules or proteins can be achieved near the IEP at low solubility and high adsorption. Electrostatic interactions with the material can bind smaller molecules [194].

A controlled drug release can be sustained or stimuli-responsive. A sustained release is used to deliver a drug at a certain rate over a specific period and can happen through diffusion or erosion control [194]. An example is hollow and porous magnetite particles that release cisplatin by a slow diffusion-controlled process [195]. The stimuli-responsive release can be induced by pH, temperature, enzymes, or light, depending on the polymer or particle type [194]. Anti-cancer drug delivery systems often use the pH difference between healthy tissue with a pH of 7.4 and a pH of ~ 6.5 around solid tumors. Therefore different polymer-based carriers (poly(acryl amide), poly(acrylic acid), poly(methyl acrylate), poly(dimethylaminoethyl methacrylate)...) can be used that change their structure and hydrophobicity depending on the protonation state [194,196]. Furthermore, the drug can be conjugated on the carrier with cleavable bonds like imine (pH $< 5-7$), hydrazone (pH < 5), acetal (pH $< 4-5$), amide (amidase), 2-nitrophenyl ester (ultraviolet (UV) light) [194].

Two types of targeted drug delivery systems exist: active and passive targeting. Passive targeting occurs as a result of the body's reaction to the physiochemical properties of the drug and the drug carrier [192]. Due to the enhanced permeability and retention (EPR) effect and slow lymphatic drainage, nanoparticles enter blood vessels better at the disease site, leading to drug accumulation at the target [197]. Active targeting uses specific ligands like antibodies, proteins, polysaccharides, nucleic acids, or peptides bound to the nanoparticles to target the biological interface [192].

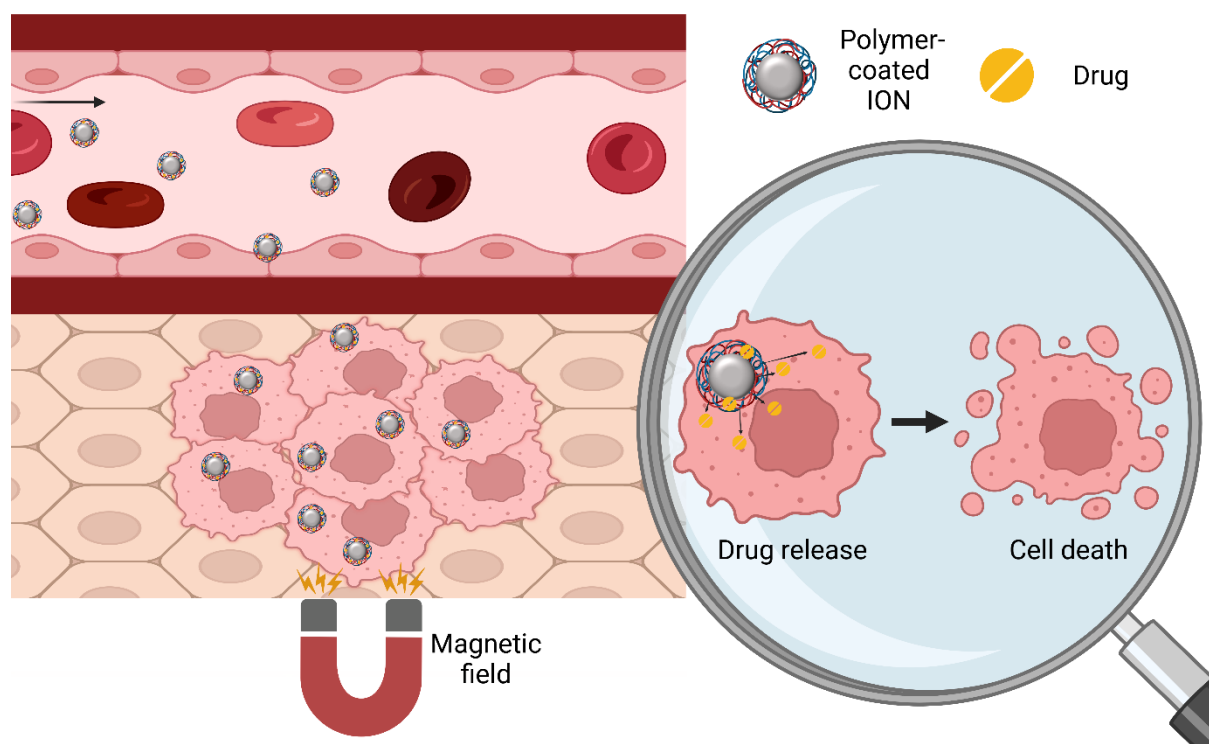


Figure 1.9: Illustration of magnetically controlled drug delivery. Drug-loaded polymer-coated IONs are guided to cancer cells by a magnetic field. After drug release, cell death is induced. It was created with BioRender.com.

Specific physical environments like a magnetic field can create active transport. Magnetic drug targeting is based on magnetic drug carriers, commonly IONs, guided by an external magnetic field to the target.

Magnetic fields are safe for the human body. Therefore they can be used to direct IONs to deep tissue. Once the drug-loaded particles have reached their target, the drug can be released, e.g., cancer cells treated (Figure 1.9) [198]. Between the 1950s and 1960s, the first experiments with magnetic particles were done. Meyers et al. used a horseshoe magnet to accumulate iron particles in dogs [199]. Today, multiple magnet designs exist for magnetic targeting. While static field magnet systems (FMS) are simple and convenient to handle, the target accuracy is comparatively low. Varying FMS leads to better accuracy with the potential of precise 3D targeting, yet leads to more complex hardware systems. Permanent magnets have lower magnetic fields and field gradients compared to electromagnets. However, the latter ones are more energy-consuming [198]. As magnetic nanocarriers, mostly polymer-coated IONs are used. Wang et al. encapsulated IONs and DOX in poly(ϵ -caprolactone), generating a pH-sensitive system with an initial and sustained release [200]. The drug delivery approach is often combined with imaging or hyperthermia to create a controllable synergistic system. Qu et al. combined magnetic hyperthermia and thermosensitive drug release by using polymer (polylactide-b-poly(N-isopropyl acrylamide-co-N, N-dimethyl acrylamide) coated magnetic nanoparticles with a lower critical solution temperature at 42.5 °C. The particles were loaded with the chemotherapeutic drug camptothecin. The method demonstrated high anticancer activity based on heat-shock protein over-expression and hyperthermia improved drug uptake by the cancer cells [201].

1.2.4. Designing nanoparticles for their application in drug delivery

Size, shape, surface chemistry, and material are critical factors in designing new nanocarrier systems for drug delivery (Figure 1.10). The particle properties highly influence immune activation, the passage of biological barriers, and internalization into cells [194]. Nanoparticles can be introduced into the human body by injection, oral administration, or inhalation. Often nanosystems are injected to shorten the response time from the human body, overcome absorption problems in the gastrointestinal tract and control the drug rate and availability. Especially for expensive drugs like peptides or proteins, intravenous delivery is preferred [202]. When the nanoparticles enter the circulatory system they are immediately exposed to the immune system, renal clearance, and the mononuclear phagocyte system (MPS). The design of the nanoparticles has a significant impact on their application. IONs are frequently coated with a biocompatible polymer to optimize their behavior in the body and prevent aggregation and oxidation. The particle characteristics considerably influence the blood circulation time, which must be sufficient to achieve the targeting. The hydrophobicity, surface charge, size, and shape of nanoparticles all have a significant impact on their applicability. Toxicity can be caused by a high positive surface charge due to hemolysis, platelet aggregation, and accelerated clearance by the MPS. Negatively charged systems, as well as neutral systems in general, have a longer blood half-life [194]. To reach their target tissue, the nanoparticles must pass various biological barriers, including blood, liver, spleen, kidneys, blood-brain barrier, and the tumor vasculature for cancer treatment (Figure 1.11). In blood, poorly designed drug delivery systems can deteriorate and destabilize, resulting in particle aggregation or embolism. Furthermore, the drug could be released early [37]. Larger particles clear

faster than smaller ones in the blood [194]. Blood consists of cells, enzymes, vitamins, hormones, proteins (albumin, globulin, fibrinogen), amino acids, inorganic components, carbohydrates, fats, and multiple small molecules [203].

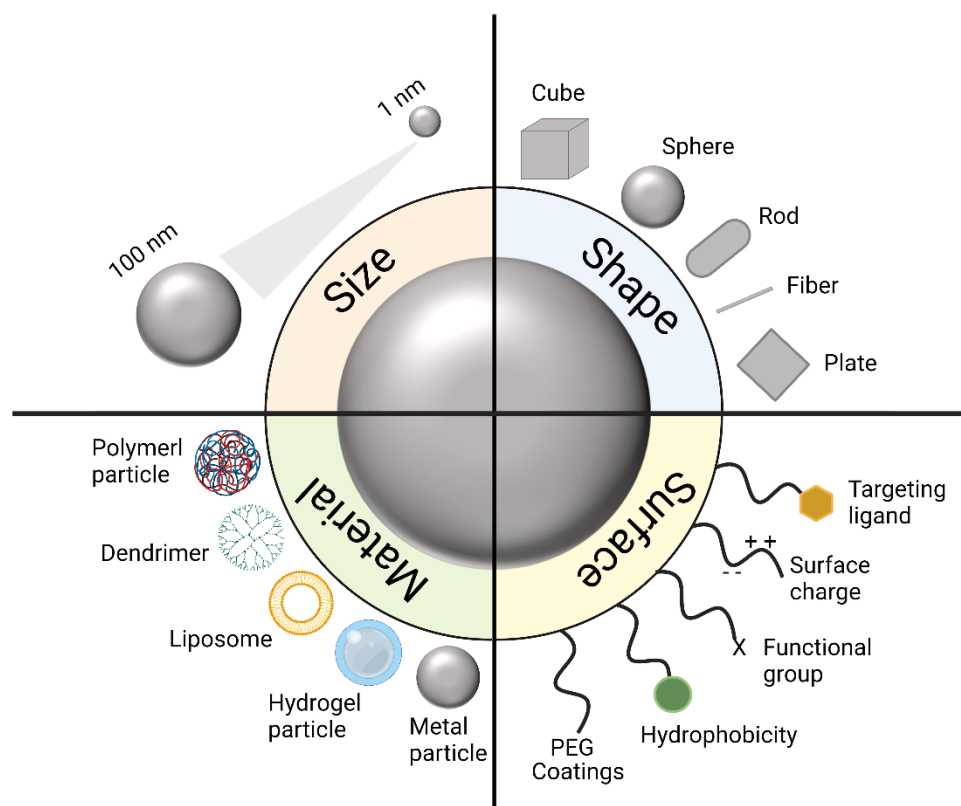


Figure 1.10: Illustration of the four parameters size, shape, surface chemistry, and material that mainly influence the properties of a drug delivery system. It was created with BioRender.com.

These elements can interact with the nanoparticle surface. PEG or zwitterionic coating materials, in particular, isolate the magnetic core and result in longer blood circulation durations. It is, therefore, advantageous to encapsulate sensitive medications within the covering [37]. Xue et al. showed that increased molecular weight of the PEG layer around IONs affected the clearance ratio and prolonged their half-life time. The particles had good biocompatibility and were predominantly cleared by the liver [204]. The particle size impacts the active clearance by the MPS, including the liver and the spleen. The liver rapidly clears particles with a diameter between 10-20 nm by phagocytic uptake or hepatic filtration. And the spleen removes particles larger than 200 nm by a filtration system composed of interendothelial cells [194]. If the hydrodynamic diameter of IONs is > 100 nm, the particles get eliminated by the reticuloendothelial system [194]. The kidneys physically filter nanoparticles by glomerular filtration and tubular secretion. Renal clearance removes particles less than 6 nm quickly and particles larger than 6-8 nm slowly. Charged nanoparticles can interact with the glomerular capillary wall and absorb serum proteins, but neutrally charged particles have the longest circulation period. When serum proteins bind, particle size increases, restricting filtration [194]. PEGylation can reduce protein

adsorption [205]. IONs with 10 – 100 nm hydrodynamic sizes are optimal for reduced kidney, liver, and spleen clearance [37].

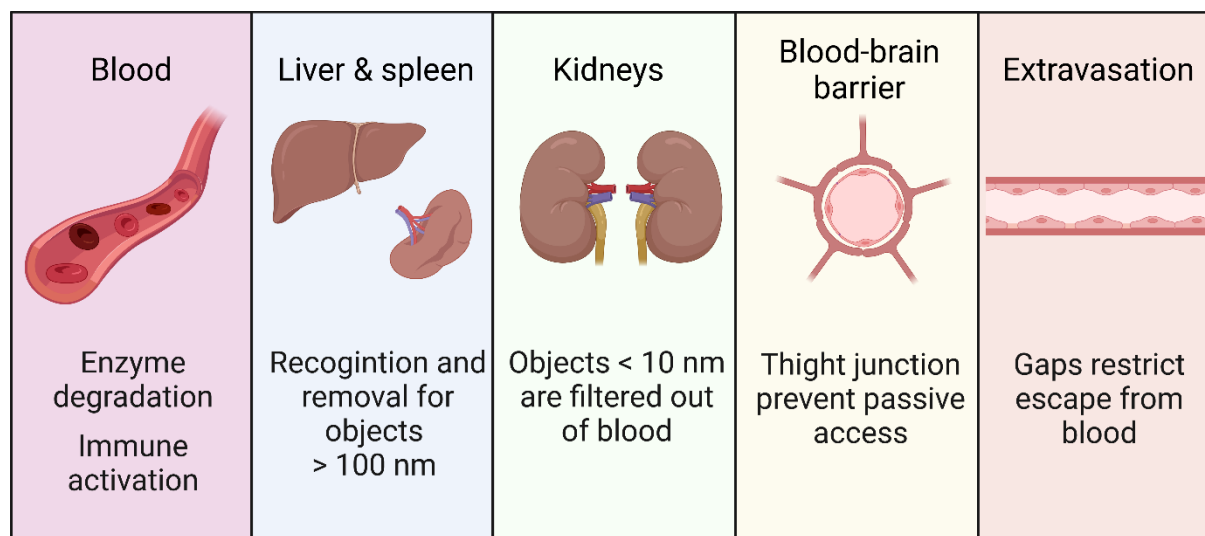


Figure 1.11: Summary of physiological barriers nanoparticles have to pass. It was created with BioRender.com.

After circulation in the bloodstream, the drug delivery system must extravasate from the vessel to the cell. This passage is determined by the size of the junction. In particular, endothelial cells in the brain have tight connections, resulting in a blood-brain barrier that limits passive access. Coating of IONs with PEG, chitosan, chlorotoxin, or amphipathic peptides and unique functionalization increases transcytosis, adsorption, or receptor-mediated endocytosis [37]. Usually, in healthy tissue, nanoparticles cannot passively pass the tight junctions. In the area of a tumor, the vessels have leaky walls, which allow passive tumor targeting. The enhanced permeability and retention are, in short, called the EPR effect. It enables the increased uptake of macromolecules and nanoparticles, leading to good tumor delivery and improved therapeutic effect [37,206]. Typically, the size of the significant gaps between the endothelial cells range between 100-800 nm, depending on the tumor type. While particles larger than 200 nm are cleared rapidly from the blood, nanoparticles < 200 nm are optimal for efficient extravasation into tumors [194].

Cellular uptake of the nanoparticles is essential for good drug delivery efficiency and the reduction of non-specific accumulation. After reaching their target, the nanoparticles are internalized into a cell by endocytosis. Depending on the particle properties, the internalization is initiated by the selective binding of a ligand on the particle to the cells' receptor or nonselective by hydrophobic or electrostatic interactions (Figure 1.12). The negatively charged cell membrane is a phospholipid bilayer containing cholesterol, glycolipids, and glycoproteins. The four major endocytic pathways are clathrin-mediated endocytosis forming vesicles ~100 nm size, caveolae-mediated endocytosis (~50 nm), pinocytosis, also known as cell drinking (~0.5-5 μm), and phagocytosis (>250 nm). Phagocytosis can only occur in macrophages, monocytes, and neutrophils.

As a result, the particle size and surface properties of the cell type determine the pathway. In tumors, cationic nanoparticles have more internalization but reduced distribution, whereas anionic nanoparticles have higher distribution but lower cellular absorption [37,194,207]. Vesicles transport the nanoparticles to organelles. The different stages have different pH values, getting more acidic from sorting endosomes (pH 6) to late endosomes (pH 5.5) and lysosomes (pH 4.5) [194,208]. Specific functionalization of IONs can target organelles or lead to intracellular escape. Lipids can fuse through the lipid bilayer, while amphiphilic molecules can induce endosome disruption at reduced pH. Furthermore, proton sponges, like polyethyleneimine, lead to osmotic swelling and rupture of the endosome [37]. Fast release from endosomes or lysosomes can be induced by pH-sensitive peptides that can interact with the membrane. One of them is GALA, a negatively charged amphiphilic α -helical peptide [194].

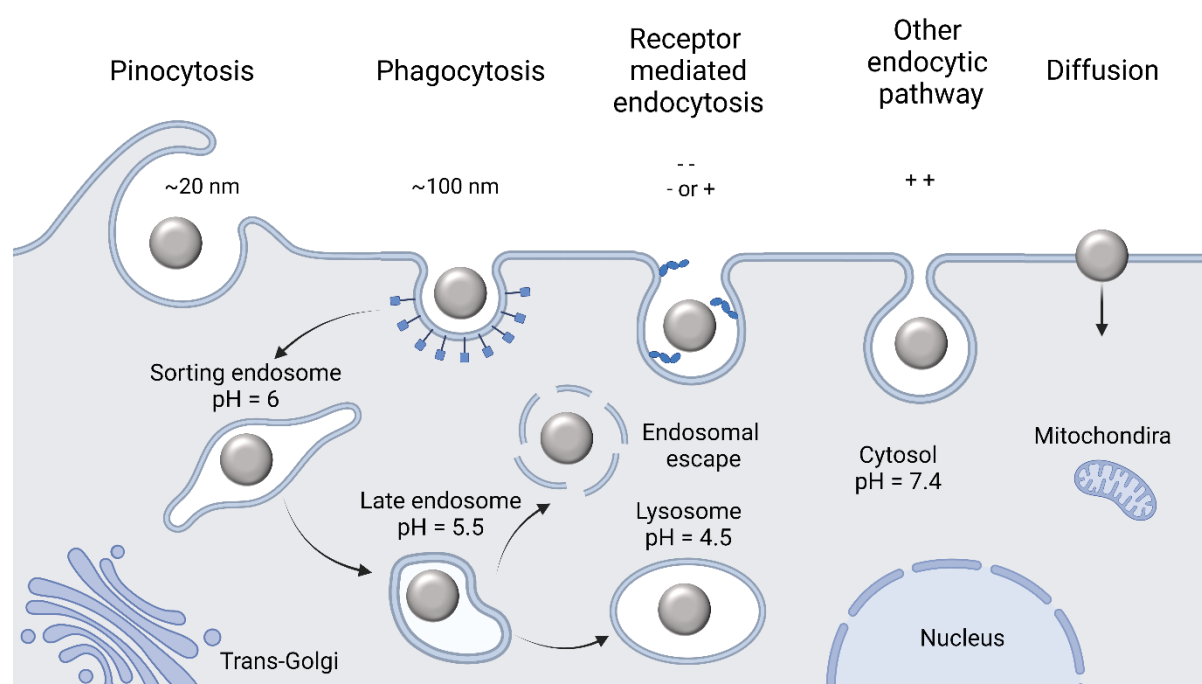


Figure 1.12: Illustration of different endocytosis pathways for nanoparticles and their intracellular transport [194]. It was created with BioRender.com.

If IONs are not released from the endosome or lysosome, they get degraded based on the acidic environment, iron-chelating molecules such as citrate, and hydrolytic enzymes. During degradation, the particle size decreases, preserving its crystalline structure and magnetic properties while releasing iron ions. Endogenous ferritin proteins store the released iron as a protein complex in ferritin iron depots. Ferritin can store excess iron (up to 4500 atoms of iron) in a non-toxic form until it is required by the metabolic process. Filled with iron, it is called holoferritin. The degradation rate is affected by the particle size and surface coating [209].

Biocompatibility and biodegradability are primary factors when designing particles for nanomedicine. Biocompatible materials are those that are not immunogenic, thrombogenic, carcinogenic, or cytotoxic. The biocompatibility of IONs is determined by the material properties, the type of tissue that is contacted

during the application, and the relationship between risks and benefits. Long-term toxicity studies, including degradation profiles, are lacking in the majority of drug delivery system studies [194,210]. The drug delivery system should be completely degraded in the body after drug administration. The biodegradability of ION-based systems is determined by their coating materials. Biodegradable polymers that are commonly used include PLGA, chitosan, gelatin, polylactic acid (PLA), polyglutaraldehyde (PGA), and poly (alkyl cyanoacrylates). If a drug is encapsulated in the coating, biodegradation and drug release can be combined [194].

Table 1.4 summarizes important properties and parameters to consider for the use of IONs in nanomedicine, specifically for influencing blood circulation time, clearance, extravasation, cellular uptake, and targeting. However, it's important to note that the specific requirements vary depending on the intended application and the specific needs of the patients [37,194, 206,207].

Table 0.4: Summary of different ION properties and parameters influencing the application in nanomedicine [37,194, 206,207].

Property/Parameter	Description
Size	A hydrodynamic diameter of 10-200 nm is preferred for use in nanomedicine as the particles can extravasate and target tumor tissues while avoiding clearance by the immune system.
Surface coating	A biocompatible surface coating, such as PEG, can increase the blood circulation time and prevent uptake by the reticuloendothelial system (RES), reducing clearance.
Surface charge	A neutral or slightly negative surface charge is preferred to avoid uptake by RES and reduce cytotoxicity.
Magnetization	A high magnetization allows magnetic targeting and guidance of the nanoparticles to the site of interest, reducing off-target effects.
Superparamagnetism	A superparamagnetic behavior allows for rapid heating and cooling under alternating magnetic fields, enabling hyperthermia therapy for cancer treatment, and improving safety due to a non remanent behavior.
Biodegradability	Biodegradable IONs and coatings can be metabolized and excreted by the body, reducing toxicity and potential long-term side effects.
Stability	Stable nanoparticles can ensure consistent performance and reduce toxicity associated with degradation products.

The Food and Drug Administration (FDA) has not yet approved magnetic nanoparticles with an iron oxide core as drug delivery systems. Though magnetite-based designs have been approved for iron deficiency therapeutics, and different IONs are accepted as MRI contrast agents, including Feraheme[®], Feridex I.V.[®], and Gastromark[®] [211].

1.3. Antimicrobial resistance and cancer

Starting in 1910 with the development of salvarsan, antibiotics have radically improved healthcare. The possibility of effectively curing infectious diseases has prolonged the human life by an average of 23 years [212]. The golden era of antibiotics between 1928 and 1950 is based on the discovery of penicillin by Alexander Fleming [212]. By producing an antibiotic-destroying enzyme, *Staphylococcus aureus* (*S. aureus*) became resistant to penicillin in 1950. Within a short time frame, it formed similar enzymes leading to resistance to other chemically unrelated antibiotics. The development of bacterial resistance highly reduces the effectiveness of antimicrobial agents. These staphylococci with multiple-antibiotic resistances were the primary cause of hospital-acquired septic infections [213]. Since then, various human pathogens have formed antibiotic resistances, and the discovery and development of new antibiotics have drastically diminished, leading to a global health crisis [212]. In 2019 bacterial antimicrobial resistance (AMR) existed for 23 pathogens and 88 pathogen-drug combinations. These AMRs were associated with 4.96 million deaths, with 1.27 million deaths directly attributed to them. *Escherichia coli* (*E.coli*), *S. aureus*, and *Klebsiella pneumoniae* (*K. pneumoniae*) are the strands most affected by AMR [214]. The Organisation for Economic Co-operation and Development (OECD) predicted in a report of 2018 that AMR could cost up to 3.5 billion US\$ per year within the next 30 years. In countries with high resistance rates (e.g., Brazil, Indonesia, Russia), the resistance is forecast to rise 4-7 times faster in the future [215]. This global health problem caused by AMR needs urgent action to avoid preventable deaths [214]. Due to the quick resistance formation against antibiotics and the comparably low profit that pharmaceutical companies expect for the development of new antibiotics, replacing antibiotics with new systems is highly considered [216].

A further global health issue with high mortality is cancer. In 2020 it caused nearly 10 million deaths worldwide, one in six deaths. The most common types are breast (2.26 million cases), lung (2.21 million cases), colon and rectum (1.93 million cases), prostate (1.41 million cases), skin (1.20 million cases), and stomach cancer (1.09 million cases) [217]. Before 1950, cancer was mainly treated by surgical removal, followed by radiation therapy after 1960. Both methods could not efficiently treat cancer because not every organ and metastatic cancer were reached [218]. A key step was the usage of chemicals to treat the disease, called “chemotherapy” [219]. Starting with the use of nitrogen mustard to treat lymphoma patients in 1943 until now, many new drugs have been developed for specific cancer-related treatments [218,219]. Even though chemotherapy has highly improved cancer treatment and healing, the diffusion of cytotoxic drugs through the whole body leads to severe side effects, including loss of hair, shortness of breath, vomiting, and tiredness that have a high impact on the quality of life [220]. In long-term chemotherapy, patients often get resistant to conventional drugs [221]. Therefore, screening for new drugs and improving targeted treatments is essential [219].

1.3.1. Antimicrobial peptides

Antimicrobial peptides (AMPs) have broad-spectrum antimicrobial activity and are ideal for overcoming antibiotic resistance. Unlike antibiotics, AMPs can kill drug-resistant bacteria by acting on multiple targets on the plasma membrane and intracellularly [221]. The Antimicrobial Peptide Database (ADP3) reports 3425 different AMPs of six life kingdoms, containing 385 from bacteria, five archaea, eight from protists, 25 from fungi, 368 from plants, and 2489 from animals, and also synthetic ones [222]. AMPs contain between 10 to 60 amino acids (an average of 33) and are generally positively charged (average net charge 3.3). Only a few negatively charged AMPs exist with excess aspartic glutamic acid. AMPs can be divided into four structural classes: α -helix, β -sheet, a combination of both, and linear extensions [216].

The different compositions of the cell membranes can explain the specific targeting of AMPs. While mammalian cell membranes contain the uncharged phosphatidylcholine and phosphatidyl ethanolamine, bacterial pathogens are built by the negatively charged phosphatidylserine, cardiolipin, and phosphatidylglycerol. Furthermore, mammalian cells contain sterols that don't appear in prokaryotic cell membranes. The negatively charged membrane of bacteria can specifically and selectively interact with the cationic AMP [221]. Cancer cells are also more negatively charged than healthy cells. They contain phosphatidylserine and anionic components gangliosides and heparan sulfates. Furthermore, cancer cells have many microvilli that increase the potential area available for AMP interaction [221,223]. During their action, AMPs bind electrostatically to the negatively charged microbial membrane and interact with its components. AMPs pass through the cell wall by capsular polysaccharides, lipoteichoic acid, and peptidoglycan (Gram-positive) or lipopolysaccharides (Gram-negative). While binding, β -sheet AMPs maintain their conformation, whereas alpha-helical peptides are transformed from a disordered structure to the amphiphilic alpha-helix. The hydrophilic side faces the solution, while the hydrophobic side interferes with the phospholipid bilayer; depending on the membrane's peptide-lipid ratio, AMPs orient parallel or vertically to the surface [216,221]. The interaction with the surface leads to higher permeability, cell membrane lysis, the release of intracellular components, and cell death. Four models describe the potential pore formation: barrel-stave, toroidal-pore, carpet, and aggregate (Figure 1.13) [221]. A non-membrane mode of action is that AMPs inhibit the protein and nucleic acid biosynthesis, the protease activity, or the cell division after penetration into the cytoplasm [216]. Environmental factors can affect the activity of AMPs. Monovalent or divalent metal ions can affect the activity against bacteria by shielding the zwitterionic membrane or influencing the assembly of the peptides. The pH manipulates the charge of amino acids and functional groups, leading to improved activity at low pH values [216]. Proteases can destroy AMPs. Diosa et al. showed that solid support of chitosan and silica improves the proteolytic stability of the AMP K-12 [224].

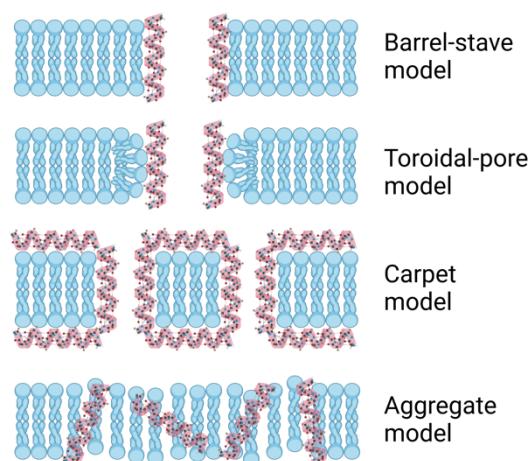


Figure 1.13: Four models of the antibacterial mode of action of AMPs: Barrel-stave model, toroidal-pore model, carpet model, and aggregate model [221]. It was created with BioRender.com.

Antibacterial peptides like nisin, cecropins, and defensins are active against Gram-positive and Gram-negative bacteria [216]. In addition to their antimicrobial activity, many AMPs have an immune regulating, angiogenic, wound healing, or antitumor activity. Due to their high specificity, low accumulation in tissues, no propensity to trigger resistance, and low toxicity, AMPs are already used to cure pathogenic infections and inflammations and improve wound healing [221,225]. The FDA approved the seven AMPs bacitracin, Polymyxin B and E, Tyrothricin, Gramicidin D and S, and Daptomycin [225]. However, no AMPs have yet been approved for cancer treatment, though a few are in the clinical stage [226]. Even so, due to stability, efficacy, and toxicity issues, the clinical application of AMPs has been limited in recent years. New technologies are required to minimize proteolytic enzyme degradation, relatively fast clearance by the kidney and liver, and the loss of anticancer activity due to interactions with negatively charged proteins and density lipoproteins [221]. Furthermore, a significant problem of many AMPs is their hemolytic activity [227].

1.3.2. Lasioglossin

In 2009 Čerovský et al. identified a new class of AMPs found in the venom of wild bees. Lasioglossins (LLs) and melectin are strongly antimicrobial and have low hemolytic activity [227]. LLs are pentadecapeptides isolated from the European eusocial bee *Lasioglossum laticeps* [227]. The bee lives in nests in clay soil, between stones or wall clefts [228]. Three new LL structures were isolated with a primary sequence of H-Val-Asn-Trp-Lys-Lys-**Val**-Leu-Gly-Lys-Ile-Ile-Lys-Val-**Ala**-Lys-NH₂ (LL-I), H-Val-Asn-Trp-Lys-Lys-**Ile**-Leu-Gly-Lys-Ile-Ile-Lys-Val-**Ala**-Lys-NH₂ (LL-II) and H-Val-Asn-Trp-Lys-Lys-**Ile**-Leu-Gly-Lys-Ile-Ile-Lys-Val-**Val**-Lys-NH₂ (LL-III). They have a cationic, α -helical structure with a concave hydrophobic and a convex hydrophilic side (Figure 1.14). LLs have an optimal charge for antimicrobial activity with a net charge of +6. The amidation of the C-terminus improves the antimicrobial activity and leads to no hemolytic activity. The different primary structures influence the physical and biological properties. LL-III has the highest mean hydrophobicity, calculated by the hydrophobicities of the amino acids (Table 1.5). All three are highly antimicrobial against Gram-positive

(*Bacillus subtilis*, *S. aureus*) and Gram-negative (*E.coli*, *Pseudomonas aeruginosa* (*P. aeruginosa*)) bacteria, low hemolytic, and active for mast cell degranulation. In general, *P. aeruginosa* is the most resistant compared to other strains. LL-III is highly antimicrobial against *S. aureus* [227].

Table 1.5: The mean hydrophobicities of the three LLs calculated using the Eisenberg consensus scale. The minimal inhibitory concentration of LLs for *B. subtilis*, *S. aureus*, *E.coli*, and *P. aeruginosa*. The concentration of the peptides leading to the lysis of 50% of red blood cells [227].

Peptide	Hydrophobicity	Antimicrobial activity MIC [μM]				Hemolytic activity LC ₅₀ [μM]
		<i>B. subtilis</i>	<i>S. aureus</i>	<i>E. coli</i>	<i>P. aeruginosa</i>	
LL-I	-0.117	0.8	14.3	1.7	15.8	>200
LL-II	-0.104	0.7	9.0	1.4	14.4	>200
LL-III	-0.085	0.7	3.9	1.4	18.7	>200

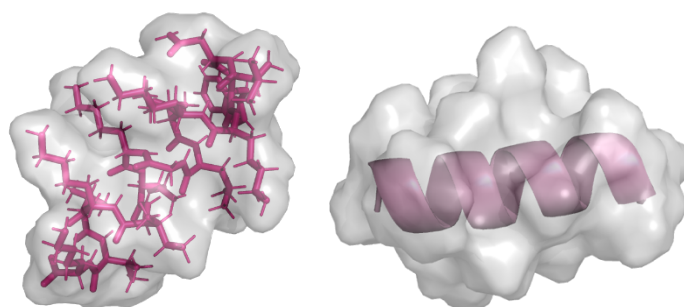


Figure 1.14: Illustration of the lasioglossin III structure as an α -helical system with and without the amino acids [227]. It was simulated based on its Van der Waals interactions with Avogadro (Wireframe, Forcefield GAFF, 4 Steps per update) based on the peptide sequence and the molecule properties ($\text{C}_{86}\text{H}_{152}\text{N}_{22}\text{O}_{17}$, Number of residues: 15, Number of atoms: 277, Number of bonds: 278 Molecular Weight $1766.26 \text{ g mol}^{-1}$).

LL-III showed the most promising antimicrobial activity profile and high activity against leukemia cells and cervix carcinoma with a half maximal inhibitory concentration (IC_{50}) $\sim 5 \mu\text{M}$ and slightly less activity against the solid tumors PC12 and colon adenocarcinoma (Table 1.6) [227].

Table 1.6: LL-III activity against malignant cell lines: L1210 (Mouse lymphocytic leukemia); CCRF-CEM T (human lymphoblastic leukemia); HL-60 (human promyelocytic leukemia); HeLa S3 (human cervix carcinoma); PC12 (pheochromocytoma of the rat adrenal medulla); SW480 (human colon adenocarcinoma) [227].

	L1210	CCRF-CEM T	HL-60	HeLa S3	PC12	SW480
IC_{50} [μM]	4.7	5.0	4.5	5.0	10.0	15.0

While many AMPs lose antimicrobial activity when exposed to ions, LL-III retains its activity at physiological salt concentrations. Mishra et al. confirmed that membrane interaction is involved in its mechanism of action and demonstrated that LL-III could bind to the outer and inner membranes of *E.coli*, *S. aureus*, and *P. aeruginosa*. It is active, soluble, and immobilized and it can prevent biofilm

formation [229]. Even though the mode of action of LL-III is not yet fully understood, Battista et al. could show that the peptide interacts selectively with an anionic model membrane leading to permeabilization by reorganizing the membrane. At this moment, little cellular fluid was released. In the cytosol, LL-III can potentially interact with intracellular biomolecules like plasmid DNA [230]. However, by molecular dynamics simulations, Saha et al. revealed that lysine residues of LL-III form H-bonds with the lipid-head groups. Once the peptide enters transmembrane orientation, the indol ring of Trp3 permeates into the hydrophobic tail region of the lipid. The orientation stayed the same during the whole simulation. If the N-terminal lysine residue would release from the surface-bound state, it might snorkel into the inner leaflet. The orientation of LL-III in bilayers leads to destabilization at the membrane/water interface [231]. LL-III can be used as an anticancer or antimicrobial drug combined with a drug delivery system [227].

2. Motivation

Two of the biggest global health problems are cancer and antimicrobial resistance (AMR)-related mortality. Per year approximately 10 million people die due to various cancers, and 5 million deaths are directly associated with AMR. Therefore, a global need for new effective, and innovative drugs and drug delivery systems exists [214,217].

One of these novel drugs is the antimicrobial peptide lasioglossin III (LL). The short, cationic, α -helical peptide is highly active against Gram-positive and Gram-negative bacteria and various cancer cells, while it has low hemolytic activity [227]. Its mode of action is not affected by physiological salt concentrations and has a low risk of resistant formation. Combined with an efficient drug delivery system, problems like stability, efficacy, and toxicity can be improved.

Magnetic drug delivery is based on cost-efficient, easy-to-synthesize superparamagnetic iron oxide nanoparticles. Their low-volume-to-area ratio bears the ability to bind a large drug dose. They can be guided by an external magnetic field directly to a target and accumulated there [21]. The target can be cancer cells or inflammatory tissue. The system enables the usage of a low drug dose with high local concentration, leading to reduced side effects and harm to healthy tissue.

This work aimed to generate, for the first time, an efficient, effective, cytocompatible, and magnetically controllable drug delivery system for LL. Therefore this project was split into three steps. Iron oxide nanoparticles (IONs) with different biocompatible coatings (bare, inorganic, organic, and supramolecular) and surface properties should be analyzed for suitability. Here, one focus point was a small particle size and good stability with a low and controllable agglomeration to make the particles applicable to the human body. This part also included analyzing the effects of the particle sizes, hydrodynamic diameters, and coatings on their magnetic behavior. In the second step, LL needed to be efficiently bound to the drug carrier without losing its antimicrobial activity. Different binding types (adsorption, covalent binding, self-assembly) should be tested and quantified for their potential drug loading. With antimicrobial experiments, the influence of binding on the activity of LL should be determined. The last part was testing the cytocompatibility of the most promising systems to ensure safe applicability to the human body. With the analysis of a variety of ION-based drug carriers and different binding mechanisms, this work lays the groundwork for generating a magnetic drug delivery system for cationic antimicrobial peptides (AMPs) and therefore improved treatment of cancer and inflammatory tissue.

Furthermore, the work wanted to improve the knowledge about the behavior of coated IONs in human body fluids. The newfound understanding of coated IONs has the potential to accelerate upcoming pre-clinical evaluations of these particles. The particular focus was here on the long-term agglomeration and degradation profile of various commonly used biocompatible coated IONs in simulated body fluids. To achieve this goal, a fast and reliable experimental setup needed to be designed.

3. Publications

3.1. Bare iron oxide nanoparticles as drug delivery carrier for the short cationic peptide lasioglossin

The drug's therapeutic effect, efficiency, and safety depend on the administration and delivery system. Magnetically controlled drug delivery enables a delivery directly to the target, leading to a high local concentration. The overall drug amount can be reduced, which minimizes toxic side effects. IONs are the focus of research due to their superparamagnetic behavior and potential high binding capacity. Especially BIONs without expensive coating are a cost-efficient magnetically controllable drug carrier. It is essential to understand a drug's binding and release processes to the ION surface and analyze its activity for a medical application.

This study gives fundamental and new insights into the binding patterns of the cationic peptide LL on BIONs, depending on the composition and pH of the medium, the particle concentration, and time. The particles are fully characterized by BET, TEM, XRD, FT-IR, DLS, SQUID, and Zeta potential measurements. Easy and quick absorption of LL is possible. Absorbance analysis and IR spectroscopy confirm the drug loading of 22.7%. The reversible, electrostatic binding leads to reduced drug loading with each washing step. The hydrodynamic diameters of BION@LL are compared in water, PBS, and HS, showing the best behavior in HS. A temperature and time-dependent desorption of LL is possible but not necessary because the bound LL showed improved antimicrobial activity in growth experiments with *E. coli*. While efficient binding and high antimicrobial activity were proven, the limiting factor of the BION@LL system is the high agglomeration (>100 nm), which impedes its usability in the human body. In further studies, the properties of BIONs should be improved by biocompatible coatings that enhance colloidal stability.

The substantial contributions of the doctoral candidate were the conception and design of the experiments after a critical review of existing literature. The doctoral candidate carried out all presented experimental work, did the data analysis and was the leading author of the manuscript.



Article

Bare Iron Oxide Nanoparticles as Drug Delivery Carrier for the Short Cationic Peptide Lasioglossin

Chiara Turrina , Sonja Berensmeier and Sebastian P. Schwaminger *

Bioseparation Engineering Group, Department of Mechanical Engineering, Technical University of Munich, 80333 München, Germany; c.turrina@tum.de (C.T.); s.berensmeier@tum.de (S.B.)

* Correspondence: s.schwaminger@tum.de

Abstract: New drug delivery systems are a potential solution for administering drugs to reduce common side effects of traditional methods, such as in cancer therapy. Iron oxide nanoparticles (IONs) can increase the drugs' biological activity through high binding efficiency and magnetically targeted drug delivery. Understanding the adsorption and release process of a drug to the carrier material plays a significant role in research to generate an applicable and controlled drug delivery system. This contribution focuses on the binding patterns of the peptide lasioglossin III from bee venom on bare IONs. Lasioglossin has a high antimicrobial behavior and due to its cationic properties, it has high binding potential. Considering the influence of pH, the buffer type, the particle concentration, and time, the highest drug loading of 22.7% is achieved in phosphate-buffered saline. Analysis of the desorption conditions revealed temperature and salt concentration sensitivity. The nanoparticles and peptide-ION complexes are analyzed with dynamic light scattering, zeta potential, and infrared spectroscopy. Additionally, cytotoxicity experiments performed on *Escherichia coli* show higher antimicrobial activity of bound lasioglossin than of the free peptide. Therefore, bare IONs are an interesting platform material for the development of drug-delivery carriers for cationic peptides.



Citation: Turrina, C.; Berensmeier, S.; Schwaminger, S.P. Bare Iron Oxide Nanoparticles as Drug Delivery Carrier for the Short Cationic Peptide Lasioglossin. *Pharmaceuticals* **2021**, *14*, 405. <https://doi.org/10.3390/ph14050405>

Academic Editor: Serge Mordon

Received: 23 March 2021

Accepted: 21 April 2021

Published: 24 April 2021

Publisher's Note: MDPI stays neutral with regard to jurisdictional claims in published maps and institutional affiliations.



Copyright: © 2021 by the authors. Licensee MDPI, Basel, Switzerland. This article is an open access article distributed under the terms and conditions of the Creative Commons Attribution (CC BY) license (<https://creativecommons.org/licenses/by/4.0/>).

Keywords: iron oxide nanoparticles; magnetically controlled drug delivery; cationic peptide; lasioglossin; agglomeration behavior in human serum; antimicrobial behavior

1. Introduction

The method of administering a pharmaceutical compound highly influences the therapeutic effect, efficiency, and drug safety [1,2]. Magnetically controlled drug delivery is attracting increasing attention due to the potential to carry a large drug dose to the target, which leads to a high local concentration and thereby high efficiency while avoiding toxicity [1,3–6]. Superparamagnetic iron oxide nanoparticles (IONs), also known as magnetite/maghemite or magnetic nanoparticles (MNP), are especially in the focus of this research field due to their non-remanent behavior, non-toxicity, and low-cost production [7–11]. IONs are non-porous and can have high specific surface areas of above 100 m²/g, leading to a huge drug loading capability [12]. The classic synthesis route is co-precipitation via the Massart process. This method can be used to generate IONs with a size range between 4 and 16 nm that have a high magnetization of around 80 emu/g [9,13–15]. The key points of IONs as a drug carrier are the possibility of targeted delivery through a magnetic field, the visualization of the delivery process via MRI, and that heat generated through hyperthermia can lead to a controlled release [16,17]. For the internalization of IONs into the cell, the ideal particle size for drug delivery ranges from 10 to 100 nm because this leads to the most prolonged blood circulation times [9,13,18]. The drug can be localized at the target site by applying an external magnetic field, where it can be efficiently released from its carrier, as shown in Figure 1a [15].

IONs are often coated with functionalized, biocompatible compounds to form a core-shell structure for biomedical application [9]. Therefore, drugs can bind to the coating

or are dispersed in the polymer matrix [16,19]. The polymers have the function of stabilizing the particles, preventing early immunogenic action, or are used to generate a controlled release mechanism [15,18,20]. In this case, the interaction with the drug, the cationic peptide lasioglossin (LL), should occur with the bare surface of IONs without coating. In drug delivery or bioseparation, the controlled adsorption and release of small biomolecules to and from the adsorbent material plays a major role. During the last few years, much research has been conducted to understand small biomolecules' interaction with the inorganic bare IONs (BIONs) and amphoteric hydroxyl groups on the metal oxide surface [21,22]. The surface charge influences the adsorption behavior of amino acids as well as the amount of charged groups such as carboxylic acids and side chains. The coordinative complex formation due to ionic interactions of the iron ions on the surface of BIONs is pH-dependent [22,23]. Rawlings et al. have proven that lysine can undergo strong hydrogen bonds with the surface of BIONs through the amine group and the peptide carbonyl [24]. This makes LLs an interesting counterpart for adsorption on BIONs.

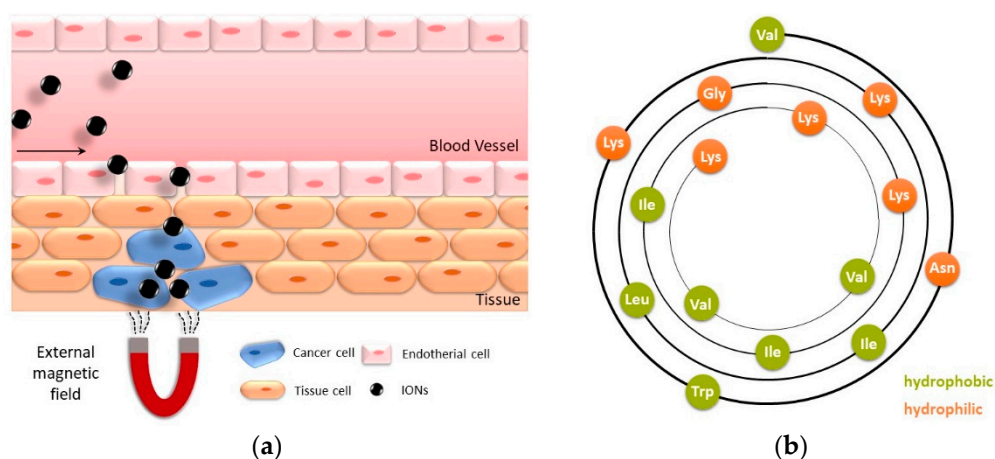


Figure 1. (a) Drug delivery of magnetic IONs accumulating in a target tissue, guided by an external magnetic field. (b) Wheel diagram of lasioglossin III: hydrophilic amino acids are shown in orange, and hydrophobic amino acids are shown in green.

LLs are cationic, α -helical pentadecapeptides isolated from bee venom of *Lasioglossum lacticeps*. They belong to the group of antimicrobial peptides that are a new alternative for antibiotics, based on their divergent mode of action. The ability of LL to form an amphipathic α -helical structure highly influences their biological activity [25–28]. Cationic peptides can target the negatively charged bacterial cell envelope and accumulate in the cell wall. This leads to the formation of transmembrane pores into the lipid bilayer, the leakage of cytoplasmic components, and therefore to cell death [29,30]. LLs appear in three different natural forms (LL I: H-Val-Asn-Trp-Lys-Lys-Val-Leu-Gly-Lys-Ile-Ile-Lys-Val-Ala-Lys-NH₂, LL II: H-Val-Asn-Trp-Lys-Lys-Ile-Leu-Gly-Lys-Ile-Ile-Lys-Val-Ala-Lys-NH₂, LL III: H-Val-Asn-Trp-Lys-Lys-Ile-Leu-Gly-Lys-Ile-Ile-Lys-Val-Val-Lys-NH₂). They all show low hemolytic and high antimicrobial behavior even at physiological salt concentrations [31]. LL III is shown in Figure 1b. The peptide is positively charged due to its five lysine residues, and it can undergo electrostatic interactions with a negatively charged BION surface [24]. The peptide has a concave hydrophobic and a convex hydrophilic side through the α -helical shape. All LLs show similar antimicrobial behavior against Gram-negative and Gram-positive bacteria such as *E. coli*, *P. aeruginosa*, and *B. subtilis* [25]. Out of the three natural peptides, LL III shows the highest activity in growth studies of *S. aureus* due to its highly hydrophobic behavior. While all LLs show potency to kill various types of cancer cells, LL III has the highest toxicity against PC-12 cancer cells [25].

This work aims to successfully generate and analyze BION@LL complexes. The particles are characterized in detail before their application in adsorption and desorption is described. The particle size and size distribution are important parameters regarding

particle delivery through the human vascular system and removal through the organs and the immune system [16]. They are determined by transmission electron microscopy (TEM) and X-ray diffraction analysis (XRD). The diffractograms are further used for the study of the crystal structure that influences the magnetic behavior. The saturation magnetization and magnetic behavior are analyzed with a superconducting quantum interference device (SQUID). Additionally, the zeta potential is investigated in dependence of the pH to calculate the isoelectric point (IEP). The knowledge of the surface charge makes it possible to understand the interaction with LL in adsorption and desorption experiments. The peptide loading to BION's surface is verified by photometric measurements and infrared spectroscopy (IR). The hydrodynamic diameter of the BION@LL complexes is analyzed with dynamic light scattering, as the size of the system plays a major role in the application in drug delivery [16]. The binding behavior of LL is tested at different pH values. Additionally, the influence of PBS buffer, particle concentration, and time are determined. For the elution process, other conditions such as a pH shift, rise of temperature, and variation of the salt concentration are analyzed. The antimicrobial behavior of LL, BIONs, and the BION@LL complex is compared to test the applicability in drug delivery. The aim is to generate a fast, controllable, efficient, and reversible LL interaction with the BIONs and high antimicrobial activity of the resulting magnetic complexes.

2. Results and Discussion

2.1. Characterization of the BIONs

The BIONs are characterized by particle size, size distribution, crystal structure, BET surface, and magnetization behavior. All these parameters play an essential role in the application in magnetic drug delivery. They influence the particle lifetime in the human vascular system, the possibility of magnetic separation, and the amount of peptide bond to the surface. With TEM analysis, the optical diameter of the particles is examined (Figure 2).

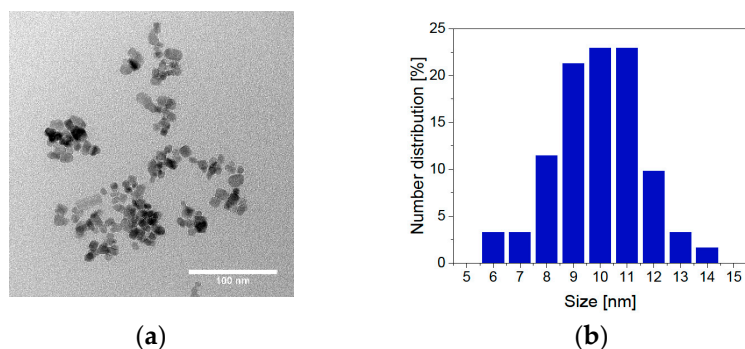


Figure 2. TEM microscopy: (a) image of BIONs and (b) number distribution of various particle diameters.

With an average diameter of 9.93 nm, the results are comparable to previous measurements of BIONs [32]. The particle size distribution of BIONs synthesized by co-precipitation lies between 6 and 14 nm [32,33]. In addition to TEM measurements, the particle size was determined with XRD analysis. Here, the magnetic particles show an average diameter of $9.2 \text{ nm} \pm 0.43 \text{ nm}$, with a deviation of 0.73 nm, similar to the TEM measurements (Figure 3a, Table S1). BET measurements have shown a specific surface area of $115 \pm 0.25 \text{ m}^2/\text{g}$ (Figure S1). This value is slightly higher compared to preceding determinations of the specific surface area of BIONs of around $80.0 \text{ m}^2/\text{g}$ [32].

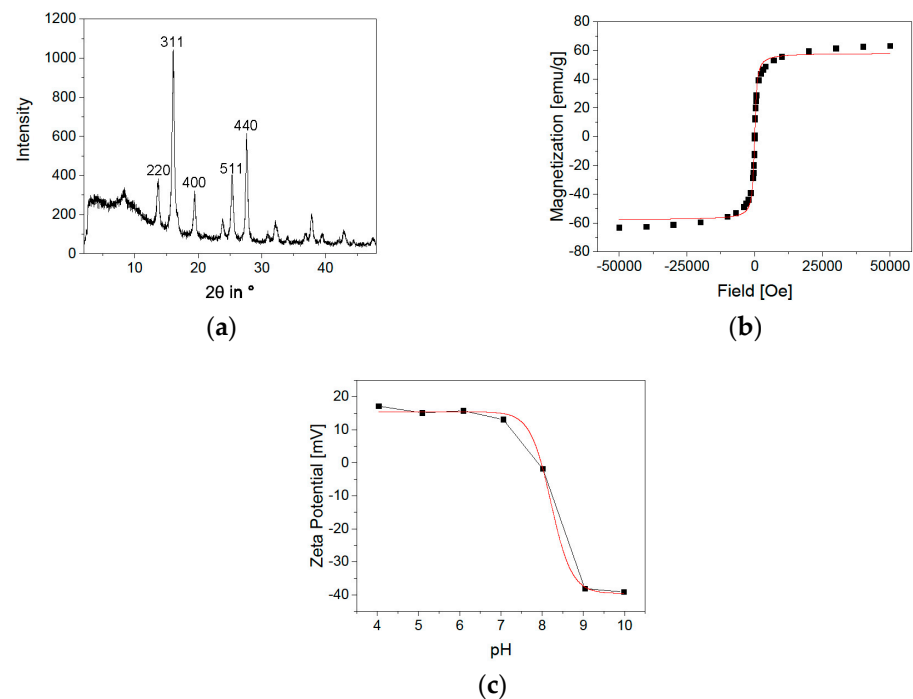


Figure 3. (a) XRD measurement of BIONs, (b) SQUID analysis of BIONs at 300 K with LangevinMod fit and (c) Zeta potential of BIONs at pH values from 4 to 10 with a Boltzmann fit.

In addition to the particle size, the crystal structure composition and the particles' magnetic behavior play an important role in developing a magnetic drug delivery system as these parameters influence the controllability by an external magnetic field [33,34]. Examination of the crystal structure with XRD analysis shows the typical reflections ((220), (311), (400), (511), and (440)) for magnetite with its cubic structure (Figure 3a) [35]. SQUID analysis of the BIONS (Figure 3b, Table S2) displays the typical sigmoidal curve of superparamagnetic nanoparticles in a magnetic field [36]. There is no hysteresis and no remanence at 0 Oe. The maximal reached magnetization is 63.2 emu/g. The modified Langevin fit is not describing the ideal curve shape of a superparamagnetic substance [37]. The slopes at high magnetic fields indicate the existence of paramagnetic material within the sample. This can occur due to free paramagnetic iron ions, water residues, or oxygen [38–40]. Figure 3c shows the zeta potential of BIONs at different pH values from pH 4 to pH 10. The IEP of 7.98 is determined by a Boltzmann fit [41]. This lies between the value of comparable measurements of magnetite with an IEP of 7.0 and the IEP of BIONs that were oxidized by air at 8.4 [32]. In summary, the determined particle size is near the ideal size between 10 and 100 nm, essential for a prolonged blood circulation time. The high magnetizability offers good manageability by a magnetic field with the necessary superparamagnetic behavior for drug delivery [13,42].

2.2. Performance of BIONs as Carrier Material for Antimicrobial Peptides

Adsorption and release experiments are performed with LL III under different conditions to examine the BIONs as drug delivery system for short cationic peptides. Since the buffer composition and the pH influence the binding states of short peptides to the BION surface, these parameters are analyzed in the binding experiments [43].

The BION surface charge (IEP 7.98) at pH 7 in water is expected to be heterogeneous, predominantly positive (Figure 3c). However, small negatively charged domains on the particles can be expected at this pH [44]. On the other hand, we observe a mainly negative charged surface at pH 9 (Figure 4d). This significantly influences the ionic interaction with the peptide LL to the BION surface (Figure 4e). The five lysine groups that generate a positive charge up to pH 9 mainly influence the peptide loading (Figure 4d) [45]. Therefore,

they give the peptide a cationic character. Hence, LL is anticipated to have a stronger ionic interaction with the negatively charged BIONs at pH 9 than at pH 7 with the prevalently positive charged surface [45]. The pH-dependent binding behavior of LL to BIONs is presented in Figure 4a (Figure S2, Table S3). As estimated, the highest loading of 0.35 g/g of the BIONs in water is reached at pH 9 (equilibrium concentration: 1.64 g/L), where the particles are negatively, and LL is positively charged. At pH 7, LL shows a maximum binding capacity of 0.20 g/g to BIONs. For both experiments, one washing step leads to a high decrease in loading, so the final loading of BIONs at pH 9 and pH 7 is 0.18 g/g. The average loss of 37% of LL can be explained by the non-covalent reversible binding of the peptide to the iron oxide surface due to electrostatic interactions. The change of the supernatant during the washing step leads to a new equilibrium concentration with a lower loading, since weakly bound LL is removed. The maximal reached drug loading after one washing step in both experiments is 15.2% (Equation (S3)). Other post-loaded nanocarriers where the interaction is also based on hydrophobic, electrostatic interactions, π - π stacking, or hydrogen bonding show drug loading between 11.8% and 68.1% depending on the drug and the material [46]. For iron-based systems, Qu et al. achieved a loading of 9.8% to 11.8% of 10-Hydroxycamptothecin on polyethylene glycol-chitosan coated IONs [47]. In comparison, Luo et al. were able to prepare mesoporous magnetic colloidal nanocrystal clusters that showed a loading capacity of 35% for paclitaxel [48].

The peptide and the BION@LL complex are analyzed with IR for independent validation of the BION LL interaction. LL shows spectroscopy bands between 3000–2800 cm^{-1} , 1655–1650 cm^{-1} , and 1542–1539 cm^{-1} due to backbone vibrations. The ones at 3000–2800 cm^{-1} are caused by stretching vibrations of the C–H groups. The band at 1655 cm^{-1} can be affiliated to stretching vibrations of C=O groups and the one at 1539 cm^{-1} to bending vibrations of N–H groups. Additionally, bands at 3400–3300 cm^{-1} are visible in consequence of N–H stretching vibrations and at 3550–3200 cm^{-1} due to the OH group's stretching vibrations in threonine. Furthermore, LL has characteristic bands at 1203 cm^{-1} and at 1133 cm^{-1} due to C–N stretching of amines and the stretching vibrations of the C–O groups, respectively (Figure 4f) [49,50]. Examining the BION@LL complexes with IR spectroscopy shows the characteristic double bands of LL at 1654 and 1539 cm^{-1} additional to the magnetite peak at \sim 572 cm^{-1} [51,52] (Figure 4g,h), which proves the formation of the BION peptide complex. Due to inhomogeneities of the sample preparation, the integrals of the bands cannot be used quantitatively. Still, they give a qualitative hint that more LL loading leads to higher characteristic double bands. Further, measurements of the hydrodynamic diameter have shown a significant influence of the presence of LL on particle agglomeration. In different media, the BIONs form different agglomerates. The hydrodynamic diameters are larger than the diameters determined via TEM measurements (Section 2.1). For both aqueous conditions, higher LL concentration led to bigger hydrodynamic diameters and broader particle size distribution. LL can allegedly act as a binder agent due to the multiple cationic functional groups. This effect explains the larger agglomerates along with an increased peptide loading. The starting peptide concentration of 0.25 g/L LL led to agglomerates larger than 4 μm . In contrast, at pH 9 smaller agglomerates were formed, so at 0.25 g/L peptide the hydrodynamic diameter is between 0.50 and 1.70 μm (Figure 4b,c). Other iron post-loaded carriers show sizes between 100 and 600 nm [46–48]. In general, the ideal size for a nanoparticle-based drug delivery system is between 10 and 100 nm to achieve long blood circulation times and make cellular uptake possible [18].

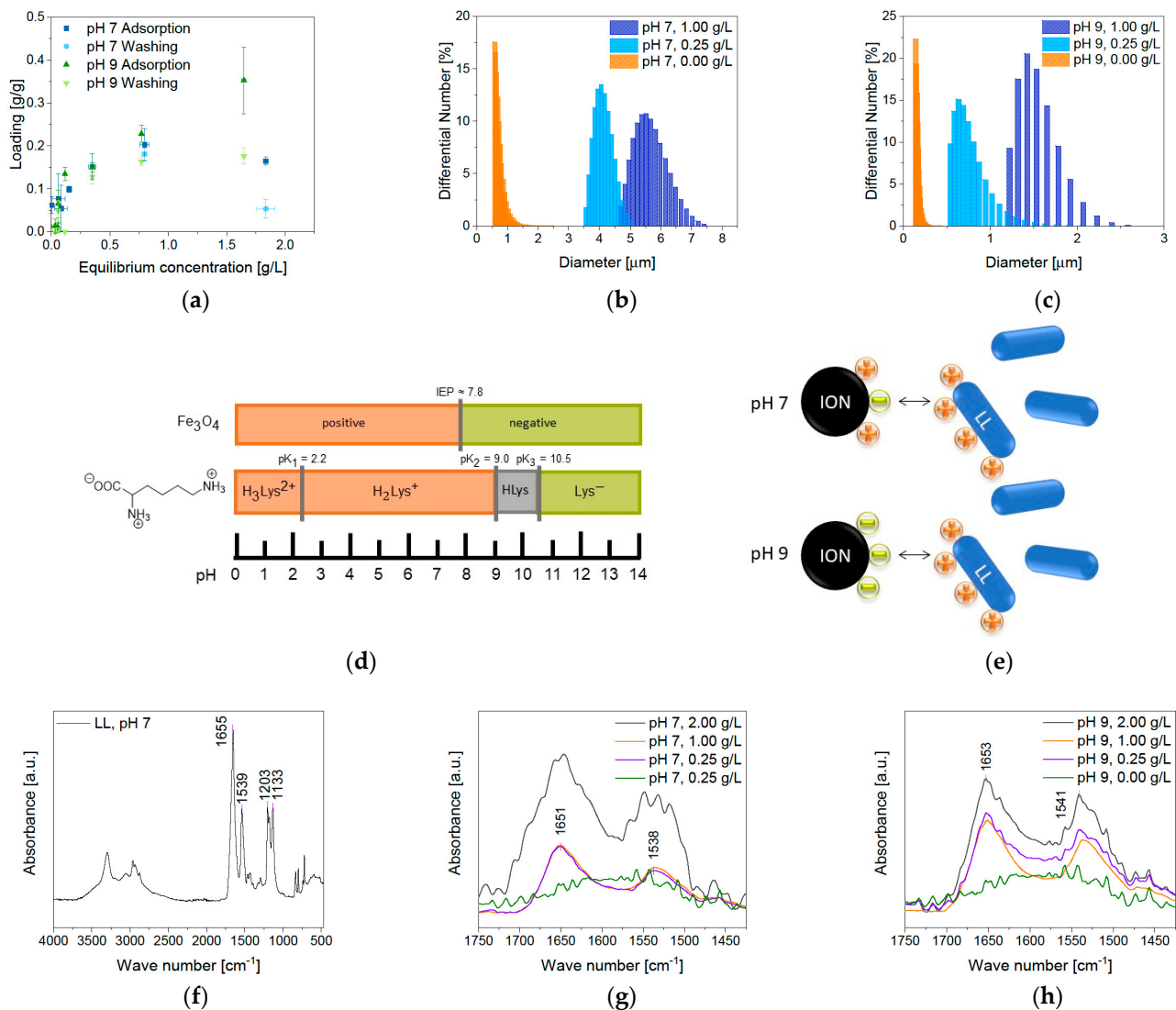


Figure 4. (a) Adsorption isotherms of LL at pH 7 and 9 in water and 1 g/L of BIONs, (b) hydrodynamic diameters after LL adsorption at pH 7 and (c) pH 9 in water, (d) illustration of the BION and lysine charge in dependence on the pH. Reprinted with permission from J. Phys. Chem. C 2015, 119, 40, 23032–23041. Copyright 2015 American Chemical Society [22,45], (e) interaction of BIONs with lasioglossin at pH 7 (top) and pH 8 (bottom) and IR spectra of (f) lasioglossin at pH 7, (g) MNP@LL complexes at pH 7 and (h) at pH 9 with different starting peptide concentrations.

The amount of LL loading shows an effect on the stability of the colloidal dispersions (Figure 5). With a higher peptide amount the zeta potential is increasing. Low amounts of LL (0 g/L and 0.25 g/L) led to a zeta potential between -10 and -30 mV, so this system shows incipient instability. Higher peptide starting concentrations increase the potentials up to a range of -10 and $+10$ mV that are characteristic for the formation of agglomerates [53]. This trend corresponds to the measurements of the hydrodynamic diameter.

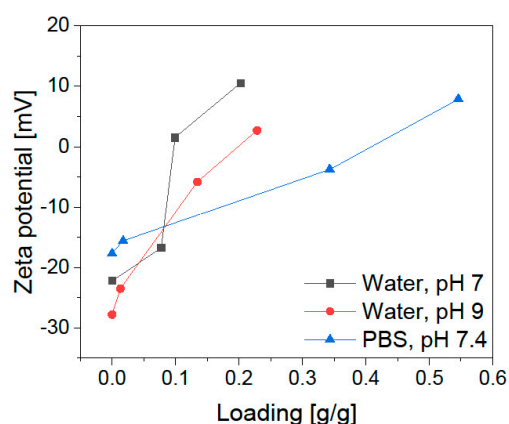


Figure 5. Zeta potential after adsorption of LL to 1 g/L of BIONs at different loadings under the three different conditions.

The influence of the buffer on the system is analyzed by interaction studies in comparable physiological conditions of 50 mM PBS buffer at pH 7.4. This favors the adsorption of LL up to a loading of 0.55 g/g (LL equilibrium concentration 0.46 g/L), while in water the highest loading was 0.35 g/g (Figure 6a). Different effects hereby play a role: (1) the buffer effect completely stabilizes the pH during the adsorption, which could have a positive impact; (2) the negative charge of phosphate can act as a linker between the positive BION surface and the cationic peptide (Figure 6d) and (3) the increase in ionic strength could positively influence the adsorption. Phosphate anions belong to a group that adsorbs by inner-sphere complexation and respond to increasing salt concentration (NaCl) with higher adsorption to metal oxides [54]. Point (2) can be underlined by the zeta potential measurements in Figure 5. Higher peptide loading in PBS does not lead to a significantly increased positive potential. The potential for the higher load is in the same range as the reference sample in water at pH 7. This shows that the phosphate anions affect the surface charge and shield the positive charge of the cationic lasioglossin. Again, washing led to a strong decrease in LL loading. The highest loading after one washing step lowered to 0.23 g/g, due to the new equilibrium adjustment. The determined drug loading is therefore 22.7%. In general, a loss of 41.9% was measured through one washing step.

Further washing steps lead to a decrease in the peptide loading of 28.6% per washing step. More detailed data can be found in the SI in Table S4. Once more, the increase in LL loading was observed in higher characteristic IR peaks (Figure 6b). As anticipated, the behavior of the hydrodynamic diameter and the zeta potential is comparable to the results in water (Figure 6c). The hydrodynamic diameter measurements show that the agglomeration of BIONs and the peptide BION complexes depend on the medium and the lasioglossin loading. Therefore, further experiments are conducted in human serum (HS) to analyze the behavior of BIONs in a more realistic drug delivery environment. HS contains various substances, such as many electrolytes, proteins and peptides, small organic molecules, and nutrients, that can influence the aggregation behavior of BIONs [55]. Furthermore, the viscosity of HS is significantly higher with an average value between 1.10–1.30 mPa·s at 37°C compared to water (0.69 mPa·s) [56]. The viscosity can especially influence the colloidal stability of particles [57]. The experiments were carried out with a concentration of 0.5 g/L BIONs because at these conditions the BION agglomerates are not overlaid by the signals of HS (Figure S3). Experiments with 0.5 g/L BIONs show a lower hydrodynamic diameter in HS (79.1 nm) compared to water at pH 7 (243 nm) (Figure 6e). For BION@LL complexes, this effect is more distinct: the determined hydrodynamic diameters are 1302 nm in PBS, 1070 nm in water, and 470 nm in HS. Therefore, in HS, the particles show diameters in the nanoscale <1000 nm and are better comparable with sizes of other iron-based drug carriers [46–48]. Still, the size is not in the ideal range of 10–100 nm. Though the media's viscosity seems to influence the agglomeration behavior strongly, it

can be assumed that blood, with even higher viscosity of around 4 mPa·s, leads to even smaller agglomerates [58].

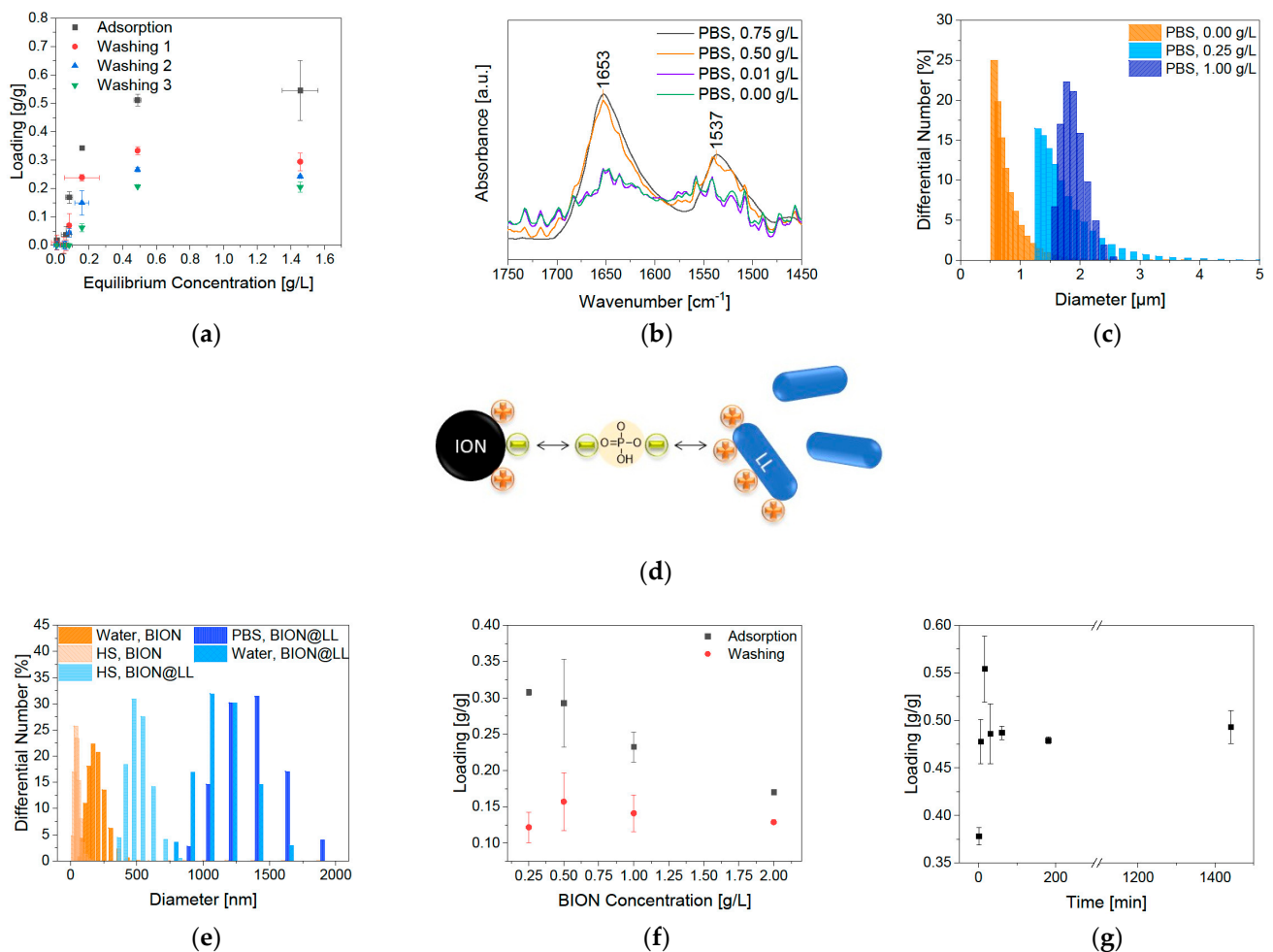


Figure 6. (a) Adsorption isotherms of LL at pH 7.4 in 50 mM PBS buffer and 1 g/L of BIONs, (b) FTIR spectra of adsorbed LL on BIONs, (c) hydrodynamic diameters after LL adsorption at pH 7 in 50 mM PBS buffer, (d) illustration of the BION LL interaction in dependence with PBS buffer (e). Agglomeration behavior of BIONs and BION@LL in water, human serum (HS) and PBS buffer, (f) binding kinetic of 1 g/L LL at pH 7.4 in 50 mM PBS and 1 g/L of BIONs, and (g) adsorption of 0.5 g/L LL at pH 7.4 in 50 mM PBS at different BION concentrations.

Lower BION concentrations led to an increase in LL loading, while after one washing step all loadings are comparable (Figure 6e). This effect can probably be ascribed to diffusion effects, so LL binds in lower amounts to denser floating agglomerates and particle bulks because it must diffuse into the pores. In contrast, it can bind more efficiently if more space is available around each agglomerate (geometrical heterogeneity). After washing, the loading is comparable for all BION concentrations. For that reason, on every particle an equal amount of binding sites (chemical homogeneity) seem to interact with the peptide. Research in the field of adsorption of inorganic compounds to char has already shown that the chemical nature of the adsorbent material influences the binding more than the geometrical heterogeneity through pores [59].

Furthermore, the binding kinetics in PBS buffer play an important role (Figure 6f). It is determined that significantly rapid adsorption occurs within the first five minutes. After 30 min, the equilibrium of 0.49 g/g LL is reached, not changing in the next 24 h.

2.3. Desorption of the Bound Peptides from BIONs

Elution experiments are performed for the analysis of the ability of drug release from the BION peptide complex. When magnetite permeates the cell wall of microorganisms, such as bacteria, an oxidative stress reaction is induced, leading to a pH shift to lower pH values in the cell [60,61]. Furthermore, different compartments of the cell have varying pH values. Endosome and lysosome have an especially low pH of 5 [20]. The impact of a pH shift is tested with elution conditions of PBS buffer at pH 5. Magnetic hyperthermia is a method in which the temperature can be increased up to 40–45 °C by the application of an alternating magnetic field to BIONs [62–64], though it is important to note that the agglomeration behavior of the BIONs can have a negative effect on its hyperthermia properties [65]. The desorption is analyzed under possible hyperthermia conditions at a temperature of 40 °C. The temperature sensitivity of the binding is also tested under extreme conditions of 60 °C. Figure 7a shows the effect of the different elution conditions after one hour of incubation. The pH shift from pH 7.4 to pH 5 led only to an elution of 19% LL. Considering that the new equilibrium adjustment plays a role, the pH shift does not influence the elution notably. At pH 5, the surface of the BIONs is predominantly positively charged and can repel the cationic peptide, but the buffer effect of PBS seems to counteract. The additional increase in temperature leads to higher desorption. After one hour at 40 °C 30%, and at 60 °C 51% of LL were desorbed. The peptide binding is therefore temperature-sensitive and the effect of hyperthermia can control elution. The influence of time on the desorption process has been tested by binding kinetics at room temperature in the PBS buffer. Even after 3 h, the elution equilibrium did not change. Only after 13.5 h, 30% of LL have been desorbed (Figure 7d). A temperature of 40 °C leads to elution of 30% after one hour and 44% after 27 h (Figure 7c). The most significant part of the elution takes place in the first minutes, subsequently it is only rising mildly over more extended periods.

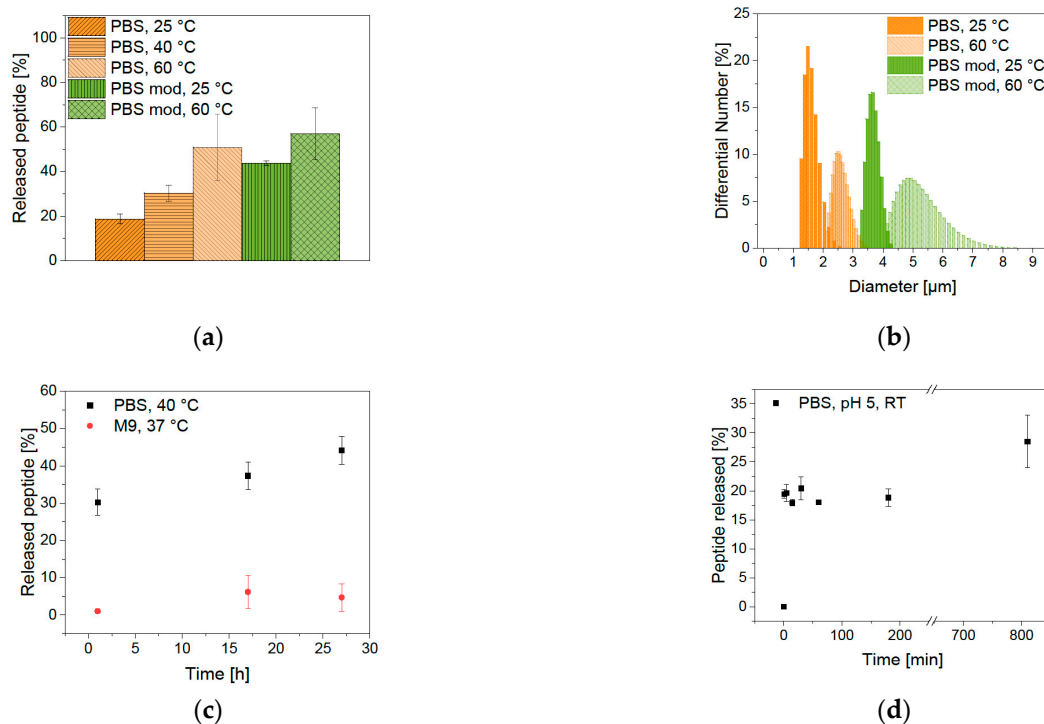


Figure 7. (a) Desorption of LL from BIONs at different conditions after one hour, (b) agglomeration behavior after one hour of elution at different conditions, (c) desorption depending on the time, and (d) kinetic of the desorption process of LL in 50 mM PBS, pH 5, and room temperature.

The binding properties are analyzed by variation of the sodium chloride amount (0.68 M in PBS buffer, 1.00 M in modified PBS buffer). Higher salt concentration led to elution of 44% at room temperature that is more than twice as much compared with the unmodified PBS buffer. Moreover, a higher temperature of 60 °C led to the highest elution of 57%. This shows that the interaction of LL with the BIONs is electrostatic and non-covalent. Measurements of the hydrodynamic diameter show higher agglomeration after elution with higher salt concentration and higher temperature (Figure 7b). In general, agglomeration can increase the heating efficiency of BIONs but makes it difficult to control the local heating at the target side [66]. For antimicrobial tests in Section 2.4. an M9 medium is used. Analysis of the LL desorption in this medium shows only an elution of 4.7% after 27 h (Figure 7c, Figure S4). Indeed, the full desorption of the peptide from the BIONs is not necessary if it still shows antimicrobial activity while being bound to the particles.

Furthermore, the stability in lysosomal fluid needs to be annotated. Milosevic et al. demonstrated that IONs dissolve in artificial lysosomal fluid within 24 h while forming free iron ions [67]. This iron transfer leads to the degradation and recycling of IONs into ferritin storage [68]. This dissolution could lead to LL release during endocytosis.

2.4. Antimicrobial Behavior

LL belongs to the group of antimicrobial peptides (AMPs) and shows antimicrobial activity against various bacteria. For example, for *E. coli* LL-III has a minimum inhibitory concentration (MIC) of 1.4–3.7 µM [25,69]. Furthermore, Zaccharia et al. are reporting a slightly lower MIC of 7.5 µM if LL-III is bound covalently to ureido-pyrimidinone antimicrobial biomaterial [69]. Other short AMPs with many lysines like SYM11KK (KKFP-WWWPFKK) or L₉K₆ (LKLLKLLKLLKLL) show MIC at comparable or slightly higher concentrations of 15 µM and 3.7 µM against *E. coli* [69–71]. Various studies of the antimicrobial activity of IONs have already been made. In general, BIONs have an antimicrobial activity at very high concentrations (>50 µM), which can be modified through the surface charge and addition of functional groups. Previous studies have shown that the decrease in BIONs' size can lead to lower cell growth of *P. aeruginosa* [72–74]. The growth rate of green fluorescent protein (GFP) expressing *E. coli* (BL 21 resistant against *ampicillin*) was tested to compare the antimicrobial behavior of LL to the BION@LL complex (Figure 8a). First, the influence of BIONs on cell growth was analyzed. Microscopic cell counting showed that in a 1.00 mg/L BION solution, the growth is comparable to experiments with no presence of BIONs. As expected, higher BION concentrations led to a decrease in *E. coli* growth, but not to full inhibition. The curve shows a negative exponential shape with the smallest colony count for 1.00 g/L BIONs. The antimicrobial peptide LL leads to complete inhibition with a concentration of 1.13 µM, while at lower concentrations a negative linear coherence was observed (Figure 8b). It has to be emphasized that in the Neubauer chamber only fluorescent colonies could be counted and the expression of GFP could be influenced under strong antimicrobial conditions. This could explain the slightly higher MIC compared to the literature discussed above [25,69]. Analysis of the toxic effects of the BION@LL complex shows less bacterial growth with comparable LL concentrations (Figure 8c). Already 0.53 µM LL on the particles lead to complete inhibition, while the peptide only showed less *E. coli* growth. Therefore, the MIC is lower than of bound LL to ureido-pyrimidinone material (7.5 µM) [69]. This can be explained by a better exposure of the peptide and the drug being bound more tightly to the *E. coli* because BIONs can interact with bacteria [75]. Another possibility is the combination of a slight antimicrobial effect of BIONs and the antimicrobial effect of LL which might lead to earlier inhibition. The peptide is fully active while being bound to the particles. Further information and pictures of the *E. coli* in the Neubauer chamber can be found in the Supporting Information in Figures S5–S8.

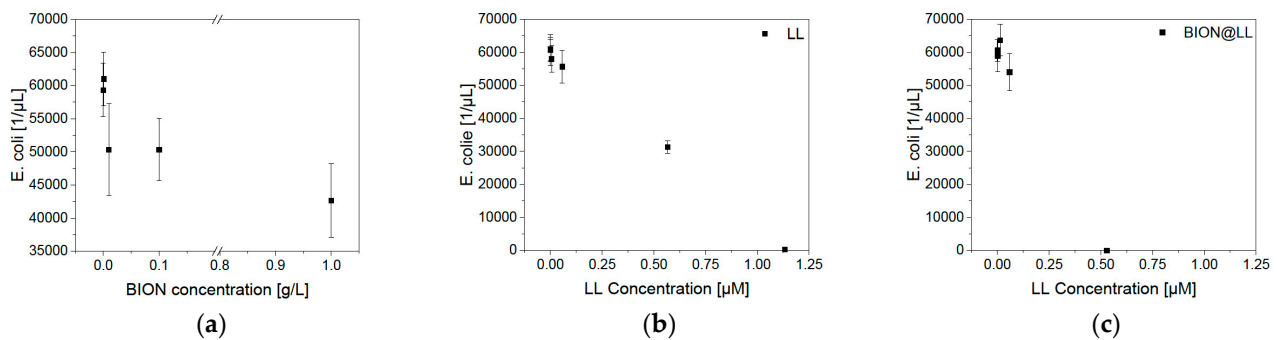


Figure 8. Growth of *E. coli* (BL21 (RH)₄GFP expressing) in M9 medium under different (a) BION concentrations, (b) LL concentrations, and (c) amounts of the MNP@LL complex. Analysis with microscopy.

Growth studies with optical density (OD₆₀₀) measurements give comparable results, showing that MNP concentrations up to 0.10 g/L do not negatively influence bacterial growth (Figure 9a). LL leads to less growth at a concentration of 1.13 μM and full inhibition at 2.83 μM or higher (Figure 9b). The BION peptide complexes show a slower growth rate at 0.85 μM of LL and full inhibition at 1.76 μM and higher ones (Figure 9c). The slight differences between these two measurement methods can be ascribed to more intense mixing of the culture in an overhead shaker before microscopy compared to linear shaking of the 96-well plate. Furthermore, for OD₆₀₀ measurements, the ability of GFP expression does not play a role in detection. Both experiments show that the antimicrobial behavior of LL is improved by the binding of LL to the BIONs.

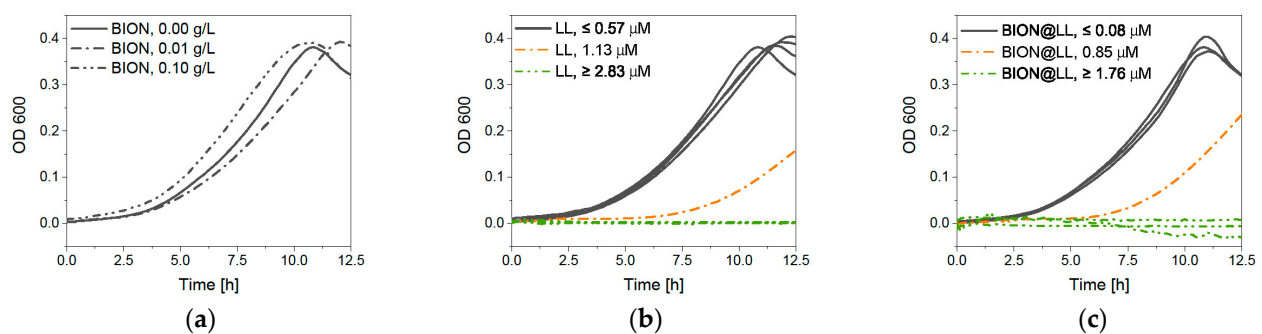


Figure 9. OD₆₀₀ measurements of *E. coli* (BL21 (RH)₄GFP expressing) in M9 medium under different (a) BION concentrations, (b) LL concentrations, and (c) amounts of the MNP@LL complex. The concentration in the diagram of MNP@LL describes to the LL concentration.

3. Materials and Methods

3.1. Synthesis of BIONs

The BIONs are synthesized by co-precipitation. We dissolved 28.9 g sodium hydroxide (723 mmol, 10.3 Eq.) in 400 mL of degassed deionized water under nitrogen atmosphere. A solution of 34.6 g FeCl₃(H₂O)₆ (128 mmol, 1.82 Eq.) and 14.0 g FeCl₂(H₂O)₄ (70.4 mmol, 1.00 Eq., Sigma Aldrich, Merck KGaA, St. Louis, MO, USA), in 160 mL degassed deionized water is slowly added under stirring and temperature control with a water bath at 27 °C. Immediately, a black precipitate forms after the complete addition of all chemicals. The reaction is continued for half an hour under constant conditions. The resulting particles are washed with degassed deionized water (15×) by magnetic decantation until a conductivity of less than 200 μS/cm is reached. The particles are stored in degassed deionized water under nitrogen atmosphere at 4 °C.

3.2. Characterization

The magnetic susceptibility is analyzed with a superconducting quantum interference device (SQUID) Quantum Design MPMS XL-7 at 300 K. The magnetic field varied from -50 kOe to $+50$ kOe. Before the analysis, the particles are lyophilized and glued into a small tube. Transmission electron microscopy (TEM) is performed with the JEM 1400 Plus microscope from JEOL. The sample ($10 \mu\text{L}$) dispersed in chloroform is dried on a carbon-coated copper grid that has been prepared via glow discharge for sample preparation. The recorded images are subsequently evaluated by using ImageJ software. For this, 30 particles are measured in at least three different areas. Furthermore, powder X-ray diffraction (XRD) is executed with a STOE Stadi-P diffractometer with a molybdenum source ($\lambda = 0.7093 \text{ \AA}$) and freeze-dried IONs. The determination of the zeta potential and the hydrodynamic diameter by DLS is performed with a Beckman Coulter Delsa Nano C Particle Analyzer of a 1 g/L ION solution. Each sample is measured in triplicate (cuvette, 10 mm length). The Fourier-transform infrared spectra (FTIR) measurement is carried out with a Bruker ALPHA II spectrometer and the matching platinum attenuated total reflection module, 64 scans per sample. After the measurements have been performed, a concave rubber band method is used to subtract a background in the software OPUS 8.1. For absorbance analysis, the photometer Tecan Infinite M200 PRO Series is used with the evaluation software Magellan. Analysis of the OD_{600} value is implemented with an Eppendorf BioSpectrometer. The BET surface evaluation took place with a Gemini VII (Micromeritics) at 77 K and nitrogen atmosphere, while the volume was determined with helium. Microscopic images are made with an AXIO Observer from Zeiss with an Axiocam 506 mono. For fluorescence analysis, a 475 nm LED is used with 20% intensity for 500 ms , while pictures of BIONs are generated with a transmitted light lamp in brightfield with 12% intensity for 500 ms .

3.3. Binding of Peptides to the Nanoparticles

pH and peptide concentration: Before conducting the adsorption experiments, the absorbance of LL III solutions, obtained from Gen-Script (Netherlands), with different concentrations are measured in triplicates. We mixed $250 \mu\text{L}$ of peptide solutions with different concentrations and pH values with $250 \mu\text{L}$ of a 2 g/L BION stock solution to generate a BION concentration of 1 g/L (LL end concentration: 2.00 g/L , 1.00 g/L , 0.50 g/L , 0.25 g/L , 0.10 g/L , 0.05 g/L , 25.0 mg/L , and 0.00 g/L). Prior, the BIONs are ultrasonicated (20%, 7 min, 10 s on, 15 s off). The experiments are performed in Millipore water (water type 1) at pH 7 and pH 9. The samples are incubated for one hour at $23 \text{ }^\circ\text{C}$ (1000 rpm) to induce peptide binding. After magnetic decantation, $100 \mu\text{L}$ of the supernatant are photometrically analyzed at 280 nm . For washing, the particles are resuspended in water at the same pH value and incubated for ten minutes ($23 \text{ }^\circ\text{C}$, 1000 rpm). Afterwards, the supernatant of the washing step is also analyzed.

Buffer and peptide concentration: The LL stock solution and further dilutions are prepared with 100 mM PBS buffer (3.20 g NaCl , 80.0 mg KCl , $576 \text{ mg NaH}_2\text{PO}_4$, $96.0 \text{ mg KH}_2\text{PO}_4$ in 40 mL Millipore water) and afterwards mixed with the BION stock solution in Millipore water at pH 7.4 to generate an overall PBS concentration of 50 mM . Adsorption experiments are performed as described above. The BIONs are washed three times, and the supernatant is analyzed at 230 nm and 280 nm . All further experiments are performed with BION@LL complexes formed in PBS buffer.

Particle concentration: BION solutions of different concentrations in Millipore water at pH 7 (resulting particle concentration: 2.00 g/L , 1.00 g/L , 0.50 g/L , and 0.25 g/L) are mixed with a 2 g/L LL solution in 100 mM PBS buffer. Adsorption experiments are performed as described above and the supernatant is analyzed at 280 nm .

Time: $575 \mu\text{L}$ of 2 g/L LL solution in 100 mM PBS buffer at pH 7 are combined with $575 \mu\text{L}$ of 2 g/L BION stock solution at pH 7 and incubated at $23 \text{ }^\circ\text{C}$ (1000 rpm). After 1 min, 5 min, 15 min, 30 min, 60 min, 180 min, and 24 h, each $120 \mu\text{L}$ of suspension are removed, magnetically decanted, and the supernatant is analyzed photometrically at 280 nm .

3.4. Agglomeration Behavior in HS

Suspensions of 0.5 g/L of BIONs and BION@LL (1 g/L LL starting concentration for adsorption in PBS) are ultrasonicated in an ultrasonic bath for 10 min. Through magnetic decantation, the supernatant is exchanged with PBS 50 mM pH 7.4, water pH 7.0, or heat-inactivated AB HS of a human male (Sigma Aldrich). Before the DLS measurement, the particle suspensions are brought to a temperature of 37 °C and then analyzed with the Zetasizer at a measurement temperature of 37 °C.

3.5. Elution of Lasioglossin from the Nanoparticles

Salt concentration and temperature: The washed lasioglossin-magnetite particles are brought to the same concentration with a 50 mM PBS buffer (1.20 g NaCl, 30.0 mg KCl, 216 mg NaH₂PO₄, 36.0 mg KH₂PO₄ in 30 mL Millipore water) and a modified PBS buffer (1.75 g NaCl, 30.0 mg KCl, 216 mg NaH₂PO₄, 36.0 mg KH₂PO₄ in 30 mL Millipore water) at pH 5. After one hour, 17 h or 27 h of incubation (1000 rpm) at 25 °C, 40 °C or 60 °C, and magnetic decantation, the supernatant's LL concentration is analyzed at 230 nm.

Time: After one washing step, the BION@LL complexes are mixed with 50 mM PBS buffer and incubated at 23 °C (1000 rpm). After 1 min, 5 min, 15 min, 30 min, 60 min, 180 min, and 13.5 h 120 µL of each suspension are removed, magnetically decanted and then the supernatant is analyzed photometrically at 230 nm.

3.6. Growth Studies

A 1 g/L LL solution in 50 mM PBS buffer (pH 7.4) is sterilized by filtration (0.22 µm filter). Furthermore, a 10 g/L BION solution is prepared in 50 mM PBS buffer. For the BION@LL complex, an adsorption experiment including one washing step is performed in 1 g/L LL solution and 1 g/L BIONs according to Section 2.4. Before, the tests solutions with different concentrations of LL (1.00 g/L, 0.50 g/L, 0.25g/L, 0.10 g/L, 0.05 g/L, 0.02 g/L, 0.01 g/L, 0.001 g/L, and 0.0001 g/L) and BIONs (10.0 g/L, 1.00 g/L, 0.10 g/L), are prepared by dilution of the stock solution with 50 mM PBS buffer in sterile LoBind reaction tubes (Eppendorf).

Cell number: M9 medium is mixed with a 100 g/L ampicillin solution (1:1000) (Table S5). An overnight culture of (RH)₄-GFP expressing *E. coli* BL21 (DE3) (resistance against ampicillin, incubation at 37 °C) is diluted to OD₆₀₀ 0.01, and 270 µL are mixed with BION and LL and BION@LL solutions in LoBind reaction tubes as described above. As a blank, 30 µL of 50 mM PBS buffer are used. The suspensions are incubated at 37 °C in an overhead shaker for 5 h (500 rpm). After the addition of 3.00 µL of a 0.10 M isopropyl-β-D-thiogalactopyranoside (IPTG) solution, the samples are further incubated for 18 h. After dilution of 10⁻², they are microscopical analyzed in a Neubauer chamber improved. Through the fluorescence of GFP, the bacteria can be differentiated to the BION agglomerates and counted.

Cell density: 180 µL of the same *E. coli* dilution are mixed with 20 µL of the BION, LL, and MNP@LL solutions in a sterile 96-well plate. For the blank, 20 µL of PBS buffer are used instead. Furthermore, for each sample, the same amount of probe is mixed with M9 medium to subtract the influence on the OD₆₀₀ from the different amounts of particles and LL. The probes are incubated at 37 °C and measured every 10 min, with a 60 sec linear amplitude, 1 mm frequency, 173.9 rpm, and 25 read operations.

4. Conclusions

It is possible to couple LL as a cationic peptide efficiently to the BION surface. The pH and PBS buffer application play a particular role in LL interaction with BIONs and the binding capacity. The absorbance measurements and IR spectroscopy verify the successful drug loading of 22.7% in PBS buffer. The equilibrium loading is already reached after 30 min and is not further influenced by time. The amount of bound LL and the medium highly influence the agglomeration behavior of BIONs and the electrical potential on the surface. In HS, the hydrodynamic diameter is distinctly smaller than in water or PBS.

Each washing step leads to a new equilibrium and, therefore, to LL loss due to reversible binding. Experiments with different amounts of BIONs have shown that this equilibrium is independent of the particle concentration.

Desorption of LL from BIONs is possible. While a pH shift is not showing effective desorption, the binding is temperature-sensitive. Incubation time does not significantly affect LL elution. Only long incubation times of 12–27 h lead to higher elution. The hydrodynamic diameter is strongly influenced by increasing salt concentration and higher temperature leading to big agglomerates. In bacterial growth experiments, the BION@LL complexes show higher antimicrobial activity compared to the antimicrobial peptide alone.

Thus, LL can be bound in high amounts to the BION surface, and the system is especially effective in growth studies; BIONs show agglomeration beyond 100 nm during all tested conditions. This impedes the applicability in the human body. Biocompatible coatings should be analyzed to stabilize the particles and enhance the tolerability of the human system. The washing and desorption processes need to be further analyzed to generate particles usable for controlled drug delivery.

The experiments have shown that new antimicrobial peptides can be combined with cost-efficient BIONs to generate a new drug delivery system. The adsorption process can be performed quickly and simply due to electrostatic binding, while the antimicrobial activity is not affected by the binding. The excellent combination of LL with IONs could lead to an efficient magnetic drug delivery system for anticancer treatment in the future, even if further optimization steps are needed.

Supplementary Materials: The following materials are available online at <https://www.mdpi.com/article/10.3390/ph14050405/s1>: Figure S1: BET measurement: Adsorbed nitrogen to relative pressure; Figure S2: *E. coli* colony grown in M9 media incubated with different concentrations of BIONs; Figure S3: *E. coli* colony grown in M9 media incubated with different concentrations of LL; Figure S4: *E. coli* colony grown in M9 media incubated with different concentrations of BION@LL; Figure S5: Amount of LL loaded on BIONs; Table S1: Modified Langevin fir for SQUID Analysis; Table S2: BION size calculation with Scherer equation from XRD; Table S3: Components of M9 Medium for 1 L; Table S4: Components for LB agar plates for 500 mL water title; Equation (S1): Boltzmann fit for Zeta Potential Analysis; Equation (S2): Scherer equation; Equation (S3): Drug loading.

Author Contributions: C.T.: Conceptualization, methodology, formal analysis, investigation, data curation, writing—original draft, visualization; S.B.: Resources, funding acquisition, writing—review and editing, Supervision; S.P.S.: Conceptualization, funding acquisition, writing—review and editing, supervision, project administration. All authors have read and agreed to the published version of the manuscript.

Funding: We appreciate the support from the German Research Foundation (DFG) and the Technical University of Munich (TUM) in the framework of the Open-Access Publishing Program and the support by TUM International Graduate School of Science and Engineering (IGSSE) and the Dr.-Ing. Leonhard-Lorenz foundation. The funders had no role in the design of the study, in the collection, analyses, or interpretation of data, in the writing of the manuscript, or in the decision to publish the results.

Institutional Review Board Statement: Not applicable.

Informed Consent Statement: Not applicable.

Data Availability Statement: All data generated or analyzed during this study are included in this published article and its supplementary information files. Further datasets used and/or analyzed during the study are available from the corresponding author on reasonable request.

Acknowledgments: We want to thank Matthias Opel for the SQUID measurement, Carsten Peters for support with TEM imaging, and Tom Nilges for providing the X-ray diffractometer. Furthermore, we want to acknowledge the work of our students Magdalena Vogel and Natalie Wagner, who performed preliminary experiments. Open access funding enabled and organized by Project DEAL.

Conflicts of Interest: The authors declare no conflict of interest.

References

1. Tiwari, G.; Tiwari, R.; Bannerjee, S.K.; Bhati, L.; Pandey, S.; Pandey, P.; Sriwastawa, B. Drug delivery systems: An updated review. *Int. J. Pharm. Investig.* **2012**, *2*, 2–11. [[CrossRef](#)]
2. Langer, R. Drug delivery and targeting. *Nature* **1998**, *392*, 5–10.
3. Piktel, E.; Niemirowicz, K.; Wątek, M.; Wollny, T.; Deptuła, P.; Bucki, R. Recent insights in nanotechnology-based drugs and formulations designed for effective anti-cancer therapy. *J. Nanobiotechnol.* **2016**, *14*, 1–23. [[CrossRef](#)] [[PubMed](#)]
4. Alvarez-Lorenzo, C.; Concheiro, A. *Smart Materials for Drug Delivery*; The Royal Society of Chemistry: Cambridge, UK, 2013.
5. Gupta, A.K.; Gupta, M. Synthesis and surface engineering of iron oxide nanoparticles for biomedical applications. *Biomaterials* **2005**, *26*, 3995–4021. [[CrossRef](#)]
6. Bruschi, M.L.; Toledo, L.D.A.S.D. Pharmaceutical Applications of Iron-Oxide Magnetic Nanoparticles. *Magnetochemistry* **2019**, *5*, 50. [[CrossRef](#)]
7. Wu, S.; Sun, A.; Zhai, F.; Wang, J.; Xu, W.; Zhang, Q.; Volinsky, A.A. Fe₃O₄ magnetic nanoparticles synthesis from tailings by ultrasonic chemical co-precipitation. *Mater. Lett.* **2011**, *65*, 1882–1884. [[CrossRef](#)]
8. Cao, S.-W.; Zhu, Y.-J.; Ma, M.-Y.; Li, L.; Zhang, L. Hierarchically Nanostructured Magnetic Hollow Spheres of Fe₃O₄ and γ -Fe₂O₃: Preparation and Potential Application in Drug Delivery. *J. Phys. Chem. C* **2008**, *112*, 1851–1856. [[CrossRef](#)]
9. Laurent, S.; Forge, D.; Port, M.; Roch, A.; Robic, C.; Elst, L.V.; Muller, R.N. Magnetic Iron Oxide Nanoparticles: Synthesis, Stabilization, Vectorization, Physicochemical Characterizations, and Biological Applications. *Chem. Rev.* **2008**, *108*, 2064–2110. [[CrossRef](#)] [[PubMed](#)]
10. Shaghasemi, B.S.; Virk, M.M.; Reimhult, E. Optimization of Magneto-thermally Controlled Release Kinetics by Tuning of Magnetoliposome Composition and Structure. *Sci. Rep.* **2017**, *7*, 1–10. [[CrossRef](#)]
11. Wnorowska, U.; Fiedoruk, K.; Piktel, E.; Prasad, S.V.; Sulik, M.; Janion, M.; Daniluk, T.; Savage, P.B.; Bucki, R. Nanoantibiotics containing membrane-active human cathelicidin LL-37 or synthetic ceragenins attached to the surface of magnetic nanoparticles as novel and innovative therapeutic tools: Current status and potential future applications. *J. Nanobiotechnol.* **2020**, *18*, 1–18. [[CrossRef](#)]
12. Křížek, M.; Pechoušek, J.; Tucěk, J.; Šafářová, K.; Medřík, I.; Machala, L. Iron oxide nanoparticle powders with high surface area. In Proceedings of the AIP Conference, Olomouc, Czech Republic, 12 October 2012; Volume 1489, pp. 88–94.
13. Lu, A.-H.; Salabas, E.-L.; Schüth, F. Magnetic Nanoparticles: Synthesis, Protection, Functionalization, and Application. *Angew. Chem. Int. Ed.* **2007**, *46*, 1222–1244. [[CrossRef](#)]
14. Yusoff Ahmad, H.M.; Salimi Midhat, N.; Jamlos Mohd, F. A review: Synthetic strategy control of magnetite nanoparticles production. *Adv. Nano Res.* **2018**, *6*, 1–19. [[CrossRef](#)]
15. Wu, W.; Wu, Z.; Yu, T.; Jiang, C.; Kim, W.-S. Recent progress on magnetic iron oxide nanoparticles: Synthesis, surface functional strategies and biomedical applications. *Sci. Technol. Adv. Mater.* **2015**, *16*, 023501. [[CrossRef](#)]
16. Arruebo, M.; Fernández-Pacheco, R.; Ibarra, M.R.; Santamaría, J. Magnetic nanoparticles for drug delivery. *Nano Today* **2007**, *2*, 22–32. [[CrossRef](#)]
17. Israel, L.L.; Galstyan, A.; Holler, E.; Ljubimova, J.Y. Magnetic iron oxide nanoparticles for imaging, targeting and treatment of primary and metastatic tumors of the brain. *J. Control. Release* **2020**, *320*, 45–62. [[CrossRef](#)] [[PubMed](#)]
18. Kievit, F.M.; Zhang, M. Surface Engineering of Iron Oxide Nanoparticles for Targeted Cancer Therapy. *Acc. Chem. Res.* **2011**, *44*, 853–862. [[CrossRef](#)] [[PubMed](#)]
19. Liechty, W.B.; Kryscio, D.R.; Slaughter, B.V.; Peppas, N.A. Polymers for Drug Delivery Systems. *Annu. Rev. Chem. Biomol. Eng.* **2010**, *1*, 149–173. [[CrossRef](#)] [[PubMed](#)]
20. Sun, T.; Zhang, Y.S.; Pang, B.; Hyun, D.C.; Yang, M.; Xia, Y. Engineered Nanoparticles for Drug Delivery in Cancer Therapy. *Angew. Chem. Int. Ed.* **2014**, *53*, 12320–12364. [[CrossRef](#)] [[PubMed](#)]
21. Schwaminger, S.P.; Blank-Shim, S.A.; Scheifele, I.; Pipich, V.; Fraga-García, P.; Berensmeier, S. Design of Interactions Between Nanomaterials and Proteins: A Highly Affine Peptide Tag to Bare Iron Oxide Nanoparticles for Magnetic Protein Separation. *Biotechnol. J.* **2019**, *14*, e1800055. [[CrossRef](#)] [[PubMed](#)]
22. Schwaminger, S.P.; García, P.F.; Merck, G.K.; Bodensteiner, F.A.; Heissler, S.; Günther, S.; Berensmeier, S. Nature of Interactions of Amino Acids with Bare Magnetite Nanoparticles. *J. Phys. Chem. C* **2015**, *119*, 23032–23041. [[CrossRef](#)]
23. Schwaminger, S.; Blank-Shim, S.A.; Borkowska-Panek, M.; Anand, P.; Fraga-García, P.; Fink, K.; Wenzel, W.; Berensmeier, S. Experimental characterization and simulation of amino acid and peptide interactions with inorganic materials. *Eng. Life Sci.* **2018**, *18*, 84–100. [[CrossRef](#)]
24. Rawlings, A.E.; Bramble, J.P.; Tang, A.A.S.; Somner, L.A.; Monnington, A.E.; Cooke, D.J.; McPherson, M.J.; Tomlinson, D.C.; Staniland, S.S. Phage display selected magnetite interacting Adhirons for shape controlled nanoparticle synthesis. *Chem. Sci.* **2015**, *6*, 5586–5594. [[CrossRef](#)]
25. Čeřovský, V.; Budešinský, M.; Hovorka, O.; Cvac̣ka, J.; Voburka, Z.; Slaninová, J.; Borovic̣ková, L.; Fuc̣ík, V.; Bednářová, L.; Votruba, I.; et al. Lasioglossins: Three Novel Antimicrobial Peptides from the Venom of the Eusocial Bee *Lasioglossum laticeps* (Hymenoptera: Halictidae). *ChemBioChem* **2009**, *10*, 2089–2099. [[CrossRef](#)]
26. Hancock, R.E.W.; Sahl, H.-G. Antimicrobial and host-defense peptides as new anti-infective therapeutic strategies. *Nat. Biotechnol.* **2006**, *24*, 1551–1557. [[CrossRef](#)]

27. Parisien, A.; Allain, B.; Zhang, J.; Mandeville, R.; Lan, C. Novel alternatives to antibiotics: Bacteriophages, bacterial cell wall hydrolases, and antimicrobial peptides. *J. Appl. Microbiol.* **2007**, *104*, 1–13. [CrossRef]
28. Bahar, A.A.; Ren, D. Antimicrobial Peptides. *Pharmaceuticals* **2013**, *6*, 1543–1575. [CrossRef] [PubMed]
29. Aoki, W.; Ueda, M. Characterization of Antimicrobial Peptides toward the Development of Novel Antibiotics. *Pharmaceuticals* **2013**, *6*, 1055–1081. [CrossRef]
30. Brogden, K.A. Antimicrobial peptides: Pore formers or metabolic inhibitors in bacteria? *Nat. Rev. Genet.* **2005**, *3*, 238–250. [CrossRef]
31. Mishra, B.; Basu, A.; Saravanan, R.; Xiang, L.; Yang, L.K.; Leong, S.S.J. Lasioglossin-III: Antimicrobial characterization and feasibility study for immobilization applications. *RSC Adv.* **2013**, *3*, 9534–9543. [CrossRef]
32. Schwaminger, S.P.; Bauer, D.; Fraga-García, P.; Wagner, F.E.; Berensmeier, S. Oxidation of magnetite nanoparticles: Impact on surface and crystal properties. *CrystEngComm* **2016**, *19*, 246–255. [CrossRef]
33. Schnell, F.; Kube, M.; Berensmeier, S.; Schwaminger, S.P. Magnetic Recovery of Cellulase from Cellulose Substrates with Bare Iron Oxide Nanoparticles. *ChemNanoMat* **2019**, *5*, 422–426. [CrossRef]
34. Shang, L.; Nienhaus, K.; Nienhaus, G.U. Engineered nanoparticles interacting with cells: Size matters. *J. Nanobiotechnol.* **2014**, *12*, 5. [CrossRef] [PubMed]
35. Dodi, G.; Hritcu, D.; Draganescu, D.; Popa, M.I. Iron oxide nanoparticles for magnetically assisted patterned coatings. *J. Magn. Mater.* **2015**, *388*, 49–58. [CrossRef]
36. Bean, C.P.; Livingston, J.D. Superparamagnetism. *J. Appl. Phys.* **1959**, *30*, S120–S129. [CrossRef]
37. Henrard, D.; Vuong, Q.L.; Delangre, S.; Valentini, X.; Nonclercq, D.; Gonon, M.F.; Gossuin, Y. Monitoring of Superparamagnetic Particle Sizes in the Langevin Law Regime. *J. Nanomater.* **2019**, *2019*, 1–9. [CrossRef]
38. Eisenberg, R.; Gray, H.B. Preface on Making Oxygen. *Inorg. Chem.* **2008**, *47*, 1697–1699. [CrossRef] [PubMed]
39. Schweser, F.; Deistung, A.; Lehr, B.W.; Reichenbach, J.R. Differentiation between diamagnetic and paramagnetic cerebral lesions based on magnetic susceptibility mapping. *Med Phys.* **2010**, *37*, 5165–5178. [CrossRef]
40. Walker, N. Paramagnetic properties of Fe(II) and Fe(III). *J. Chem. Educ.* **1977**, *54*. [CrossRef]
41. Hoppe, T. A simplified representation of anisotropic charge distributions within proteins. *J. Chem. Phys.* **2013**, *138*, 174110. [CrossRef]
42. Dobson, J. Magnetic nanoparticles for gene and drug delivery. *Int. J. Nanomed.* **2008**, *3*, 169–180. [CrossRef] [PubMed]
43. Schwaminger, S.P.; Blank-Shim, S.A.; Scheifele, I.; Fraga-García, P.; Berensmeier, S. Peptide binding to metal oxide nanoparticles. *Faraday Discuss.* **2017**, *204*, 233–250. [CrossRef] [PubMed]
44. Blank-Shim, S.A.; Schwaminger, S.P.; Borkowska-Panek, M.; Anand, P.; Yamin, P.; Fraga-García, P.; Fink, K.; Wenzel, W.; Berensmeier, S. Binding patterns of homo-peptides on bare magnetic nanoparticles: Insights into environmental dependence. *Sci. Rep.* **2017**, *7*, 14047. [CrossRef] [PubMed]
45. Nelson, D.L.; Lehninger, A.L.; Cox, M.M. *Lehninger Principles of Biochemistry*, 6th ed.; W.H. Freeman: New York, NY, USA, 2013.
46. Liu, Y.; Yang, G.; Jin, S.; Xu, L.; Zhao, C. Development of High-Drug-Loading Nanoparticles. *ChemPlusChem* **2020**, *85*, 2143–2157. [CrossRef] [PubMed]
47. Qu, J.-B.; Shao, H.-H.; Jing, G.-L.; Huang, F. PEG-chitosan-coated iron oxide nanoparticles with high saturated magnetization as carriers of 10-hydroxycamptothecin: Preparation, characterization and cytotoxicity studies. *Colloids Surf. B Biointerfaces* **2013**, *102*, 37–44. [CrossRef]
48. Luo, B.; Xu, S.; Luo, A.; Wang, W.-R.; Wang, S.-L.; Guo, J.; Lin, Y.; Zhao, D.-Y.; Wang, C.-C. Mesoporous Biocompatible and Acid-Degradable Magnetic Colloidal Nanocrystal Clusters with Sustainable Stability and High Hydrophobic Drug Loading Capacity. *ACS Nano* **2011**, *5*, 1428–1435. [CrossRef]
49. Ebrahimezhad, A.; Ghasemi, Y.; Rasoul-Amini, S.; Barar, J.; Davaran, S. Impact of Amino-Acid Coating on the Synthesis and Characteristics of Iron-Oxide Nanoparticles (IONs). *Bull. Korean Chem. Soc.* **2012**, *33*, 3957–3962. [CrossRef]
50. Morhardt, C.; Ketterer, B.; Heißler, S.; Franzreb, M. Direct quantification of immobilized enzymes by means of FTIR ATR spectroscopy—A process analytics tool for biotransformations applying non-porous magnetic enzyme carriers. *J. Mol. Catal. B Enzym.* **2014**, *107*, 55–63. [CrossRef]
51. Bordbar, A.K.; Rastegari, A.A.; Amiri, R.; Ranjbakhsh, E.; Abbasi, M.; Khosropour, A.R. Characterization of Modified Magnetite Nanoparticles for Albumin Immobilization. *Biotechnol. Res. Int.* **2014**, *2014*, 1–6. [CrossRef]
52. Sigma Aldrich. IR Spectrum Table & Chart. Available online: <https://www.sigmaaldrich.com/technical-documents/articles/biology/ir-spectrum-table.html> (accessed on 17 November 2020).
53. Kumar, A.; Dixit, C.K. Methods for characterization of nanoparticles. In *Advances in Nanomedicine for the Delivery of Therapeutic Nucleic Acids*; Woodhead Publishing: Cambridge, UK, 2017; pp. 43–58.
54. Almasri, D.A.; Saleh, N.B.; Atieh, M.A.; McKay, G.; Ahzi, S. Adsorption of phosphate on iron oxide doped halloysite nanotubes. *Sci. Rep.* **2019**, *9*, 1–13. [CrossRef]
55. Psychogios, N.; Hau, D.D.; Peng, J.; Guo, A.C.; Mandal, R.; Bouatra, S.; Sinelnikov, I.; Krishnamurthy, R.; Eisner, R.; Gautam, B.; et al. The Human Serum Metabolome. *PLoS ONE* **2011**, *6*, e16957. [CrossRef]
56. Készmárky, G.; Kenyeres, P.; Rábai, M.; Tóth, K. Plasma viscosity: A forgotten variable. *Clin. Hemorheol. Microcirc.* **2008**, *39*, 243–246. [CrossRef]
57. Benítez, E.I.; Genovese, D.B.; Lozano, J.E. Effect of typical sugars on the viscosity and colloidal stability of apple juice. *Food Hydrocoll.* **2009**, *23*, 519–525. [CrossRef]

58. Coppola, L.; Caserta, F.; De Lucia, D.; Guastafierro, S.; Grassia, A.; Coppola, A.; Marfella, R.; Varricchio, M. Blood viscosity and aging. *Arch. Gerontol. Geriatr.* **2000**, *31*, 35–42. [[CrossRef](#)]
59. Yakout, S.M. Effect of porosity and surface chemistry on the adsorption-desorption of uranium(VI) from aqueous solution and groundwater. *J. Radioanal. Nucl. Chem.* **2016**, *308*, 555–565. [[CrossRef](#)]
60. Zhu, M.-T.; Wang, Y.; Feng, W.-Y.; Wang, B.; Wang, M.; Ouyang, H.; Chai, Z.-F. Oxidative Stress and Apoptosis Induced by Iron Oxide Nanoparticles in Cultured Human Umbilical Endothelial Cells. *J. Nanosci. Nanotechnol.* **2010**, *10*, 8584–8590. [[CrossRef](#)] [[PubMed](#)]
61. Rivolta, I.; Panariti, A.; Misericocchi, G. The effect of nanoparticle uptake on cellular behavior: Disrupting or enabling functions? *Nanotechnol. Sci. Appl.* **2012**, *5*, 87–100. [[CrossRef](#)]
62. Hauser, A.K.; Wydra, R.J.; Stocke, N.A.; Anderson, K.W.; Hilt, J.Z. Magnetic nanoparticles and nanocomposites for remote controlled therapies. *J. Control. Release* **2015**, *219*, 76–94. [[CrossRef](#)] [[PubMed](#)]
63. Saeed, M.; Ren, W.; Wu, A. Therapeutic applications of iron oxide based nanoparticles in cancer: Basic concepts and recent advances. *Biomater. Sci.* **2017**, *6*, 708–725. [[CrossRef](#)]
64. Gomes, I.P.; Duarte, J.A.; Maia, A.L.C.; Rubello, D.; Townsend, D.M.; De Barros, A.L.B.; Leite, E.A. Thermosensitive Nanosystems Associated with Hyperthermia for Cancer Treatment. *Pharmaceuticals* **2019**, *12*, 171. [[CrossRef](#)]
65. Abu-Bakr, A.F.; Zubarev, A.Y. Effect of ferromagnetic nanoparticles aggregation on magnetic hyper-thermia. *Eur. Phys. J. Spec. Top.* **2020**, *11*, 323–329. [[CrossRef](#)]
66. Perigo, E.A.; Hemery, G.; Sandre, O.; Ortega, D.; Garaio, E.; Plazaola, F.; Teran, F.J. Fundamentals and advances in magnetic hyperthermia. *Appl. Phys. Rev.* **2015**, *2*, 041302. [[CrossRef](#)]
67. MilosevicAc, A.; Bourquin, J.; Burnand, D.; Lemal, P.; Crippa, F.; Monnier, C.A.; Rodriguez-Lorenzo, L.; Petri-Fink, A.; Rothen-Rutishauser, B. Artificial Lysosomal Platform to Study Nanoparticle Long-term Stability. *Chim. Int. J. Chem.* **2019**, *73*, 55–58. [[CrossRef](#)]
68. Lartigue, L.; Alloyeau, D.; Kolosnjaj-Tabi, J.; Javed, Y.; Guardia, P.; Riedinger, A.; Péchoux, C.; Pellegrino, T.; Wilhelm, C.; Gazeau, F. Biodegradation of Iron Oxide Nanocubes: High-Resolution In Situ Monitoring. *ACS Nano* **2013**, *7*, 3939–3952. [[CrossRef](#)]
69. Zaccaria, S.; Van Gaal, R.C.; Riool, M.; Zaat, S.A.J.; Dankers, P.Y.W. Antimicrobial peptide modification of biomaterials using supramolecular additives. *J. Polym. Sci. Part A: Polym. Chem.* **2018**, *56*, 1926–1934. [[CrossRef](#)]
70. Braunstein, A.; Papo, N.; Shai, Y. In Vitro Activity and Potency of an Intravenously Injected Antimicrobial Peptide and Its dl Amino Acid Analog in Mice Infected with Bacteria. *Antimicrob. Agents Chemother.* **2004**, *48*, 3127–3129. [[CrossRef](#)]
71. Papo, N.; Oren, Z.; Pag, U.; Sahl, H.-G.; Shai, Y. The Consequence of Sequence Alteration of an Amphipathic α -Helical Antimicrobial Peptide and Its Diastereomers. *J. Biol. Chem.* **2002**, *277*, 33913–33921. [[CrossRef](#)] [[PubMed](#)]
72. Chatterjee, S.; Bandyopadhyay, A.; Sarkar, K. Effect of iron oxide and gold nanoparticles on bacterial growth leading towards biological application. *J. Nanobiotechnol.* **2011**, *9*, 34. [[CrossRef](#)] [[PubMed](#)]
73. Arakha, M.; Pal, S.; Samantarai, D.; Panigrahi, T.K.; Mallick, B.C.; Pramanik, K.; Mallick, B.; Jha, S. Antimicrobial activity of iron oxide nanoparticle upon modulation of nanoparticle-bacteria interface. *Sci. Rep.* **2015**, *5*, 14813. [[CrossRef](#)]
74. Borchering, J.; Baltrusaitis, J.; Chen, H.; Stebounova, L.; Wu, C.-M.; Rubasinghege, G.; Mudunkotuwa, I.A.; Caraballo, J.C.; Zabner, J.; Grassian, V.H.; et al. Iron oxide nanoparticles induce *Pseudomonas aeruginosa* growth, induce biofilm formation, and inhibit antimicrobial peptide function. *Environ. Sci. Nano* **2014**, *1*, 123–132. [[CrossRef](#)] [[PubMed](#)]
75. Thomas, J.A.; Schnell, F.; Kaveh-Baghbaderani, Y.; Berensmeier, S.; Schwaminger, S.P. Immunomagnetic Separation of Microorganisms with Iron Oxide Nanoparticles. *Chemosensors* **2020**, *8*, 17. [[CrossRef](#)]

3.2. Silica-coated superparamagnetic iron oxide nanoparticles: New insights into the influence of coating thickness on the particle properties and lasioglossin binding

BIONs tend to agglomerate if uncontrolled, oxidize from magnetite to maghemite over time, and undergo undesired interactions. These adverse properties can be improved with a specific coating. Silica-coated IONs play an essential role in catalysis, biotechnology, and nanomedicine. The standard method by Stöber uses TEOS to generate the inorganic silica coating. Even though multiple synthesis approaches and applications for ION@TEOS exist, a complete characterization of the particle properties is missing.

This work synthesized and characterized four different ION@TEOS (0.98 Eq., 1.96 Eq., 3.91 Eq., and 7.82 Eq.). The study illustrates the significant influence of the coating thickness on particle properties and, therefore, their usability. Several analytic methods are used to analyze this effect, containing TEM, XRD, TGA, BET, DLS, SQUID, STEP, and zeta potential measurements. All ION@TEOS have a core-shell character. The investigations revealed new insights into the agglomeration behavior in different media, magnetophoresis, and surface properties in dependency on the coating thickness. Thinner coating led to smaller particle sizes, higher surface-to-volume ratio, lower IEP, and higher saturation magnetization. Though, the slowest sedimentation speed was measured for ION@TEOS0.98. The silica coating can generally prevent oxidation and improve the colloidal stability in water and PBS, making the particles an exciting material in biotechnology and nanomedicine.


This work enhances the understanding of the peptide interaction in dependence on the coating thickness. The negatively charged silica coating improves the interaction with the cationic peptide lasioglossin. Electrostatic interactions and hydrogen bonds strongly bound the peptide to the silica surface. Therefore, the loading stays constant after one washing step. ION@TEOS0.98 generated the highest LL loading of 0.23 g g⁻¹. The ION@TEOS@LL system could find applications in magnetically controlled drug delivery or in biotechnology with an LL tag. Due to the improved knowledge, ION@TEOS can be specifically designed and synthesized with different silica-thicknesses for their target application.

The doctoral candidate's substantial contribution was the study's conception and design after critically reviewing existing literature. A. Oppelt, M. Mitzkus, and the doctoral candidate carried out the experiments, data analysis, and data processing. The doctoral candidate was the leading author.



Silica-coated superparamagnetic iron oxide nanoparticles: New insights into the influence of coating thickness on the particle properties and lasioglossin binding

Chiara Turrina , Anne Oppelt, Michaela Mitzkus, and Sonja Berensmeier , Bioseparation Engineering Group, TUM School of Engineering and Design, Technical University of Munich, Boltzmannstraße 15, 85748 Garching, Germany

Sebastian P. Schwaminger , Bioseparation Engineering Group, TUM School of Engineering and Design, Technical University of Munich, Boltzmannstraße 15, 85748 Garching, Germany; Division of Medicinal Chemistry, Otto Loewi Research Center, Medical University of Graz, Neue Stiftingtalstraße 6, 8010 Graz, Austria

Address all correspondence to Sebastian P. Schwaminger at sebastian.schwaminger@medunigraz.at

(Received 28 April 2022; accepted 29 July 2022; published online: 12 August 2022)

Abstract

Silica-coated iron oxide nanoparticles are of enormous importance in biotechnology, nanomedicine, and catalysis. The study demonstrates the significant influence of the coating thickness on the particle properties. Though slow magnetophoresis, a thinner shell leads to higher surface areas, lower isoelectric points, and higher magnetizations. However, thick layers prevent oxidation and lead to stabilization. The coating thickness influenced the binding of the cationic peptide lasioglossin, with a maximal loading of 0.23 g g^{-1} for the smallest particles. This knowledge can be used to specifically design particles for usage with a cationic tag system in biotechnology or drug delivery with antimicrobial peptides.

Introduction

Iron oxide nanoparticles (IONs) can be applied in various fields: in biotechnology, they can be applied to purify proteins, peptides, and other molecules or to immobilize enzymes.^[1] In nanomedicine, they show a huge potential as contrast agents for imaging, hyperthermia, drug delivery, or cell therapy.^[2] The IONs are also in the focus of the research field of heterogeneous and homogeneous catalysis.^[1,2] Especially magnetite impresses through high biocompatibility and high magnetic saturation with superparamagnetic properties. Moreover, these particles can be produced through easy, fast, and cost-efficient synthesis methods with a small particle size distribution and a high specific surface area.^[3] Though bare IONs (BIONs) tend to agglomerate uncontrolled, oxidize over time, and undergo undesired interactions.^[4,5] Specific coatings can prevent these negative aspects and even improve the interaction with the desired target molecule. Commonly organic coatings such as dextran, alginate, polyvinyl alcohols, or inorganic silica coatings are used to stabilize the BIONs.^[4,5] ION@Silica are in the focus of research for multiple applications, from protein binding to nanomedicine (SI-Table 1). Even though various synthesis methods and applications have been analyzed before. Often a full characterization regarding the core and shell size, magnetophoretic properties, agglomeration behavior, and surface properties are missing (SI-Table 2). The Stöber-method is mainly used to generate a silica coating. This process uses the slow hydrolysis and fast condensation of tetraethyl orthosilicate (TEOS) to form a shell structure around the BIONs in controlled growth.^[3,6] The inert silica layer stabilizes the iron oxide core by shielding magnetic dipole interactions, and

the negative surface charge increases the electrostatic repulsion between particles.^[7] Moreover, the negative charge facilitates the possibility of electrostatic interaction with positively charged peptides. Antimicrobial peptides are generally short, positively charged and found in various microorganisms or animals. Examples are pexiganan, omiganan, hLF₁₋₁₁, and lasioglossin.^[8] Especially the short cationic peptide Lasio-glossin-III (LL, H-Val-Asn-Trp-Lys-Lys-Ile-Leu-Gly-Lys-Ile-Ile-Lys-Val-Val-Lys-NH₂) from the bee *Lasioglossum laticeps* is an exciting molecule as it could be used as affinity peptide tag in biotechnology or as an anticancer and antimicrobial drug in drug delivery.^[4,9] The peptide interaction with surfaces depends highly on the peptide structure and conformation and the binding conditions like pH, temperature, and salt concentration.^[10] LL is an α -helical pentadecapeptide with a hydrophilic and a hydrophobic side. The five lysine residues give a strong positive character.^[9] Guo et al. have analyzed the interaction of fumed silica nanoparticles and L-lysine. They demonstrate a strong hydrogen bonding between the amine groups of lysine and the hydroxy groups on the silica surface. Especially at high salt concentrations the potential of the amino acid to form a monolayer on the silica surface rises.^[11]

To apply silica-coated IONs in biotechnology or nanomedicine with antimicrobial peptides, it is of central interest to improve the understanding of the peptide interaction that highly depends on the particle properties. In this work, different silica-coated IONs, synthesized with varying amounts of TEOS (0.98 Eq., 1.96 Eq., 3.91 Eq., and 7.82 Eq.) are analyzed regarding their particle composition with Fourier-transform infrared spectra (FT-IR), thermogravimetric analysis (TGA),

and X-ray diffraction (XRD). The influence on the thickness of the silica layer on the surface properties is analyzed by zeta potential and Brunauer, Emmett, Teller (BET) method. The particle size distribution is determined with transmission electron microscopy (TEM) and dynamic light scattering (DLS). With this, specifically, the influence of phosphate-buffered saline (PBS) on the agglomeration behavior is analyzed. The behavior of the IONs@TEOS in a magnetic field is investigated by the superconducting quantum interference device (SQUID) magnetometer and space and time-resolved extinction profiles (STEP) technology. The particle properties are highly dependent on the silica layer, influenced by the variation of TEOS equivalents. The knowledge about these differences is used to give a better understanding of the LL binding. The adsorption is analyzed in PBS buffer at different peptide concentrations, giving insights into the cationic peptide binding on the silica surface.

Materials and methods

Synthesis of IONs@TEOS

The BIONs are synthesized by co-precipitation analogously to a previous paper by Turrina et al.^[4] The silica coating is prepared by the Massart process, similar to the prescription by Zanker et al.^[12] Four mmol of bare IONs are dispersed in 180 mL of a citric acid solution (AppliChem GmbH, 2.00 g, 10.4 mmol). The stabilized particles are ultrasonicated to ensure homogeneity. A neutral pH is generated by titration with 25 wt% tetramethylammonium hydroxide (Sigma-Aldrich). Under a nitrogen atmosphere, the particle suspension is mixed with absolute EtOH (VWR, 2.72 L), bi-distilled water (720 mL), ammonium hydroxide (Sigma-Aldrich, 180 mL), and different amounts of tetraethyl orthosilicate (Sigma-Aldrich, ION@TEOS0.98, 0.87 mL, 3.89 mmol, 0.98 Eq.; ION@TEOS1.96, 1.74 mL, 7.78 mmol, 1.96 Eq.; ION@TEOS3.91, 3.47 mL, 15.6 mmol, 3.91 Eq.; ION@TEOS7.82, 6.94 mL, 31.1 mmol, 7.82 Eq.) in a 4-L round bottom flask. In an ultrasonic bath, the suspension is sonicated for 1 h at 0°C. The IONs@TEOS are washed by magnetic decantation and centrifugation (4000 rpm, 15 min) to a neutral pH with EtOH. Subsequently, the particles are washed several times with bi-distilled, degassed water until the conductivity drops below 200 $\mu\text{S cm}^{-1}$. The silica-coated IONs are stored under a nitrogen atmosphere at 4°C.

Characterization

The SQUID magnetometer MPMS XL-7 (Quantum Design) is used to measure the magnetization of the IONs. 10 mg of a sample are glued in the middle of a small plastic tube (Fixogum) and analyzed at 300 K and a magnetic field variation between ± 50 kOe. The FT-IR spectra are generated by an Alpha II (Bruker Corporation, Billerica) with a platinum attenuated total reflection module. For each sample, 3 μL ($> 1.00 \text{ g L}^{-1}$) spectra between the wavenumber range of 4000–400 cm^{-1} (24 scans) are measured. With the software OPUS8.1, the background is subtracted by the concave rubber band method. The spectra

are normalized to the vibration corresponding to magnetite ($\sim 570 \text{ cm}^{-1}$). The BET method is used to determine the specific surface area of the IONs with the Gemini VII, Micromeritics Instrument Corp. (software Gemini VII version 2.00) at 77 K. The nitrogen adsorption isotherms are generated between 0.05 and 0.30 mPa. The diffractometer STOE Stadi-P Diffractometer with a molybdenum source (0.7093 Å, $l=0$) is used for flatbed XRD of freeze-dried IONs (Alpha 1–2 Ldplus, Christ, -60°C overnight in vacuum). To determine the silica content, TGA is applied on STA 449C Jupiter of freeze-dried IONs (50 μL aluminum oxide jar) over a temperature range between 25 and 700°C (constant for 10 min). For TEM 10 μL of a 0.02 g L^{-1} ION solution are dried on a carbon-coated copper grid that has been glow discharged. The device JEM JEOL 1400 plus is used for creating images in $\times 100\text{k}–120\text{k}$ magnification. The images are analyzed with the software ImageJ to measure at least 90 different particles in three other areas. The Zetasizer Ultra (Malvern Panalytical) is used to determine the zeta potential (flow cell, DTS1070, Malvern Instruments) and hydrodynamic diameters by DLS (Cuvette STD UV clear side, KARTELL S.p.a). A 1 g L^{-1} solution (25°C) is used for all measurements. The isoelectric point is determined via Boltzmann fit. The LUMiReader (4532–123, LUM GmbH; for STEP measurements) is used to analyze the sedimentation rate of the IONs under a magnetic field (five stacked cylindrical neodymium boron ferrite magnets ($d=12 \text{ mm}$, $h=2 \text{ mm}$, N45, Webcraft GmbH, magnetization between 29.1 and 54.4 $\text{Am}^2 \text{ kg}^{-1}$). The measurements take place at the wavelength 870 nm (profile: 700, 300; interval: 0 s, 1 s, angle 0° , light factor 1.00, temperature 25°C). The data is processed with the software PSA-Wizard (SEP view™, Analysis positions: 12.3 mm, 15.0 mm, 16.9 mm, and 18.7 mm).

Peptide binding

The electrostatic binding of LL (Genscript, Netherlands) is tested in triplicates. 250 μL of a 2.00 g L^{-1} ION@TEOS solution in 50 mM PBS at pH 7.4 is mixed (1:1) with 250 μL LL concentration (4.00 g L^{-1} , 2.00 g L^{-1} , 1.00 g L^{-1} , 0.50 g L^{-1} , 0.20 g L^{-1} , 0.10 g L^{-1} , 0.05 g L^{-1} , 0.00 g L^{-1}) in 50 mM PBS at pH 7.4. The suspensions are incubated at 25°C (1000 rpm) for 1 h. After magnetic decantation, the clear supernatant is removed and measured at 280 nm (Tecan, Magellan-Data 7). The particles are resuspended in a fresh buffer for the washing steps and incubated for 10 min (25°C, 1000 rpm). Each supernatant is analyzed, and the LL content is calculated via a calibration line.^[4]

Results and discussion

Particle characterization

The silica-coated IONs are synthesized with four different equivalents of TEOS (0.98 Eq., 1.96 Eq., 3.91 Eq., and 7.82 Eq.) to generate four different thicknesses of coating. All IONs@TEOS and BIONs, for comparison, are analyzed regarding their composition, particle size, surface properties, and magnetization. The different coating properties influence

the adsorption of the cationic peptide LL. The BIONs used as base material show comparable characteristics to previous measurements of BIONs (Figs. 1 and 2).^[4,13] The diameter is 8.25 nm determined with TEM and 9.00 nm calculated with

the Scherrer equation of XRD data (Table I, SI-Table 4), the BET surface is 103 m² g⁻¹ (Table I), and the magnetization is 64.9 emu g⁻¹ [Fig. 1(d)].

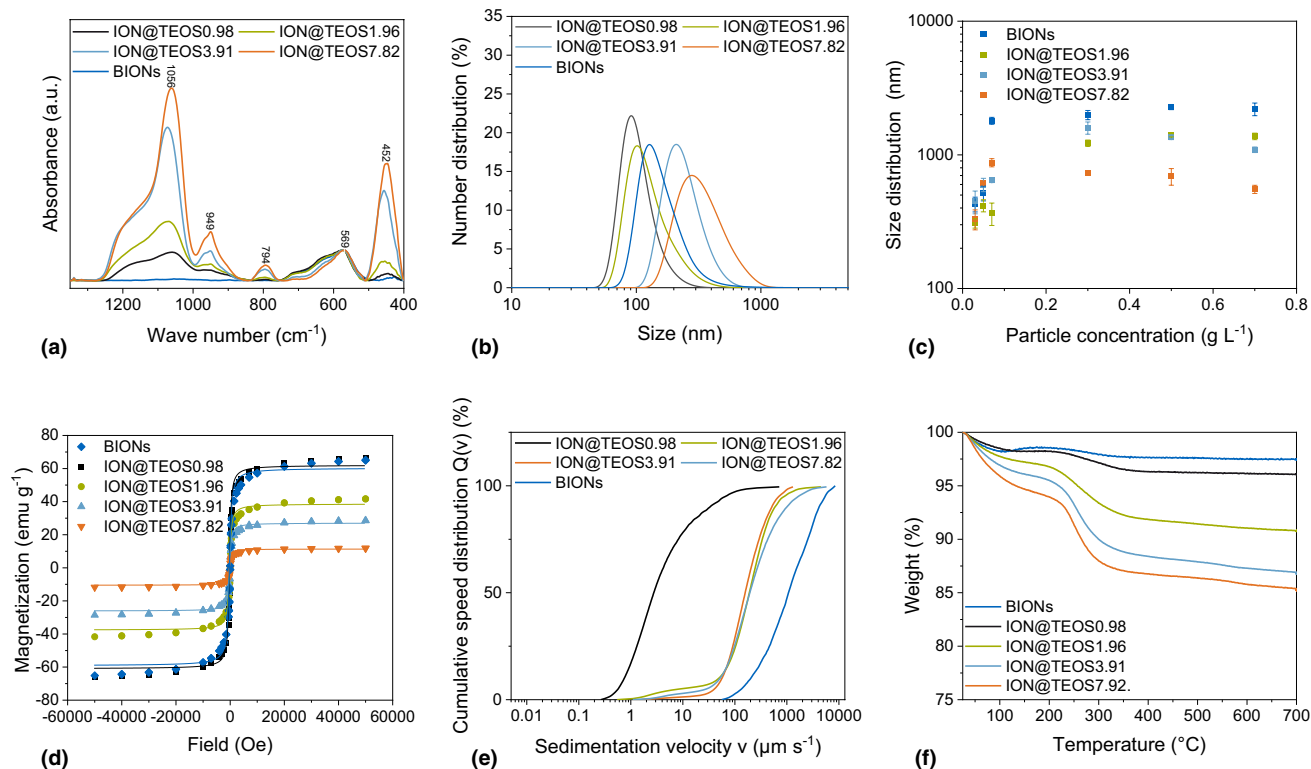


Figure 1. Comparison of different IONs@TEOS with BIONs by (a) IR spectra normalized on the magnetite peak (~570 nm), (b) size distribution by number at 25°C in water for a 1 g L⁻¹ solution at pH 7, and (c) in 50 mM PBS buffer (pH 7.4), (d) magnetization fitted with LangevinMod, (e) cumulative speed distribution in contact with a magnetic field in water, and (f) TGA curves until 700°C.

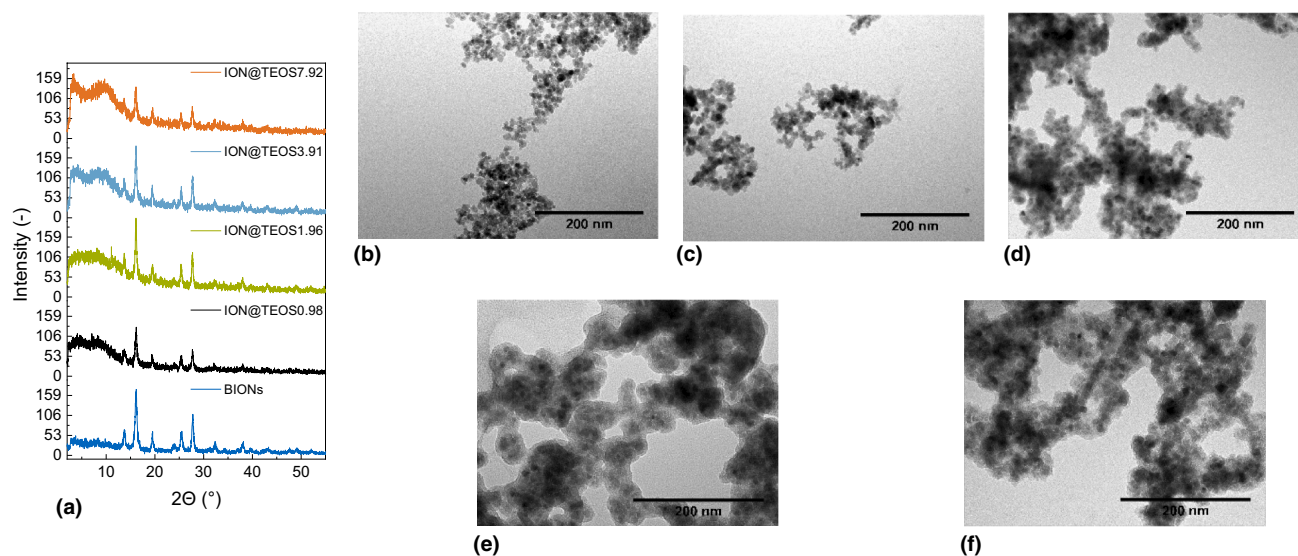


Figure 2. XRD diffractograms (a) and TEM images of (b) BIONs (100 k), (c) ION@TEOS0.98 (100 k), (d) ION@TEOS1.96 (100 k), (e) ION@TEOS3.91 (120 k), (f) and ION@TEOS7.82 (120 k).

Table I. The particle's diameter and hydrodynamic diameter measured with TEM, XRD, and DLS, the IEP, BET area, and the weight loss during TGA.

Particles	TEM (nm)	XRD Scherrer (nm)	DLS (nm)	IEP	BET (m ² g ⁻¹)	TGA silica amount (%)
BIONs	8.25±0.16	9.00±1.77	153±21.5	7.98 [4]	103±0.36	
ION@TEOS0.98	8.67±0.36	8.83±1.03	88.2±22.7	1.87	115±0.65	1.38
ION@TEOS1.96	12.0±0.13	8.96±0.87	125±17.8	3.77	50.6±0.77	6.74
ION@TEOS3.91	22.7±0.07	8.99±0.82	223±4.33	4.20	27.9±0.38	10.7
ION@TEOS7.82	31.3±3.92	7.68±0.91	329±19.9	4.17	23.2±0.13	12.3

The IEP of BIONs is used from a previous publication by Turrina et al.^[4]

Furthermore, via IR spectroscopy, the typical Fe–O stretching vibration at ~570 cm⁻¹ is visible [Fig. 1(a)], and the XRD diffractogram shows the iron oxide reflections [(220), (311), (400), (511), and (440)] exemplary for magnetite or maghemite [Fig. 2(a)].^[14–16]

Particle composition

The compositions of the IONs@TEOS are determined with IR, TGA, and XRD measurements. The successful silica coating is examined with FT-IR spectroscopy [Fig. 1(a)]. In addition to the magnetite peak at 570 cm⁻¹, all IONs@TEOS show the Si–O rocking vibration at 452 cm⁻¹, the Si–O bending vibrations at 794 cm⁻¹, the Si–OH bond at 949 cm⁻¹, and the Si–O–Si stretching vibrations at 1058 cm⁻¹.^[17] The intensity of the typical silica peaks rises with the higher used TEOS amounts, showing the thickest coating for ION@TEOS7.82. The thermal stability based on TGA gives information about the silica amount of each particle [Fig. 1(e)]. The BIONs exhibit high thermal stability with an overall mass loss of 2.52%. This behavior is based on the melting point of magnetite, which is 1538°C.^[18] To calculate the amount of bound silica, the difference between the residual weight of each particle and the BIONs is used. The curve shapes of all IONs@TEOS are comparable. The first weight loss below 200°C can be explained by the evaporation of adsorbed water and ethanol.^[19] Between 200 and 350°C, the degradation of the silica layer takes place.^[20] The slope gets steeper with higher amounts of silica degrading. After the complete silica degradation, the course of the curve stays constant. The amount of bound silica varies between 1.38 and 12.3%, depending on the TEOS equivalents. By XRD measurements of all IONs@TEOS, the characteristic iron oxide reflexes are visible, which means that the coating is not influencing the crystal structure [Fig. 2(a)]. Additionally, the diffractograms show a typical hump of the amorphous silica between 2° and 10°, which increases with the used TEOS amount.^[21] The diameter of the magnetic core can be calculated by the Scherrer equation (Table I, SI-Table 4, SI-Eq. 1). All IONs@TEOS show comparable diameters to the BIONs around 9.00 nm, except the ION@TEOS7.82 with 7.68 nm. The lattice constants are not influenced by the coating (SI-Table 2). The deviation can be explained by the thick layer shielding the magnetic core, leading to a higher signal-to-noise ratio. The

silica coating does not modify the iron oxide core. All three analytical methods show that the generated particles have a crystalline iron oxide core surrounded by a silica layer which size varies with the used TEOS equivalents.

Surface properties

The surface properties are determined by zeta potential and BET measurements (Table I, SI-Fig. 2). The specific surface area of ION@TEOS0.89 of 115 m² g⁻¹ (ION@TEOS0.98) is comparable to BIONs of around 100 m² g⁻¹.^[4] Here, the effect of silica coating is comparably thin and does not influence the surface significantly. However, rising TEOS equivalents, which means thicker silica coating, lead to a decrease of the BET surface to 23.2 m² g⁻¹ (ION@TEOS7.82). This effect is similar to previous studies by Mendonca et al.^[22] The particles size consequently lowers the specific surface area. This effect highly influences the amount of free reactive groups on the particle surface. The silica surface exists of siloxane groups (Si–O–Si) that can form through dissociative chemisorption silanol groups (Si–OH) that can create depending on the pH deprotonated hydroxy groups (Si–O⁻).^[23] Since the surface area of the smaller IONs@TEOS is bigger than the thicker ones, the ION@TEOS0.98 have the most deprotonated hydroxy groups compared to the other particles. Zeta potential measurements determine the IEP electric point. It shows comparable values for ION@TEOS7.82 and ION@TEOS3.91 at around pH 4.20, while the thinner coatings lead to lower IEP until 1.87 for ION@TEOS0.98 (Fig. 1 Table, SI Fig. 1). These values fit into the range of previously synthesized magnetic silica particles that had an IEP between 1.0 and 4.50.^[23,24] The IEP of BIONs lies between 7.00 and 8.40 depending on the oxidation state from magnetite to maghemite.^[4,13] The curious behavior that lower TEOS equivalents lead to lower IEP could be explained by the fact that these particles have a higher specific surface area and smaller agglomerates, with more silanol groups on the surface that can be ionized. This trend is a sign of a consistent silica coating, not showing the magnetite surface.

Particle size distribution

The particle size is influenced by the thickness of the coating and the agglomeration behavior. Therefore, all IONs@TEOS are analyzed by TEM and DLS. TEM images of the particles

clearly show a core–shell structure for ION@TEOS1.96 until 7.82 [Fig. 2(d–f)]. Therefore, the iron oxide core is visible as a dark crystal surrounded by lighter silica. Only for ION@TEOS0.98 [Fig. 2(c)], the silica shell is not visible because it is too thin. The size difference with a diameter of 8.67 nm to BIONs (8.25 nm) is only 0.42 nm (Fig. 1, Table I). Higher equivalents of TEOS lead to a particle size between 12.0 and 31.3 nm. That means the ION@TEOS1.96 have a 3.75 nm, the ION@TEOS3.91 a 14.5 nm, and the ION@TEOS7.82 a 23.1 nm thick silica shell.

It is well known that the TEM diameters vary from the hydrodynamic diameters depending on the medium and pH. In water at pH 7 (around the IEP), the BIONs tend to agglomerate. Therefore, DLS measurements show a hydrodynamic diameter of around 150 nm.^[4] The IONs@TEOS diameters between 88.2 and 329 nm are measured, rising with the silica thickness. If the TEM diameter is used to calculate the number of particles for an average agglomerate, this leads to a number of 18.5 BIONs. For all IONs@TEOS, this value lowers to only ~10.2 particles. Therefore, all IONs@TEOS show the same amount of stabilization toward the BIONs, indicating a comparable continuous silica surface. That different TEOS equivalents form uniform homogenous silica coatings has already been shown by Lu et al.^[25] In 50 mM PBS, agglomeration behavior is very different in comparison to deionized water. As shown in other publications, BIONs possess high hydrodynamic diameters of more than one micrometer in PBS buffer.^[4] This effect can be explained by free potassium and sodium ions that could interact with the free hydroxy groups on the BION surface and therefore balance the surface loading.^[26] Figure 1(c) shows that this behavior is highly dependent on the particle concentration. High BIONs concentrations between 0.07 and 0.70 g L⁻¹ show a comparable diameter of around 2 μm. While for lower concentrations such as 0.05 g L⁻¹ or 0.03 g L⁻¹, the particles form smaller agglomerates, smaller than 1 μm (518 nm and 428 nm). Even for the lowest concentration, the aggregation is 2.85 times higher than in water, with an average amount of 51.9 nm. The silica coating shows an apparent stabilization leading to less agglomeration with a thicker layer. ION@TEOS1.96 and ION@TEOS3.91 show a similar behavior at the concentrations 0.3 to 0.7 g L⁻¹ with an average diameter of 1327 nm. ION@TEOS7.82 builds the smallest agglomerates at these particle concentrations of around 657 nm. This is a factor of only 2.00 times as high as in water. The lowest ION@TEOS7.82 concentrations of 0.03 g L⁻¹ even show comparable agglomeration to water with a hydrodynamic diameter of 331 nm. In summary, the particle size increases with a thicker silica coating, and the silica coating leads to the formation of smaller agglomerates in water and PBS buffer.

Behavior in a magnetic field

The magnetization of all particles is determined by SQUID measurements, and further magnetic sedimentation is analyzed in water by STEP technology. As XRD experiments have shown, all particles, BIONs, and IONs@TEOS, have

the same iron oxide core. It is typical for magnetite to show a superparamagnetic behavior, which means that the particles have no hysteresis and are only magnetic in the existence of an external magnetic field.^[27] The BIONs and IONs@TEOS show the characteristic sigmoidal curve [Fig. 1(d)]. Though, with a thinner coating, the ION@TEOS and especially the BIONs experience a higher slope from the ideal curve shape simulated by the LangevinMod fit, starting with the magnetic field of around ±20 kOe. If magnetite oxidates to maghemite, the paramagnetic content rises, explaining the curve variation.^[28] That effect means that the increasing thickness of the silica coating leads to preventing the magnetite core from oxidation. The coating shields the magnetic core; thus, the magnetization decreases from ION@TEOS0.98 from a maximal magnetization of 66 emu g⁻¹, comparable to the BIONs, to 11.8 emu g⁻¹ for ION@TEOS7.82. In solution, the magnetic behavior is not only influenced by the magnetization. The STEP technology is used to analyze the sedimentation under magnetophoresis in water. Figure 1(e) shows the cumulative speed distribution dependent on the sedimentation speed. Contacted with a magnetic field, the BIONs sediment the fastest. The comparably high magnetization and agglomeration can explain this behavior. The ION@TEOS7.82, ION@TEOS3.91, and ION@TEOS1.96 have a similar sedimentation speed distribution, which is notably lower than the one of the BIONs. ION@TEOS0.98 is sedimenting even slower, ~291 times slower than the BIONs (SI-Table 2). The measured sedimentation speed is contrary to the magnetization of the silica-coated particles. In water, the IONs@TEOS form agglomerates with the same amount of particles, so this factor can be neglected. However, the sedimentation behavior of the BIONs and the IONs@TEOS is influenced by a significant difference: The surface is covered in silanol groups that lead to electrostatic stabilization. The particles are repelled by each other because of their dissociating behavior.^[29] The amount of silanol groups rises with a higher specific surface area. This explains the slowest sedimentation of ION@TEOS0.98 in the magnetic field. All in all, the IONs@TEOS have a core–shell structure. The rising thickness of the silica coating leads to bigger particles and, therefore, lower specific surface area, less magnetization, higher IEP, and better electrostatic repulsion. The silica shell prevents the particles from oxidation and leads to a better stabilization in water and PBS buffer. All these characteristics majorly influence the applicability of the different IONs@TEOS.

Performance of ION@TEOS for electrostatic peptide binding

All IONs@TEOS are predominantly negatively charged at pH 7.4 regarding their IEPs. The peptide LL has five lysine residues which mainly influence its cationic character. Between its two pK values of pK₁ 2.2 and pK₂ 9.2, lysine is in the form H₂Lys⁺.^[30] Previous binding experiments of LL with BIONs have shown the best electrostatic interaction in 50 mM PBS buffer (pH 7.4), due to its pH stabilization, increase in ionic strength, and phosphate ion linkage between the mainly

positive charged BION surface and the LL. As a result, 0.55 g g^{-1} of LL was adsorbed, but each washing step led to a loss of an average of 35% of the bound peptide. For example, only 0.23 g g^{-1} was left after three washing steps.^[4] Adsorption experiments of all IONs@TEOS in 50 mM PBS buffer at pH 7.4 are shown in Fig. 3. The loading of LL for all four particles rises with higher starting concentrations of LL up to a specific maximal loading. For ION@TEOS1.96, the effect is less visible due to the high standard deviation of the last point. As thicker the coating gets as sooner the maximal loading is reached. For example, the ION@TEOS0.98 [Fig. 3(a)] reach a constant LL loading from a peptide starting concentration of 0.5 g L^{-1} , while ION@TEOS7.82 [Fig. 3(d)] experiences the saturation already at 0.1 g L^{-1} of the peptide. The maximal loading decreases from 0.28 g g^{-1} at an equilibrium concentration of 1.70 g L^{-1} of ION@TEOS0.98 to 0.10 g g^{-1} at 1.89 g L^{-1} of ION@TEOS7.82 with the increasing silica thickness. The higher specific surface area can explain this trend, and with this, the higher number of reactive silanol groups on the surface for the ION@TEOS with a thinner silica layer. The stabilizing effect of silica on the agglomeration in PBS does not outweigh this behavior. On the contrary, to the BIONs, the bound LL is not washed away continuously with every washing step.^[4] The first washing step removes LL bound to the electrochemical double layer, while the peptide loading stays constant after a second washing step for all four IONs@

TEOS. That behavior demonstrates that LL is bound stronger to the silica surface than to the bare iron oxide surface because of the different IEPs. Furthermore, the five lysines of LL can form hydrogen bonds with the silanol groups.^[11] In Fig. 3(e) the ION@TEOS are compared after the second washing step. The highest reached peptide loading is 0.23 g g^{-1} for ION@TEOS0.98, 0.21 g g^{-1} for ION@TEOS1.96, 0.12 g g^{-1} for ION@TEOS3.91, and 0.07 g g^{-1} for ION@TEOS7.82 after washing. The loading of ION@TEOS0.98 is comparable to the one of BIONs after three washing steps. Still, it shows a more robust and more efficient electrostatic binding because the loading will stay constant with further washing steps.^[4]

Conclusion

Four different silica-coated nanoparticles have been successfully synthesized. All ION@TEOS have a core-shell character. The characterization of the particles gave new insights into the agglomeration behavior, magnetophoresis, and surface properties depending on the diameter of the silica layer. The thickness of the silica layer influences the particle composition, size, agglomeration, magnetization, and surface properties. ION@TEOS0.98, the particles with the thinnest coating, showed the smallest particle size, highest specific surface area, lowest IEP, and highest magnetization.

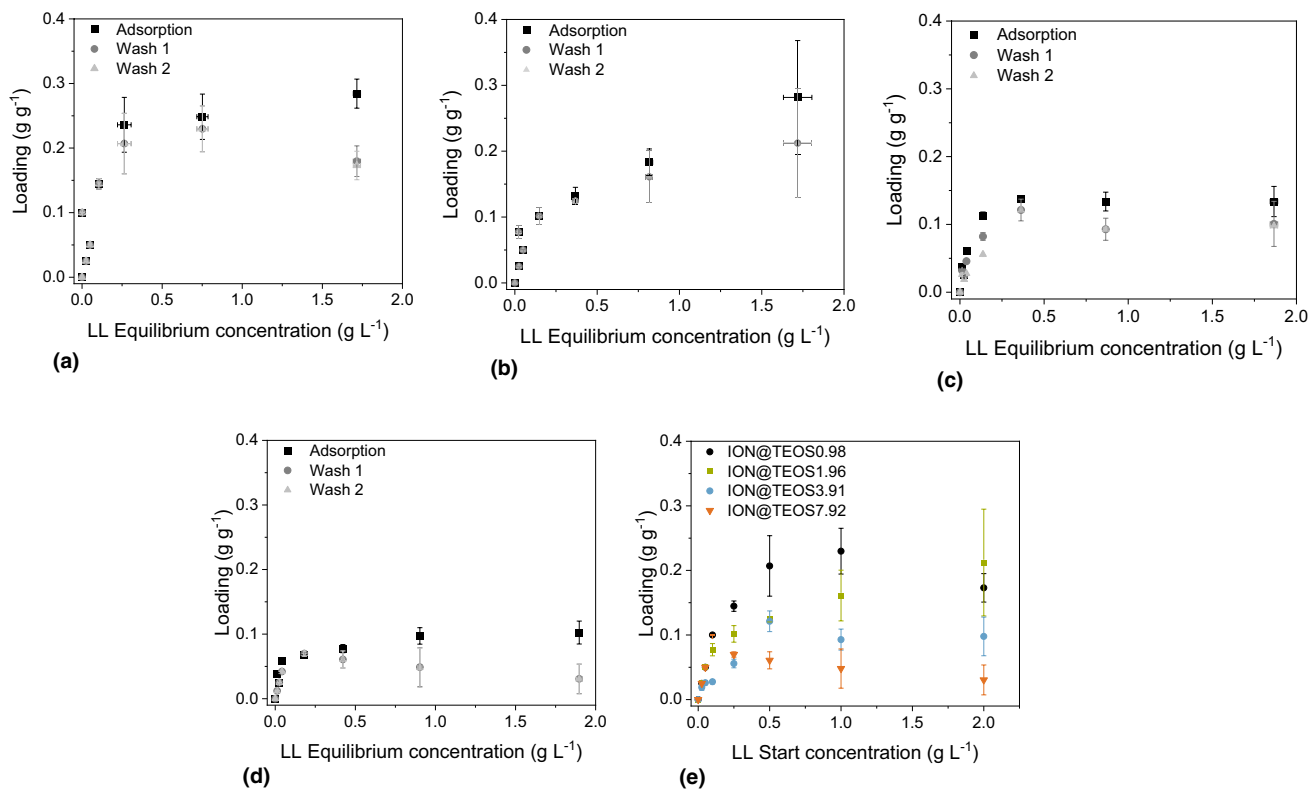


Figure 3. Adsorption isotherms of the electrostatic interaction of LL and (a) ION@TEOS0.98, (b) ION@TEOS1.96, (c) ION@TEOS3.91, and (d) ION@TEOS.7.82. (e) Comparison of the LL loading depending on the particle species and the peptide starting concentration.

However, these particles also experienced the slowest sedimentation speed in a magnetic field. The silica coating, in general, can prevent the oxidation of the magnetite core and leads to the formation of smaller agglomerates in water and PBS buffer. Significantly, the ION@TEOS7.82 showed the lowest aggregation in buffer due to its thick silica coating. The stabilization and protection of silica make the ION@TEOS an exciting material for multiple applications in biotechnology and nanomedicine.

All four particles bind the cationic peptide LL by strong electrostatic interactions and hydrogen bonds. The peptide loading stays constant after one washing step. The highest LL loading of 0.23 g g^{-1} was reached with ION@TEOS0.98. The silica-coated IONs are a promising material for adsorbing cationic, antimicrobial peptides in general and specific to LL, which could also be used as a tag. These facts give them a huge potential for application in nanomedicine and biotechnology. Depending on their potential applications, the IONs@TEOS can be specifically designed and synthesized with different coating thicknesses. In combination with LL or other short positively charged drugs, IONs@TEOS could be used in cancer therapy as a magnetically controlled drug delivery system.

Acknowledgments

We are thankful for the support with TEM imaging of Carsten Peters, for Tom Nilges to provide the X-ray diffractometer, and for the help of Matthias Opel with SQUID measurements.

Author contributions

CT: conceptualization, methodology, validation, formal analysis, investigation, data curation, writing—original draft, visualization; AO: investigation, data curation, visualization; MM: investigation, data curation, SB: resources, funding acquisition, writing—review & editing, supervision; SS: conceptualization, funding acquisition, writing—review & editing, supervision, project administration.

Funding

We appreciate the support from TUM International Graduate School of Science and Engineering (IGSSE). The funders had no role in the design of the study, the collection, analysis, and interpretation of data, in the writing of the manuscript, or in the decision to publish the results.

Data availability

The datasets generated and/or analyzed during this study are available from the corresponding author on reasonable request.

Declarations

Conflict of interest

The authors declare no conflict of interest.

Open Access

This article is licensed under a Creative Commons Attribution 4.0 International License, which permits use, sharing, adaptation, distribution and reproduction in any medium or format, as long as you give appropriate credit to the original author(s) and the source, provide a link to the Creative Commons licence, and indicate if changes were made. The images or other third party material in this article are included in the article's Creative Commons licence, unless indicated otherwise in a credit line to the material. If material is not included in the article's Creative Commons licence and your intended use is not permitted by statutory regulation or exceeds the permitted use, you will need to obtain permission directly from the copyright holder. To view a copy of this licence, visit <http://creativecommons.org/licenses/by/4.0/>.

Supplementary Information

The online version contains supplementary material available at <https://doi.org/10.1557/s43579-022-00228-y>.

References

1. L.S. Ganapathe, M.A. Mohamed, R. Mohamad Yunus, D.D. Berhanuddin, Magnetite (Fe_3O_4) nanoparticles in biomedical application: from synthesis to surface functionalisation. *Magnetochemistry* **6**, 68 (2020). <https://doi.org/10.3390/magnetochemistry6040068>
2. I. Khan, K. Saeed, I. Khan, Nanoparticles: properties, applications and toxicities. *Arab. J. Chem.* **12**, 908–931 (2019). <https://doi.org/10.1016/j.arabjc.2017.05.011>
3. A.-H. Lu, E.L. Salabas, F. Schüth, Magnetic nanoparticles: synthesis, protection, functionalization, and application. *Angew. Chem. Int. Ed.* **46**, 1222–1244 (2007). <https://doi.org/10.1002/anie.200602866>
4. C. Turrina, S. Berensmeier, S.P. Schwaminger, Bare iron oxide nanoparticles as drug delivery carrier for the short cationic peptide lasioglossin. *Pharmaceuticals (Basel)* (2021). <https://doi.org/10.3390/ph14050405>
5. S.P. Schwaminger, K. Schwarzenberger, J. Gatzemeier, Z. Lei, K. Eckert, Magnetically induced aggregation of iron oxide nanoparticles for carrier flotation strategies. *ACS Appl. Mater. Interfaces* **13**, 20830–20844 (2021). <https://doi.org/10.1021/acsmi.1c02919>
6. W. Stöber, A. Fink, E. Bohn, Controlled growth of monodisperse silica spheres in the micron size range. *J. Colloid Interface Sci.* **26**, 62–69 (1968). [https://doi.org/10.1016/0021-9797\(68\)90272-5](https://doi.org/10.1016/0021-9797(68)90272-5)
7. S. Laurent, D. Forge, M. Port, A. Roch, C. Robic, L. Vander Elst, R.N. Muller, Magnetic iron oxide nanoparticles: synthesis, stabilization, vectorization, physicochemical characterizations, and biological applications. *Chem. Rev.* **108**, 2064–2110 (2008). <https://doi.org/10.1021/cr068445e>
8. M. Mahlapuu, J. Håkansson, L. Ringstad, C. Björn, Antimicrobial peptides: an emerging category of therapeutic agents. *Front. Cell. Infect. Microbiol.* **6**, 194 (2016). <https://doi.org/10.3389/fcimb.2016.00194>
9. V. Cerovský, M. Budesinský, O. Hovorka, J. Cvacka, Z. Voburka, J. Slaninová, L. Borovicková, V. Fucík, L. Bednářová, I. Votruba, J. Straka, Lasiglossins: three novel antimicrobial peptides from the venom of the

- eusocial bee *Lasioglossum laticeps* (Hymenoptera: Halictidae). *ChemBioChem* (2009). <https://doi.org/10.1002/cbic.200900133>
10. S.A. Blank-Shim, S.P. Schwaminger, M. Borkowska-Panek, P. Anand, P. Yamin, P. Fraga-García, K. Fink, W. Wenzel, S. Berensmeier, Binding patterns of homo-peptides on bare magnetic nanoparticles: insights into environmental dependence. *Sci. Rep.* **7**, 14047 (2017). <https://doi.org/10.1038/s41598-017-13928-6>
 11. C. Guo, G.P. Holland, Investigating lysine adsorption on fumed silica nanoparticles. *J. Phys. Chem. C* **118**, 25792–25801 (2014). <https://doi.org/10.1021/jp508627h>
 12. A.A. Zanker, P. Stargardt, S.C. Kurzbach, C. Turrina, J. Mairhofer, S.P. Schwaminger, S. Berensmeier, Direct capture and selective elution of a secreted polyglutamate-tagged nanobody using bare magnetic nanoparticles. *Biotechnol. J.* (2022). <https://doi.org/10.1002/biot.202100577>
 13. S.P. Schwaminger, D. Bauer, P. Fraga-García, F.E. Wagner, S. Berensmeier, Oxidation of magnetite nanoparticles: impact on surface and crystal properties. *Cryst. Eng. Comm.* **19**, 246–255 (2017). <https://doi.org/10.1039/C6CE02421A>
 14. A.K. Bordbar, A.A. Rastegari, R. Amiri, E. Ranjbakhsh, M. Abbasi, A.R. Khosropour, Characterization of modified magnetite nanoparticles for albumin immobilization. *Biotechnol. Res. Int.* **2014**, 705068 (2014). <https://doi.org/10.1155/2014/705068>
 15. Sigma Aldrich, IR Spectrum Table & Chart. <https://www.sigmaaldrich.com/technical-documents/articles/>. Accessed 7 Apr 2022
 16. G. Dodi, D. Hritcu, D. Draganescu, M.I. Popa, Iron oxide nanoparticles for magnetically assisted patterned coatings. *J. Magn. Mater.* **388**, 49–58 (2015). <https://doi.org/10.1016/j.jmmm.2015.04.011>
 17. H. Moghanian, M.A.B. Fard, A. Mobinikhaledi, N. Ahadi, Bis(p-sulfoanilino) triazine-functionalized silica-coated magnetite nanoparticles as an efficient and magnetically reusable nano-catalyst for Biginelli-type reaction. *Res. Chem. Intermed.* **44**, 4083–4101 (2018). <https://doi.org/10.1007/s11164-018-3357-5>
 18. C.C. Wu, T.O. Mason, Thermopower measurement of cation distribution in magnetite. *J. Am. Ceram. Soc.* **64**, 520–522 (1981). <https://doi.org/10.1111/j.1151-2916.1981.tb10317.x>
 19. R. Chadha, P. Arora, A. Saini, D.S. Jain, Solvated crystalline forms of nevirapine: thermoanalytical and spectroscopic studies. *AAPS PharmSciTech* **11**, 1328–1339 (2010). <https://doi.org/10.1208/s12249-010-9511-z>
 20. J. Azadmanjiri, G.P. Simon, K. Suzuki, C. Selomulya, J.D. Cashion, Phase reduction of coated maghemite (γ -Fe₂O₃) nanoparticles under microwave-induced plasma heating for rapid heat treatment. *J. Mater. Chem.* **22**, 617–625 (2012). <https://doi.org/10.1039/C1JM12524A>
 21. A. Taufiq, A. Nikmah, A. Hidayat, S. Sunaryono, N. Mufti, N. Hidayat, H. Susanto, Synthesis of magnetite/silica nanocomposites from natural sand to create a drug delivery vehicle. *Heliyon* **6**, e03784 (2020). <https://doi.org/10.1016/j.heliyon.2020.e03784>
 22. E.S.D.T. de Mendonça, A.C.B. de Faria, S.C.L. Dias, F.F.H. Aragón, J.C. Mantilla, J.A.H. Coaquira, J.A. Dias, Effects of silica coating on the magnetic properties of magnetite nanoparticles. *Surf. Interfaces* **14**, 34–43 (2019). <https://doi.org/10.1016/j.surfin.2018.11.005>
 23. S.E. Favela-Camacho, E.J. Samaniego-Benítez, A. Godínez-García, L.M. Avilés-Arellano, J.F. Pérez-Robles, How to decrease the agglomeration of magnetite nanoparticles and increase their stability using surface properties. *Colloids Surf. A* **574**, 29–35 (2019). <https://doi.org/10.1016/j.colsurfa.2019.04.016>
 24. K. Gdula, A. Dąbrowski, E. Skwarek, Synthesis, surface characterization and electrokinetic properties of colloidal silica nanoparticles with magnetic core. *Adsorption* **22**, 681–688 (2016). <https://doi.org/10.1007/s10450-015-9755-8>
 25. Y. Lu, Y. Yin, B.T. Mayers, Y. Xia, Modifying the surface properties of superparamagnetic iron oxide nanoparticles through a sol–gel approach. *Nano Lett.* **2**, 183–186 (2002). <https://doi.org/10.1021/nl015681q>
 26. J. Lin, Y. Zhao, Y. Zhan, Y. Wang, Influence of coexisting calcium and magnesium ions on phosphate adsorption onto hydrous iron oxide. *Environ. Sci. Pollut. Res.* **27**, 11303–11319 (2020). <https://doi.org/10.1007/s11356-020-07676-w>
 27. K.N. Koo, A.F. Ismail, M.H.D. Othman, N. Bidin, M.A. Rahman, Preparation and characterization of superparamagnetic magnetite (Fe₃O₄) nanoparticles: a short review. *Malays. J. Fundam. Appl. Sci.* **15**, 23–31 (2019). <https://doi.org/10.11113/mjfas.v15n2019.1224>
 28. M.C. Mascolo, Y. Pei, T.A. Ring, Room temperature co-precipitation synthesis of magnetite nanoparticles in a large pH window with different bases. *Materials (Basel)* **6**, 5549–5567 (2013). <https://doi.org/10.3390/ma6125549>
 29. I.A. Bakhteeva, I.V. Medvedeva, M.A. Uimin, I.V. Byzov, S.V. Zhakov, A.E. Yermakov, N.N. Shchegoleva, Magnetic sedimentation and aggregation of Fe₃O₄@SiO₂ nanoparticles in water medium. *Sep. Purif. Technol.* **159**, 35–42 (2016). <https://doi.org/10.1016/j.seppur.2015.12.043>
 30. S.P. Schwaminger, P.F. García, G.K. Merck, F.A. Bodensteiner, S. Heissler, S. Günther, S. Berensmeier, Nature of interactions of amino acids with bare magnetite nanoparticles. *J. Phys. Chem. C* **119**, 23032–23041 (2015). <https://doi.org/10.1021/acs.jpcc.5b07195>

3.3. Carboxymethyl-dextran coated superparamagnetic iron oxide nanoparticles for drug delivery: Influence of coating thickness on the particle properties

CMD is an organic coating for IONs that can improve their properties and is of great interest in nanomedicine. This study reveals new insights essential for developing a magnetically controlled drug delivery system, including particle composition surface properties, particle size and colloidal stability, magnetization, magnetophoresis, cytocompatibility, and drug activity. The focus is on the coating thickness's influence on the particle properties and binding of the antimicrobial peptide LL.

This work synthesized five different thicknesses of CMD coating (6.25 g L^{-1} , 12.5 g L^{-1} , 25.0 g L^{-1} , 125 g L^{-1} , and 250 g L^{-1}) by adding the polymer to the co-precipitation process. A complete characterization was done, including FT-IR, TEM, HAADF-STEM and iDPC, DLS, Zeta potential, Raman, XRD, SQUID, STEP, and TGA. New trends regarding the impact of coating thickness in the oxidation of magnetite, the core size, the magnetophoretic behavior, and the agglomeration behavior in different media could be visualized. The particles showed good cytocompatibility with smooth muscle cells and hydrodynamic diameter $< 100 \text{ nm}$, which are essential criteria for developing a drug delivery system.

Two different binding techniques, adsorption and covalent coupling, were analyzed and compared. The covalent coupling shows superior behavior with highly efficient binding and high drug loadings of 62%. Both systems have high antimicrobial activity and complete inhibition at low concentrations.

The ION@CMD@LL system is an efficient new, cytocompatible, antimicrobial active method for potential magnetically controlled drug delivery to cancer or intracellular infections.

The doctoral candidate's substantial contributions were the study's conception and design after critically reviewing existing literature. The doctoral candidate was the leading author of the manuscript. D. Milani, A. Klassen, D. Rojas-González, J. Cookman, and the doctoral candidate carried out the experiment. D. Milani and the doctoral candidate did data analysis and processing.



Article

Carboxymethyl-Dextran-Coated Superparamagnetic Iron Oxide Nanoparticles for Drug Delivery: Influence of the Coating Thickness on the Particle Properties

Chiara Turrina ¹, Davide Milani ¹, Anna Klassen ¹, Diana M. Rojas-González ², Jennifer Cookman ³, Matthias Opel ⁴, Barbara Sartori ⁵, Petra Mela ², Sonja Berensmeier ¹ and Sebastian P. Schwaminger ^{1,6,7,*}

- ¹ Chair of Bioseparation Engineering, School of Engineering and Design, Technical University of Munich, 85748 Garching, Germany
 - ² Chair of Medical Materials and Implants, Department of Mechanical Engineering, Munich Institute of Biomedical Engineering, TUM School of Engineering and Design, Technical University of Munich, 85748 Garching, Germany
 - ³ Department of Chemical Sciences, Bernal Institute, University of Limerick, Castletroy, V94 T9PX Limerick, Ireland
 - ⁴ Walther-Meißner-Institut, Bayerische Akademie der Wissenschaften, 85748 Garching, Germany
 - ⁵ Institute of Inorganic Chemistry, Graz University of Technology, Stremayrgasse 9/IV, 8010 Graz, Austria
 - ⁶ Division of Medicinal Chemistry, Otto Loewi Research Center, Medical University of Graz, Neue Stiftingtalstraße 6, 8010 Graz, Austria
 - ⁷ BioTechMed-Graz, 8010 Graz, Austria
- * Correspondence: sebastian.schwaminger@medunigraz.at; Tel.: +43-316-3857-2125



Citation: Turrina, C.; Milani, D.; Klassen, A.; Rojas-González, D.M.; Cookman, J.; Opel, M.; Sartori, B.; Mela, P.; Berensmeier, S.; Schwaminger, S.P. Carboxymethyl-Dextran-Coated Superparamagnetic Iron Oxide Nanoparticles for Drug Delivery: Influence of the Coating Thickness on the Particle Properties. *Int. J. Mol. Sci.* **2022**, *23*, 14743. <https://doi.org/10.3390/ijms232314743>

Academic Editors: Mojtaba Falahati and Timo L. M. Ten-Hagen

Received: 8 November 2022

Accepted: 21 November 2022

Published: 25 November 2022

Publisher's Note: MDPI stays neutral with regard to jurisdictional claims in published maps and institutional affiliations.

Abstract: Carboxymethyl-dextran (CMD)-coated iron oxide nanoparticles (IONs) are of great interest in nanomedicine, especially for applications in drug delivery. To develop a magnetically controlled drug delivery system, many factors must be considered, including the composition, surface properties, size and agglomeration, magnetization, cytocompatibility, and drug activity. This study reveals how the CMD coating thickness can influence these particle properties. ION@CMD are synthesized by co-precipitation. A higher quantity of CMD leads to a thicker coating and a reduced superparamagnetic core size with decreasing magnetization. Above 12.5–25.0 g L⁻¹ of CMD, the particles are colloidally stable. All the particles show hydrodynamic diameters < 100 nm and a good cell viability in contact with smooth muscle cells, fulfilling two of the most critical characteristics of drug delivery systems. New insights into the significant impact of agglomeration on the magnetophoretic behavior are shown. Remarkable drug loadings (62%) with the antimicrobial peptide lasioglossin and an excellent efficiency (82.3%) were obtained by covalent coupling with the EDC/NHS (N-ethyl-N'-(3-(dimethylamino)propyl)carbodiimide/N-hydroxysuccinimide) method in comparison with the adsorption method (24% drug loading, 28% efficiency). The systems showed high antimicrobial activity with a minimal inhibitory concentration of 1.13 μM (adsorption) and 1.70 μM (covalent). This system successfully combines an antimicrobial peptide with a magnetically controllable drug carrier.

Keywords: carboxymethyl dextran; iron oxide nanoparticles; antimicrobial peptide; magnetically controlled drug delivery; agglomeration behavior



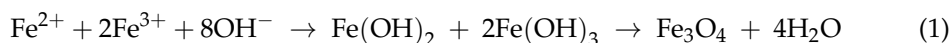
Copyright: © 2022 by the authors. Licensee MDPI, Basel, Switzerland. This article is an open access article distributed under the terms and conditions of the Creative Commons Attribution (CC BY) license (<https://creativecommons.org/licenses/by/4.0/>).

1. Introduction

Nanomedicine has introduced novel therapeutic and diagnostic capabilities that can address previously inaccessible issues in medicine, e.g., targeted delivery or improved medical imaging [1]. As a result of their simple and inexpensive production, good biocompatibility, high surface area to volume ratio, and superparamagnetic behavior, functionalized iron oxide nanoparticles (IONs) are ideal for applications in nanomedicine [2,3]. Their properties render them appropriate for use as T2 contrast agents in magnetic resonance

imaging (MRI), cancer therapy such as hyperthermia treatment or inhibitory factor replacement, and even as carriers in magnetically controlled drug delivery systems [4–8]. The implementation of IONs as drug carriers for the targeted drug delivery of, e.g., anticancer (doxorubicin) or antimicrobial drugs (lasioglossin (LL)) increases the efficacy by improving the bioavailability of the drug and reduces the dose and associated systemic toxicity, including undesirable side effects [1,9–11]. IONs can be taken up by a cell through adsorptive endocytosis or by the macrophages. The binding of a drug, e.g., a peptide, to IONs can improve its cellular uptake [12]. When developing a new nanomedicine product such as a drug delivery system, a complete physicochemical characterization of the product must be carried out and be made readily available [13–15]. In addition, the biocompatibility and pharmacokinetic or pharmacodynamic behavior of the nanomedicine must be known before its use in the human body and in therapy [16–18]. The European Medicines Agency (EMA) has emphasized the importance of these criteria for developing new nanomedicines to ensure and simplify the development and approval process [1,19].

Magnetite (Fe_3O_4) is one of the variants of iron oxide found in nature and is often used for applications in nanomedicine due to its superparamagnetic behavior, high specific surface area, and biocompatibility [20]. The most common synthesis route used to produce iron oxide nanoparticles is co-precipitation using the Massart process (Equation (1)) [2,20,21]:



Magnetite is unstable in an oxygen atmosphere and can quickly oxidize to maghemite ($\gamma\text{-Fe}_2\text{O}_3$), leading to a decrease in the saturation magnetization [22,23]. Furthermore, uncoated iron oxide cores tend to agglomerate over time due to surface energy minimization, thus reducing the dispersibility and usable surface area [20]. Agglomerates of >100 nm may be formed, which impede the application in biomedical fields [23–25]. Bare IONs (BIONs) can form non-specific interactions with blood serum proteins [22,26]. This interaction can reduce the half-life of the particles in the body due to their opsonization and subsequent rapid removal from the bloodstream [27–29]. The abovementioned disadvantages limit the usability of BIONs in the field of drug delivery.

A solution to these problems is the method of coating with organic or inorganic polymers [22,23]. Carboxymethyl dextran (CMD) is an interesting coating for drug delivery applications for the following reasons. ION@CMD can be easily synthesized by an in situ co-precipitation (Figure 1) [21,30,31].

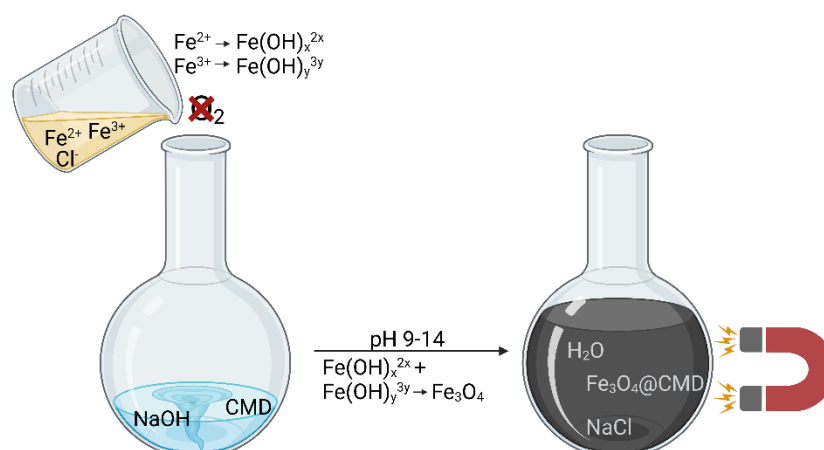


Figure 1. Schematic illustration of ION@CMD synthesis by the in situ co-precipitation technique according to Massart. It was created with BioRender.com.

The Food and Drug Administration has already approved IONs with a modified dextran coating in combination with the drugs Ferumoxytol and Feridex IV for the treatment of anemia and as a contrast agent in MRI [32–34]. The variant of dextran is increasingly used

as a coating due to its high density of free carboxyl groups [35,36]. The carboxyl groups are efficient tools for cross-linking the particles with primary amines in therapeutic proteins or peptides. Li et al. exploited this hypothesis by covalently binding anti-BSA antibodies to the particle surface via EDC/NHS (N-ethyl-N'-(3-(dimethylamino)propyl)carbodiimide/N-hydroxysuccinimide) activation [37]. Vasic et al. immobilized alcohol dehydrogenases (ADH) onto the particle surface without activity loss [30]. In previous studies of CMD-coated IONs, the negative surface charge led to a slower clearance from the bloodstream and less fouling activity and promoted the cellular uptake in Caco2-cells [35,36,38]. Furthermore, the negatively charged coated IONs enable the adsorption of positively charged drugs, such as antimicrobial peptides (AMP) [31].

AMPs, with their cationic properties, can accumulate on the negatively charged membrane surface of bacteria and disrupt the structure of the lipid bilayer. Therefore, cytoplasmic components can leak out, eventually leading to cell death [39]. Due to their rapid action and complex resistance formation, AMPs have proven to be an excellent alternative to conventional antibiotics [40,41]. The cationic peptide lasioglossin III (LL, H-Val-Asn-Trp-Lys-Lys-Ile-Leu-Gly-Lys-Ile-Ile-Lys-Val-Val-Lys-NH₂) is isolated from the venom of the bee *Lasioglossum laticeps* and belongs to the group of AMPs. It is an alpha-helical peptide with a hydrophobic and a hydrophilic side [39,40,42]. It shows a high antimicrobial activity against Gram-positive and Gram-negative bacteria, such as *B. subtilis*, *S. aureus*, and *E. coli* [42], and anticancer activity against PC12 or leukemia cells [42]. Due to its activity at physiological salt concentrations, LL is a promising substance for cancer therapy [42]. The positive charge and free amine groups make the peptide suitable for loading on IONs@CMD carrier particles [31,40,42].

Although many research groups have focused on the use of particles in therapeutic settings, little is known about the influence of the coating thickness on the particle properties. Thus, a need has arisen to identify critical parameters that can influence and help to standardize the design of CMD-coated IONs, as emphasized by the EMA. Yet, in particular, a lack of knowledge exists regarding the influence on agglomeration, magnetophoretic behavior, and oxidation. [1,43]. Furthermore, it is of general interest to improve the knowledge about the application of antimicrobial peptides for targeted drug delivery. In this work, five CMD-coated IONs were synthesized with a systematic increase in the CMD quantity (6.25 g L⁻¹, 12.5 g L⁻¹, 25.0 g L⁻¹, 125 g L⁻¹, and 250 g L⁻¹), which were fully characterized. The presented data provide new insights into the applicability of CMD-coated IONs for magnetically controlled drug delivery in combination with the antimicrobial peptide LL.

2. Results and Discussion

IONs@CMD were synthesized by applying increasing amounts of CMD to the reaction mixture: 6.25 g L⁻¹ (ION@CMD6.25), 12.5 g L⁻¹ (ION@CMD12.5), 25.0 g L⁻¹ (ION@CMD25.0), 125 g L⁻¹ (ION@CMD125), and 250 g L⁻¹ (ION@CMD250). The particle properties and the influence of the coating thickness on them were analyzed in detail, providing new trends and results regarding their agglomeration behavior, magnetophoresis, oxidation, and cytocompatibility. Two different TEM techniques were used to visualize the coating. The new knowledge was used to choose the ideal ION@CMD for the drug delivery of LL. The system was analyzed for its binding abilities of the AMP and its antimicrobial properties.

2.1. Particle Composition

The particle composition defines the critical parameters of IONs@CMD influencing the particle size, surface properties, agglomeration, and magnetic behavior. The successful binding of CMD to the ION surface was determined by FT-IR (Figure 2a). The BIONs show a characteristic ν Fe-O peak at 582 cm⁻¹ and additional bands at 1630 cm⁻¹ and 3386 cm⁻¹ that can be assigned to the ν O-H vibration. These result from adsorbed water on the iron oxide surface [44,45]. The IONs@CMD have further ν O-H and δ O-H vibrations

at 3363 cm^{-1} and $\nu\text{C-H}$ and $\delta\text{C-H}$ vibrations at 2922 cm^{-1} and around 1410 cm^{-1} , and $\nu\text{C=O}$ vibration is visible at 1593 cm^{-1} . The peak at 1017 cm^{-1} is attributed to the $\nu\text{C-O}$ bonds [30,44]. Increasing CMD concentrations led to higher characteristic CMD bands and a thicker CMD layer [35,46]. Das et al. confirmed this trend with ATR-IR and XPS measurements, finding that increasing the addition of the polysaccharide in co-precipitation led to a higher C-Fe ratio on the particle surface [47]. Raman spectroscopy can observe a similar trend to FT-IR but also provides information about the oxidation state of the iron oxide core (Figure 2c). The typical vibration for Fe-O in iron oxide is visible at 680 cm^{-1} [48]. Two bands are characteristic in the CMD spectrum and suggest that the (C-OH) and (C-O-C) frequencies form a broad band between 1060 cm^{-1} and 1125 cm^{-1} , respectively (SI-Figure S1) [49,50]. The intensity of the iron oxide peak decreases with the increasing CMD on the surface. In the case of ION@CMD250, the signal is significantly stronger than that of ION@CMD6.25–125 and probably blankets that of the IONs. Specifically, the iron oxide peak is composed of magnetite (660 cm^{-1}) and maghemite (710 cm^{-1}), depending on the oxidation state [48,51,52]. Therefore, the Raman spectra were used to calculate the magnetite content (Figure 2d, SI-Formula (S1), SI-Table S1). The BIONs have a calculated magnetite content of 15.6%. The content is consistent with those in the literature [48,52]. The magnetite content increases with the thicker CMD coating from ION@CMD6.25, with 15.6%, to ION@CMD25.0, with 47.5% (Table 1). ION@CMD125 consists of 41.6% magnetite, suggesting that a plateau was reached. The increasing magnetite content is illustrated in Figure 2d by Voigt fits, showing that the CMD coating slightly protects the IONs from oxidation [53]. The crystal structure of the IONs was determined using XRD measurements (ION@CMD12.5: Figure 2b, other particles: SI-Figure S2). All the particles show the characteristic iron oxide reflections at 13.7° , 16.1° , 19.5° , 25.4° , and 27.7° , which can be assigned to the crystal plane of iron oxide located at (220), (311), (400), (511), and (440), according to Miller's index [23].

Table 1. Magnetite contents of BIONs and ION@CMD6.25 to 125, determined by comparing the magnetite peak area (660 cm^{-1}) and maghemite peak area (710 cm^{-1}). For ION@CMD250, no iron oxide peak could be measured due to the thick CMD coating. The mean diameter was determined via TEM and Scherrer equation and IEPs.

Particles	Fe ₃ O ₄ (%)	d _{TEM} (nm)	d _{Scherrer} (nm)	IEP
BIONs	15.6	8.7 ± 1.6	8.8 ± 0.9	7.1
ION@CMD6.25	21.0	11 ± 2.1	10 ± 0.5	4.6
ION@CMD12.5	33.9	11 ± 2.8	8.6 ± 0.1	4.4
ION@CMD25.0	47.5	8.0 ± 1.7	5.6 ± 0.6	3.9
ION@CMD125	41.6	7.6 ± 1.6	4.7 ± 0.4	2.4
ION@CMD250		6.3 ± 1.2	0.6 ± 0.3	1.7

Therefore, the coating does not influence the crystal structure of the particles. Furthermore, CMD leads to amorphous signals between 2° and 10° . A comparable phenomenon has been observed with silica-coated IONs [54]. FT-IR and Raman show that higher CMD concentrations increase the CMD coating thickness, protecting the magnetite from oxidation to maghemite. The particles have a characteristic crystalline iron oxide core (spinel).

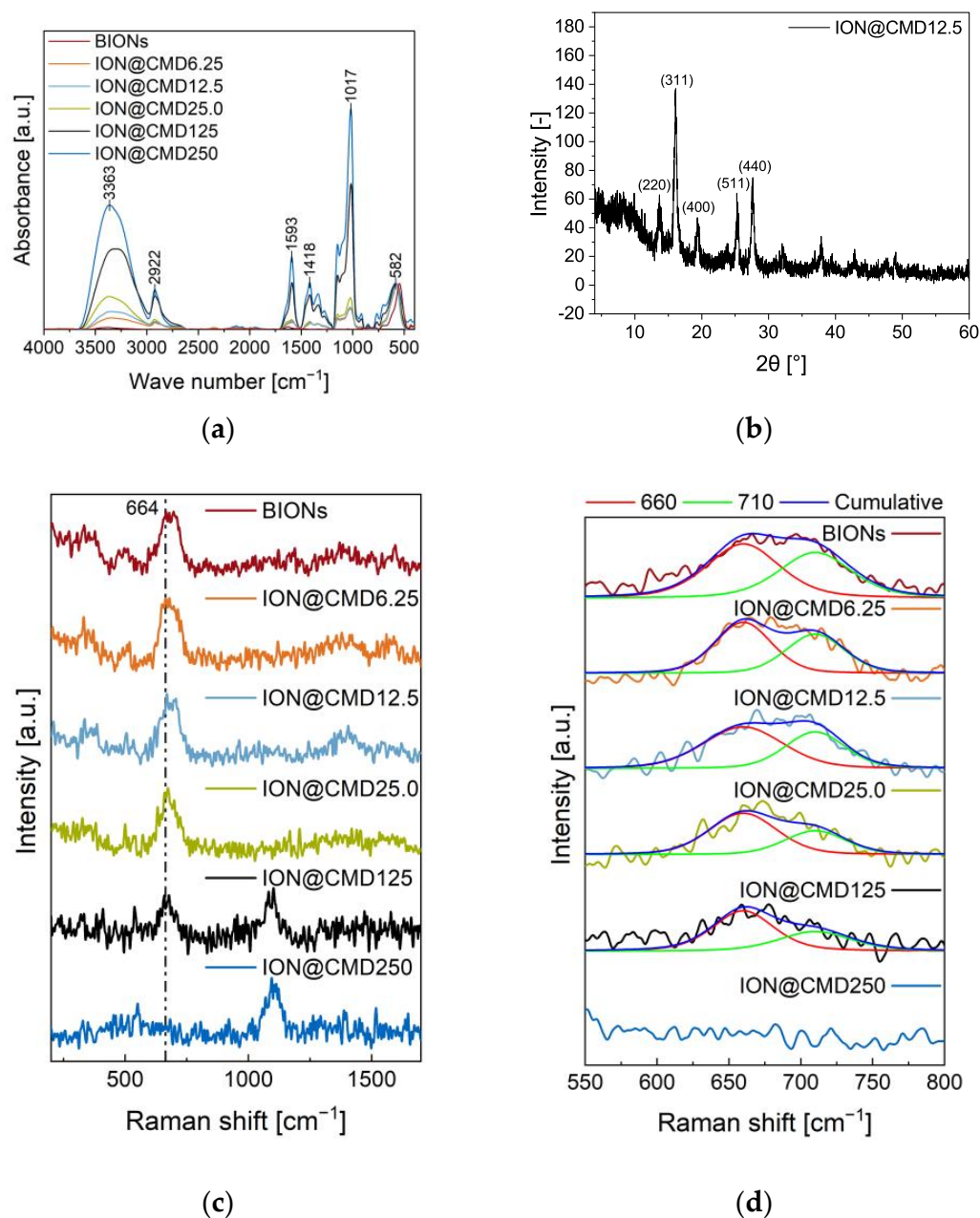


Figure 2. FT-IR Spectra of synthesized IONs@CMD and BIONs at wavenumbers between 4000 and 450 cm^{-1} (a). All spectra were normalized on the magnetite band around 582 cm^{-1} . Raman spectra of ION@CMDs and BIONs (b). The fit of the A_{1g} band is between 600 and 750 cm^{-1} using Voigt functions in Origin (c). X-ray diffractogram of ION@CMD12.5 (d).

2.2. Surface Properties

In biomedical applications, the particles are subjected to the different pH values and ionic strengths in the human body. The pH values vary from pH 7.4 in the blood and cytosol to pH 6.4 in cancer cells, pH 4–5 in endosomes and lysosomes, and pH 2 in gastric acid [55–57]. Consequently, obtaining colloidal stable particles over a broad pH spectrum is essential. The stability and surface charge of the particles were determined by zeta potential and DLS measurements (SI-Figure S2, Equation (S2)). The IEP of the BIONs was determined to have a pH of 7.10, which is consistent with the literature values [31]. The BIONs show significant agglomeration ($d_H = 503.9 \text{ nm}–2042 \text{ nm}$) around the IEP, since they have a zeta potential of $\pm 10 \text{ mV}$, making the particles unstable [58]. At pH < 6.5 and > 8.5, the BIONs have a hydrodynamic diameter (d_H) of around 100 nm. Here, the zeta

potentials are in a range in which the particles are moderate to very stable. The isoelectric point (IEP) of the IONs@CMDs is between 4.6 and 1.7, shifting in the acidic pH region as the coating of the particles becomes thicker (Table 1) [35]. The charge density of the CMD-coated IONs varies with the pH by changing the degree of ionization of the CMD. With a modification degree of one carboxyl group per glucose unit, the pKa value may vary from 3.3–4.5 [59]. Since it is assumed that the number of carboxyl groups increases with the coating thickness, the trend can be explained. ION@CMD6.25 and ION@CMD12.5 have IEPs of 4.6 and 4.4, respectively. These particles agglomerate around the IEP (zeta potential of ± 10 mV). The CMD side chains' steric repulsive forces are hypothesized to be insufficient to ensure colloidal stability around the IEP. In addition, for the low CMD concentrations, the threshold value necessary for the complete coating of the particles is not exceeded and, thus, the particles are not entirely coated [47]. Therefore, ION@CMD6.25 and ION@CMD12.5 are influenced by the BION-like properties.

Nonetheless, both particle types are in the ideal size range of <100 nm at a physiological pH, with hydrodynamic diameters of 66.3 ± 7.35 nm for ION@CMD6.25 and 87.1 ± 11.0 nm for ION@CMD12.5. Thicker CMD coatings lead to a good colloidal stability over the broad pH spectrum and no agglomeration ($d_H < 100$ nm) at the IEP at pH 3.9 for ION@CMD25.0, pH 2.4 for ION@CMD125, and pH 1.73 for ION@CMD250 (SI-Figure S3). However, agglomeration with a plate-like shape is visible in the SAXS curve of ION@CMD250 at pH 7, while the primary particle size is determined to be 20 nm (SI-Figure S4). All the particles have a negative surface charge from a pH value of ~ 4.6 and higher, making them a promising material for nanomedicine. It is well known that negatively charged particles experience prolonged blood circulation, increased cellular uptake, and a lower cytotoxicity [35,60]. Furthermore, they have the potential to adsorb the positively charged LL.

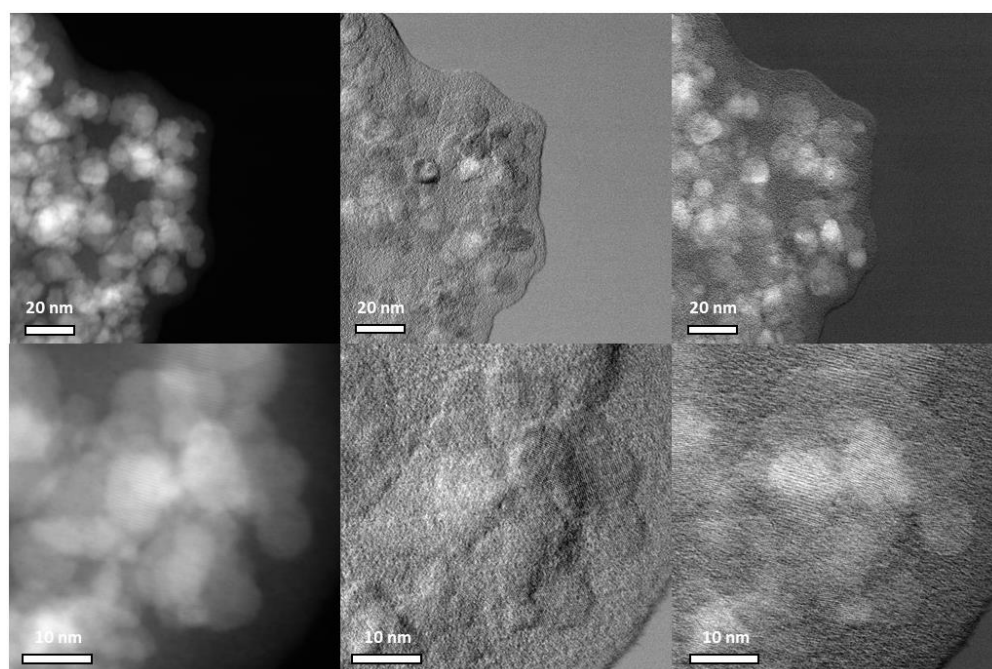
2.3. Particle Size

The size and agglomeration behavior of the nanoparticles are crucial criteria for their applications in nanomedicine. Here, adverse effects and the blood circulation time depend strongly on the hydrodynamic diameter, shape, and surface chemistry [24,25]. An ideal particle diameter lies between 10 and 100 nm for intravenous injection, avoiding extravasation and rapid elimination by the kidneys (<10 nm) or opsonization and removal from the bloodstream by the macrophages (>100 nm). For the crossing of the blood–brain barrier, similar sizes are favorable [61]. Popovtzer et al. showed that gold nanoparticles with a size of 20 nm accumulate in the brain within two hours post-injection [62]. In addition, a large specific surface area and functional groups are desirable for high drug loadings [23,24]. Before the influences of various simulated body fluids can be analyzed, it is necessary to determine the diameter of the iron oxide core and the coating thickness. The magnetic core size is calculated from the data of the XRD spectra using the Scherrer equation (SI-Equation (S3), Table 1). The BIONs' size of 8.8 ± 0.9 nm is comparable with the literature data [23,31]. The ION core decreases from ION@CMD6.25, with 10 ± 0.5 nm, to ION@CMD250, with 0.6 ± 0.3 nm. The larger diameter of ION@CMD6.25 compared to the BIONs can be explained by the higher reaction temperature (85 °C vs. 25 °C) [63,64]. Increasing CMD concentrations lead to smaller core sizes. The reason, therefore, lies in the conventional nucleation theory [63,65]. With higher amounts of polymer added, the CMD is more likely to meet the freshly formed crystals and stop the nuclei growth. Thus, more CMD accumulates on the particle surface [30]. Even with extended measurement times, the thicker the CMD coating is, the higher the signal-to-noise ratio will be during XRD analysis (SI-Figure S2). For that reason, the inaccuracy of the calculated diameters slightly increases. The average d_{TEM} of 8.7 ± 1.6 nm for the BIONs fits the literature and is comparable to the $d_{Scherrer}$ (Table 1, SI-Figure S5) [23,31,48]. ION@CMD6.25 and ION@CMD12.5 reach a similar size of 11 ± 2.1 nm and 11 ± 2.8 nm. Thus, ION@CMD12.5 accumulates in smaller clusters (SI-Figure S5c). With the increasing input of CMD in the co-precipitation reaction, the size of the particles decreases. ION@CMD250, 125, and 25 have smaller diameters than

the BIONs, with measurements of 6.3 ± 1.2 nm, 7.6 ± 1.6 nm, and 8.0 ± 1.7 nm, respectively. This trend is consistent with the decrease in the d_{Scherrer} . ION@CMD25, 125, and 250 also tend to collect in larger clusters.

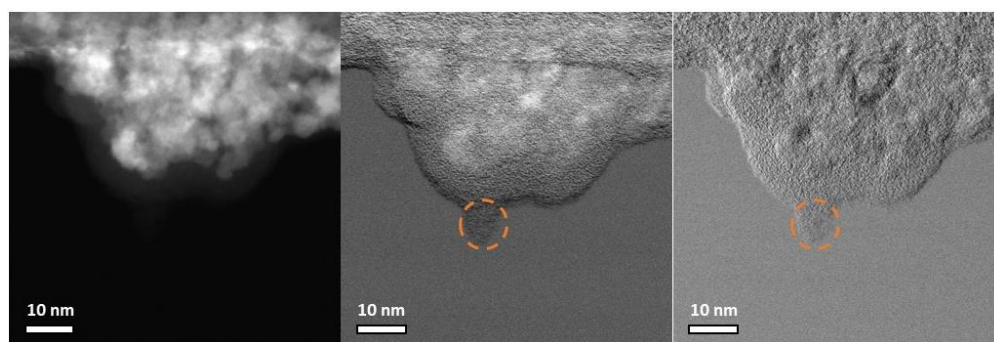
This phenomenon can be attributed to the fact that smaller particles have a higher surface-to-volume ratio and high surface energy. Accordingly, they agglomerate to reduce this surface energy [46]. Since the diameters of the BIONs determined by XRD and TEM coincide, the thickness of the CMD coating was calculated by determining the difference between d_{TEM} and d_{Scherrer} .

It is necessary to emphasize that liquid conditions can influence the properties of the polymer coating. In agreement with the IR and Raman spectra, it can be observed that the CMD layer increases from ION@CMD6.25 to ION@CMD250. With a Δd of 5.68 nm, ION@CMD250 has the thickest coating. The thicknesses of ION@CMD125, 25, 12.5, and 6.25 are 2.82 nm, 2.42 nm, 2.35 nm, and 0.77 nm, respectively. The particles of ION@CMD12.5 appear to have a suitable layer thickness, because they fall in the size range of 10–100 nm and do not collect into larger clusters. Imaging with high-angle annular dark-field scanning transmission electron microscopy (HAADF-STEM) provides further insight. The particles show atomic lattice planes (Figure 3, SI-Figure S6). With differential phase-contrast (DPC) imaging, the nanoparticle core can be easily distinguished from the polymer due to the fact that the sample deflects the beam significantly in both DPC_x and DPC_y. Again, in the experiments, atomic lattice planes were observed in the core, confirming the presence of a crystalline core and amorphous exterior polymer coating. The CMD coating showed sensitivity to the scanning electron beam in the STEM mode, leading to the growth of the polymer layer and causing unforeseen artifacts (Figure 3b orange circle). To ensure that the CMD layer's visual representation was minimally influenced by the electron beam and, hence, artifact-free, the TEM mode was coupled with a direct electron detector to quantify and control the imminent electron dose. To conduct the imaging in this manner, the dose rate was kept under $15 \text{ e}^-/\text{\AA}^2/\text{s}$ by monitoring the dose rate output according to the direct electron readout and adjusting the monochromator accordingly. By applying a slight defocus, the CMD layer became more apparent compared to the iron oxide core (Figure 4).



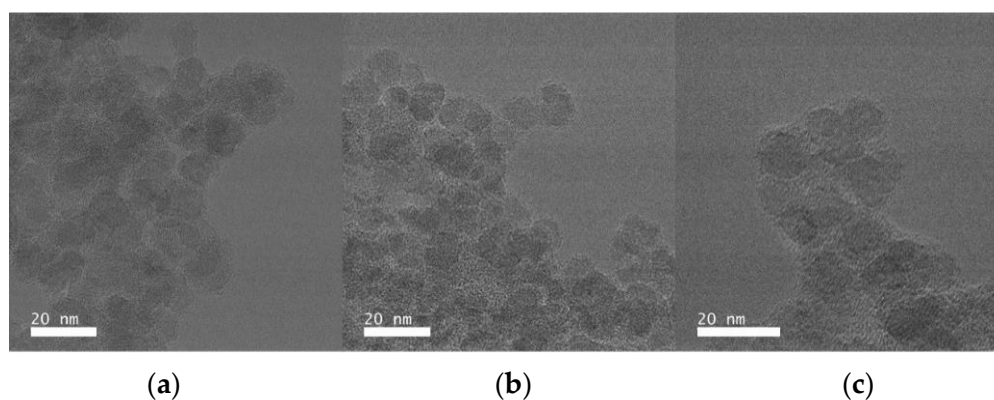
(a)

Figure 3. Cont.



(b)

Figure 3. HAADF-STEM micrographs indicate the nanoparticle core with an amorphous coating for (a) ION@CMD6.25 and (b) ION@CMD250 on the left. The picture in the middle shows DPCx (A–C), and the right one shows DPCy (B–D). The orange markers show the artifacts created by the scanning electron beam. Scale bars are inset.



(a)

(b)

(c)

Figure 4. Low-dose TEM micrographs of (a) ION@CMD250, (b) ION@CMD12.5, and (c) IONs@CMD6.25. These micrographs were acquired using the dose fractionation method, where 40 micrographs were taken with bursts of 0.1 s of exposure and subsequently aligned and summed. Scale bars: 20 nm.

Our detailed analysis of the low-dose TEM micrographs showed a core diameter of 6.6 nm and a medium coating thickness of 1.4 nm for ION@CMD250, while ION@CMD12 had a core size of 9.7 nm and a CMD layer of 2.1 nm, and ION@CMD6.25 showed values of 8.9 nm and 2.6 nm (SI-Figure S7). These data fit the trends observed previously. The size of the dried, not perfectly round agglomerates lies between 92 and 101 nm for ION@CMD250, 296 and 404 nm for ION@CMD12.5, and 146 and 275 nm for ION@CMD6.25 (SI-Figure S8). The agglomeration behavior, which is highly dependent on the medium, is essential for analyzing the applicability of drug delivery systems [40,59]. Figure 5 shows the size distributions of the BIONs and IONs@CMD in water (pH 7.4), PBS (pH 7.4), and human plasma, determined by DLS. For all the media, the BIONs have a higher tendency to agglomerate than the CMD-coated particles. In water, at a pH close to the IEP, the BIONs experience a lack of electrostatic repulsion due to their unfunctionalized surface. They form agglomerations of around 57.9 particles, with a d_H of 503 ± 10.5 nm. The CMD coating positively influences the particles' stability. Therefore, all the IONs@CMD experience less agglomeration (Figure 5) [35,46]. For ION@CMD12.5, 25, 125, and 250, in ascending order, the agglomeration rises with the increasing coating thickness to 87.1 nm ($7.99 \times d_{TEM}$ of one particle), 94.2 nm ($11.8 \times$ particles), 162 nm ($21.5 \times$ particles), and 200 nm ($31.6 \times$ particles, Figure 5a, SI-Table S2). The only exception is the particles with the thinnest CMD coating, with a hydrodynamic diameter of 137 nm (12.6 particles), being higher than ION@CMD12.5. Das et al. also observed increasing DLS sizes when the

Fe/CMD ratio was reduced to a limit where the particle surface is no longer entirely coated (17.143:1 to 12.000:1) [47]. The stabilizing effect of CMD can be explained by the negative surface charge and resulting repulsion of the particles with the same net charge. All the coated particles have a zeta potential of < -15 mV at a pH of 7–7.4, reflecting moderately stable particles (SI-Figure S3) [58,66]. The effect of the electrolytes was studied in 50 mM PBS (pH = 7.4). The high electrolyte concentration of the medium stimulates the agglomeration of the BIONs. With a diameter of 1902 nm, which is $3.78 \times (d_{H,PBS}/d_{H,H_2O})$ greater than that in water, the uncoated particles reach agglomerate sizes in the μm range (Figure 5b, SI-Table S2) [31,67]. CMD-coated particles are stably dispersed in biological media throughout a wide range of pH and ionic strength values [35,47,68]. Therefore, CMD coating also leads to stabilization in PBS buffer. ION@CMD6.25, 12.5, 25, 125, and 250 have hydrodynamic diameters in PBS of 165.7 nm ($d_{H,PBS}/d_{H,H_2O} = 1.21 \times$), 157.6 nm ($1.81 \times$), 73.6 nm ($0.78 \times$), 34.5 nm ($0.21 \times$), and 69.3 nm ($0.35 \times$), respectively (SI-Table S2).

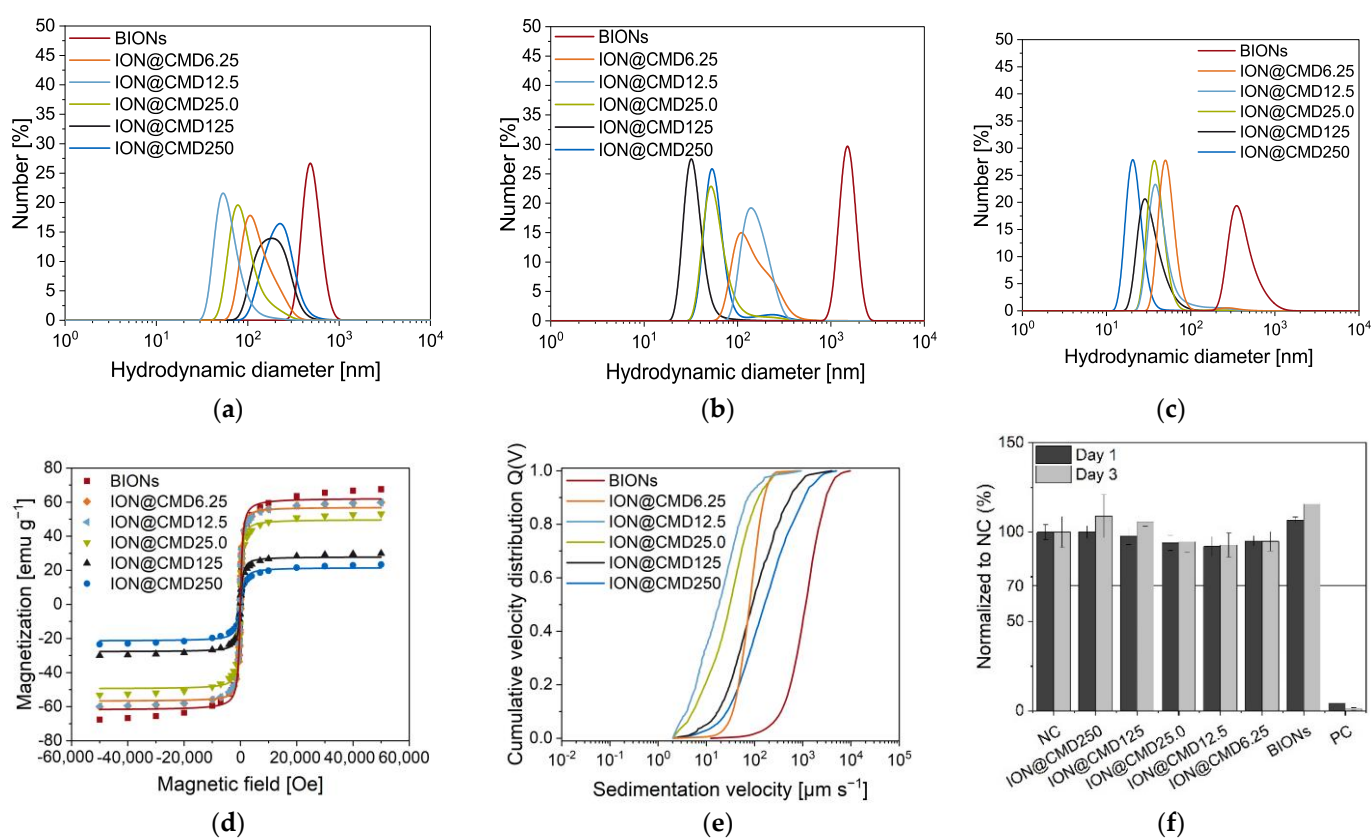


Figure 5. DLS measurements of BIONs and IONs@CMD in (a) dH₂O pH = 7, (b) 50 mM PBS (pH = 7.4), and (c) human plasma. The equilibration time was set as 120 s. The temperature set for the water and PBS was 25 °C and the human plasma temperature was 37 °C. SQUID analysis at a temperature of 300 K using the LangevinMod fit (d), cumulative velocity distribution at room temperature, and (e) a pH ~ 7 in water. Cytocompatibility was analyzed by XTT assay with smooth muscle cells (f) with a negative control (NC) and a positive control (PC). Results are normalized to NC.

With higher CMD amounts, the agglomeration in PBS is less significant than that in water. Almasri et al. reported that negatively charged phosphate ions can be adsorbed more strongly on negative surfaces in the presence of other anions [69]. The ionic effects enhance the stability of the particles. PBS buffer at pH 7.4 corresponds to the cytosol conditions in the human body. The good stabilization renders the IONs@CMD favorable in drug delivery systems. For this application, the CMD-coated particles are analyzed in human serum (Figure 5c). The BIONs and IONs@CMD show a reduced agglomeration

behavior due to the increased viscosity (4 mPa·s) and the potential stabilizing biomolecular corona formation [31,70–72]. The BIONs are agglomerated 0.87 times less than they are in water, with a diameter of 442 nm, while the increasing CMD amounts lead to up to 0.13 times less agglomeration for ION@CMD250, with 25.8 nm. The decrease in the hydrodynamic diameter in human plasma with the increasing CMD coating correlates with the charge of the particles. Tekie et al. showed that particles with increasing carboxyl groups on the surface and, correspondingly, more negative charges are very stable in serum conditions [73].

In summary, a reduction in the magnetite size with increasing CMD was detected. The particles are more stable than the BIONs in all the media used and, thus, show advantageous properties for their use as drug delivery systems. A trend can be seen with the PBS and human serum, where the particles with thicker coatings form smaller agglomerates than those with thinner layers.

2.4. Magnetization

SQUID and STEP technologies analyze magnetic behavior depending on the particle composition, size, surface properties, and agglomeration. The BIONs and IONs@CMD show the characteristic sigmoidal curve typical of a superparamagnetic behavior (Figure 5d) [2,23]. Superparamagnetic particles are only magnetic in the presence of an external magnetic field and have no remanence [74]. The ideal curve shape is simulated using the LangevinMod fit (SI-Equation (S4)). With less CMD coating, the particles' slope deviates from the fit more significantly above a magnetic field strength of ± 20 kOe. The saturation magnetization decreases with a thicker layer and a smaller iron oxide core. ION@CMD6.25, with a maximum saturation magnetization of ± 60 emu g^{-1} , is comparable with the BIONs (± 67 emu g^{-1}), while ION@CMD20 has a significantly lower saturation magnetization of only 25 emu g^{-1} . Unterweger et al. observed a decrease in the saturation magnetization in the case of dextran-coated IONs [75]. The hydrodynamic diameters of the particles influence the magnetophoretic behavior in water to a greater extent than the magnetization (Figure 5e). Agglomeration increases the sedimentation velocity, therefore explaining the increasing sedimentation rate [76]. The BIONs sink the fastest in a magnetic field compared to the coated particles, with a sedimentation velocity of $1152 \mu m s^{-1}$ (SI-Table S3). Similar to the DLS measurements in water, the increasing stabilization of the particles can be seen from ION@CMD250 to ION@CMD12.5. ION@CMD250, 125, and 25 settle at $160 \mu m s^{-1}$, $90.2 \mu m s^{-1}$, and $30.7 \mu m s^{-1}$, respectively. The most stable particles, ION@CMD12.5, have a sedimentation velocity of $18.4 \mu m s^{-1}$. At the lowest coating thickness, the ION@CMD6.25 particles sink faster at a rate of $78.9 \mu m s^{-1}$, proving the agglomeration behavior. Previous studies of oleate-coated IONs have shown the effect of a distinct acceleration of the magnetic field on the sedimentation velocity [77].

In conclusion, all the particles exhibit superparamagnetic properties, with lower magnetizations detected with higher CMD coatings due to the smaller iron oxide cores and higher polymer mass. The agglomeration of the particles strongly influences the magnetophoretic sedimentation rate. All the IONs@CMD, compared with the BIONs, show a slower sedimentation speed because of their better stabilization. The ION@CMD12.5 particle type proved to be the most stable.

2.5. Cytocompatibility

The cytocompatibility of the BIONs and the various IONs@CMD was analyzed in direct contact with the HUASMCs after one and three days (Figure 5f). All the particles show more than 70% viability at the tested concentrations, the threshold suggested by ISO-10993 for cytocompatibility. Furthermore, there are no visible influences on the cell morphology and proliferation compared to the negative control (SI-Figure S9). The data fit several cell viability tests of IONs in the literature. For example, Kumar et al. showed a good cell viability for MCF-7 and HepG2 cells, with values between 0.06 and $1.00 g L^{-1}$ for superparamagnetic IONs and folic-acid-coated ones [78]. Zhang et al. found a slight

decrease of up to 20% in the cell viability of smooth muscle cells incubated with three different coated IONs (DMSO, APTS, GLU) [79]. The excellent cytocompatibility of IONs@CMD makes them suitable for application in drug delivery.

Characterizing the different CMD thicknesses provided us with a better understanding of the size intervals, stability in physiological-like media, controllability in magnetic fields, and the negative surface charge. ION@CMD12.5 stands out as the particle type with the best properties due to the ideal diameter d_{TEM} of >10 nm, the colloidal stability in water and human plasma with a hydrodynamic diameter in the range of 10–100 nm, and the good magnetization. In this context, we decided to examine the loading of LL on the ION@CMD12.5 particles.

2.6. Electrostatic and Covalent Binding of Lasioglossin

For the generation of a new and efficient drug delivery system, the binding of the antimicrobial peptide lasioglossin was examined by electrostatic and covalent binding. The adsorption was performed in 50 mM PBS buffer (pH = 7.4), showing a peptide loading of 0.32 ± 0.06 g g⁻¹ (equilibrium concentration 3.68 g L⁻¹, Figure 6a, SI-Figure S10c). Comparable to Turrina et al., where the interaction of LL with BIONs was analyzed, a substantial decrease in the loading was observed after one wash step, with a loading of 0.09 ± 0.05 g g⁻¹ and 0.02 ± 0.02 g g⁻¹ after the second wash step (Figure 6a) [31]. The LL, bound by weak electrostatic forces, detached from the surface as the supernatant changed with each wash step, and new equilibrium concentrations were established [31]. Although good drug loadings (24.27%) were achieved in the adsorption step, only 1.30% of LL (stock solution of 4.00 g L⁻¹) remained on the surface after the two washing steps. Comparable values were also obtained by Qu et al. and Luo et al., with a maximum loading of 11.8% for 10-hydrodycamptothecin on PEG-chitosan-coated IONs and 35% for paclitaxel on magnetic colloidal nanocrystal clusters [80,81]. The peptide adsorbs quickly on the ION surface, and after only five minutes, an equilibrium is formed (SI-Figure S10b). Contrary to electrostatic bonds, covalent bonds are stronger, pH-independent, and more thermostable [82]. The following covalent binding was performed using a two-step EDC/NHS coupling protocol (Figure 6b) [83]. A peptide bond was formed between the activated carboxyl group of CMD on the particle surface and a free amine group of LL. Five concentrations of LL (0.80 g L⁻¹–2.50 g L⁻¹) were added, and FT-IR, DLS, and the zeta potential were used to characterize the particle-peptide complex.

The loading was determined by UV/VIS analysis of the supernatants at 280 nm and by TGA measurements. A loading of 0.55 g g⁻¹ was achieved with a 0.80 g L⁻¹ LL input. With a drug loading (DL) of 35.4% (280 nm), 11.2% more was loaded than the highest loading during adsorption (Table 2). From this point, increasingly higher loadings were achieved with the progressive addition of LL (Figure 6a). At the initial LL concentrations of 1.00, 1.50, 2.00, and 2.50 g L⁻¹ peptide, loadings of 0.60 g g⁻¹ (DL 15.0%), 0.94 g g⁻¹ (DL 43.8%), 1.32 g g⁻¹ (DL 52.4%), and 1.65 g g⁻¹ (DL 62.3%) were achieved (Table 2). The binding efficiency varied between 28.4% and 8.07% (SI-Table S4). Studies on the conjugates of xylane- and dextran-coated particles with ibuprofen and naproxen achieved comparably high drug loadings (30–70 wt%) by covalent coupling [84,85]. Analogous with adsorption, the FT-IR spectra of the loaded particles show the characteristic LL bands at 1653 cm⁻¹ ($\nu_{\text{C=O}}$) and 1535 cm⁻¹ ($\delta_{\text{C-N}}$, Figure 6d). The loading was additionally confirmed and determined using TGA measurements of the dried particles (Figure 5c).

The TGA measurements of the pure peptide show a multistep breakdown process, which is consistent with the thermal behavior of freeze-dried proteins (SI-Figure S11). At a temperature of 450 °C, approximately 20.0% of the LL is not completely burned, which is included in the calculations [86–88]. A constant profile with no further decrease in the weight can be seen from 300 °C until the final process temperature of 700 °C is reached. The magnetite is not completely burned, since its melting point is 1538 °C [89]. Drug loadings of 15.4%, 15.3%, 26.9%, 33.2%, and 49.7% are achieved with inputs of 0.80, 1.00, 1.50, 2.00,

and 2.50 g L^{-1} LL, respectively (Table 2). The two different analytical methods vary from each other. The TGA profiles of the unbound and bound LL deviate from each other.

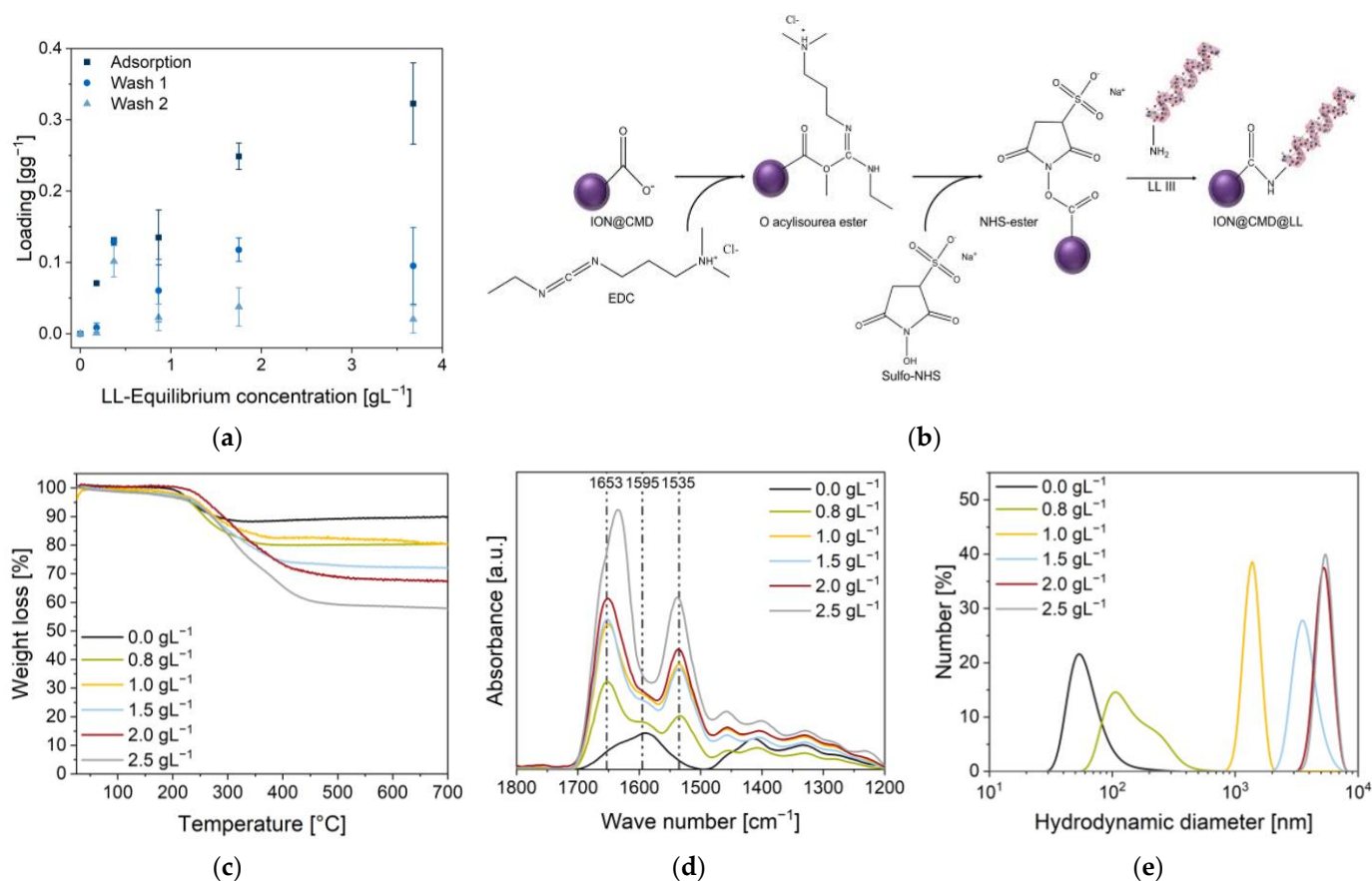


Figure 6. (a) Adsorptions of LL at pH 7.4 in 50 mM of PBS buffer and 1 g L^{-1} of ION@CMD12.5. Covalent binding of cationic peptide LL (0.0 g L^{-1} – 2.5 g L^{-1} input) to the surface of the ION@CMD12.5 particles. (b) EDC reacted with the free carboxyl group of CMD to form an unstable O-acylisourea ester intermediate. Sulfo-NHS was added to the reaction to form a more stable NHS ester, which reacts slowly with primary amines of LL to form stable amid bonds. LL was created with [BioRender.com](#). (c) TGA measurements until $700 \text{ }^\circ\text{C}$. (d) FT-IR spectra of the ION@CMD and ION@CMD@LL particles (24 scans) with labeled characteristic LL bands at 1653 cm^{-1} and 1535 cm^{-1} and the characteristic CMD band at 1595 cm^{-1} . (e) Hydrodynamic diameters of the unloaded (ION@CMD) and loaded particles in an aqueous medium (pH = 7–8).

Table 2. Loadings achieved by covalently bound LL. Drug loadings were calculated from the photometric and TGA data. Zeta potential and DLS measurements were performed in Millipore® H_2O at a pH between 7 and 7.5.

LL Used (g L^{-1})	Loading 280 nm (g g^{-1})	Drug Loading 280 nm (%)	Drug Loading TGA (%)	Zeta Potential (mV)	d_H (nm)
0.8	0.55	35.4	15.4	-29 ± 1.0	96.4 ± 45.7
1.0	0.60	35.0	15.3	2.9 ± 1.0	1599 ± 401
1.5	0.94	43.8	26.9	2.4 ± 0.3	4662 ± 797
2.0	1.32	52.4	33.2	13 ± 0.4	5274 ± 11.2
2.5	1.65	62.3	49.7	32 ± 0.9	5340 ± 263

Higher peptide binding increases the hydrodynamic diameters, leading to a plateau of around $5 \mu\text{m}$ (1.32 g g^{-1} and 1.65 g g^{-1}). The smallest hydrodynamic diameter is achieved

at a loading of 0.55 g g^{-1} (96.4 nm). Here, the peptide binds with an efficiency of 82.2% (SI-Table S4). Compared to the adsorption, the zeta potential of the particles rises with the increasing loading (Table 2). In the experiments, charges of $-29 \pm 1.0 \text{ mV}$, $2.9 \pm 1.0 \text{ mV}$, $2.4 \pm 0.3 \text{ mV}$, $13 \pm 0.4 \text{ mV}$, and $32 \pm 0.9 \text{ mV}$ were measured.

In summary, significantly higher drug loadings and a higher efficiency were achieved with the two-step EDC/NHS protocol than with the adsorptive method. The weak interactions during adsorption (electrostatic binding, van der Waals forces) are not sufficient for the efficient loading of the particles [90,91]. High-bound peptide amounts increased the hydrodynamic diameters.

2.7. Antimicrobial Activity

With their antimicrobial properties, ION@CMD12.5, ION@CMD@LL (ads), and ION@CMD@LL (cov) were co-incubated with green fluorescent protein (GFP)-expressing *E. coli* (BL21, amp resistance). Two different methods, namely OD600 measurements (SI-Figure S12) and microscopy, were used to determine the antimicrobial activity (SI-Figure S13). First, ION@CMD12.5 without the bound peptide was investigated (Figure 7a). Concentrations between 0.01 g L^{-1} and 0.40 g L^{-1} led to comparable *E. coli* growth, as was the case without the particles. The LL's minimum inhibition concentration (MIC) lay at 1.13 to $3.70 \text{ }\mu\text{M}$ [31]. Adsorbed to BIONs, the antimicrobial activity of LL could be slightly improved to $0.53 \text{ }\mu\text{M}$ in previous works [31]. ION@CMD12.5@LL (ads) showed less bacterial growth with comparable LL ($\leq 1.13 \text{ }\mu\text{M}$) concentrations. Starting at a concentration of $1.13 \text{ }\mu\text{M}$ of adsorbed LL, the inhibition of *E. coli* could be seen for 13 h in the OD600 measurements (SI-Figure S12). At $1.70 \text{ }\mu\text{M}$ of adsorbed LL, the growth was completely inhibited. In microscopic cell counts, the complete inhibition of cell growth was evident at a concentration of $1.13 \text{ }\mu\text{M}$ (Figure 7b, SI-Figure S13). The slight difference between the two methods can be explained by the fact that the samples used for the microscopy were shaken more intensively with an overhead shaker than the linear gentle shaking of the 96-well plate [31]. Covalently bound LL affected the cell growth, starting with a concentration of $2.83 \text{ }\mu\text{M}$ (OD600) or $0.40 \text{ }\mu\text{M}$ for the microscopy experiment (Figure 7b).

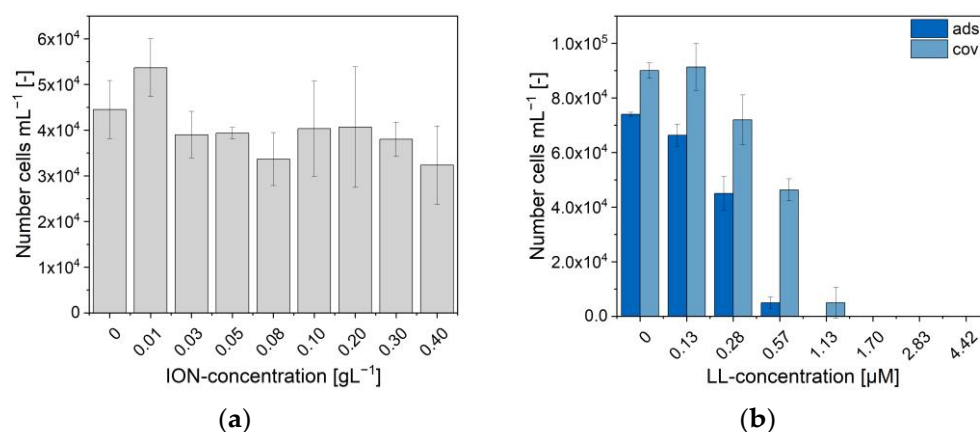


Figure 7. Growth of *E. coli* (BL21 (RH)4GFP-expressing) in M9 medium at different (a) ION@CMD12.5 concentrations and (b) amounts of the ION@CMD@LL complex obtained through adsorption and covalent binding. The concentration of ION@CMD@LL in diagram B describes the LL concentration.

The complete inhibition of the cell growth was seen at the $4.42 \text{ }\mu\text{M}$ (OD600) and $1.70 \text{ }\mu\text{M}$ bound LL concentrations, respectively. Although the MIC was slightly higher than the LL bound by physisorption, the biological activity of the covalently bound LL could be confirmed. The covalent binding of other drugs on CMD-coated IONs showed no or a slightly negative effect on the drugs' activity [30,92].

In summary, the ION@CMD showed no or little effect on the cell growth. ION@CMD@LL (ads) and ION@CMD@LL (cov) could completely inhibit the bacterial growth at concentrations of bound LL as low as 1.13 μM and 1.70 μM .

3. Materials and Methods

3.1. Synthesis of ION@CMD

According to the Massart process, the CMD-coated IONs were synthesized by coprecipitation [30,31]. A total of 20 mL of CMD solution (250 g L^{-1} (CMD250); 125 g L^{-1} (CMD125); 25 g L^{-1} (CMD25.0); 12.5 g L^{-1} (CMD12.5); 6.25 g L^{-1} (CMD6.25); CMD sodium salt, BioXtra, Sigma Aldrich, Darmstadt, Germany, 39422-83-8); and 2.5 mL of aqueous 25% ammonium hydroxide solution (Aldrich Chemistry) were added to a 100 mL round-bottomed flask in a nitrogen atmosphere. The reaction was induced by adding 20 mL of an iron (II/III) solution ($\text{FeCl}_2 \cdot 4\text{H}_2\text{O}$ (1 eq., 347 mg 1.75 mmol), EmsureTM; $\text{FeCl}_3 \cdot 6\text{H}_2\text{O}$ (2 eq., 945 mg, 3.50 mmol), Fluka Sigma Aldrich, Darmstadt, Germany) to the reaction mixture and by stirring it uniformly for one hour at a temperature of 85 °C. After the completion of the reaction, the synthesized particles were centrifuged (CMD250, CMD125) at $4000 \times g$ for 10 min or magnetically separated (CMD25.0, CMD12.5, CMD6.25) and washed with ethanol absolute (2 \times) and degassed using double-distilled water (ddH₂O, 2–3 \times) until a conductivity lower than 200 $\mu\text{S cm}^{-1}$ was obtained. The particles were stored in an N₂ atmosphere at 4 °C in degassed ddH₂O.

3.2. Characterization

The presence of the functional groups of CMD and the presence of LL (lasioglossin III) on the particle surface were confirmed by FT-IR spectroscopy (Fourier-transform infrared spectroscopy) (Alpha II; Bruker Corporation; Billerica, MA, USA) and platinum attenuated total reflection module. A total of 3 μL ($>1.00 \text{ g L}^{-1}$) of the particle solution was measured over a wavenumber range of 4000 cm^{-1} to 400 cm^{-1} (24 scans). The background was subtracted with the software OPUS8.1 using the concave rubber band method. Each spectrum was normalized to the magnetite band at approx. 580 cm^{-1} . Transmission electron microscopy (TEM) was used to determine the particles' morphology and size. After ultrasonication, the samples (10 μL) with a concentration of 0.03 g L^{-1} were deposited onto a carbon-coated copper grid that was prepared via glow discharge and dried by blow-drying. Images at a magnification of $\times 120 \text{ k}$ were recorded with the TEM JEM JEOL 1400 plus and analyzed using ImageJ software, v1.52a. At least 100 particles were measured per synthesis from a minimum of three different areas.

High-angle annular dark-field scanning TEM (HAADF-STEM) and integrated differential contrast (iDPC) STEM imaging were conducted using a Thermo Fisher Scientific Titan Themis Cubed microscope operating at an acceleration voltage of 300 kV and tuned with a monochromator and probe corrector. HAADF-STEM and iDPC imaging were conducted using Velox software (Thermo Fisher Scientific, Ma, USA). TEM imaging was conducted using the same instrument and tuned with the image corrector. The micrographs were acquired with a direct electron detector (K2, Gatan Inc., Ca, USA) using the dose fractionation method (40 micrographs taken with bursts of 0.1 s of exposure), and the electron dose was kept under $15 \text{ e}^- / \text{\AA}^2 / \text{s}$ to ensure minimal damage due to the electron beam. The dose fractionation data were processed in Gatan Microscopy Suite 3 by importing each stack. The image stack was then subjected to $2 \times$ automated alignment procedures and then summed. To prepare the samples, a Lacey carbon 200 mesh copper grid (Agar Scientific, Essex, UK) was plasma treated using a Gatan Solarus 950 Advanced plasma system (Gatan Inc.) with O₂ for 30 s at 65 W. The TEM grid was suspended using reverse-action tweezers and using a micropipette, and a 7 μL aliquot of $100 \times$ diluted sample was deposited on the grid and left under cover overnight to enable the droplet to evaporate. To ensure complete evaporation and to minimize imaging artefacts, the grid was placed in an opened Eppendorf tube and kept under high vacuum overnight. The hydrodynamic diameters were determined by dynamic light scattering (DLS) and the zeta potential with

the Zetasizer Ultra (Malvern Panalytical) of a 1 g L^{-1} solution. For the measurements in different media (ddH₂O pH = 1–8, 50 mM PBS pH = 7.4, human plasma (Blutspendedienst des BRK, Munich, Germany)), 1 mL of the sample was sonicated for 30 min and then placed in a cuvette (Cuvette STD UV 4 clear side, KARTELL S.p.a.) and measured at 25 °C or 37 °C. Each determined number distribution resulted from a triple measurement evaluated with the Zetasizer software. The isoelectric point (IEP) was determined by the zeta potential measurements at different pH values (pH = 1–8). For the measurements, 800 μL of the sample was added to the flow cell (DTS1070, Malvern Instruments, $5\times$ measured). A Boltzmann fit was used to determine the pH value at which the surface charge reached zero. By powder X-ray diffraction (XRD), the lyophilized particles (Alpha 1-2 Ldplus, Christ, $-60 \text{ }^\circ\text{C}$ overnight in vacuum) were analyzed with the diffractometer STOE Stadi-P (flatbed measurement, molybdenum source (0.7093 \AA)). The saturation magnetization of the particles was determined with the use of the superconducting quantum interference device (SQUID) magnetometer. The samples (10 mg) were fixed in the center of a small plastic tube with the adhesive Fixogum (Marabu GmbH & Co KG, Tamm, Germany) and measured with the SQUID magnetometer MPMS XL-7 (Quantum Design, San Diego, CA, USA) at 300 K with a magnetic field variation of -50 kOe to $+50 \text{ kOe}$. Raman spectroscopy measurements were carried out using a Raman Senterra spectrometer from Bruker Optics, Germany (488 nm laser, 1 mW, exposure 10 s, 2 co-additions). The A_{1g} band of iron oxide was fitted between 600 and 750 cm^{-1} using Pseudovoigt functions (Origin) to investigate the influences of the different coatings on the magnetite to maghemite ratio [48]. The thermogravimetric analysis (TGA) of the lyophilized samples was carried out using STA 449C Jupiter in a $50.0 \text{ }\mu\text{L}$ aluminum oxide crucible ($5 \text{ mm} \times 4 \text{ mm}$). The weight change was detected from $25 \text{ }^\circ\text{C}$ to $700 \text{ }^\circ\text{C}$, holding an isotherm at $700 \text{ }^\circ\text{C}$ for ten minutes. The sedimentation rate as a function of the magnetic field was assessed with the LUMiReader (4532-123; LUM GmbH, Berlin, Germany). After ultrasonication, samples of 1.00 g L^{-1} (pH 7–7.4) were placed in contact with five stacked cylindrical neodymium boron ferrite (NdFeB) magnets ($d = 12 \text{ mm}$; $h = 2 \text{ mm}$, N45, Webcraft GmbH, Gottmadingen, Germany) and measured at wavelengths of 870 nm, 630 nm, and 420 nm (profile: 1000; interval: 1 s; angle: 0° ; light factor: 1.00; temperature: $25 \text{ }^\circ\text{C}$; magnetization $29.1\text{--}54.4 \text{ Am}^2 \text{ kg}^{-1}$). The processing of the obtained data was performed using the software PSA-Wizard (SEPviewTM; analysis positions: 13.0 mm, 15.0 mm, 17.0 mm, 19.0 mm).

3.3. Cytocompatibility

The cytocompatibility was assessed following the ISO-10993 guidelines. For the cytocompatibility assay, human umbilical artery smooth muscle cells (HUAECs, Promocell) were expanded in a culture medium consisting of DMEM supplemented with 10% fetal calf serum (FCS, Gibco) and a 1% antibiotic/antimycotic mix (ABM, Gibco). HUASMCs between passages 4 and 5 were used for the experiments. Before the experiments, the BIONs and IONs@CMD were sterilized using H₂O₂ low-temperature plasma and resuspended in the culture medium. After intense overhead shaking (30 min), the samples were diluted to 0.075 g L^{-1} . For the experiments, the cells were seeded on 96-well plates (Greiner Bio-One, Frickenhausen, Germany) at a concentration of $10.000 \text{ cells cm}^{-2}$ and incubated at $37 \text{ }^\circ\text{C}$ with 5% CO₂ for 24 h to allow for cell adhesion. Subsequently, the BIONs and IONs@CMD suspensions were added to the cells, and the cytotoxic effects were determined after 24 and 72 h qualitatively through cell imaging using a phase-contrast microscope (BZ-X800E, Keyence, Neu-Isenburg, Germany) and quantitatively using a commercial cell proliferation test (XTT; Roche, Mannheim, Germany). A culture medium served as a negative control, while a culture medium supplemented with 2% Triton x-100 (Sigma) was used as a positive control. The XTT test was performed according to the manufacturer's instructions. Briefly, after preparing the work solution by combining the electron coupling reagent (ECR) with the XTT solution (1:50), $50 \text{ }\mu\text{L}$ was transferred to each well, and the cells were incubated for two hours. The optical density of the formazan was measured at a wavelength of 450 nm and a reference wavelength of 630 nm using a spectrophotometer (Spark, Tecan,

Männendorf, Swiss). An additional measure at 0 h served as a reference to exclude the contribution of the particles to the optical density. The results are presented as normalized to the optical density of the negative control.

3.4. Peptide Loading

Electrostatic Binding: For the adsorption, different LL III (Genscript) solutions of 8 g L^{-1} , 4 g L^{-1} , 2 g L^{-1} , 1 g L^{-1} , 0.5 g L^{-1} , 0.2 g L^{-1} , and 0 g L^{-1} (also used as the calibration line) in 50 mM of PBS buffer (pH 7.4) were mixed (1:1, total volume 400 μL) with a 2 g L^{-1} ION@CMD12.5 particle solution. The triplicates were incubated for one hour at 25°C and 1000 rpm in a shaking incubator (Thermomixer C, Eppendorf). After incubation, the supernatant was removed for analysis via magnetic decantation for 10 min. The following two washing steps were performed with 200 μL of fresh PBS buffer (incubation: 10 min, 25°C , 1000 rpm). After the second washing step, 400 μL of PBS was added again to reach a particle concentration of 1 g L^{-1} . Before the LL content in the supernatant was determined, the samples were centrifuged for 5 min at $17,000\times g$ (Centrifuge 5418, Eppendorf, Hamburg, Germany) to separate any nanoparticles. After each step, 2.5 μL of supernatant was photometrically analyzed at 280 nm using the NanoPhotometer (Implen Nanophotometer N129).

Covalent Binding: For the generation of a covalent peptide bond between LL III and the free carboxyl group on the surface of the ION@CMD12.5 particles, a protocol developed by Merck Millipore was used [83]. Deviating from the protocol, a particulate stock solution of 2 g L^{-1} was washed and activated and then mixed in a 600:400 ratio with the LL stock solutions (6.25 g L^{-1} , 5 g L^{-1} , 3.75 g L^{-1} , 2.5 g L^{-1} , and 2 g L^{-1}). The incubation times, washing steps, and buffer compositions were performed analogously to the protocol. After the completion of the reaction, the samples were washed ($2\times$) with Millipore water.

3.5. Antimicrobial Behavior

The antimicrobial behavior of the covalent and adsorptive bound LL, as well as the ION@CMD12.5 particles, was tested with (RH)₄-GFP-expressing *E. coli* (BL21, DE3), performed analogously to Turrina et al. [31]. The ION@CMD@LL were diluted to 7.8 mg L^{-1} , 5 mg L^{-1} , 3 mg L^{-1} , 2 mg L^{-1} , 1 mg L^{-1} , 0.5 mg L^{-1} , 0.2 mg L^{-1} , and 0 mg L^{-1} . For the unloaded particles, a dilution series of 0 g L^{-1} , 0.1 g L^{-1} , 0.3 g L^{-1} , 0.5 g L^{-1} , 0.7 g L^{-1} , 1 g L^{-1} , 2 g L^{-1} , and 3 g L^{-1} was prepared. In the experiment, both particle types were finally diluted at 1:10.

4. Conclusions

Five CMD-coated IONs were successfully synthesized. Higher CMD concentrations in the synthesis led to an increasing polymer layer thickness and a reduced core size. With FT-IR, Raman, and XRD, a core-shell character was determined that can reduce the oxidation from magnetite to maghemite. While all the particles exhibited superparamagnetic properties, the saturation magnetization decreased due to the reduced core size. This study provides new insights into the physicochemical characteristics, e.g., particle agglomeration, magnetophoresis, and the zeta potentials. The coating could be visualized using different TEM techniques. Between a threshold range of $12.5\text{--}25.0 \text{ g L}^{-1}$, the CMD particles were deemed colloiddally stable over a broad pH spectrum (pH 1.5–8). All the IONs@CMD exhibited a negative surface charge at physiological pH values, promoting their stability in PBS and human plasma. Moreover, the negative zeta potentials were beneficial in binding an antimicrobial peptide to the surface. All the IONs@CMD were significantly more stable than uncoated IONs and showed hydrodynamic diameters of $<100 \text{ nm}$, fulfilling one of the most critical characteristics of drug delivery systems [23,25]. The STEP analysis demonstrated the significant impact of agglomeration on magnetophoresis ($18.4\text{--}160 \mu\text{m s}^{-1}$) and the overall stability attributed to the electrostatic and static repulsion of the CMD side chains. All the particles showed cytocompatibility ($>70\%$) over three days in smooth muscle cells. The ION@CMD12.5 particles showed ideal properties due to their ideal diameter

$d_{\text{TEM}} > 10$ nm, colloidal stability in water and human plasma, and good magnetization, making these nanocomposite materials an excellent candidate for magnetically controlled drug delivery.

The ION@CMD12.5 materials were suitable for both the adsorptive and covalent binding of therapeutic peptides. Significantly higher drug loadings (up to 62%) and an excellent efficiency (82.3%) were obtained with EDC/NHS coupling compared to the adsorptive method (DL 24%). The weaker electrostatic interactions were insufficient for efficient particle loading (28% efficiency). The DLS, zeta potential, FT-IR, and TGA measurements also proved the peptide loading capacity. Although the particles tended to agglomerate with increasing LL loading, an optimal hydrodynamic diameter was achieved at a drug loading of 0.55 g g^{-1} . The antimicrobial experiments showed that the unloaded particles had little or no effect on the cell growth. ION@CMD@LL (ads) and ION@CMD@LL (cov) have MICs of $1.13 \mu\text{M}$ and $1.70 \mu\text{M}$, respectively. These experiments demonstrated that the IONs@CMD can be successfully combined with antimicrobial peptides, producing an inexpensive and effective drug carrier.

Supplementary Materials: The following supporting information can be downloaded at: <https://www.mdpi.com/article/10.3390/ijms232314743/s1>, Figure S1: Raman Spectra of CMD; Equation (S1): Magnetite content; Table S1: Magnetite contents; Figure S2: Diffractograms; Equation (S2): Einstein–Stokes law; Figure S3: IEPs; Figure S4: SAXS profiles; Equation (S3): Scherrer equation; Figure S5: TEM micrographs; Figure S6: HAADF-STEM micrographs; Figure S7: Low-dose TEM micrographs; Figure S8: Low-dose TEM micrographs: agglomerate size; Table S2: Mean hydrodynamic diameters; Equation (S4): LangevinMod fit; Table S3: Sedimentation velocity; Figure S9: Cytocompatibility phase-contrast images; Figure S10: Additional content for adsorption of LL; Figure S11: TGA curve of LL; Table S4: Binding efficiency; Figure S12: OD600 measurements; Figure S13: Images of *E.coli* growth; Movie S1: ION@CMD@LL contacted to a magnet.

Author Contributions: The manuscript was written through the contributions of all the authors. C.T.: conceptualization, methodology, validation, formal analysis, investigation, data curation, writing—original draft, visualization; D.M.: investigation, data curation, writing—original draft, visualization; A.K.: investigation, data curation; D.M.R.-G.: methodology, investigation, data curation, writing—original draft; J.C.: methodology, investigation, data curation, writing—original draft; M.O.: methodology, investigation; B.S.: data curation, formal analysis; P.M.: resources, supervision; S.B.: resources, funding acquisition, writing—review and editing, supervision; S.P.S.: conceptualization, funding acquisition, writing—review and editing, supervision, project administration. All authors have read and agreed to the published version of the manuscript.

Funding: We appreciate the support of the TUM International Graduate School of Science and Engineering (IGSSE). Furthermore, we value the support of the Science Foundation Ireland (grant reference number: 12/RI/2345/SOF). The funders had no role in the design of the study; the collection, analyses, and interpretation of data; in the writing of the manuscript; or in the decision to publish the results.

Informed Consent Statement: Not applicable.

Data Availability Statement: The datasets generated and/or analyzed during the current study are available from the corresponding author on reasonable request.

Acknowledgments: We are thankful to Tom Nilges (Technical University of Munich) for providing the X-ray diffractometer and for supporting Carsten Peters (Technical University of Munich) with the TEM measurements. The graphical abstract and Figure 6c were created with BioRender.com.

Conflicts of Interest: The authors declare no conflict of interest.

Abbreviations

CMD, carboxymethyl-dextran; IONs, iron oxide nanoparticles; BIONs, bare iron oxide nanoparticles; FT-IR, Fourier transform infrared; DLS, dynamic light scattering; XRD, X-ray diffraction; LL, la-sioglossin III; SQUID, superconducting quantum interference device; IEP, isoelectric point; SAXS, small-angle X-ray scattering; TEM, transmission electron microscopy; EMA, European Medicines Agency

References

1. Soares, S.; Sousa, J.; Pais, A.; Vitorino, C. Nanomedicine: Principles, Properties, and Regulatory Issues. *Front. Chem.* **2018**, *6*, 360. [[CrossRef](#)] [[PubMed](#)]
2. Lu, A.-H.; Salabas, E.L.; Schüth, F. Magnetic nanoparticles: Synthesis, protection, functionalization, and application. *Angew. Chem. Int. Ed.* **2007**, *46*, 1222–1244. [[CrossRef](#)] [[PubMed](#)]
3. Bleul, R.; Baki, A.; Freese, C.; Paysen, H.; Kosch, O.; Wiekhorst, F. Continuously manufactured single-core iron oxide nanoparticles for cancer theranostics as valuable contribution in translational research. *Nanoscale Adv.* **2020**, *2*, 4510–4521. [[CrossRef](#)] [[PubMed](#)]
4. He, X.; Zhu, Y.; Yang, L.; Wang, Z.; Wang, Z.; Feng, J.; Wen, X.; Cheng, L.; Zhu, R. Embryonic Stem Cell Pluripotency: MgFe-LDH Nanoparticles: A Promising Leukemia Inhibitory Factor Replacement for Self-Renewal and Pluripotency Maintenance in Cultured Mouse Embryonic Stem Cells. *Adv. Sci.* **2021**, *8*, 2170049. [[CrossRef](#)]
5. Saxena, S.K. *NanoBioMedicine*; Springer Singapore Pte. Limited: Singapore, 2020.
6. Pierre, V.C.; Allen, M.J. (Eds.) *Contrast Agents for MRI: Experimental Methods*; Royal Society of Chemistry: Cambridge, UK, 2018.
7. Qiao, R.; Yang, C.; Gao, M. Superparamagnetic iron oxide nanoparticles: From preparations to in vivo MRI applications. *J. Mater. Chem.* **2009**, *19*, 6274. [[CrossRef](#)]
8. Barani, M.; Rahdar, A.; Mukhtar, M.; Razzaq, S.; Qindeel, M.; Olam, S.A.H.; Paiva-Santos, A.C.; Ajalli, N.; Sargazi, S.; Balakrishnan, D.; et al. Recent application of cobalt ferrite nanoparticles as a theranostic agent. *Mater. Today Chem.* **2022**, *26*, 101131. [[CrossRef](#)]
9. Bleeker, E.A.J.; de Jong, W.H.; Geertsma, R.E.; Groenewold, M.; Heugens, E.H.W.; Koers-Jacquemijns, M.; van de Meent, D.; Popma, J.R.; Rietveld, A.G.; Wijnhoven, S.W.P.; et al. Considerations on the EU definition of a nanomaterial: Science to support policy making. *Regul. Toxicol. Pharmacol.* **2013**, *65*, 119–125. [[CrossRef](#)] [[PubMed](#)]
10. Tinkle, S.; McNeil, S.E.; Mühlebach, S.; Bawa, R.; Borchard, G.; Barenholz, Y.C.; Tamarkin, L.; Desai, N. Nanomedicines: Addressing the scientific and regulatory gap. *Ann. N. Y. Acad. Sci.* **2014**, *1313*, 35–56. [[CrossRef](#)] [[PubMed](#)]
11. Pita, R.; Ehmann, F.; Papaluca, M. Nanomedicines in the EU-Regulatory Overview. *AAPS J.* **2016**, *18*, 1576–1582. [[CrossRef](#)] [[PubMed](#)]
12. Feng, Q.; Liu, Y.; Huang, J.; Chen, K.; Huang, J.; Xiao, K. Uptake, distribution, clearance, and toxicity of iron oxide nanoparticles with different sizes and coatings. *Sci. Rep.* **2018**, *8*, 2082. [[CrossRef](#)] [[PubMed](#)]
13. Lin, P.-C.; Lin, S.; Wang, P.C.; Sridhar, R. Techniques for physicochemical characterization of nanomaterials. *Biotechnol. Adv.* **2014**, *32*, 711–726. [[CrossRef](#)] [[PubMed](#)]
14. Nano on reflection. *Nat. Nanotechnol.* **2016**, *11*, 828–834. [[CrossRef](#)] [[PubMed](#)]
15. Wu, W.; Jiang, C.Z.; Roy, V.A.L. Designed synthesis and surface engineering strategies of magnetic iron oxide nanoparticles for biomedical applications. *Nanoscale* **2016**, *8*, 19421–19474. [[CrossRef](#)] [[PubMed](#)]
16. Keck, C.M.; Müller, R.H. Nanotoxicological classification system (NCS)—A guide for the risk-benefit assessment of nanoparticulate drug delivery systems. *Eur. J. Pharm. Biopharm.* **2013**, *84*, 445–448. [[CrossRef](#)] [[PubMed](#)]
17. de Jong, W.H.; Hagens, W.I.; Krystek, P.; Burger, M.C.; Sips, A.J.A.M.; Geertsma, R.E. Particle size-dependent organ distribution of gold nanoparticles after intravenous administration. *Biomaterials* **2008**, *29*, 1912–1919. [[CrossRef](#)] [[PubMed](#)]
18. Adabi, M.; Naghibzadeh, M.; Adabi, M.; Zarrinfard, M.A.; Esnaashari, S.S.; Seifalian, A.M.; Faridi-Majidi, R.; Aiyelabegan, H.T.; Ghanbari, H. Biocompatibility and nanostructured materials: Applications in nanomedicine. *Artif. Cells Nanomed. Biotechnol.* **2017**, *45*, 833–842. [[CrossRef](#)]
19. Gaspar, R.S. Therapeutic Products: Regulating Drugs and Medical Devices. In *International Handbook on Regulating Nanotechnologies*; Hodge, G., Bowman, D., Maynard, A., Hodge, G.A., Maynard, A.D., Eds.; Edward Elgar Publishing: Northampton, MA, USA; Cheltenham, UK, 2010.
20. Wu, W.; Wu, Z.; Yu, T.; Jiang, C.; Kim, W.-S. Recent progress on magnetic iron oxide nanoparticles: Synthesis, surface functional strategies and biomedical applications. *Sci. Technol. Adv. Mater.* **2015**, *16*, 23501. [[CrossRef](#)] [[PubMed](#)]
21. Massart, R. Preparation of aqueous magnetic liquids in alkaline and acidic media. *IEEE Trans. Magn.* **1981**, *17*, 1247–1248. [[CrossRef](#)]
22. Mylkie, K.; Nowak, P.; Rybczynski, P.; Ziegler-Borowska, M. Polymer-Coated Magnetite Nanoparticles for Protein Immobilization. *Materials* **2021**, *14*, 248. [[CrossRef](#)] [[PubMed](#)]
23. Laurent, S.; Forge, D.; Port, M.; Roch, A.; Robic, C.; Elst, L.V.; Muller, R.N. Magnetic iron oxide nanoparticles: Synthesis, stabilization, vectorization, physicochemical characterizations, and biological applications. *Chem. Rev.* **2008**, *108*, 2064–2110. [[CrossRef](#)] [[PubMed](#)]
24. Kievit, F.M.; Zhang, M. Surface engineering of iron oxide nanoparticles for targeted cancer therapy. *Acc. Chem. Res.* **2011**, *44*, 853–862. [[CrossRef](#)]
25. Jain, S.; Devarajan, P.V. (Eds.) *Targeted Drug Delivery Concepts and Design*; Springer: Cham, Switzerland, 2015.
26. Muthiah, M.; Park, I.-K.; Cho, C.-S. Surface modification of iron oxide nanoparticles by biocompatible polymers for tissue imaging and targeting. *Biotechnol. Adv.* **2013**, *31*, 1224–1236. [[CrossRef](#)] [[PubMed](#)]
27. Wolfram, J.; Yang, Y.; Shen, J.; Moten, A.; Chen, C.; Shen, H.; Ferrari, M.; Zhao, Y. The nano-plasma interface: Implications of the protein corona. *Colloids Surf. B Biointerfaces* **2014**, *124*, 17–24. [[CrossRef](#)] [[PubMed](#)]

28. Tenzer, S.; Docter, D.; Kuharev, J.; Musyanovych, A.; Fetz, V.; Hecht, R.; Schlenk, F.; Fischer, D.; Kiouptsi, K.; Reinhardt, C.; et al. Rapid formation of plasma protein corona critically affects nanoparticle pathophysiology. *Nat. Nanotechnol.* **2013**, *8*, 772–781. [[CrossRef](#)] [[PubMed](#)]
29. Albanese, A.; Tang, P.S.; Chan, W.C.W. The effect of nanoparticle size, shape, and surface chemistry on biological systems. *Annu. Rev. Biomed. Eng.* **2012**, *14*, 1–16. [[CrossRef](#)] [[PubMed](#)]
30. Vasić, K.; Knez, Ž.; Konstantinova, E.A.; Kokorin, A.I.; Gyergyek, S.; Leitgeb, M. Structural and magnetic characteristics of carboxymethyl dextran coated magnetic nanoparticles: From characterization to immobilization application. *React. Funct. Polym.* **2020**, *148*, 104481. [[CrossRef](#)]
31. Turrina, C.; Berensmeier, S.; Schwaminger, S.P. Bare Iron Oxide Nanoparticles as Drug Delivery Carrier for the Short Cationic Peptide Lasioglossin. *Pharmaceuticals* **2021**, *14*, 405. [[CrossRef](#)] [[PubMed](#)]
32. Ahmadi, M. Iron oxide nanoparticles for delivery purposes. In *Nanoengineered Biomaterials for Advanced Drug Delivery*; Mozafari, M., Ed.; Elsevier: San Diego, CA, USA, 2020; pp. 373–393.
33. de Chickera, S.N.; Snir, J.; Willert, C.; Rohani, R.; Foley, R.; Foster, P.J.; Dekaban, G.A. Labelling dendritic cells with SPIO has implications for their subsequent in vivo migration as assessed with cellular MRI. *Contrast Media Mol. Imaging* **2011**, *6*, 314–327. [[CrossRef](#)] [[PubMed](#)]
34. Santosh, S.; Podaralla, P.; Miller, B. Anaphylaxis with elevated serum tryptase after administration of intravenous ferumoxytol. *NDT Plus* **2010**, *3*, 341–342. [[CrossRef](#)] [[PubMed](#)]
35. Ayala, V.; Herrera, A.P.; Latorre-Esteves, M.; Torres-Lugo, M.; Rinaldi, C. Effect of surface charge on the colloidal stability and in vitro uptake of carboxymethyl dextran-coated iron oxide nanoparticles. *J. Nanopart. Res.* **2013**, *15*, 1874. [[CrossRef](#)]
36. Ning, S.; Huang, Q.; Sun, X.; Li, C.; Zhang, Y.; Li, J.; Liu, Y.-N. Carboxymethyl dextran-coated liposomes: Toward a robust drug delivery platform. *Soft Matter* **2011**, *7*, 9394. [[CrossRef](#)]
37. Li, J.; Zhou, Y.; Li, M.; Xia, N.; Huang, Q.; Do, H.; Liu, Y.-N.; Zhou, F. Carboxymethylated dextran-coated magnetic iron oxide nanoparticles for regenerable bioseparation. *J. Nanosci. Nanotechnol.* **2011**, *11*, 10187–10192. [[CrossRef](#)] [[PubMed](#)]
38. Dubiel, E.A.; Kuehn, C.; Wang, R.; Vermette, P. In vitro morphogenesis of PANC-1 cells into islet-like aggregates using RGD-covered dextran derivative surfaces. *Colloids Surf. B Biointerfaces* **2012**, *89*, 117–125. [[CrossRef](#)] [[PubMed](#)]
39. Mishra, B.; Basu, A.; Saravanan, R.; Xiang, L.; Yang, L.K.; Leong, S.S.J. Lasioglossin-III: Antimicrobial characterization and feasibility study for immobilization applications. *RSC Adv.* **2013**, *3*, 9534. [[CrossRef](#)]
40. Battista, F.; Oliva, R.; del Vecchio, P.; Winter, R.; Petraccone, L. Insights into the Action Mechanism of the Antimicrobial Peptide Lasioglossin III. *Int. J. Mol. Sci.* **2021**, *22*, 2857. [[CrossRef](#)] [[PubMed](#)]
41. Seo, M.-D.; Won, H.-S.; Kim, J.-H.; Mishig-Ochir, T.; Lee, B.-J. Antimicrobial peptides for therapeutic applications: A review. *Molecules* **2012**, *17*, 12276–12286. [[CrossRef](#)] [[PubMed](#)]
42. Cerošský, V.; Budešínský, M.; Hovorka, O.; Cvacka, J.; Voburka, Z.; Slaninová, J.; Borovicková, L.; Fucík, V.; Bednářová, L.; Votruba, I.; et al. Lasioglossins: Three novel antimicrobial peptides from the venom of the eusocial bee *Lasioglossum laticeps* (Hymenoptera: Halictidae). *Chembiochem* **2009**, *10*, 2089–2099. [[CrossRef](#)]
43. *International Handbook on Regulating Nanotechnologies*; Edward Elgar Publishing: Northampton, MA, USA; Cheltenham, UK, 2010.
44. Sigma Aldrich, IR Spectrum Table & Chart. 2022. Available online: <https://www.sigmaaldrich.com/DE/de/technical-documents/technical-article/analytical-chemistry/photometry-and-reflectometry/ir-spectrum-table> (accessed on 11 November 2022).
45. Kawni, I.A.; Garcia, R.; Youssef, S.; Abboud, M.; Podlecki, J.; Habchi, R. Stabilization and encapsulation of magnetite nanoparticles. *Mater. Res. Express* **2016**, *3*, 125024. [[CrossRef](#)]
46. Liu, G.; Hong, R.Y.; Guo, L.; Li, Y.G.; Li, H.Z. Preparation, characterization and MRI application of carboxymethyl dextran coated magnetic nanoparticles. *Appl. Surf. Sci.* **2011**, *257*, 6711–6717. [[CrossRef](#)]
47. Das, M.; Oyarzabal, E.A.; Chen, L.; Lee, S.-H.; Shah, N.; Gerlach, G.; Zhang, W.; Chao, T.-H.H.; van den Berge, N.; Liu, C.; et al. One-pot synthesis of carboxymethyl-dextran coated iron oxide nanoparticles (CION) for preclinical fMRI and MRA applications. *Neuroimage* **2021**, *238*, 118213. [[CrossRef](#)]
48. Schwaminger, S.; Syhr, C.; Berensmeier, S. Controlled Synthesis of Magnetic Iron Oxide Nanoparticles: Magnetite or Maghemite? *Crystals* **2020**, *10*, 214. [[CrossRef](#)]
49. Mathlouthi, M.; Luu, D.V. Laser-Raman spectra of d-glucose and sucrose in aqueous solution. *Carbohydr. Res.* **1980**, *81*, 203–212. [[CrossRef](#)]
50. Deshmukh, S.; Bhandal, K.; Carpick, B.; Kirkitadze, M. Identification of Individual Components from the Manufacturing Chain of a Final Vaccine Product by Raman Spectroscopy. *American Pharmaceutical Review* **2016**, *5*.
51. Rebodos, R.L.; Vikesland, P.J. Effects of oxidation on the magnetization of nanoparticulate magnetite. *Langmuir* **2010**, *26*, 16745–16753. [[CrossRef](#)] [[PubMed](#)]
52. Schwaminger, S.P.; Bauer, D.; Fraga-García, P.; Wagner, F.E.; Berensmeier, S. Oxidation of magnetite nanoparticles: Impact on surface and crystal properties. *CrystEngComm* **2017**, *19*, 246–255. [[CrossRef](#)]
53. McBain, S.C.; Yiu, H.H.P.; Dobson, J. Magnetic nanoparticles for gene and drug delivery. *Int. J. Nanomed.* **2008**, *3*, 169–180. [[CrossRef](#)]
54. Taufiq, A.; Nikmah, A.; Hidayat, A.; Sunaryono, S.; Mufti, N.; Hidayat, N.; Susanto, H. Synthesis of magnetite/silica nanocomposites from natural sand to create a drug delivery vehicle. *Heliyon* **2020**, *6*, e03784. [[CrossRef](#)]
55. Griffiths, J.R. Are cancer cells acidic? *Br. J. Cancer* **1991**, *64*, 425–427. [[CrossRef](#)]

56. Modi, S.; Swetha, M.G.; Goswami, D.; Gupta, G.D.; Mayor, S.; Krishnan, Y. A DNA nanomachine that maps spatial and temporal pH changes inside living cells. *Nat. Nanotechnol.* **2009**, *4*, 325–330. [[CrossRef](#)]
57. Ray, S. The Cell: A Molecular Approach. *Yale J. Biol. Med.* **2014**, *87*, 603–604.
58. Lunardi, C.N.; Gomes, A.J.; Rocha, F.S.; de Tommaso, J.; Patience, G.S. Experimental methods in chemical engineering: Zeta potential. *Can. J. Chem. Eng.* **2021**, *99*, 627–639. [[CrossRef](#)]
59. Gekko, K.; Noguchi, H. Potentiometric studies of hydrophobic effect on ion binding of ionic dextran derivatives. *Biopolym. Orig. Res. Biomol.* **1975**, *14*, 2555–2565. [[CrossRef](#)]
60. Sun, T.; Zhang, Y.S.; Pang, B.; Hyun, D.C.; Yang, M.; Xia, Y. Engineered nanoparticles for drug delivery in cancer therapy. *Angew. Chem. Int. Ed Engl.* **2014**, *53*, 12320–12364. [[CrossRef](#)] [[PubMed](#)]
61. Ceña, V.; Játiva, P. Nanoparticle crossing of blood-brain barrier: A road to new therapeutic approaches to central nervous system diseases. *Nanomedicine* **2018**, *13*, 1513–1516. [[CrossRef](#)]
62. Betzer, O.; Shilo, M.; Opochninsky, R.; Barnoy, E.; Motiei, M.; Okun, E.; Yadid, G.; Popovtzer, R. The effect of nanoparticle size on the ability to cross the blood-brain barrier: An in vivo study. *Nanomedicine* **2017**, *12*, 1533–1546. [[CrossRef](#)]
63. Roth, H.-C.; Schwaminger, S.P.; Schindler, M.; Wagner, F.E.; Berensmeier, S. Influencing factors in the CO-precipitation process of superparamagnetic iron oxide nano particles: A model based study. *J. Magn. Magn. Mater.* **2015**, *377*, 81–89. [[CrossRef](#)]
64. Martínez-Mera, I.; Espinosa-Pesqueira, M.E.; Pérez-Hernández, R.; Arenas-Alatorre, J. Synthesis of magnetite (Fe₃O₄) nanoparticles without surfactants at room temperature. *Mater. Lett.* **2007**, *61*, 4447–4451. [[CrossRef](#)]
65. Sebastian, V.; Arruebo, M.; Santamaria, J. Reaction engineering strategies for the production of inorganic nanomaterials. *Small* **2014**, *10*, 835–853. [[CrossRef](#)]
66. Gupta, N.; Chan, R.; Nimesh, S. (Eds.) *Advances in Nanomedicine for the Delivery of Therapeutic Nucleic Acids*; Woodhead Publishing: Duxford, UK, 2017.
67. Ahn, T.; Kim, J.H.; Yang, H.-M.; Lee, J.W.; Kim, J.-D. Formation Pathways of Magnetite Nanoparticles by Coprecipitation Method. *J. Phys. Chem. C* **2012**, *116*, 6069–6076. [[CrossRef](#)]
68. Latorre-Esteves, M.; Cortés, A.; Torres-Lugo, M.; Rinaldi, C. Synthesis and characterization of carboxymethyl dextran-coated Mn/Zn ferrite for biomedical applications. *J. Magn. Magn. Mater.* **2009**, *321*, 3061–3066. [[CrossRef](#)]
69. Almasri, D.A.; Saleh, N.B.; Atieh, M.A.; McKay, G.; Ahzi, S. Adsorption of phosphate on iron oxide doped halloysite nanotubes. *Sci. Rep.* **2019**, *9*, 3232. [[CrossRef](#)] [[PubMed](#)]
70. Coppola, L.; Caserta, F.; de Lucia, D.; Guastafierro, S.; Grassia, A.; Coppola, A.; Marfella, R.; Varricchio, M. Blood viscosity and aging. *Arch. Gerontol. Geriatr.* **2000**, *31*, 35–42. [[CrossRef](#)] [[PubMed](#)]
71. Zhang, H.; Wu, T.; Yu, W.; Ruan, S.; He, Q.; Gao, H. Ligand Size and Conformation Affect the Behavior of Nanoparticles Coated with in Vitro and in Vivo Protein Corona. *ACS Appl. Mater. Interfaces* **2018**, *10*, 9094–9103. [[CrossRef](#)] [[PubMed](#)]
72. Safi, M.; Courtois, J.; Seigneuret, M.; Conjeaud, H.; Berret, J.-F. The effects of aggregation and protein corona on the cellular internalization of iron oxide nanoparticles. *Biomaterials* **2011**, *32*, 9353–9363. [[CrossRef](#)]
73. Tekie, F.S.M.; Hajiramezani, M.; Geramifar, P.; Raoufi, M.; Dinarvand, R.; Soleimani, M.; Atyabi, F. Controlling evolution of protein corona: A prosperous approach to improve chitosan-based nanoparticle biodistribution and half-life. *Sci. Rep.* **2020**, *10*, 9664. [[CrossRef](#)]
74. Koo, K.N.; Ismail, A.F.; Othman, M.H.D.; Bidin, N.; Rahman, M.A. Preparation and characterization of superparamagnetic magnetite (Fe₃O₄) nanoparticles: A short review. *Mal. J. Fund. Appl. Sci.* **2019**, *15*, 23–31. [[CrossRef](#)]
75. Unterweger, H.; Tietze, R.; Janko, C.; Zaloga, J.; Lyer, S.; Dürr, S.; Taccardi, N.; Goudouri, O.-M.; Hoppe, A.; Eberbeck, D.; et al. Development and characterization of magnetic iron oxide nanoparticles with a cisplatin-bearing polymer coating for targeted drug delivery. *Int. J. Nanomed.* **2014**, *9*, 3659–3676. [[CrossRef](#)]
76. Wittmann, L.; Turrina, C.; Schwaminger, S.P. The Effect of pH and Viscosity on Magnetophoretic Separation of Iron Oxide Nanoparticles. *Magnetochemistry* **2021**, *7*, 80. [[CrossRef](#)]
77. Schwaminger, S.P.; Schwarzenberger, K.; Gatzemeier, J.; Lei, Z.; Eckert, K. Magnetically Induced Aggregation of Iron Oxide Nanoparticles for Carrier Flotation Strategies. *ACS Appl. Mater. Interfaces* **2021**, *13*, 20830–20844. [[CrossRef](#)]
78. Kumar, M.; Singh, G.; Arora, V.; Mewar, S.; Sharma, U.; Jagannathan, N.R.; Sapra, S.; Dinda, A.K.; Kharbanda, S.; Singh, H. Cellular interaction of folic acid conjugated superparamagnetic iron oxide nanoparticles and its use as contrast agent for targeted magnetic imaging of tumor cells. *Int. J. Nanomedicine* **2012**, *7*, 3503–3516. [[CrossRef](#)]
79. Zhang, S.; Chen, X.; Gu, C.; Zhang, Y.; Xu, J.; Bian, Z.; Yang, D.; Gu, N. The Effect of Iron Oxide Magnetic Nanoparticles on Smooth Muscle Cells. *Nanoscale Res. Lett.* **2009**, *4*, 70–77. [[CrossRef](#)]
80. Luo, B.; Xu, S.; Luo, A.; Wang, W.-R.; Wang, S.-L.; Guo, J.; Lin, Y.; Zhao, D.-Y.; Wang, C.-C. Mesoporous biocompatible and acid-degradable magnetic colloidal nanocrystal clusters with sustainable stability and high hydrophobic drug loading capacity. *ACS Nano* **2011**, *5*, 1428–1435. [[CrossRef](#)]
81. Qu, J.-B.; Shao, H.-H.; Jing, G.-L.; Huang, F. PEG-chitosan-coated iron oxide nanoparticles with high saturated magnetization as carriers of 10-hydroxycamptothecin: Preparation, characterization and cytotoxicity studies. *Colloids Surf. B Biointerfaces* **2013**, *102*, 37–44. [[CrossRef](#)] [[PubMed](#)]
82. Abarca-Cabrera, L.; Fraga-García, P.; Berensmeier, S. Bio-nano interactions: Binding proteins, polysaccharides, lipids and nucleic acids onto magnetic nanoparticles. *Biomater. Res.* **2021**, *25*, 12. [[CrossRef](#)]

83. Millipore, M. *Microsphere Coupling—Two-Step EDC/Sulfo NHS Covalent Coupling Procedure for Estapor[®] Carboxyl-Modified Dyed Microspheres*; EMD Millipore Corporation: Burlington, MA, USA, 2015.
84. Hornig, S.; Bunjes, H.; Heinze, T. Preparation and characterization of nanoparticles based on dextran-drug conjugates. *J. Colloid Interface Sci.* **2009**, *338*, 56–62. [[CrossRef](#)] [[PubMed](#)]
85. Daus, S.; Heinze, T. Xylan-based nanoparticles: Prodrugs for ibuprofen release. *Macromol. Biosci.* **2010**, *10*, 211–220. [[CrossRef](#)]
86. Dandurand, J.; Samouillan, V.; Lacoste-Ferre, M.H.; Lacabanne, C.; Bochicchio, B.; Pepe, A. Conformational and thermal characterization of a synthetic peptidic fragment inspired from human tropoelastin: Signature of the amyloid fibers. *Pathol. Biol.* **2014**, *62*, 100–107. [[CrossRef](#)]
87. Samouillan, V.; Dandurand-Lods, J.; Lamure, A.; Maurel, E.; Lacabanne, C.; Gerosa, G.; Venturini, A.; Casarotto, D.; Gherardini, L.; Spina, M. Thermal analysis characterization of aortic tissues for cardiac valve bioprostheses. *J. Biomed. Mater. Res.* **1999**, *46*, 531–538. [[CrossRef](#)]
88. Sionkowska, A.; Skopinska-Wisniewska, J.; Gawron, M.; Kozłowska, J.; Planecka, A. Chemical and thermal cross-linking of collagen and elastin hydrolysates. *Int. J. Biol. Macromol.* **2010**, *47*, 570–577. [[CrossRef](#)] [[PubMed](#)]
89. Wu, C.C.; Mason, T.O. Thermopower Measurement of Cation Distribution in Magnetite. *J. Am. Ceram. Soc.* **1981**, *64*, 520–522. [[CrossRef](#)]
90. Chakraborty, S.; Rusli, H.; Nath, A.; Sikder, J.; Bhattacharjee, C.; Curcio, S.; Drioli, E. Immobilized biocatalytic process development and potential application in membrane separation: A review. *Crit. Rev. Biotechnol.* **2016**, *36*, 43–58. [[CrossRef](#)] [[PubMed](#)]
91. Eş, I.; Vieira, J.D.G.; Amaral, A.C. Principles, techniques, and applications of biocatalyst immobilization for industrial application. *Appl. Microbiol. Biotechnol.* **2015**, *99*, 2065–2082. [[CrossRef](#)] [[PubMed](#)]
92. Chen, J.-P.; Yang, P.-C.; Ma, Y.-H.; Lu, Y.-J. Superparamagnetic iron oxide nanoparticles for delivery of tissue plasminogen activator. *J. Nanosci. Nanotechnol.* **2011**, *11*, 11089–11094. [[CrossRef](#)] [[PubMed](#)]

3.4. Iron oxide nanoparticles with supramolecular ureidopyrimidinone coating

Uniquely designed nanostructures and nanomaterials can be used to overcome current medical issues. A new and innovative approach is the combination of supramolecular engineering and IONs. IONs offer a fast and cost-efficient synthesis, superparamagnetic behavior, a high surface-to-volume ratio, and the possibility to bind a considerable amount of drugs. Furthermore, they can be visualized by MRI and heated by an alternating magnetic field. This process is called hyperthermia. The combination with UPy-molecules allows the formation of a supramolecular network as a coating. UPy-moieties can form dimers with hydrophobic pockets by hydrogen bonding. These dimers can stack and form long fibers.

In this study, UPy-coated IONs are synthesized in a three-step process. The particles get coated with APTS, functionalized with PGA, and UPy-NH₂ can interact with the free aldehydes by imine formation. The successful binding was demonstrated with FT-IR and TGA measurements. Furthermore, the properties of the new ION species were determined by XRD, SQUID, DLS, Zeta potential, and the Nile red analysis. The UPy-layer leads to a positive surface charge around the superparamagnetic core. NR indicates the formation of hydrophobic pockets and the formation of fibers due to a significant blue shift. ION@UPy-NH₂ have a hydrodynamic diameter of 177 nm at pH 7 and a saturation magnetization of 31 emu g⁻¹. This successful coating is the first essential step in generating an innovative magnetically controlled drug delivery system that can flexibly bind UPy-drug molecules by self-assembly.

The study was carried out supported by our cooperation partner Prof. Patricia Y.W. Dankers at the Eindhoven University of Technology. The doctoral candidate's substantial contribution was the study's conception and design after a critical review of existing literature. The doctoral candidate carried out all experimental work, data analysis, and processing and was the leading author.

Chiara Turrina, Patricia Y.W. Dankers, Sonja Berensmeier and Sebastian Schwaminger*

Iron oxide nanoparticles with supramolecular ureidopyrimidinone coating

<https://doi.org/10.1515/cdbme-2022-1004>

Abstract: Superparamagnetic iron oxide nanoparticles are a promising material in nanomedicine, especially for generating magnetically controlled drug delivery systems. We developed an innovative ureidopyrimidinone (UPy) coating based on supramolecular hydrogen bonding units. The synthesized nanoparticles possess a positively charged surface with a hydrodynamic diameter of 177 nm at pH 7 and magnetization of 31 emu g⁻¹. The system has the potential to be modified by drugs or bioactive molecules altered with UPy units.

Keywords: Iron oxide nanoparticles, ureidopyrimidinone, cationic coating, supramolecular system

1 Introduction

In nanomedicine, specially designed nano-devices or nanostructures are used to offer new solutions to biomedical problems. The focus of research are mainly the four big multidisciplinary areas of diagnostics, therapeutics, drug delivery systems, and regenerative medicine [1]. Iron oxide nanoparticles (IONs) are biocompatible, can be fast and cost-efficient synthesized by co-precipitation, have a high specific surface area with the potential to bind a considerable amount of drug, and have the possibility of external guidance by a magnetic field because of their superparamagnetic character [2]. The IONs can be used as T2 contrast agents for magnetic resonance imaging and in cancer therapy through hyperthermia [1]. An external alternating magnetic field can be applied to generate heat, leading to cell death by lysosomal permeability [3].

*Corresponding author: **Sebastian Schwaminger:** Technical University of Munich, School of Engineering and Design, Munich, Germany; Medical University Graz, Stiftingtalstraße 6, Graz, Austria, e-mail: s.schwaminger@tum.de; sebastian.schwaminger@medunigraz.at

1s Author Chiara Turrina, 3rd Author Sonja Berensmeier: Technical University of Munich, School of Engineering and Design Munich, Germany

2nd Author Patricia Dankerst: Eindhoven University of Technology, Eindhoven, Department of Biomedical Engineering Netherlands

Furthermore, the IONs can be used for magnetically guiding stem cells for tissue engineering [1, 4]. Magnetically controlled drug delivery allows carrying the drug directly to cancer cells and generates a high local concentration [5]. This accumulation can lead to an overall drug reduction and efficient treatment by avoiding the drug's toxicity to healthy cells [5, 6]. Organic or inorganic coatings are often applied to improve the particle properties of bare IONs (BIONs). Specially designed layers generate a biocompatible core-shell structure and protect the BIONs from uncontrolled oxidation and aggregation [2, 7].

Supramolecular systems based on the fourfold hydrogen bonding ureido-pyrimidinone moieties can be applied as coating materials. The amphiphilic supramolecular molecule is based on a UPy unit combined with a urea moiety, a hydrophobic alkyl spacer connected to an amine-functionalized, water-soluble oligo ethylene glycol group by a urethane unit. [8]. The UPy molecules can assemble into fibrous aggregates by hydrogen bonding protected by hydrophobic pockets composed of additional hydrogen bonding of the urethane groups [9]. UPy-moieties can be designed to form different biomaterials like hydrogels, elastomers, or self-healing polymers. Dankers et al. have analyzed eleven different UPy-compounds regarding their cytotoxicity. They showed that the UPy-based materials did not affect the cell viability and did not show immunogenic or mutagenic behavior. The in vitro experiments have shown good biocompatibility for the UPy-based biomaterials. A large library of differently covalently functionalized UPy units exists [10]. For example, a drug bound to a UPy moiety can be easily mixed in to form a multi-component functional supramolecular system [11, 12] UPy-coated IONs have the potential to be used for magnetically controlled drug delivery with flexible added UPy functionalized drugs.

In this work, UPy-coated IONs are synthesized by imine formation of polyglutaraldehyde functionalized IONs with UPy-NH₂ (C₅₀H₉₇CIN₈O₁₆, UPy-C6-Urea-C12-Urethane-PEG12-C2-NH₃Cl, 1101.82 g/mol) The ION@UPy-NH₂ are characterized by Fourier-transform infrared spectra (FT-IR), X-ray diffraction (XRD), and thermogravimetric analysis (TGA) regarding their composition. The magnetization is analyzed by the superconducting quantum interference device (SQUID). The surface properties are determined with zeta potential measurements. The formation of hydrophobic

pockets was analyzed with the dye Nile Red, which is strongly fluorescent when encapsulated in a hydrophobic compartment. The hydrodynamic diameters are compared at different pH values in the last step.

2 Materials and methods

2.1 Synthesis of ION@PGA@UPy-NH₂

BIONs are synthesized by co-precipitation via the Massart process [13]. To prepare ION@APTS, 2.00 g BIONs are dispersed in 600 mL absolute ethanol and ultrasonicated for one hour. After adding 12.0 mL (3-Aminopropyl)triethoxysilan (APTS, Sigma-Aldrich), the particles are ultrasonicated for one hour. Via magnetic decantation, the ION@APTS are washed with ethanol (4x) and water (3x) until the conductivity drops below 150 $\mu\text{S}/\text{cm}$.

400 mg ION@APTS are dispersed in 400 mL of a 2% glutaraldehyde water solution. The pH is adjusted to pH 11 NaOH solution, and the dispersion is stirred for one hour. The ION@APTS@PGA are washed multiple times with water (10x), 0.50 M NaCl (2x), water (10x), and 0.50 M NaCl (2x), and finally three times with water.

20.0 mg of ION@APTS@PGA are dispersed in 1.00 mL 20.0 mM Na₃PO₄ and 1.00 M NaCl buffer (pH 6.8). Before adding 6.70 mg UPy-NH₂, the particles are ultrasonicated for 15 min. The suspension is again ultrasonicated for 5 min and incubated at 25 °C, 1000 rpm overnight, washed with buffer (5x), and water (2x) by magnetic decantation (conductivity <150 $\mu\text{S}/\text{cm}$).

2.2 Characterizations

Zeta potential and dynamic light scattering (DLS) experiments are performed with the Malvern Zetasizer Ultra of 1.00 g/L ION solutions. For DLS, the samples are measured in triplicates (disposable 10x10 plastic cell) and zeta potential (disposable, folded capillary cell) in quintuplets with an equilibration time of 120 s at 25 °C. A Bruker ALPHA II spectrometer obtains FT-IR spectra (24 scans, 4000-400 cm^{-1}). Background subtraction is done with a concave rubber band method (OPUS 8.1). The magnetization is measured with the SQUID magnetometer MPMS XL-7 (Quantum Design) at 300 K and a magnetic field variation between ± 3979 kA/m (10 mg sample). The amount of bound UPy-NH₂ is analyzed by TGA of freeze-dried IONs (50 μL aluminum oxide jar) with the STA 449C Jupiter between 25-700 °C.

3 Results and discussion

The cationic supramolecular moiety UPy-NH₂ was successfully coupled to polyglutaraldehyde functionalized IONs (ION@PGA) via imine formation by reaction of the aldehyde group and the amine of the UPy (Figure 1 a) [14]. The IONs@UPy-NH₂ are characterized by their particle composition, surface properties, magnetization, and hydrodynamic diameters.

3.1 Particle composition

XRD, FT-IR, TGA, and SQUID are used to analyze the particle composition of the IONs@UPy-NH₂. The effective UPy coating is visualized by FT-IR measurements (Figure 1 b).

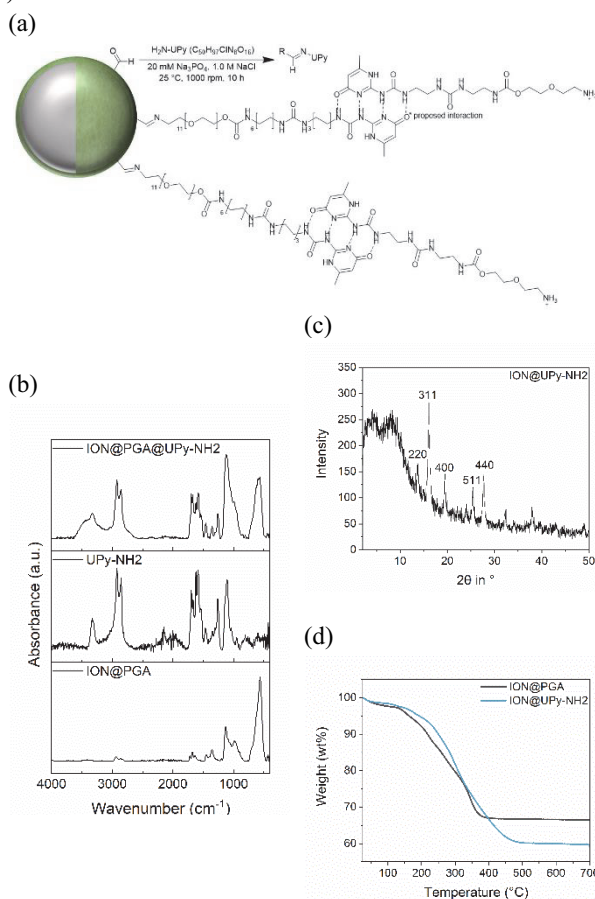


Figure 1: Schematic illustration of ION@UPy-NH₂ with the PGA coating in green and the imine formation. The Hydrogen bonding is proposed (a). FT-IR Spectra of UPy-NH₂, ION@PGA, and ION@UPy-NH₂ (b), XRD spectra of ION@UPy-NH₂ (Mo source, (c)), TGA curve of the both particle species (d).

The iron oxide core is represented by its characteristic Fe-O stretching vibration at 574 cm^{-1} [13]. Typical peaks of UPy are visible at 2853 cm^{-1} and 2923 cm^{-1} for C-H stretching vibrations, 1700 cm^{-1} and 1669 cm^{-1} for C=N and C=O

stretching vibrations, and at 1262 cm^{-1} and 1123 cm^{-1} for C-N and C-O stretching vibrations [15]. The typical iron oxide reflexes (220), (311), (400), (511), and (440) for magnetite are visible in the X-ray diffractogram (Figure 1 c) [13]. The amorphous coating generates a brought reflex between 2° and 10° . Similar behavior was already seen by amorphous silica coatings [16]. The UPy coating does not influence the crystal structure of the magnetite core. The amount of bound UPy-NH₂ was determined by TGA (Figure 1 d). The weight difference between ION@UPy-NH₂ and its precursor ION@PGA is 7.23wt%; this is the UPy-NH₂ bound to the nanoparticle surface. SQUID measurements of ION@UPy-NH₂ show the characteristic sigmoidal curve of superparamagnetic nanoparticles, which is only a slightly deviating to the simulated curve by the LangevinMod Fit (Figure 2 a). The UPy coated particles show a magnetization of $\pm 31.3\text{ Am}^2/\text{kg}$. As the particles contain additional nonmagnetic material as coating the magnetization is lower than the one of BIONs at around $60\text{ Am}^2/\text{kg}$ [12]. The analytics show that ION@UPy-NH₂ comprises a superparamagnetic, crystalline iron oxide core and a UPy coating. The influence of the coating on the surface properties and the particle size is analyzed by dynamic light scattering (DLS), zeta potential, and Nile Red assay.

3.2 Surface properties and particle size

Zeta potential and Nile Red assay are used to determine the surface properties of the ION@UPy-NH₂. Contrary to ION@PGA, ION@UPy-NH₂ particles have a positive surface charge for pH 5, 7, and 9 (Figure 2 c). It is hypothesized that the hydrogen bonding between the UPy-NH₂ moieties builds fibrous networks with a positive charge on the outside (Figure 1 a). The zeta potential rises with lower pH indicating a stabilization from moderate to good stability [17]. This effect can also be seen in DLS measurements. The hydrodynamic diameters in water at pH 5 and 7 ($168 \pm 44.1\text{ nm}$, $177 \pm 32.0\text{ nm}$) are 0.5 times smaller than at pH 9 ($345 \pm 61.5\text{ nm}$, Figure 2 a). The ION@UPy-NH₂ fit into the range of other nanoparticles synthesized for drug delivery of around 60 to 400 nm [18]. The Nile Red (NR) assay is used to determine the formation of hydrophobic pockets that form in the lateral direction of the UPy-network [9]. It becomes strongly fluorescent if the NR is encapsulated into the hydrophobic pockets. The fluorescent dye's red color in water shifts to a lower wavelength (blue shift) in a hydrophobic environment [19]. The more UPy-aggregates, the higher the fluorescence of the NR [20]. A shift to lower wavelength with higher particle concentrations because of more hydrophobic pockets available and a slightly increasing peak intensity with decreasing pH (Figure 2 d). It is proposed that covalently bound UPy-units can interact with free molecules by H-bonding and form

supramolecular structures. This behavior could also explain the better stability at more acidic pH values.

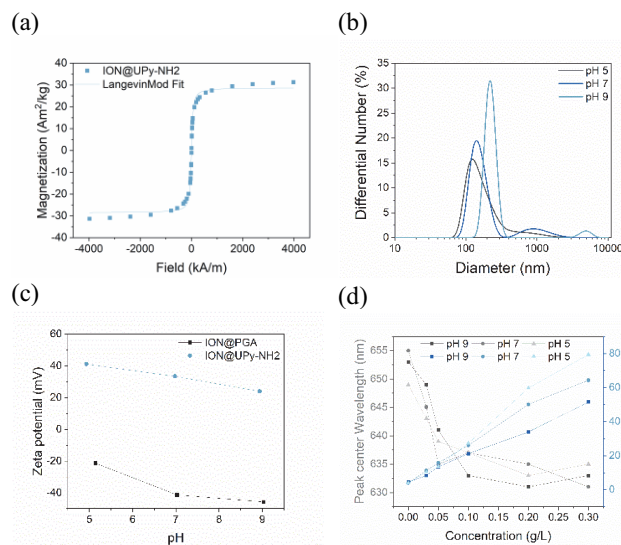


Figure 2: Magnetization of ION@UPy-NH₂ with LangevinMod fit (a), hydrodynamic diameters in water (b) zeta potential of ION@UPy-NH₂ in comparison with ION@PGA (c), at pH 5, 7, and 9, and Nile Red Assay of ION@UPy-NH₂ (d),

4 Conclusion

The IONs are successfully functionalized with UPy-NH₂. The UPy shell generates a positively charged layer surrounding the superparamagnetic crystalline magnetite core. It is proposed that hydrophobic pockets form by hydrogen bonding of UPy units. The stability of the particles is slightly influenced by pH, generating smaller aggregates at pH 5 with higher zeta potential. The work shows that the free UPy units are self-assembled around the IONs by hydrogen bonding to the covalently bound ones. This supramolecular interaction allows adding UPy-drug molecules and generating an innovative magnetically controlled drug delivery system.

Author Statement

Research funding: We appreciate the support of the Technical University of Munich International Graduate School of Science and Engineering (IGSSE). We are thankful for the support of Dutch Antimicrobial Resistance Technology development and Biofilm Assessment Consortium (Dartbac), and Regenerative Medicine Crossing Borders (RegMed). We appreciate the support from the German Research Foundation (DFG) and the Technical University of Munich (TUM) in the framework of the Open-Access Publishing Program. The funders had no role in the study's design, the collection, analysis, and interpretation of data, the manuscript's writing, or the decision to publish the results. **Conflict of interest:** The authors state no conflict of interest. **Informed consent:**

Informed consent has been obtained from all individuals included in this study. Ethical approval: The conducted research is not related to either human or animals use. Acknowledgments: We thank Dr. Matthias Opel for the support with SQUID measurements and Riccardo Bellan for the help with the Nile Red Assay. Data availability: The datasets of this study are available from the corresponding author on reasonable request.

Literatur

- Saxena SK, Khurana SMP. *NanoBioMedicine*. Singapore: Springer Singapore; 2020.
- Lu A-H, Salabas EL, Schüth F. Magnetic nanoparticles: synthesis, protection, functionalization, and application. *Angew Chem Int Ed Engl* 2007; 46(8):1222–44. doi: 10.1002/anie.200602866.
- Jose J, Kumar R, Harilal S, Mathew GE, Della Parambi GT, Prabhu A et al. Magnetic nanoparticles for hyperthermia in cancer treatment: an emerging tool. *Environ Sci Pollut Res Int* 2020; 27(16):19214–25. doi: 10.1007/s11356-019-07231-2.
- Walmsley GG, McArdle A, Tevlin R, Momeni A, Atashroo D, Hu MS et al. Nanotechnology in bone tissue engineering. *Nanomedicine* 2015; 11(5):1253–63. doi: 10.1016/j.nano.2015.02.013.
- Wu W, Wu Z, Yu T, Jiang C, Kim W-S. Recent progress on magnetic iron oxide nanoparticles: synthesis, surface functional strategies and biomedical applications. *Sci Technol Adv Mater* 2015; 16(2):23501. doi: 10.1088/1468-6996/16/2/023501.
- Tiwari G, Tiwari R, Sriwastawa B, Bhati L, Pandey S, Pandey P et al. Drug delivery systems: An updated review. *Int J Pharm Investig* 2012; 2(1):2–11. doi: 10.4103/2230-973X.96920.
- Laurent S, Forge D, Port M, Roch A, Robic C, Vander Elst L et al. Magnetic iron oxide nanoparticles: synthesis, stabilization, vectorization, physicochemical characterizations, and biological applications. *Chem Rev* 2008; 108(6):2064–110. doi: 10.1021/cr068445e.
- Dankers PYW, Hermans TM, Baughman TW, Kamikawa Y, Kieltyka RE, Bastings MMC et al. Hierarchical formation of supramolecular transient networks in water: a modular injectable delivery system. *Adv Mater* 2012; 24(20):2703–9. doi: 10.1002/adma.201104072.
- Bakker MH, Kieltyka RE, Albertazzi L, Dankers PYW. Modular supramolecular ureidopyrimidinone polymer carriers for intracellular delivery. *RSC Adv*. 2016; 6(112):110600–3. doi: 10.1039/C6RA22490C.
- Besseling PJ, Mes T, Bosman AW, Peeters JW, Janssen HM, Bakker MH et al. The in-vitro biocompatibility of ureido-pyrimidinone compounds and polymer degradation products. *Journal of Polymer Science* 2021; 59(12):1267–77. doi: 10.1002/pol.20210072.
- Nicole E. Botterhuis, D. J. M. van Beek, Gaby M. L. van Gemert, Anton W. Bosman, Rint P. Sijbesma. Self-assembly and morphology of polydimethylsiloxane supramolecular thermoplastic elastomers. *Journal of Polymer Science Part A: Polymer Chemistry* 2008; 46(12):3877–85. doi: 10.1002/pola.22680.
- Dankers PYW, Boomker JM, Huizinga-van der Vlag A, Wisse E, Appel WPJ, Smedts FMM et al. Bioengineering of living renal membranes consisting of hierarchical, bioactive supramolecular meshes and human tubular cells. *Biomaterials* 2011; 32(3):723–33. doi: 10.1016/j.biomaterials.2010.09.020.
- Turrina C, Berensmeier S, Schwaminger SP. Bare Iron Oxide Nanoparticles as Drug Delivery Carrier for the Short Cationic Peptide Lasioglossin. *Pharmaceuticals* 2021; 14(5):405. doi: 10.3390/ph14050405.
- Ernest I. *Bindung, Struktur und Reaktionsmechanismen in der organischen Chemie*. Wien: Springer; 1972.
- Parvin Shokrollahi. *Supramolecular Poly(tetrahydrofuran) Based on a Pyrimidinone Associating Motif*. *Iranian Polymer Journal* 2010; (19):65–74.
- Taufiq A, Nikmah A, Hidayat A, Sunaryono S, Mufti N, Hidayat N et al. Synthesis of magnetite/silica nanocomposites from natural sand to create a drug delivery vehicle. *Heliyon* 2020; 6(4):e03784. doi: 10.1016/j.heliyon.2020.e03784.
- Parveen S, Rana S, Fangueiro R. A Review on Nanomaterial Dispersion, Microstructure, and Mechanical Properties of Carbon Nanotube and Nanofiber Reinforced Cementitious Composites. *Journal of Nanomaterials* 2013; 2013:1–19. doi: 10.1155/2013/710175.
- Liu Y, Yang G, Jin S, Xu L, Zhao C-X. Development of High-Drug-Loading Nanoparticles. *Chempluschem* 2020; 85(9):2143–57. doi: 10.1002/cplu.202000496.
- Sackett DL, Wolff J. Nile red as a polarity-sensitive fluorescent probe of hydrophobic protein surfaces. *Analytical Biochemistry* 1987; 167(2):228–34. doi: 10.1016/0003-2697(87)90157-6.
- Greenspan P, Fowler SD. Spectrofluorometric studies of the lipid probe, nile red. *J Lipid Res* 1985; 26(7):781–9.

3.5. Iron oxide nanoparticles with supramolecular ureido-pyrimidinone coating for antimicrobial peptide delivery

AMPs are an ideal alternative to antibiotics that highly suffer from antimicrobial resistance. AMPs are highly active against Gram-positive and Gram-negative bacteria and show activity against various cancer cells. Due to their unique mode of action, they are hardly affected by resistance formation. Yet their application in medicine has been limited by their potential toxicity to human cells. A combination of supramolecular engineering and targeted magnetic drug delivery could overcome this problem by influencing their activity in healthy cells and reducing the necessary amount of drug.

This study uses UPy-coated IONs as a drug carrier for the AMP LL, functionalized with a UPy-unit. The cytocompatibility of the carrier and the drug delivery system was analyzed by resazurin assay and live dead staining. The carrier by itself showed high cytocompatibility with human kidney cells (HK-2) and a concentration-dependent effect on the metabolic activity of macrophagic THP-1 cells. Internalization experiments determined a successful delivery into both cell types within 24 hours.

The binding of UPy-LL on the ION@UPy-NH₂ is generated by the highly efficient (99%) self-assembly of the UPy-dimers. Combining Cryo-TEM, HAADF-STEM, and NR assay could visualize a core-shell system with fibers directly bound to the surface. The introduction of UPy-LL showed an effect on fiber formation, leading to new and shorter fibers. The binding of the peptide increased the antimicrobial behavior against *E.coli* (MIC 1.77 μ M) and improved the cytocompatibility with HK-2 cells (10.6 μ M).

This new drug delivery system proves that supramolecular engineering leads to a reduced cytotoxicity and enhanced antimicrobial activity. The system improves the usability of AMPs and could be used to cure intracellular infections or improve cancer treatment.

The majority of the study was carried out at the Eindhoven University of Technology supported by Prof. Patricia Y.W. Dankers. The doctoral candidate's substantial contributions were the study's conception and design after critically reviewing existing literature. The doctoral candidate was the leading author of the manuscript, carried out the assembly, antimicrobial, and cell experiments, and did data processing. J. Cookman and R. Bellan provided the micrographs with different TEM technics.



Article

Iron Oxide Nanoparticles with Supramolecular Ureido-Pyrimidinone Coating for Antimicrobial Peptide Delivery

Chiara Turrina ¹, Jennifer Cookman ², Riccardo Bellan ³, Jiankang Song ³, Margret Paar ⁴, Patricia Y. W. Dankers ³, Sonja Berensmeier ¹ and Sebastian P. Schwaminger ^{1,4,5,*}

- ¹ Chair of Bioseparation Engineering, School of Engineering and Design, Technical University of Munich, Boltzmannstr. 15, 85748 Garching, Germany; c.turrina@tum.de (C.T.)
- ² Department of Chemical Sciences, Bernal Institute, University of Limerick, V94 T9PX Castletroy, Ireland; jennifer.cookman@ul.ie
- ³ Department of Biomedical Engineering, Institute for Complex Molecular Systems, Eindhoven University of Technology, 5600 MB Eindhoven, The Netherlands; r.bellan@tue.nl (R.B.)
- ⁴ Division of Medicinal Chemistry, Otto Loewi Research Center, Medical University of Graz, Neue Stiftingtalstraße 6, 8010 Graz, Austria
- ⁵ BioTechMed-Graz, Mozartgasse 12, 8010 Graz, Austria
- * Correspondence: sebastian.schwaminger@medunigraz.at; Tel.: +43-3163-8572-125

Abstract: Antimicrobial peptides (AMPs) can kill bacteria by disrupting their cytoplasmic membrane, which reduces the tendency of antibacterial resistance compared to conventional antibiotics. Their possible toxicity to human cells, however, limits their applicability. The combination of magnetically controlled drug delivery and supramolecular engineering can help to reduce the dosage of AMPs, control the delivery, and improve their cytocompatibility. Lasioglossin III (LL) is a natural AMP from bee venom that is highly antimicrobial. Here, superparamagnetic iron oxide nanoparticles (IONs) with a supramolecular ureido-pyrimidinone (UPy) coating were investigated as a drug carrier for LL for a controlled delivery to a specific target. Binding to IONs can improve the antimicrobial activity of the peptide. Different transmission electron microscopy (TEM) techniques showed that the particles have a crystalline iron oxide core with a UPy shell and UPy fibers. Cytocompatibility and internalization experiments were carried out with two different cell types, phagocytic and nonphagocytic cells. The drug carrier system showed good cytocompatibility (>70%) with human kidney cells (HK-2) and concentration-dependent toxicity to macrophagic cells (THP-1). The particles were internalized by both cell types, giving them the potential for effective delivery of AMPs into mammalian cells. By self-assembly, the UPy-coated nanoparticles can bind UPy-functionalized LL (UPy-LL) highly efficiently (99%), leading to a drug loading of 0.68 g g⁻¹. The binding of UPy-LL on the supramolecular nanoparticle system increased its antimicrobial activity against *E. coli* (MIC 3.53 μM to 1.77 μM) and improved its cytocompatible dosage for HK-2 cells from 5.40 μM to 10.6 μM. The system showed higher cytotoxicity (5.4 μM) to the macrophages. The high drug loading, efficient binding, enhanced antimicrobial behavior, and reduced cytotoxicity makes ION@UPy-NH₂ an interesting drug carrier for AMPs. The combination with superparamagnetic IONs allows potential magnetically controlled drug delivery and reduced drug amount of the system to address intracellular infections or improve cancer treatment.

Keywords: iron oxide nanoparticles; ureido-pyrimidinone; supramolecular system; antimicrobial peptide; intracellular delivery; cytocompatibility



Citation: Turrina, C.; Cookman, J.; Bellan, R.; Song, J.; Paar, M.; Dankers, P.Y.W.; Berensmeier, S.; Schwaminger, S.P. Iron Oxide Nanoparticles with Supramolecular Ureido-Pyrimidinone Coating for Antimicrobial Peptide Delivery. *Int. J. Mol. Sci.* **2023**, *24*, 14649. <https://doi.org/10.3390/ijms241914649>

Academic Editor: Yuri Lyubchenko

Received: 3 September 2023

Revised: 15 September 2023

Accepted: 16 September 2023

Published: 27 September 2023



Copyright: © 2023 by the authors. Licensee MDPI, Basel, Switzerland. This article is an open access article distributed under the terms and conditions of the Creative Commons Attribution (CC BY) license (<https://creativecommons.org/licenses/by/4.0/>).

1. Introduction

The 17 global grand challenges stated in the United Nations Sustainable Development Goals target good health and well-being. One of the goals within this challenge is to

address the growing resistance of pathogenic bacteria to conventional antibiotics [1–3]. A newly developed therapeutic option is the use of antimicrobial peptides (AMPs) that appear in various life forms, have a broad spectrum of antimicrobial activity, and differ from traditional antibiotics' mode of action [4–7]. Most AMPs are cationic and contain between 10 and 60 amino acids [8]. The specific targeting of the positively charged peptides is based on the cell membrane composition. The bacterial cell envelope contains negatively charged components like phosphatidylserine, whereas human cell membranes are based on neutral units such as phosphatidylcholine. The AMPs interact electrostatically with the negatively charged membranes and accumulate there. This behavior induces higher permeability, membrane lysis, release of intracellular components, and, therewith, cell death [7,8]. AMPs are highly specific and have a low tendency to trigger antimicrobial resistance [7]. The best-analyzed group of AMPs comprises linear, amphiphilic, α -helical peptides [9]. One of these is lasioglossin III (LL, H-Val-Asn-Trp-Lys-Lys-Ile-Leu-Gly-Lys-Ile-Ile-Lys-Val-Val-Lys-NH₂), a part of the venom of the bee *Lasioglossum laticeps* [10]. It shows high antimicrobial activity against Gram-positive and Gram-negative bacteria, e.g., *B. subtilis*, *S. aureus*, and *E. coli* [10]. Furthermore, it has anticancer activity against leukemia cells and solid tumors like PC12, HeLa S3, and SW480 and has a low hemolytic potential [10]. Though AMPs show multiple advantageous properties, their application in the human body is often limited due to stability and toxicity problems [4,7]. Therefore only a few AMPs are already approved by the FDA or are in the clinical stage [4,11,12]. Effective drug delivery can help overcome high pharmacological doses that result in toxic side effects [13,14]. Both supramolecular engineering and nanoparticles as drug carriers have the potential to improve the behavior of AMPs, for example, by reducing cytotoxicity and enhancing antimicrobial behavior [15–19].

Supramolecular engineering is the deliberate design and assembly of molecular structures and materials through noncovalent interactions to create functional systems with specific properties. Prominent examples are the self-assembly of DNA, host–guest chemistry, and supramolecular polymers [20,21]. A supramolecular AMP assembly is a modular and tunable approach, allowing the flexible incorporation of functionalized molecules to generate multifunctional systems [22–24]. The ureido-pyrimidinone (UPy) unit is a common monomer that is connected to a urea group and a hydrophobic alkyl spacer linked with a water-soluble oligo (ethylene glycol) by a urethane unit. The UPy unit can form amphiphilic supramolecular systems based on a fourfold hydrogen bonding approach [25]. It can form hydrogen-bonded dimers protected by hydrophobic pockets [26]. The UPy dimers can laterally stack and assemble into fibrous structures [26,27]. LL can be functionalized with a UPy unit and self-assembled with other UPy moieties like amine-functionalized UPy (Figure 1) [28]. Song et al. formed UPy–AMP assemblies by self-assembly and with controlled antimicrobial activity. Furthermore, they influenced the cytocompatibility by adjusting the AMP concentration [28].

Nanotechnology has the potential to reinvent medicine in the future, leading to improved diagnosis of, therapy for, and drug delivery for diseases [29,30]. Combining supramolecular engineering with iron oxide nanoparticles (IONs) enables a magnetically controlled drug delivery system [31,32]. IONs have the potential to carry a large drug dose due to the high surface area compared to its volume and can be guided by an external magnetic field directly to a target. Therefore, a high local concentration can be reached while lower drug amounts must be incorporated into the human body, which reduces toxicity and side effects [32–35]. Furthermore, IONs can be visualized by magnetic resonance imaging (MRI) and administered for hyperthermia patients by alternating the magnetic field to generate heat [36–38]. A fast and cost-efficient synthesis method used to manufacture the IONs is coprecipitation using the Massart process [17,39]. In this method, superparamagnetic iron oxide nanoparticles ranging in size between 4 and 16 nm and with a high specific surface area $>100 \text{ m}^2 \text{ g}^{-1}$ are generated [40–43]. The combination of bare IONs with LL showed improved antimicrobial activity yet led to uncontrolled agglomeration and a nonspecific weak binding with potential loss of the AMP [17].

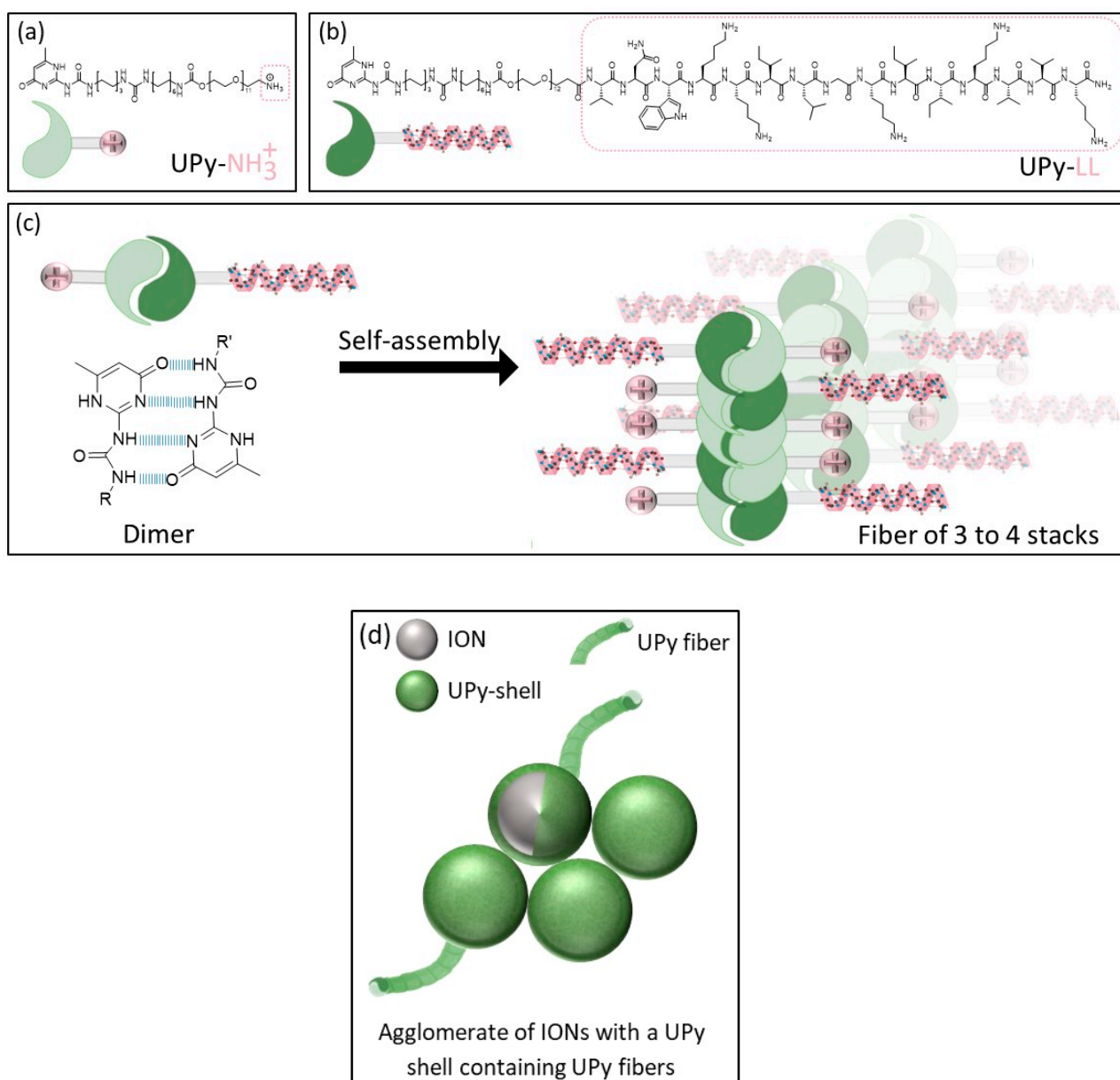


Figure 1. Schematic illustration of (a,b) the UPy unities (UPy-NH_2 , UPy-LL) forming dimers, stacks, and fibers, (c) fiber formation, and (d) schematic illustration of agglomerated IONs with a UPy shell containing UPy fibers [27].

The usage of UPy-coated IONs can combine the advantages of supramolecular engineering like efficient binding by self-assembly, adjustable cytocompatibility, and a controlled magnetic drug delivery with enhanced antimicrobial activity [44]. We showed the synthesis route and characterization (infrared spectroscopy, X-ray diffraction, thermogravimetric analysis, dynamic light scattering, zeta potential, Nile red assay, and superconducting quantum interference device) of ION@UPy-NH_2 in a previous work [44]. Bare IONs (BIONs) synthesized by the Massart process built the magnetic core of ION@UPy-NH_2 with a d_{TEM} of 8.74 ± 1.61 nm [15]. After a two-step functionalization with polyglutaraldehyde (PGA), UPy- NH_2 can interact with the particles via imine binding [44]. ION@UPy-NH_2 was previously characterized by Turrina et al. as showing a crystalline iron oxide core with superparamagnetic behavior, saturation magnetization around $31 \text{ Am}^2 \text{ kg}^{-1}$, a hydrodynamic diameter of 177 nm (pH 7), and a positive surface charge [44]. An amount of 7.23 wt% of UPy- NH_2 was bound, and Nile red assay indicated the lateral UPy stacking [44]. Yet, the

particle's morphology, cytocompatibility, internalization behavior, and interaction with a potential drug have not been analyzed.

This study aims to add to the knowledge of ION@UPy-NH₂ as a potential supramolecular-based, magnetically controllable drug carrier for LL. Its morphology was analyzed by combining high-angle annular dark field scanning transmission electron microscopy (HAADF-STEM), integrated differential phase contrast (iDPC), and cryo-TEM imaging. Its biological performance, including antimicrobial activity, cytocompatibility, and internalization with THP-1-derived macrophages as phagocytic cells and human kidney cells (HK-2) as non-phagocytic cells of the drug carrier alone and in combination with UPy-LL, was analyzed.

2. Results and Discussion

2.1. ION@UPy-NH₂

The multiple-step synthesis route is described in a previous publication of Turrina et al. [39]. The bare IONs were synthesized by coprecipitation. For the UPy coating, first, the particles were functionalized with (3-Aminopropyl)triethoxysilan (APTS), followed by a poly(glutaraldehyde) (PGA) coating, and finally a coating with UPy-NH₂ [39].

2.1.1. Particle Morphology

The morphology of ION@UPy-NH₂ was analyzed with a combination of different TEM techniques. Imaging with HAADF-STEM provided more insights into the composition and shape of the ION@UPy-NH₂ (Figure 2). In combination with DPC imaging, the crystalline nanoparticle core (green circle), showing atomic lattice planes, can be differentiated from the amorphous supramolecular core. Moiré fringes were also observed (Figure 2, red outline), suggesting that a smaller crystalline particle is present, causing a lattice plane overlap, creating the larger planes known as Moiré fringes. Due to the size and low z-contrast of the combined nanoparticle construct, HAADF-STEM does not allow for easy distinction between the ION core and the biomolecular coating. By using an alternative imaging technique known as integrated differential phase contrast imaging, this distinction can be made. The iDPC-STEM imaging technique takes advantage of the phase signal resulting from electron beam interactions with the sample. In magnetic materials such as IONs, the transmitted phase signal is drastically deflected compared to the nonmagnetic coating. The coating showed sensitivity to the scanning electron beam in STEM mode (Figure 2b,c, red arrow).

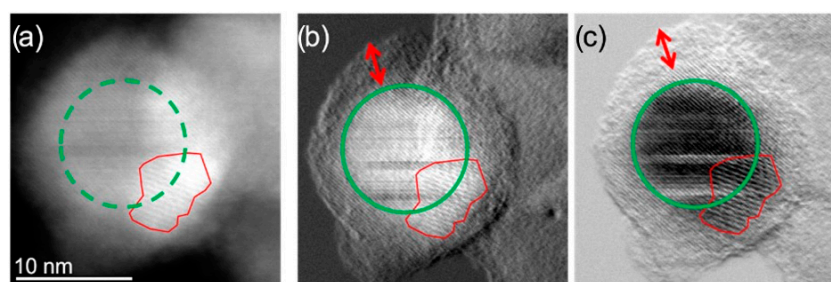


Figure 2. (a) HAADF-STEM micrographs of the same single ION@UPy-NH₂ indicating the crystalline NP core (green circle) and an overlapping smaller particle creating Moiré fringes (red outline); (b) DPC_x (A–C) and (c) DPC_y (B–D) images showing more clearly the NP core and the amorphous coating. (A–C) and (B–D) indicate different detector segments. The red arrow indicates the coating thickness.

DPC allowed lower electron doses to be used while acquiring higher-resolution images (Figure 2). In the HAADF-STEM, atomic lattice planes could not be clearly identified, but when the DPC_x and DPC_y images were observed, atomic lattice planes and even atomic resolution were visible. Figure 3 shows the agglomerate where the iron oxide core can be identified with respect to the amorphous exterior.

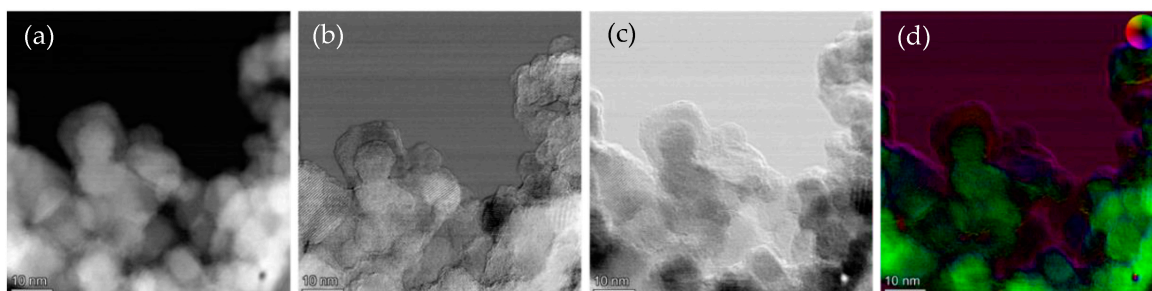


Figure 3. (a) HAADF-STEM micrographs of ION@UPy-NH₂ agglomerates; (b) DPC_x (A–C) and (c) DPC_y (B–D) images; and (d) iDPC color display.

Cryo-TEM analysis indicated the formation of $\sim 1 \mu\text{m}$ ($928 \text{ nm} \pm 128 \text{ nm}$) sized, UPy-NH₂-based fibers that could not be visualized with the former techniques (Figure 4a,b) [45]. Two fibers interact directly with the ION@UPy-NH₂ agglomerate, while one appears to be loose, which could be induced by the preparation. UPy-NH₂ binds on the surface and forms a core-shell structure. The fibers can either grow from the surface or form independently and complex afterward with the particles. Because after synthesis, the particles were ultrasonicated and intensely washed ($7\times$) by magnetic decantation, we hypothesize a binding. Previous Nile red assay showed a huge shift from approximately 656 nm to a lower wavelength of 632 nm, confirming UPy-NH₂ fiber formation [44].

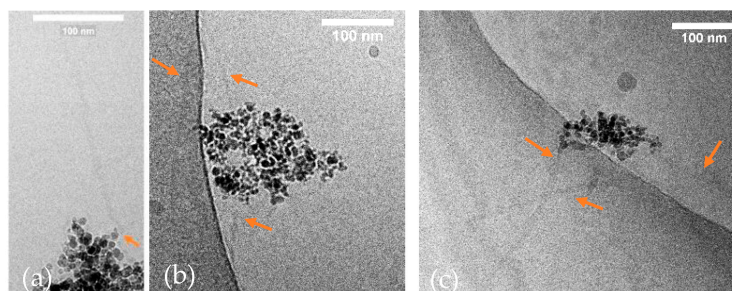


Figure 4. (a,b) Cryo-TEM micrographs of ION@UPy-NH₂, and (c) ION@UPy-NH₂@UPy-LL (35.3 μM UPy-LL were bound to 0.1 g L^{-1} ION@UPy-NH₂). The fibers are marked with orange arrows.

2.1.2. Cytocompatibility

The cytocompatibility of ION@UPy-NH₂ and its precursors ION@PGA and BIONs were analyzed quantitatively and qualitatively at various concentrations. Inside the body, the particles meet phagocytic cells and nonphagocytic cells; therefore, the effect of the particles' interactions on HK-2- and THP-1-derived macrophages was investigated by resazurin assay and, additionally, live/dead staining (Figure 5) [46]. The cell viability assay uses the reducing agent nicotinamide adenine dinucleotide (NADH) as an electron source to transform resazurin and induce a color shift [47]. Therefore, it can be used as a marker for metabolic activity [47]. Calcein-AM is used as green staining for the entire living cell. Propidium iodide stains the dead cells red [48]. For HK-2 cells, all investigated particles (concentrations between 0.03 g L^{-1} and 0.50 g L^{-1}) showed cell viability greater than 70%, a threshold value for cytocompatibility (ISO-10993, Figure 5a). Good cell viability for BIONs and IONs with various coatings, e.g., folic acid and carboxymethyl dextran (CMD), was previously reported for multiple cell lines [44,49]. In contrast, resazurin experiments with THP-1 cells demonstrated concentration-dependent cytotoxicity for all particles (Figure 5b). Particle concentrations higher than 0.30 g L^{-1} reduced the metabolic activity by around 53%. It is hypothesized that high particle concentrations embody a nonideal environment for the THP-1 cells, where the conditions are unfavorable for proliferation and the metabolic activity is reduced while the cells remain alive. This state of reversible cell cycle arrest is called quiescence [50]. Similar behavior was analyzed by Fernandes et al., who used

doxorubicin-loaded nanocubes in combination with magnetic hyperthermia to induce low proliferation quiescence to cancer stem cells [51]. Furthermore, IONs can release free iron to the cytoplasm when endosomes or lysosomes transport them under acidic conditions [52]. Toxic reactive oxygen species (ROS) can be generated by free radical formation due to the Fenton reaction [53]. Kim et al. showed that dextran-coated IONs increased ROS production in hematopoietic stem cells [54,55].

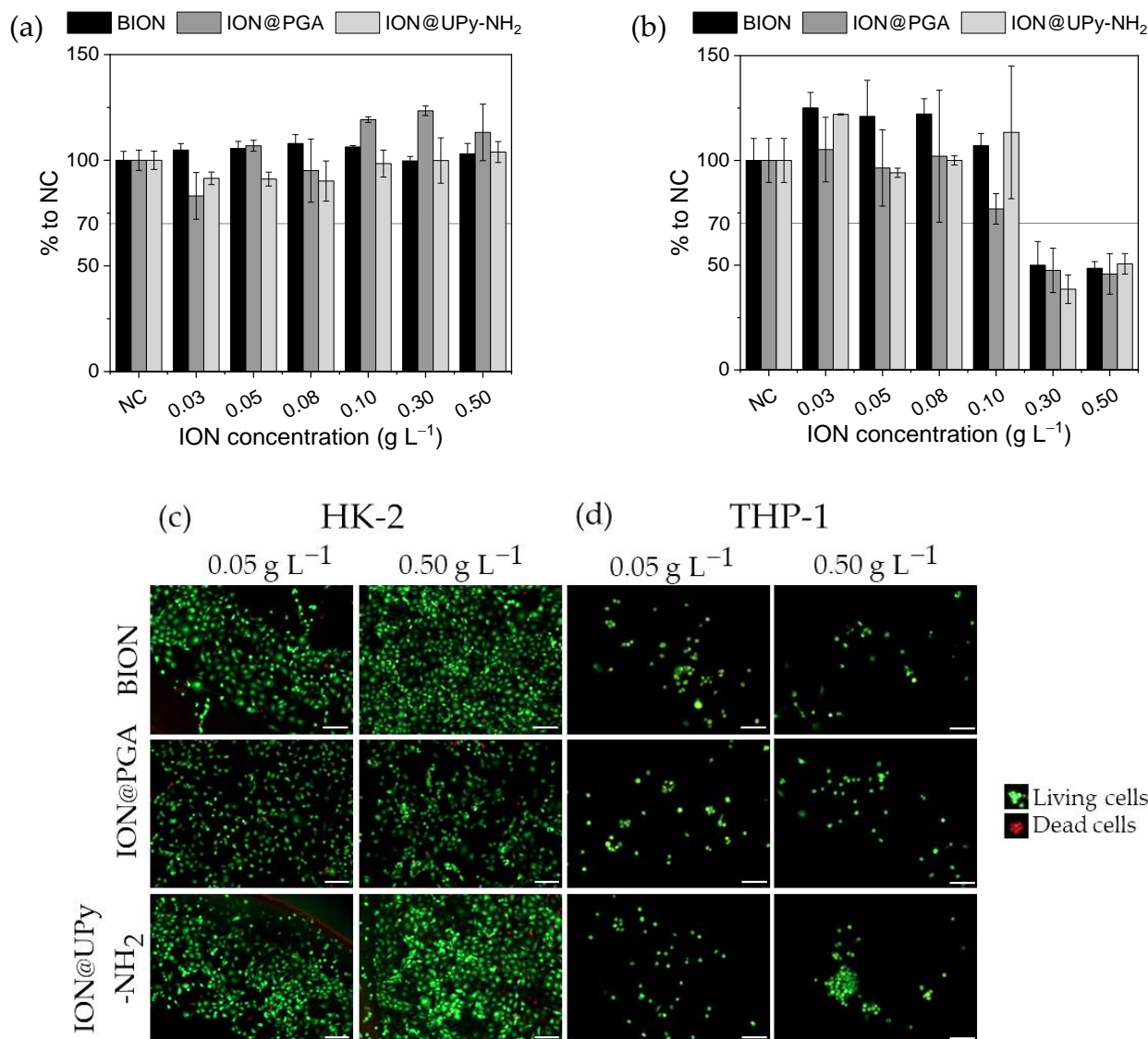


Figure 5. Cytocompatibility examination of ION, ION@PGA, and ION@UPy-NH₂ by resazurin assay for (a) HK-2 cells and (b) THP-1 cells, and live/dead staining of (c) HK-2 and (d) THP-1 cells. The living cells were stained green, and the dead cells were stained red. Scale bars represent 200 μm.

After the drug carrier and its precursors showed good cytocompatibility to both cell types at various concentrations, the next step is to check if internalization is taking place.

2.1.3. Internalization

The ION@UPy-NH₂ shape is a combination of spherical nanoparticles and UPy fibers as evidenced by the cryo-TEM analysis in Figure 4. For internalization experiments,

Endocytosis is a dynamic and versatile internalization process that leads to the internalization of extracellular IONs [56]. IONs can nonspecifically adsorb on the cell surface by electrostatic interaction, which induces the activation of endocytic mechanisms and

leads to internalization [57]. Also, for macrophagic cells (RAW264.7), it was shown that endocytic pathways, including macropinocytosis or phagocytosis, internalize IONs [58]. Specifically, positively charged IONs are attracted by the negatively charged phospholipids and proteins on the plasma membrane [57]. Our experiments did not allow us to identify the internalization mechanism of the here-synthesized materials conclusively.

ION@UPy-NH₂ were labeled with UPy-Cy5 (Figure S1) to generate red fluorescent particles. HK-2 cells showed complete adsorption of the particles on the cellular envelope within 120 min (Figure 6). After 24 h, the visible particles were internalized. Size shape and surface charge highly impact internalization [59]. In THP-1 macrophages, ION@UPy-NH₂ adsorbed in the first 5 min and showed a high degree of internalization after 2 h, which increased within 24 h. While spherical particles were internalized within 2 min, wormlike particles were not internalized in the first 30 min and showed a lower degree of internalization after 22 h [60]. Champion et al. analyzed the internalization of differently shaped particles into alveolar macrophages by phagocytosis [60].

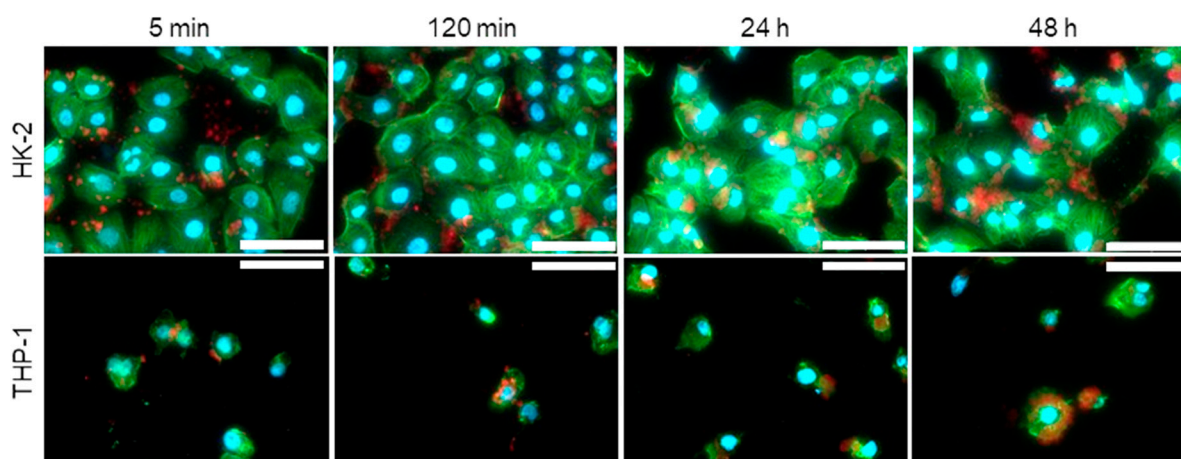


Figure 6. Fluorescent micrographs of internalization of ION@UPy-NH₂ by HK-2 and THP-1 cells after 5 min, 120 min, 24 h, and 48 h. The ION@UPy-NH₂ were labeled with 0.025 g L⁻¹ UPy-Cy5 (red, Figure S1), and the nuclei (DAPI) and cell skeleton (Phalloidin Alexa 488) of the cells were stained blue and green, respectively. Scale bars represent 30 μm. All samples were examined under the same settings.

The cell experiments demonstrated good cytocompatibility (>70%) of ION@UPy-NH₂ for HK-2 cells and potential toxicity for macrophagic cells (THP-1) at high concentrations. The particles were internalized in both cells types. Because of these aspects, ION@UPy-NH₂ represents a promising new drug carrier system.

2.2. Binding of UPy-LL to ION@UPy-NH₂

The supramolecular interaction caused by hydrogen bonding of UPy units allows the addition of UPy-based drug molecules and generates an innovative magnetically controlled drug delivery system.

The binding of UPy-LL on ION@UPy-NH₂ was analyzed in binding experiments. UPy-LL can self-assemble with UPy-NH₂ [28]. After magnetic decantation, the supernatant was photometrically analyzed at 280 nm, and the bound UPy-LL amount was calculated. The binding was highly efficient (Figure 7a). To find the ideal binding conditions, different particle and UPy-LL concentrations were analyzed. Independent of the particle concentration, 99% of UPy-LL (<0.5 g L⁻¹) was bound. Compared to the binding of bare IONs with LL, where a maximal loading of 0.23 g g⁻¹ LL on bare IONs with a starting concentration of 2 g L⁻¹ was reached (efficiency: 11.5%), the supramolecular engineering highly improved the binding efficiency (99%) [17]. It is hypothesized that saturation occurs because of sterical hindrance due to the α-helical shape of LL. The highest reached drug loading was

0.68 g UPy-LL per gram ION@UPy-NH₂ (Figure S2, Table S1). Nile red assay demonstrated a blue shift from 656 nm to 638 nm by increasing the UPy-LL amount (Figure 7b). The shift indicates the formation of UPy-LL or UPy-NH₂-UPy-LL fibers. Cryo-TEM imaging of ION@UPy-NH₂@UPy-LL showed particle agglomerates with directly bound short fibers with a size of 135 ± 55 nm (Figure 7c). The following experiments were conducted with ION@UPy-NH₂@UPy-LL in which the particle concentration during adsorption was 0.4 g L⁻¹.

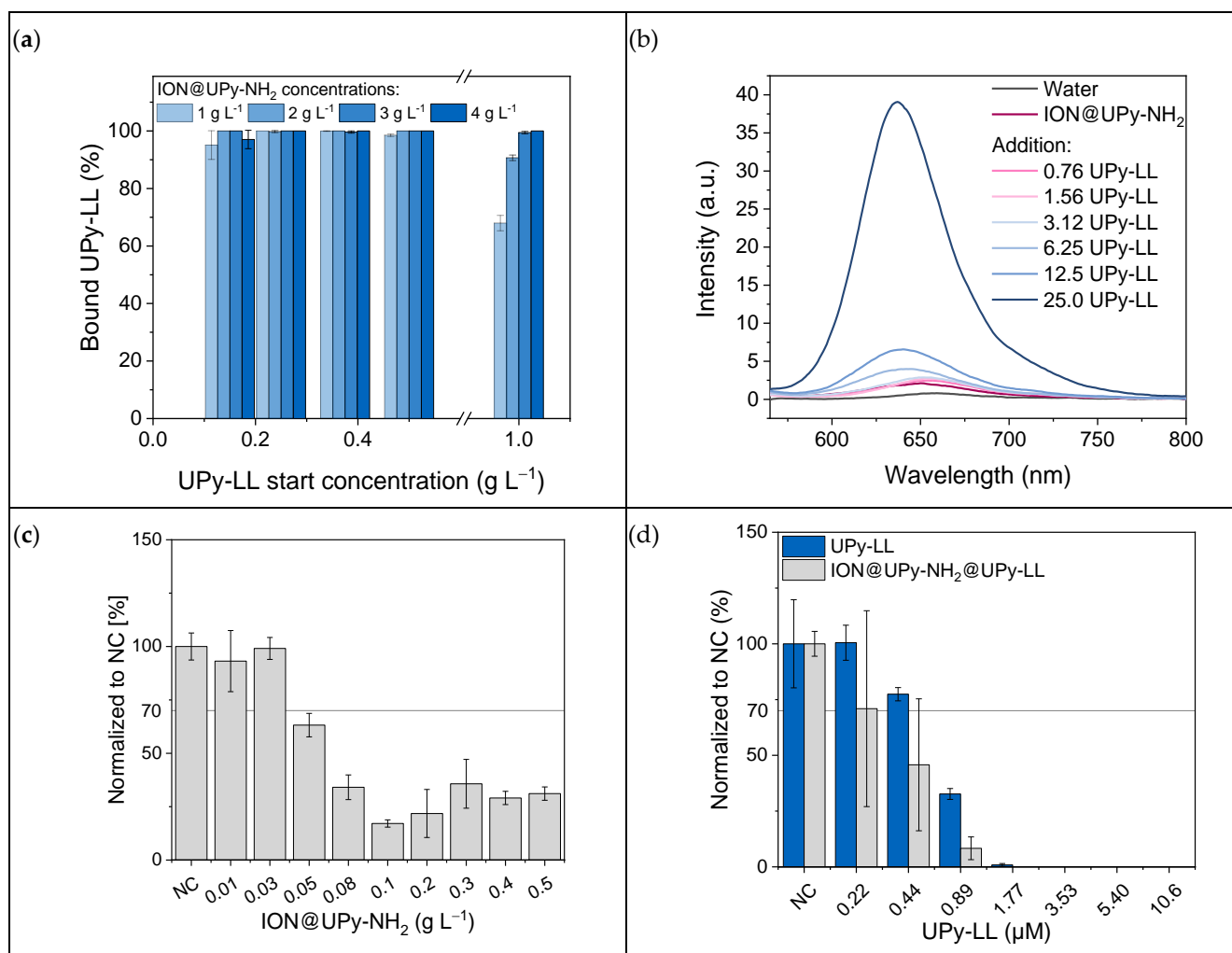


Figure 7. (a) Binding of UPy-LL to different concentrations of ION@UPy-NH₂ and (b) Nile red assay of ION@UPy-NH₂@UPy-LL with different UPy-LL concentrations. Growth studies with *E. coli* and (c) different concentrations of ION@UPy-NH₂ and (d) various amounts of UPy-LL and ION@UPy-NH₂@UPy-LL complexes.

The high binding efficiency allows the generation of a drug delivery system with high drug loading. Antimicrobial tests can be used to analyze if the drug is still active while being bound to the drug carrier.

2.2.1. Antimicrobial Activity

The antimicrobial properties of ION@UPy-NH₂, ION@UPy-NH₂@UPy-LL, and free UPy-LL were analyzed by culturing these materials with a green fluorescent protein (GFP)-expressing *E. coli* (BL21, ampicillin resistance). Therefore, the fluorescent bacteria were counted after 24 h. ION@UPy-NH₂ without AMP led to comparable growth of the negative control (cells that were not combined with particles or AMP) for concentrations ≤ 0.03 g L⁻¹

(Figure 7c). Higher particle concentrations induced less growth with 28% viability. Previous experiments with BIONs showed a reduction in *E. coli* growth at high particle concentrations of around 68% viability [17]. The stronger decrease could come from the positive ION@UPy-NH₂ surface being more attracted to the negative bacteria surface. Free LL-III has a minimum inhibitory concentration of 1.13–3.7 μM for *E. coli* [10,17,19]. In our experiments, the UPy-LL led to nearly no bacteria growth at 1.77 μM and complete inhibition at 3.53 μM (Figure 7d). Bound to ION@UPy-NH₂, the antimicrobial behavior is slightly improved, leading to a MIC of 1.77 μM (0.02 g L⁻¹ particle concentration). Measurements of the growth with OD600 confirm these data (Figure S3). Because of the low particle concentration, the effect of ION@UPy-NH₂ can be neglected. A similar effect of bound LL showing higher antimicrobial activity was shown by Turrina et al. for BION@LL and ION@CMD@LL (adsorbed) [15,17]. Because of the efficient UPy-LL binding, low particle concentrations can generate the highly efficient antimicrobial behavior of ION@UPy-NH₂@UPy-LL.

2.2.2. Cytocompatibility

The cationic nature of AMPs is likely to make them highly antibacterial but also bears potential cytotoxicity against mammalian cells, limiting their successful usage [4,61,62]. Similar to ION@UPy-NH₂, the cytocompatibility of ION@UPy-NH₂@UPy-LL and free UPy-LL was investigated (Figure 8). UPy-LL showed cell viability >70% until 5.4 μM for HK-2 and 3.53 μM for THP-1 in resazurin assay (Figure 8a,b). Live/dead staining showed a similar trend: UPy-LL was more cytotoxic for the macrophagic THP-1 cells than for HK-2 (Figure 8c,d). For both resazurin assay and live/dead staining, nearly no living cells were left at 14.1 μM for HK-2 and 10.6 μM for THP-1. The resazurin data show ION@UPy-NH₂@UPy-LL led to good cytocompatibility (>70%) until 10.6 μM (0.12 g L⁻¹ particle concentration) for HK-2 cells and 3.53 μM for THP-1-derived macrophages (0.04 g L⁻¹ particle concentration). At the respective particle concentration, no cytotoxic effect was measured for ION@UPy-NH₂ (Section 2.1.2). Especially for higher concentrations of UPy-LL, the combination with the particles improves the cytocompatible behavior for both HK-2 and THP-1. At 14.1 μM of bound UPy-LL, metabolic activity is 50.4% HK-2 and 34.7% THP-1.

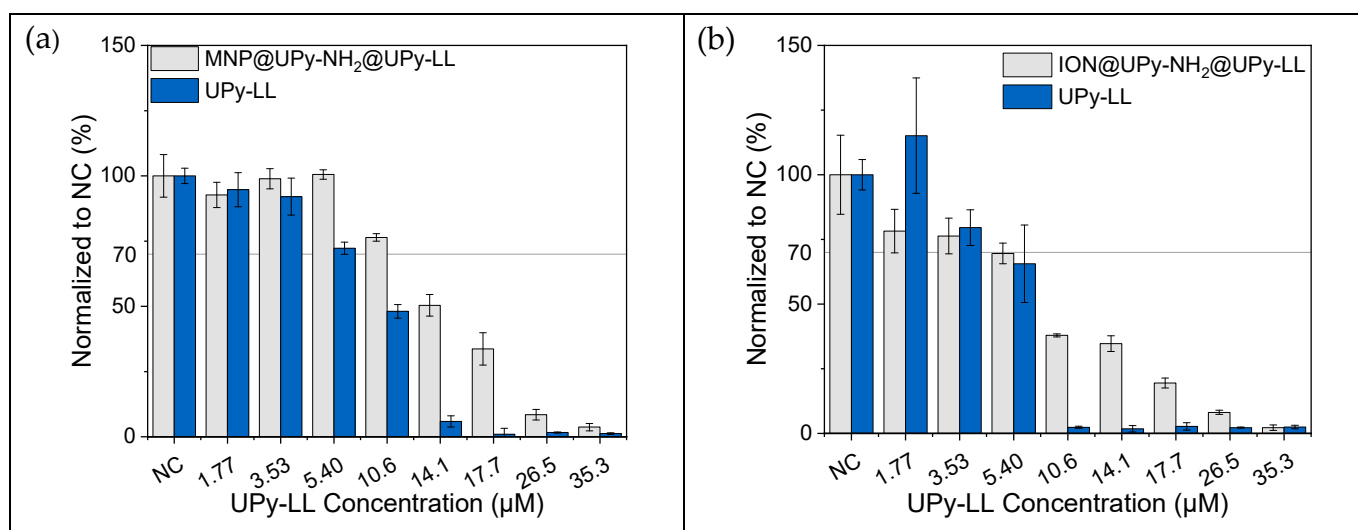


Figure 8. Cont.

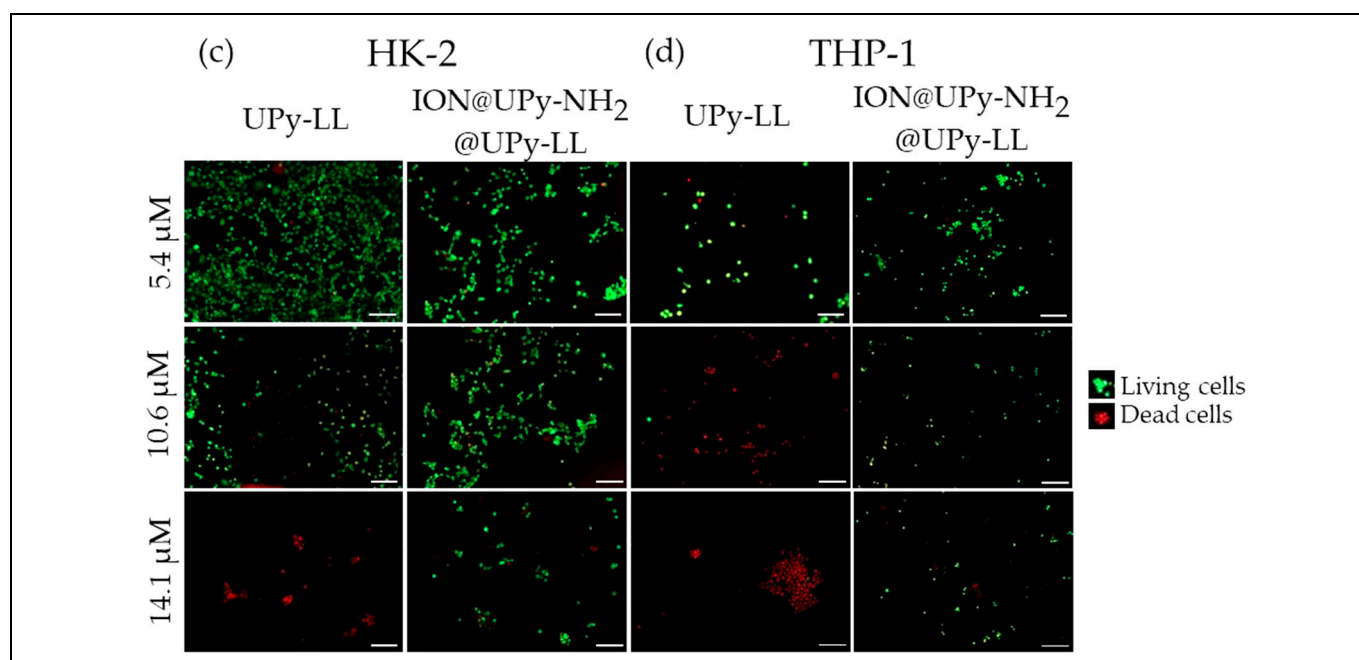


Figure 8. Cytocompatibility examination by resazurin assay for UPy-LL and ION@UPy-NH₂-UPy-LL in (a) HK-2 cells and (b) THP-1 cells, and live/dead staining of (c) HK-2 and (d) THP-1 cells. The living cells are colored green and the dead cells red. Scale bars represent 200 μm .

The cytotoxic effect of UPy-LL is impeded by binding to the particles, and ION@UPy-NH₂@UPy-LL is less cytotoxic towards HK-2 cells than towards THP-1 cells (Figure 8a,b). Figure 8c,d illustrate differences in live and dead staining for different lasioglossin concentrations. Čerovský et al. observed toxicity against rat epithelial cells (IEC-6) of 19 μM for free LL [10].

3. Materials and Methods

We showed the detailed three-step synthesis route and characterization (infrared spectroscopy, X-ray diffraction, thermogravimetric analysis, dynamic light scattering, zeta potential, Nile red assay, and superconducting quantum interference device) of ION@UPy-NH₂ in a previous work [39]. The bare IONs were synthesized by coprecipitation. For the UPy coating, first, the particles were functionalized with (3-Aminopropyl)triethoxysilan (APTS), followed by a poly(glutaraldehyde) (PGA) coating, and finally a coating with UPy-NH₂ [39]. ION@UPy-NH₂ showed superparamagnetic behavior with a saturation magnetization of 31 Am² kg⁻¹, a positively charged surface, and a hydrodynamic diameter of 177 nm at pH 7. Thermogravimetric analysis determined that 7.23 wt% of the overall particle weight is the bound Upy-NH₂. Nile red assay showed a shift to lower wavelength (631 nm at pH 7), indicating the formation of hydrophobic pockets [44].

3.1. Morphology

High-angle annular dark field scanning transmission electron microscopy (HAADF-STEM) and integrated differential contrast (iDPC) STEM imaging were conducted on a Thermo Fisher Scientific Titan Themis Cubed operating at an acceleration voltage of 300 kV and tuned with a monochromator and probe corrector. HAADF-STEM and iDPC imaging were acquired using Velox (Thermo Fisher Scientific, Dreieich, Germany) software. For sample preparation, a Lacey carbon 200 mesh copper grid (Agar Scientific, Stansted, UK) was plasma-treated using a Gatan Solarus 950 Advanced plasma system (Gatan Inc., Berwyn, PA, USA) with O₂ for 30 s at 65 W to induce a hydrophilic surface on the grid. The TEM grid was suspended using reverse-action tweezers, and using a micropipette, a 7 μL aliquot of 100 \times diluted sample was deposited on the grid and left under cover

until the droplet was evaporated. Furthermore, the grid was kept under a high vacuum overnight, ensuring complete evaporation and minimizing imaging artifacts. For the DPC measurement the detector is segmented into different areas (A–D). The sample can deflect the electronic beam. Such deflection can create images where the A–C (DPC_x (A–C)) and B–D (DPC_y (B–D)) detector segments are differentiated. Cryo-TEM imaging was performed on samples with 0.5 g L^{-1} particles and incubated overnight in Millipore water using quantifoil carbon-covered grids (Electron Microscopy Sciences, Hatfield, PA, US 200 mesh, 50 μm hole size). Before sample addition, grids were surface-plasma-treated (at 5 mA for 40 s) using a Cressington 208 carbon coater. Using an automated vitrification robot (FEI VitroBot™ Mark III, Hillsboro, OR, US) operating at 22 °C and a relative humidity of 100%, a 3 μL sample was applied to the grids. The excess sample was removed using blotting filter paper for 3 s at -3 mm . The thin film formed was vitrified by plunging the grid into liquid ethane and subsequently, liquid nitrogen. The vitrified grid was transferred to a cryo-transfer holder and prepared for TEM imaging. TEM imaging was conducted using a CryoTITAN equipped with a field emission gun operating at an acceleration voltage of 300 kV, a postcolumn Gatan energy filter, and a 2048×2048 Gatan CCD camera. Vitrified films were observed with the CryoTITAN microscope at temperatures below $-170 \text{ }^\circ\text{C}$. Micrographs were taken at low-dose conditions using a defocus setting of $-5 \text{ }\mu\text{m}$ or $-1 \text{ }\mu\text{m}$ at 25 k magnification.

3.2. Cell Culture

For cell culture, Dulbecco's Modified Eagle Medium (DMEM (1 \times), gibco, ref. 42430-025) and Roswell Park Memorial Institute 1640 (RPMI (1 \times), gibco, ref. A10491-01) were supplemented with 10% fetal bovine serum (FBS) and 1% penicillin/streptomycin (P/S), respectively. Human kidney cells (HK-2, passaged 2 \times per week) and monocytic human THP-1 cells (ATCC, passaged every 2nd day) were cultured at 37 °C in 95% air/5% CO₂ atmosphere with DMEM and RPMI medium, respectively. The differentiation of THP-1 monocytes into macrophages was induced by adding 50 ng/mL phorbol 12-myristate 13-acetate (PMA) to the culture medium and incubated for 48 h. The experiments were carried out with a seeding density of 2.5×10^5 cells/cm² for the THP-1 cells and 2.5×10^4 cells/cm² for the HK-2 cells.

3.3. Cytocompatibility

The cytocompatibility of BIONs, ION@PGA, ION@UPy-NH₂, ION@UPy-NH₂@UPy-LL (preparation can be found in 2.6 UPy-LL binding), and free UPy-LL for THP-1 macrophages and HK-2 cells was investigated by resazurin assay. The cells were seeded onto a 96-well plate ($n = 3$). The THP-1 cells were induced with PMA for 48 h, and the HK-2 cells were cultured overnight to allow cell adhesion. The particles were suspended in 70% EtOH by magnetic decantation and sterilized for two hours under UV light. Afterward, the supernatant was changed to PBS by magnetic decantation, removing the EtOH supernatant and resuspending the nanoparticles in PBS. The IONs were then ultrasonicated for 30 min in an ultrasonic bath to ensure full resuspension. The respective medium exchanged the buffer. After attachment, the culture medium was exchanged for a medium containing BIONs, ION@PGA, and ION@UPy-NH₂ at the concentrations of 0 g L^{-1} , 0.03 g L^{-1} , 0.05 g L^{-1} , 0.08 g L^{-1} , 0.10 g L^{-1} , 0.30 g L^{-1} , and 0.50 g L^{-1} , respectively, or ION@UPy-NH₂@UPy-LL and UPy-LL at $0 \text{ }\mu\text{M}$, $1.77 \text{ }\mu\text{M}$, $3.53 \text{ }\mu\text{M}$, $5.40 \text{ }\mu\text{M}$, $10.6 \text{ }\mu\text{M}$, $14.1 \text{ }\mu\text{M}$, $17.7 \text{ }\mu\text{M}$, $26.5 \text{ }\mu\text{M}$, or $35.3 \text{ }\mu\text{M}$ (based on the UPy-LL concentration, detailed explanation in Table S1). After 24 h of incubation, the medium was removed, and the cells were washed with PBS buffer. After adding 200 μL of culture medium enriched with 44 μM resazurin (three empty wells were filled as control samples without cells), the cells were incubated for 3.5 h at 37 °C. Amounts of $2 \times 80 \text{ }\mu\text{L}$ of resazurin-enriched medium were transferred to a flat black 96-well plate, and the fluorescence was measured with a Synergy™ HT plate reader and Gen5™ software (BioTek Instruments, Inc.) at $\lambda_{\text{ex}} = 550 \text{ nm}$ and $\lambda_{\text{em}} = 584 \text{ nm}$. Results

were presented normalized to the fluorescence of the negative control (cells that were not in contact with the nanoparticles or the AMP).

3.4. Live/Dead Staining

The cell viability of both cell types in combination with BIONs, ION@PGA, ION@UPy-NH₂, ION@UPy-NH₂@UPy-LL, and free UPy-LL was determined by live/dead staining. An amount of 50 μ L of cell suspension was seeded (with a seeding density of 2.5×10^5 cells/cm² for the THP-1 cells and 2.5×10^4 cells/cm² for the HK-2 cells) into a 15-well Ibidi slide ($n = 3$). The particles were sterilized as described above in Section 3.3. After the cell's attachment (HK-2 overnight, THP-1 with PMA-induced medium for 48 h), the respective medium was exchanged for a medium containing 0.05 g L⁻¹ or 0.50 g L⁻¹ BIONs, ION@PGA, and ION@UPy-NH₂ or 5.40 μ M, 10.6 μ M, or 14.1 μ M ION@UPy-NH₂@UPy-LL or UPy-LL. The cells were incubated for 24 h and washed with PBS (2 \times), incubated with 10 μ M calcein AM and 10 μ M propidium iodide-enriched medium (30 min, 37 $^{\circ}$ C), and washed with PBS (2 \times). Imaging acquisition of the cells was performed using a Zeiss Axio Observer 7 with a 10 \times objective.

3.5. Internalization

The internalization experiments of ION@UPy-NH₂ containing UPy-Cy5 (Figure S1) were prepared by adding 2 μ L of a 1.25 g L⁻¹ UPy-Cy5 solution in chloroform to 100 μ L of an 11.6 g L⁻¹ ION@UPy-NH₂ suspension in water. The particles were shaken at 30 $^{\circ}$ C and 1500 rpm for 6 h and washed by magnetic decantation (3 \times) to ensure the binding. They were sterilized as described before and diluted to a 0.1 g L⁻¹ suspension in the respective medium. An amount of 50 μ L of THP-1 or HK-2 cells was seeded onto a 15-well Ibidi slide ($n = 3$). After incubation with ION@UPy-NH₂/UPy-Cy5 for 5 min, 2 h, 24 h, and 48 h, the cells were washed with PBS (2 \times), fixed with 15 μ L of 10% formaldehyde solution at room temperature (25 $^{\circ}$ C), and washed with PBS (2 \times). The cells were sequentially stained with Phalloidin Alexa 488 staining solution (1:300, 30 min, 25 $^{\circ}$ C) for the membrane and 4',6-Diamidin-2-phenylindol solution (DAPI, 2:1000, 10 min, RT) for the nuclei in PBS, respectively. After washing (2 \times PBS), imaging was performed with a Zeiss Axio Observer 7 with a 40 \times objective.

3.6. UPy-LL Binding

To combine ION@UPy-NH₂ with UPy-LL, 1.0 mg of UPy-LL was dissolved in 176.5 μ L 99:1 MeOH:1 \times PBS pH 7.4 (gibco) containing 2 mM 2-hydroxyethylpiperazine-N'-2-ethane sulfonic acid (HEPES) [28]. An amount of 28.7 μ L of this solution was combined with 1.12 mL of 0.56 g L⁻¹ ION@NH₂ solution in PBS. The particles were shaken at 1000 rpm overnight. The particles were sterilized under UV light for 30 min, and the buffer was changed by magnetic decantation.

To analyze the binding behavior, different ION@UPy-NH₂ concentrations (8 g L⁻¹, 6 g L⁻¹, 4 g L⁻¹, 2 g L⁻¹) in PBS were mixed 1:1 with various UPy-LL solutions (2 g L⁻¹, 1 g L⁻¹, 0.75 g L⁻¹, 0.5 g L⁻¹, 0.3 g L⁻¹, 0 g L⁻¹). The experiment was conducted in triplicate. The suspensions were mixed for one hour at room temperature at 1000 rpm. After magnetic decantation, the supernatants were photometrically measured at 280 nm, and the concentrations of unbound UPy-LL were calculated with the help of a calibration line.

The formation of the UPy-NH₂ (bound to the IONs) and UPy-LL assemblies was examined by the Nile red (NR) encapsulation test on a Varian Cary Eclipse fluorescence spectrometer (Agilent Technologies, Santa Clara, CA, USA). A 0.1 g L⁻¹ ION@UPy-NH₂ suspension was combined with 0 μ L, 0.08 μ L, 0.16 μ L, 0.32 μ L, 0.64 μ L, 1.28 μ L, and 2.56 μ L of UPy-LL as described above. After overnight incubation to let the fibers assemble, 0.53 μ L of a 1 mM Nile red solution in MeOH was added (NR to UPy-LL 10:1). The particles were shaken at 400 rpm at room temperature for 20 min and then measured five times using a quartz cuvette (emission 565–800 nm, excitation 550 nm).

3.7. Antimicrobial Activity

The antimicrobial activity of ION@UPy-NH₂, ION@UPy-NH₂@UPy-LL, and free UPy-LL was analyzed with (RH)₄-GFP-expressing *E. coli* (BL21, DE3) performed in a manner analogous to the method stated in Turrina et al. [17]. ION@UPy-NH₂ in 50 mM PBS at pH 7.4 was diluted to 0, 0.1 g L⁻¹, 0.3 g L⁻¹, 0.5 g L⁻¹, 0.8 g L⁻¹, 1.0 g L⁻¹, 2.0 g L⁻¹, 3.0 g L⁻¹, 4.0 g L⁻¹, and 5.0 g L⁻¹. After dissolving, probes containing 0.0 μM, 2.2 μM, 4.4 μM, 8.9 μM, 18 μM, 35 μM, 54 μM, and 106 μM of the free UPy-LL were prepared. After binding, ION@UPy-NH₂@UPy-LL was diluted to similar UPy-LL concentrations (reaching a maximal particle concentration of 1.17 g L⁻¹). During the experiment, all samples were finally diluted 1:10.

4. Conclusions

ION@UPy-NH₂ is an interesting drug carrier material combining the favorable properties of IONs and supramolecular self-assembling systems. The UPy network forms a shell around the iron oxide core and small agglomerates, and it forms fibers. ION@UPy-NH₂ and its precursor showed high cytocompatibility in HK-2 cells and a concentration-dependent effect on the metabolic activity of macrophagic THP-1 cells. The particles were internalized faster by THP-1-derived macrophages and were fully internalized after 24 h by both cell types. ION@UPy-NH₂ binds UPy-LL with high efficiency (99%), inducing the reassembly and formation of smaller fibers. Attached to the drug carrier, the antimicrobial activity of UPy-LL is improved, leading to a MIC of 1.77 μM in *E. coli*. The combined system improved the cytocompatibility from 5.4 μM to 10.6 μM of the antimicrobial peptide for HK-2 cells, while it reduced the metabolic activity of THP-1-derived macrophages. The experiments demonstrated that ION@UPy-NH₂ can be easily combined with UPy–drug molecules and could be used as a magnetically controlled drug delivery system for the antimicrobial peptide LL. The usage of low concentrations and improved cytocompatibility makes the AMP applicable.

Supplementary Materials: The following supporting information can be downloaded at: <https://www.mdpi.com/article/10.3390/ijms241914649/s1>.

Author Contributions: The manuscript was written with the contributions of all authors. C.T.: conceptualization, methodology, validation, formal analysis, investigation, data curation, writing—original draft, visualization; J.C.: investigation, data curation, writing—original draft; R.B.: data curation, writing—original draft; J.S.: conceptualization, writing—review and editing; M.P.: validation, formal analysis, investigation; P.Y.W.D.: resources, funding acquisition, writing—review and editing, supervision; S.B.: resources, funding Acquisition, writing—review and editing, supervision; S.P.S.: conceptualization, funding acquisition, writing—review and editing, supervision, project administration. All authors have read and agreed to the published version of the manuscript.

Funding: We appreciate the support of TUM International Graduate School of Science and Engineering (IGSSE). We acknowledge the support of the partners of Regenerative Medicine Crossing Borders (RegMed XB), Powered by Health~Holland, Top Sector Life Sciences & Health, the Dutch Ministry of Education, Culture and Science (Gravitation program 024.003.013), the DPI (project 731.015.505), and the Dutch Antimicrobial Resistance Technology development and Biofilm Assessment Consortium (DartBac). The funders had no role in the design of this study, in the collection, analyses, and interpretation of data, in the writing of the manuscript, or in the decision to publish the results.

Institutional Review Board Statement: Not applicable.

Informed Consent Statement: Not applicable.

Data Availability Statement: The datasets generated and/or analyzed during the current study are available from the corresponding author on reasonable request.

Acknowledgments: The graphical abstract and Figure 1 were created with [BioRender.com](https://www.biorender.com) (accessed on 1 February 2023).

Conflicts of Interest: The authors declare no conflict of interest.

References

1. French, G.L. Clinical impact and relevance of antibiotic resistance. *Adv. Drug Deliv. Rev.* **2005**, *57*, 1514–1527. [CrossRef] [PubMed]
2. Bryson, V.; Szybalski, W. Microbial drug resistance. *Adv. Genet.* **1955**, *7*, 1–46. [PubMed]
3. United Nations. Sustainable Development Goals: Take Action for the Sustainable Development Goals. Available online: <https://www.un.org/sustainabledevelopment/sustainable-development-goals/> (accessed on 22 November 2022).
4. Hancock, R.E.W.; Sahl, H.-G. Antimicrobial and host-defense peptides as new anti-infective therapeutic strategies. *Nat. Biotechnol.* **2006**, *24*, 1551–1557. [CrossRef]
5. Parisien, A.; Allain, B.; Zhang, J.; Mandeville, R.; Lan, C.Q. Novel alternatives to antibiotics: Bacteriophages, bacterial cell wall hydrolases, and antimicrobial peptides. *J. Appl. Microbiol.* **2008**, *104*, 1–13. [CrossRef]
6. Toke, O. Antimicrobial peptides: New candidates in the fight against bacterial infections. *Biopolymers* **2005**, *80*, 717–735. [CrossRef] [PubMed]
7. Zhang, Q.-Y.; Yan, Z.-B.; Meng, Y.-M.; Hong, X.-Y.; Shao, G.; Ma, J.-J.; Cheng, X.-R.; Liu, J.; Kang, J.; Fu, C.-Y. Antimicrobial peptides: Mechanism of action, activity and clinical potential. *Mil. Med. Res.* **2021**, *8*, 48. [CrossRef]
8. Huan, Y.; Kong, Q.; Mou, H.; Yi, H. Antimicrobial Peptides: Classification, Design, Application and Research Progress in Multiple Fields. *Front. Microbiol.* **2020**, *11*, 582779. [CrossRef]
9. Tossi, A.; Sandri, L.; Giangaspero, A. Amphipathic, α -helical antimicrobial peptides. *Biopolymers* **2000**, *55*, 4–30. [CrossRef]
10. Cerovský, V.; Budesínský, M.; Hovorka, O.; Cvacka, J.; Voburka, Z.; Slaninová, J.; Borovicková, L.; Fucík, V.; Bednářová, L.; Votruba, I.; et al. Lasioglossins: Three novel antimicrobial peptides from the venom of the eusocial bee *Lasioglossum laticeps* (Hymenoptera: Halictidae). *Chembiochem* **2009**, *10*, 2089–2099. [CrossRef]
11. Matsuzaki, K. *Antimicrobial Peptides: Basics for Clinical Application*; Springer: Singapore, 2019; ISBN 9789811335884.
12. Costa, F.; Teixeira, C.; Gomes, P.; Martins, M. Clinical Application of AMPs. In *Advances in Experimental Medicine and Biology*; Springer: Singapore, 2019.
13. Tewabe, A.; Abate, A.; Tamrie, M.; Seyfu, A.; Abdela Siraj, E. Targeted Drug Delivery-From Magic Bullet to Nanomedicine: Principles, Challenges, and Future Perspectives. *J. Multidiscip. Healthc.* **2021**, *14*, 1711–1724. [CrossRef]
14. Sun, T.; Zhang, Y.S.; Pang, B.; Hyun, D.C.; Yang, M.; Xia, Y. Engineered nanoparticles for drug delivery in cancer therapy. *Angew. Chem. Int. Ed. Engl.* **2014**, *53*, 12320–12364. [CrossRef] [PubMed]
15. Turrina, C.; Milani, D.; Klassen, A.; Rojas-González, D.M.; Cookman, J.; Opel, M.; Sartori, B.; Mela, P.; Berensmeier, S.; Schwaminger, S.P. Carboxymethyl-Dextran-Coated Superparamagnetic Iron Oxide Nanoparticles for Drug Delivery: Influence of the Coating Thickness on the Particle Properties. *Int. J. Mol. Sci.* **2022**, *23*, 14743. [CrossRef] [PubMed]
16. Kumar, A.; Dixit, C.K. 3-Methods for characterization of nanoparticles. In *Advances in Nanomedicine for the Delivery of Therapeutic Nucleic Acids*; Gupta, N., Chan, R., Nimesh, S., Eds.; Woodhead Publishing: Duxford, UK, 2017; pp. 43–58, ISBN 978-0-08-100557-6.
17. Turrina, C.; Berensmeier, S.; Schwaminger, S.P. Bare Iron Oxide Nanoparticles as Drug Delivery Carrier for the Short Cationic Peptide Lasioglossin. *Pharmaceuticals* **2021**, *14*, 405. [CrossRef] [PubMed]
18. Lombardi, L.; Shi, Y.; Falanga, A.; Galdiero, E.; de Alteriis, E.; Franci, G.; Chourpa, I.; Azevedo, H.S.; Galdiero, S. Enhancing the Potency of Antimicrobial Peptides through Molecular Engineering and Self-Assembly. *Biomacromolecules* **2019**, *20*, 1362–1374. [CrossRef]
19. Zaccaria, S.; van Gaal, R.C.; Riool, M.; Zaat, S.A.J.; Dankers, P.Y.W. Antimicrobial peptide modification of biomaterials using supramolecular additives. *J. Polym. Sci. Part A Polym. Chem.* **2018**, *56*, 1926–1934. [CrossRef]
20. Shao, Y.; Jia, H.; Cao, T.; Liu, D. Supramolecular Hydrogels Based on DNA Self-Assembly. *Acc. Chem. Res.* **2017**, *50*, 659–668. [CrossRef]
21. de Greef, T.F.A.; Meijer, E.W. Materials science: Supramolecular polymers. *Nature* **2008**, *453*, 171–173. [CrossRef]
22. Webber, M.J.; Langer, R. Drug delivery by supramolecular design. *Chem. Soc. Rev.* **2017**, *46*, 6600–6620. [CrossRef]
23. Bakker, M.H.; Lee, C.C.; Meijer, E.W.; Dankers, P.Y.; Albertazzi, L. Multicomponent Supramolecular Polymers as a Modular Platform for Intracellular Delivery. *ACS Nano* **2016**, *10*, 1845–1852. [CrossRef]
24. Goor, O.J.; Hendrikse, S.I.; Dankers, P.Y.; Meijer, E.W. From supramolecular polymers to multi-component biomaterials. *Chem. Soc. Rev.* **2017**, *46*, 6621–6637. [CrossRef]
25. Dankers, P.Y.W.; Hermans, T.M.; Baughman, T.W.; Kamikawa, Y.; Kieltyka, R.E.; Bastings, M.M.C.; Janssen, H.M.; Sommerdijk, N.A.J.M.; Larsen, A.; van Luyn, M.J.A.; et al. Hierarchical formation of supramolecular transient networks in water: A modular injectable delivery system. *Adv. Mater.* **2012**, *24*, 2703–2709. [CrossRef] [PubMed]
26. Bakker, M.H.; Kieltyka, R.E.; Albertazzi, L.; Dankers, P.Y.W. Modular supramolecular ureidopyrimidinone polymer carriers for intracellular delivery. *RSC Adv.* **2016**, *6*, 110600–110603. [CrossRef]
27. Besseling, P.J.; Mes, T.; Bosman, A.W.; Peeters, J.W.; Janssen, H.M.; Bakker, M.H.; Fledderus, J.O.; Teraa, M.; Verhaar, M.C.; Gremmels, H.; et al. The in-vitro biocompatibility of ureido-pyrimidinone compounds and polymer degradation products. *J. Polym. Sci.* **2021**, *59*, 1267–1277. [CrossRef]
28. Song, J.; Schmitz, M.G.; Riool, M.; Guo, S.; Zaat, S.A.; Dankers, P.Y. Engineering Antimicrobial Supramolecular Polymer Assemblies. *J. Polym. Sci.* **2023**, pol.20230282. [CrossRef]
29. Saxena, S.K.; Khurana, S.M.P. *NanoBioMedicine*; Springer: Singapore, 2020; ISBN 978-981-32-9897-2.
30. Bayford, R.; Rademacher, T.; Roitt, I.; Wang, S.X. Emerging applications of nanotechnology for diagnosis and therapy of disease: A review. *Physiol. Meas.* **2017**, *38*, R183–R203. [CrossRef]

31. Tiwari, G.; Tiwari, R.; Sriwastawa, B.; Bhati, L.; Pandey, S.; Pandey, P.; Bannerjee, S.K. Drug delivery systems: An updated review. *Int. J. Pharm. Investig.* **2012**, *2*, 2–11. [[CrossRef](#)]
32. Langer, R. Drug delivery and targeting. *Nature* **1998**, *392*, 5–10.
33. Carmen Alvarez-Lorenzo, A.C. *Smart Materials for Drug Delivery*; Royal Society of Chemistry: London, UK, 2013; ISBN 978-1-84973-552-0.
34. Gupta, A.K.; Gupta, M. Synthesis and surface engineering of iron oxide nanoparticles for biomedical applications. *Biomaterials* **2005**, *26*, 3995–4021. [[CrossRef](#)]
35. Bruschi, M.L.; de Toledo, L.A.S. Pharmaceutical Applications of Iron-Oxide Magnetic Nanoparticles. *Magnetochemistry* **2019**, *5*, 50. [[CrossRef](#)]
36. Sun, C.; Lee, J.S.; Zhang, M. Magnetic Nanoparticles in MR Imaging and Drug Delivery. *Adv. Drug Deliv. Rev.* **2008**, *60*, 1252–1265. [[CrossRef](#)]
37. Israel, L.L.; Galstyan, A.; Holler, E.; Ljubimova, J.Y. Magnetic iron oxide nanoparticles for imaging, targeting and treatment of primary and metastatic tumors of the brain. *J. Control. Release* **2020**, *320*, 45–62. [[CrossRef](#)] [[PubMed](#)]
38. Giustini, A.J.; Petryk, A.A.; Cassim, S.M.; Tate, J.A.; Baker, I.; Hoopes, P.J. Magnetic Nanoparticle Hyperthermia in Cancer Treatment. *Nano Life* **2010**, *1*, 17–32. [[CrossRef](#)] [[PubMed](#)]
39. Bee, A.; Massart, R.; Neveu, S. Synthesis of very fine maghemite particles. *J. Magn. Magn. Mater.* **1995**, *149*, 6–9. [[CrossRef](#)]
40. Křížek, M.; Pechoušek, J.; Tuček, J.; Šafařová, K.; Medřík, I.; Machala, L. Iron oxide nanoparticle powders with high surface area. *AIP Conf. Proc.* **2012**, *1489*, 88. [[CrossRef](#)]
41. Laurent, S.; Forge, D.; Port, M.; Roch, A.; Robic, C.; Vander Elst, L.; Muller, R.N. Magnetic iron oxide nanoparticles: Synthesis, stabilization, vectorization, physicochemical characterizations, and biological applications. *Chem. Rev.* **2008**, *108*, 2064–2110. [[CrossRef](#)] [[PubMed](#)]
42. Lu, A.-H.; Salabas, E.L.; Schüth, F. Magnetic nanoparticles: Synthesis, protection, functionalization, and application. *Angew. Chem. Int. Ed. Engl.* **2007**, *46*, 1222–1244. [[CrossRef](#)]
43. Wu, W.; Wu, Z.; Yu, T.; Jiang, C.; Kim, W.-S. Recent progress on magnetic iron oxide nanoparticles: Synthesis, surface functional strategies and biomedical applications. *Sci. Technol. Adv. Mater.* **2015**, *16*, 23501. [[CrossRef](#)]
44. Turrina, C.; Dankers, P.Y.W.; Berensmeier, S.; Schwaminger, S. Iron oxide nanoparticles with supramolecular ureidopyrimidinone coating. *Curr. Dir. Biomed. Eng.* **2022**, *8*, 13–16. [[CrossRef](#)]
45. Hendrikse, S.I.S.; Wijnands, S.P.W.; Lafleur, R.P.M.; Pouderoijen, M.J.; Janssen, H.M.; Dankers, P.Y.W.; Meijer, E.W. Controlling and tuning the dynamic nature of supramolecular polymers in aqueous solutions. *Chem. Commun.* **2017**, *53*, 2279–2282. [[CrossRef](#)]
46. Stern, S.T.; Adisheshaiah, P.P.; Crist, R.M. Autophagy and lysosomal dysfunction as emerging mechanisms of nanomaterial toxicity. *Part. Fibre Toxicol.* **2012**, *9*, 20. [[CrossRef](#)]
47. Präbst, K.; Engelhardt, H.; Ringgeler, S.; Hübner, H. Basic Colorimetric Proliferation Assays: MTT, WST, and Resazurin. *Methods Mol. Biol.* **2017**, *1601*, 1–17. [[CrossRef](#)] [[PubMed](#)]
48. Collins, A.M.; Donoghue, A.M. Viability assessment of honey bee, *Apis mellifera*, sperm using dual fluorescent staining. *Theriogenology* **1999**, *51*, 1513–1523. [[CrossRef](#)] [[PubMed](#)]
49. Kumar, M.; Singh, G.; Arora, V.; Mewar, S.; Sharma, U.; Jagannathan, N.R.; Sapra, S.; Dinda, A.K.; Kharbanda, S.; Singh, H. Cellular interaction of folic acid conjugated superparamagnetic iron oxide nanoparticles and its use as contrast agent for targeted magnetic imaging of tumor cells. *Int. J. Nanomed.* **2012**, *7*, 3503–3516. [[CrossRef](#)]
50. Valcourt, J.R.; Lemons, J.M.; Haley, E.M.; Kojima, M.; Demuren, O.O.; Collier, H.A. Staying alive. *Cell Cycle* **2012**, *11*, 1680–1696. [[CrossRef](#)]
51. Fernandes, S.; Fernandez, T.; Metze, S.; Balakrishnan, P.B.; Mai, B.T.; Conteh, J.; de Mei, C.; Turdo, A.; Di Franco, S.; Stassi, G.; et al. Magnetic Nanoparticle-Based Hyperthermia Mediates Drug Delivery and Impairs the Tumorigenic Capacity of Quiescent Colorectal Cancer Stem Cells. *ACS Appl. Mater. Interfaces* **2021**, *13*, 15959–15972. [[CrossRef](#)]
52. Soenen, S.J.H.; de Cuyper, M. Assessing cytotoxicity of (iron oxide-based) nanoparticles: An overview of different methods exemplified with cationic magnetoliposomes. *Contrast Media Mol. Imaging* **2009**, *4*, 207–219. [[CrossRef](#)]
53. Fenton, H.J.H. LXXIII.—Oxidation of tartaric acid in presence of iron. *J. Chem. Soc. Trans.* **1894**, *65*, 899–910. [[CrossRef](#)]
54. Jang, Y.-Y.; Sharkis, S.J. A low level of reactive oxygen species selects for primitive hematopoietic stem cells that may reside in the low-oxygenic niche. *Blood* **2007**, *110*, 3056–3063. [[CrossRef](#)]
55. Kim, S.J.; Lewis, B.; Steiner, M.-S.; Bissa, U.V.; Dose, C.; Frank, J.A. Superparamagnetic iron oxide nanoparticles for direct labeling of stem cells and in vivo MRI tracking. *Contrast Media Mol. Imaging* **2016**, *11*, 55–64. [[CrossRef](#)]
56. Rueda-Gensini, L.; Cifuentes, J.; Castellanos, M.C.; Puentes, P.R.; Serna, J.A.; Muñoz-Camargo, C.; Cruz, J.C. Tailoring Iron Oxide Nanoparticles for Efficient Cellular Internalization and Endosomal Escape. *Nanomaterials* **2020**, *10*, 1816. [[CrossRef](#)]
57. Fröhlich, E. The role of surface charge in cellular uptake and cytotoxicity of medical nanoparticles. *Int. J. Nanomed.* **2012**, *7*, 5577–5591. [[CrossRef](#)] [[PubMed](#)]
58. Gu, J.; Xu, H.; Han, Y.; Dai, W.; Hao, W.; Wang, C.; Gu, N.; Xu, H.; Cao, J. The internalization pathway, metabolic fate and biological effect of superparamagnetic iron oxide nanoparticles in the macrophage-like RAW264.7 cell. *Sci. China Life Sci.* **2011**, *54*, 793–805. [[CrossRef](#)] [[PubMed](#)]
59. Di, J.; Gao, X.; Du, Y.; Zhang, H.; Gao, J.; Zheng, A. Size, shape, charge and “stealthy” surface: Carrier properties affect the drug circulation time in vivo. *Asian J. Pharm. Sci.* **2021**, *16*, 444–458. [[CrossRef](#)] [[PubMed](#)]

60. Champion, J.A.; Mitragotri, S. Shape induced inhibition of phagocytosis of polymer particles. *Pharm. Res.* **2009**, *26*, 244–249. [[CrossRef](#)] [[PubMed](#)]
61. Lam, S.J.; O'Brien-Simpson, N.M.; Pantarat, N.; Sulistio, A.; Wong, E.H.H.; Chen, Y.-Y.; Lenzo, J.C.; Holden, J.A.; Blencowe, A.; Reynolds, E.C.; et al. Combating multidrug-resistant Gram-negative bacteria with structurally nanoengineered antimicrobial peptide polymers. *Nat. Microbiol.* **2016**, *1*, 16162. [[CrossRef](#)] [[PubMed](#)]
62. Nederberg, F.; Zhang, Y.; Tan, J.P.K.; Xu, K.; Wang, H.; Yang, C.; Gao, S.; Guo, X.D.; Fukushima, K.; Li, L.; et al. Biodegradable nanostructures with selective lysis of microbial membranes. *Nat. Chem.* **2011**, *3*, 409–414. [[CrossRef](#)]

Disclaimer/Publisher's Note: The statements, opinions and data contained in all publications are solely those of the individual author(s) and contributor(s) and not of MDPI and/or the editor(s). MDPI and/or the editor(s) disclaim responsibility for any injury to people or property resulting from any ideas, methods, instructions or products referred to in the content.

3.6. Superparamagnetic iron oxide nanoparticles for their application in the human body: Influence of the surface

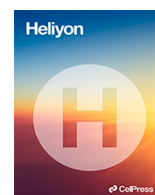
IONs are the focus of research in nanomedicine, especially for the topics of diagnosis, therapeutics, and drug delivery. For application in the human body, IONs are often coated to introduce specific functionalities, to improve biocompatible, or make them colloidal stable. Much research on the coating of IONs has been done, focusing on the synthesis and application. However, the effect of the surface properties on long-term agglomeration, degradation, and oxidative stress has often been neglected.

This study provided an improved experimental setup to screen various particles within three days. Four different simulated body fluids were used to mimic the path of IONs after injection from the bloodstream into the cell. As a result, the particles encounter physiological pH of 7.4 in the blood and the cytosol to pH 4-5 in the endosome or lysosome. An improved incubation and shaking protocol ensured that the IONs were fully dispersed over 72 hours and did fasten the preclinical screening by factor 4.6. A combination of DLS and phenanthroline assay showed detailed agglomeration and iron ion release coherences. An oxidative stress assay underlined this data based on low-density lipoproteins (LDL).

Four different IONs, BIONs, ION@Dex, ION@PVA, and ION@PLGA were applied in this study. These coating materials are commonly used and of high interest in nanomedicine. The particles were fully characterized by their particle composition, surface properties, particle size distribution, behavior in the magnetic field, and cytocompatibility in smooth muscle cells. All particles showed good cytocompatibility within three days. ION@PVA had the highest colloidal stability over a broad pH range in water and around the IEP. The composition and pH of the simulated media highly influenced the agglomeration of IONs and, therefore, their potential behavior in the human body. The aggregation and degradation directly affected each other. The iron ion release was increased or decreased depending on the coating material. ION@PVA experienced the fastest degradation in artificial lysosomal fluid and the highest colloidal stability in all media. ION@Dex showed rapid degradation in artificial endosomal fluid and the fastest oxidation profile for LDL.

The work provided new and essential insights into the effect of various standard coatings on properties like magnetophoretic behavior, cytocompatibility, hydrodynamic diameters, particle degradation, and oxidative stress. The new analytical setup allows fast and reliable screening of IONs to analyze the effect of coating on their aggregation and dissolution.

The doctoral candidate's substantial contributions were the study's conception and design after critically reviewing existing literature. The doctoral candidate was the leading author of the manuscript. The experiments were carried out by the doctoral candidate together with A. Klassen, D. Milani, D. Rojas-González, and S. Schwaminger. A. Klassen, D. Milani, and S. Schwaminger and the doctoral candidate did data analysis and processing.



Research article

Superparamagnetic iron oxide nanoparticles for their application in the human body: Influence of the surface



Chiara Turrina^a, Anna Klassen^a, Davide Milani^a, Diana M. Rojas-González^b, Gerhard Ledinski^c, Doris Auer^d, Barbara Sartori^e, Gerhard Cvirn^c, Petra Mela^b, Sonja Berensmeier^a, Sebastian P. Schwaminger^{a,c,f,*}

^a Chair of Bioseparation Engineering, TUM School of Engineering and Design, Technical University of Munich, Germany

^b Chair of Medical Materials and Implants, TUM School of Engineering and Design, Munich Institute of Biomedical Engineering, Technical University of Munich, Germany

^c Division of Medicinal Chemistry, Otto Loewi Research Center, Medical University of Graz, Austria

^d Division of Medical Physics and Biophysics, Gottfried Schatz Research Center, Medical University of Graz, Austria

^e Institute of Inorganic Chemistry, Graz University of Technology, Stremayrgasse 9/IV, Graz, 8010, Austria

^f BioTechMed-Graz, Austria

ARTICLE INFO

Keywords:

Iron oxide nanoparticles
Nanomedicine
Simulated body fluids
Cytocompatibility
Agglomeration
Magnetic separation

ABSTRACT

Iron oxide nanoparticles (IONs) are of great interest in nanomedicine for imaging, drug delivery, or for hyperthermia treatment. Although many research groups have focused on the synthesis and application of IONs in nanomedicine, little is known about the influence of the surface properties on the particles' behavior in the human body. This study analyzes the impact of surface coatings (dextran, polyvinyl alcohol, polylactide-co-glycolide) on the nanoparticles' cytocompatibility, agglomeration, degradation, and the resulting oxidative stress induced by the particle degradation. All particles, including bare IONs (BIONs), are highly cytocompatible (>70%) and show no significant toxicity towards smooth muscle cells. Small-angle X-ray scattering profiles visualize the aggregation behavior of nanoparticles and yield primary particle sizes of around 20 nm for the investigated nanoparticles. A combined experimental setup of dynamic light scattering and phenanthroline assay was used to analyze the long-term agglomeration and degradation profile of IONs in simulated body fluids, allowing fast screening of multiple candidates. All particles degraded in simulated endosomal and lysosomal fluid, confirming the pH-dependent dissolution. The degradation rate decreased with the shrinking size of particles leading to a plateau. The fastest Fe²⁺ release could be measured for the polyvinyl-coated IONs. The analytical setup is ideal for a quick preclinical study of IONs, giving often neglected yet crucial information about the behavior and toxicity of nanoparticles in the human body. Moreover, this study allows for the development and evaluation of novel ferroptosis-inducing agents.

1. Introduction

One of nanotechnology's most active research fields is nanomedicine, which applies nanotechnology to precise medical interventions for preventing, diagnosing, and treating diseases [1,2]. With 76% of scientific papers and 59% of patents, drug delivery is

* Corresponding author. Division of Medicinal Chemistry, Otto Loewi Research Center, Medical University of Graz, Austria.
E-mail address: sebastian.schwaminger@medunigraz.at (S.P. Schwaminger).

<https://doi.org/10.1016/j.heliyon.2023.e16487>

Received 15 March 2023; Received in revised form 16 May 2023; Accepted 18 May 2023

Available online 25 May 2023

2405-8440/© 2023 The Authors. Published by Elsevier Ltd. This is an open access article under the CC BY license (<http://creativecommons.org/licenses/by/4.0/>).

the most dominant part of nanomedicine [3]. Iron oxide nanoparticles (IONs) can be applied for targeted or magnetically controlled drug delivery [4]. Additional to their superparamagnetic behavior, high surface-to-volume ratio, fast and cost-efficient synthesis, and low toxicity, IONs can encapsulate, disperse, adsorb, or conjugate drugs [5]. Guided by an external magnetic field, drug-loaded particles can be specifically transported to unhealthy tissue, like cancerous tumors, thereby reducing systemic side effects and decreasing the overall amount of drugs [6,7]. To date, intravenous injection of drug-loaded nanoparticles is one of the most widely explored systems in targeted drug delivery [8]. IONs are already well accepted as T2 (transverse relaxation time) contrast agents for noninvasive magnetic resonance imaging (MRI). The superparamagnetic core of IONs affects the transverse relaxation time of protons in nearby tissues and can be measured by a darkened tissue [9]. IONs have also found an application in hyperthermia, an alternative cancer treatment [10]. Here, an alternating magnetic field is used to heat the temperature-sensitive tumor cells to temperatures ≥ 41 °C [10].

For the application in nanomedicine, IONs must be biocompatible, colloiddally stable, and often need to be specifically functionalized [10–12]. These criteria are usually not fulfilled by bare IONs (BIONs), leading to massive research in nanoparticle coatings in recent years [11,12]. Often a core-shell structure is preferred, leading to stabilized and flexible particle systems [10]. Organic coatings are advantageous due to their biocompatibility and water solubility [12,13]. Polyethylene glycol (PEG), polyvinylpyrrolidone (PVP), polyvinyl alcohol (PVA), chitosan, and dextran (Dex) are well known to prolong the circulation of particles in the blood [12–15]. For this study, poly(lactid-co-glycolid) (PLGA), Dex, and PVA-coated IONs are analyzed as they are already established and commonly used coatings [11].

Dex-coated IONs are used as contrast agents in MRI scans and to treat anemia in patients [16,17]. For drug delivery application, Khalkhali et al. were able to bind and slowly release a polyphenolic plant constituent (curcumin) with pharmacological properties from Dex-coated IONs [18]. Unterweger et al. and Peng et al. also investigated the use of ION@Dex as a drug delivery system in cancer therapy by loading the particles with the chemotherapeutic drug doxorubicin or hypericin [19,20]. For some of the described applications, the Dex-coating has already been approved by the Food and Drug Administration (FDA) [16,17,21]. PLGA is biodegradable. It can be hydrolyzed to the metabolic monomers lactic acid and glycolic acid [22]. Furthermore, PLGA as material is approved by the FDA and European Medicines Agency (EMA) [22,23]. ION@PLGA can encapsulate hydrophobic and hydrophilic molecules and protect the drug from degradation, making it ideal for drug delivery systems [22]. Saengruengrit et al. used ION@PLGA to deliver proteins to bone marrow-derived primary dendritic cells [24]. Ruggiero et al. synthesized ION@PLGA particles loaded with multiple anticancer drugs that perform a magneto fluid hyperthermia-triggered drug release [25]. PVA has a hydrophilic character and is biodegradable [26]. It is widely used as a protective agent to stabilize IONs and is approved by the FDA [11,27]. Kayal et al. confirmed that ION@PVA is a promising candidate for magnetically targeted drug delivery of doxorubicin [28]. Furthermore, Ebadi et al. used PVA/LDH (magnesium-aluminium-layered double hydroxide)-coated particles with the drug sorafenib and showed high drug release in simulated acidic tumor environments [29].

For an application in the human body, degradation and colloidal stability over time are critical factors to consider in the preclinical development of IONs [30]. Thus long-term agglomeration and Fe^{2+} -release studies are essential to better understand the particles' behavior after injection into the body. The latter is important since the degradation of IONs, depending on the coating, can be very slow, with a half-life of several weeks [31]. The morphology, size, and agglomeration behavior influence the degradation of particles [32]. Smaller particles dissolve faster than large ones [32]. Long-term studies in mice showed that maghemite nanoparticles were degraded in the lysosome and were ultimately stored in the liver and the spleen [31]. Levy et al. demonstrated that colloidal stability due to the degradation profile of three differently coated IONs is influenced by the pH and they identified a degradation optimum for these particles at pH 4 [33]. Undesirable side effects can occur if the particles agglomerate in the body. For biomedical applications, particles smaller than 100 nm are recommended to prevent toxic effects such as thrombogenesis and prolonged blood circulation [11]. In addition, Limbach et al. reported that slight variations in the particle's surface chemistry significantly impact the stability, slow down the aggregation rate, and enhance the colloidal stability [34]. Following intravenous injection, the particles encounter a physiological pH of 7.4 in the blood and cytosol to more acidic pH (4–5) in degradation compartments [35–37].

Simulated fluids represent an interesting and cost-efficient alternative to *in vivo* experiments, which have been increasingly used in recent years [36,38]. They allow the conception of fast and effective screenings of potentially applicable and safe nanoparticles in nanomedicine in the preclinical phase. Additionally, animal experiments can be reduced to a minimum [36]. SBF (simulated body fluid, pH = 7.4) simulates the conditions in the blood circulation, and PBS (phosphate buffered saline, pH = 7.4) simulates the cytosol [36,39,40]. Late endosomes and lysosomes degrade the particles within the cells. AEF (artificial endosomal fluid, pH = 5.5) simulates the conditions in the late endosome, and ALF (artificial lysosomal fluid, pH = 4.5) the conditions after particle uptake in the lysosome [41]. The buffers simulate the path a particle can take in the body after intravenous administration. They have a much more complex composition than simple acids and are similar to the original hard-to-reach fluids due to their salt composition [31,35,42,43].

Under these acidic conditions, IONs are easily dissolved. This is especially true for complexing and reducing buffers containing carboxylic acids such as citrate [44]. This results in the formation of iron ions. Iron ions have gained great interest for usage in ferroptosis applications. Especially the combination of ferric and ferrous ions is interesting for use in ferroptosis applications and the generation of reactive oxygen species (ROS) in cells [45]. Thus, multiple nanoparticle-based systems have been developed in the last years to deliver iron ions for ferroptosis therapy [46]. Aside from crystalline materials, amorphous iron nanoparticles and metal organic frameworks (MOFs) have also been developed for the specific release of ferrous and ferric ions [47]. Acidic environments allow for Fenton reactions and hydrogen peroxide production, which can be used in tumor treatment [48]. The general pathway for the treatment is via the production of very reactive hydroxyl radicals, which oxidize lipoproteins. Following this oxidation, lipid peroxides induce ferroptosis [49].

Although many research groups have focused on the synthesis and application of IONs in nanomedicine, little is known about the

influence of the surface properties on the particle's behavior in the human body. To better understand the impact of different coating materials on the IONs degradation and agglomeration profile, BIONs, ION@Dex, ION@PVA, and ION@PLGA were incubated in simulated body fluid (SBF), artificial lysosomal fluid (ALF), artificial endosomal fluid (AEF), and phosphate-buffered saline (PBS) for 72 h at 37 °C. The hydrodynamic diameters were analyzed by dynamic light scattering (DLS) and the Fe²⁺ release by phenanthroline assay. Oxidative stress was analyzed with an low-density lipoprotein (LDL) assay. The novelty of this investigation is the release of iron ions in artificial bodily fluids depending on the surface modifications of iron oxide nanoparticles. The presented data gives essential insights into the applicability of IONs in nanomedicine and shows a fast screening method that can be used in the preclinical phase.

2. Material and methods

2.1. Synthesis

2.1.1. BIONs

BIONs were synthesized by the co-precipitation method according to the Massart process [50]. The experiment was performed analogously to Turrina et al. [51]. The characterization data was previously published and is only used for comparison [52].

2.1.2. Dextran-coated IONs

Dextran-coated particles were prepared similarly to BIONs using the Massart process. In this process, 9.5 mL of Dextran solution (10.0 g L⁻¹, Sigma Aldrich) was added with 83 mL of iron (II/III) solution (FeCl₂ × 4H₂O (735 mg), Sigma Aldrich; FeCl₃ × 6H₂O (2000 mg), Carl Roth) in a 100 mL round bottom flask under N₂ atmosphere. Co-precipitation is started after adding 7.5 mL of 25% NH₄OH solution, and the reaction was run under homogeneous stirring at 70 °C for 30 min. After completion of the reaction, the excess salts are removed by washing with degassed ddH₂O (4×) until a conductivity lower than 200 μS cm⁻¹ is obtained.

2.1.3. PVA-coated IONs

The principles of the Massart process were applied for the synthesis of the ION@PVA particles. Beforehand, 2.88 g NaOH (Carl Roth) and 3.00 g PVA (Sigma Aldrich) were mixed in 20 mL degassed water and treated in an ultrasonic bath until everything had dissolved. In parallel, 40 mL of iron (II/III) solution (FeCl₂ × 4H₂O (1.40 g), Sigma Aldrich; FeCl₃ × 6H₂O (3.47 g), Carl Roth) was prepared in degassed water. The reaction was started by mixing the two solutions in a 100 mL round bottom flask under nitrogen conditions. The reaction was run for 30 min at 80 °C. The reaction broth was washed with absolute ethanol (2×, VWR chemicals) and degassed ddH₂O (3×) until a conductivity below 200 μS cm⁻¹ was achieved.

2.1.4. PLGA-coated IONs

ION@PLGA was synthesized by a single emulsion method [53]. In this preparation technique, 40.0 mg, PLGA 50:50 of 38–54 kDa (Fluka Sigma Aldrich) were dissolved in an organic phase comprised of dichloromethane and acetone at a 2:1 vol ratio. Additionally, 100 μL of ultrasonicated 3-aminopropyltrimethoxysilane (APTS) coated IONs suspended in ethanol (10.0 g L⁻¹) were added. Afterward, 6.00 mL of an aqueous phase containing 0.30% PVA (Fluka Sigma Aldrich) was poured into the solution and emulsified by ultrasonication in the Branson Digital Sonifier 450 (Emerson Electric Co, 30 s, 30.0%, 15 s ON, 15 s OFF). Complete evaporation of the organic phase was ensured by continuous stirring at 550 rpm and at a temperature of 25 °C for 17 h. The particles were magnetically separated and washed with 2.00 mL of deionized water (3×) to remove excess PVA and other loosely adsorbed excipients. All particles are stored in deionized water under a N₂ atmosphere at 4 °C.

2.2. Characterization

(Fourier-transform infrared spectroscopy) FT-IR spectroscopy (Alpha II; Bruker Corporation; Billerica) and platinum attenuated total reflection module (4000 cm⁻¹ to 400 cm⁻¹, 24 scans) were used to confirm functional groups' presence on the IONs' surface. The background was subtracted with the concave rubber band method (OPUS 8.1). Lyophilized IONs (Alpha 1–2 Ldplus, Christ, -60 °C overnight in vacuum) were analyzed by powder X-ray diffraction (XRD) with the STOE Stadi-P Diffractometer (flatbed measurement, molybdenum source, 0.7093 Å). The saturation magnetization was determined by SQUID analysis. 10 mg of particles were fixed in a small plastic tube (Fixogum, Marabu GmbH & Co KG, Tamm, Germany) and measured with the magnetometer MPMS XL-7 (Quantum Design, San Diego USA) at 300 K and a magnetic field variation of -50 kOe to +50 kOe. The LUMIReader (4532-123; LUM GmbH) was used to analyze the sedimentation rate of the IONs in a magnetic field by STEP technology. The particles (1.00 g L⁻¹, pH 7) were ultrasonicated and then contacted with five stacked cylindrical neodymium (NdFeB) magnets (d = 12 mm; h = 2 mm, N45, Webcraft GmbH, Gottmadingen, Germany) and measured at wavelengths of 870 nm, 630 nm, and 420 nm (Profile: 1000; Interval: 1s; Angle: 0°; Light factor: 1.00; Temperature: 25 °C; magnetization 29.1–54.4 Am² kg⁻¹). The processing of the obtained data was performed by the software PSA-Wizard (SEPview™; Analysis positions: 13.0 mm, 15.0 mm, 17.0 mm, 19.0 mm). The particle size and morphology are measured by Transmission electron microscopy (TEM) with the TEM JEM JEOL 1400 (×120k). The samples (0.03 g L⁻¹, 10 μL, after ultrasonication) were dried onto a glow-discharged carbon-coated copper grid. For analysis (ImageJ), at least 100 particles from three different areas were measured. The Zetasizer Ultra (Malvern Panalytical) was used to measure dynamic light scattering (DLS) and the zeta potential of a 1 g L⁻¹ solution (ddH₂O pH = 2–10, after ultrasonication, Cuvette STD UV 4 clear side, KARTELL S. p.a., and DTS1070, Malvern Instruments). A Boltzmann fit determined the isoelectric point (IEP).

Small angle X-ray scattering (SAXS) data were acquired at the Austrian SAXS beamline at the Elettra Synchrotron in Trieste; the

beamline length was set to 1386.101 mm, corresponding to a q range of 0.07 nm^{-1} - 5.3 nm^{-1} , where $q = 4\pi \sin\theta/\lambda$, λ is the wavelength of the incident X-rays, and 2θ is the scattering angle. The photon energy was set to 8 keV corresponding to a wavelength of 0.154 nm. The sample was loaded in a quartz capillary with 1.5 mm diameter and exposed to X-rays. 10 images of 10 s each were collected by a Pilatus 3 1 M detector (Dectris Ltd., Baden, Switzerland). The angular scale of the diffraction pattern was calibrated with silver behenate (d-spacing 5.8376 nm). The acquired images were azimuthally integrated by SAXSDog, the automatic data integration pipeline available at the SAXS outstation, normalized on transmission and fluctuation of the primary beam intensity, and background subtracted.

The experimental setup for optofluidic force induction (OF2i) measurements consists of a 2D optical trap in a cylindrical flow cell using a weakly focused doughnut-shaped vortex beam. The laser beam is generated by a 532 nm linear polarized CW DPSS laser (Laser Quantum, GEM532) with a maximum output power of 2 W. The beam alignment is achieved using two mirrors and a $5\times$ expander. A vortex phase plate generates a Laguerre-Gaussian mode with topological charge $m = 2$. The ultramicroscope consists of a $10\times$ PLAN microscope objective, an optical filtering bank, a 50 mm focusing lens, and a CCD camera for imaging. The microfluidic flow cell consists of a continuous, dead volume optimized pumping and laminar fluid handling setup, following derivable fluid continuity principles [54]. Particles have been dispersed in acetate buffer solutions and ultrasonicated at concentrations of around $1 \mu\text{g mL}^{-1}$ prior to OF2i measurements.

Human low-density lipoprotein (LDL) was obtained from the plasma of normolipemic, fasting male donors by sequential ultracentrifugation within the density of $1.020\text{--}1.050 \text{ g mL}^{-1}$. Diethylenetriaminepentaacetic acid (DTPA) and Pefabloc were present during all steps of lipoprotein preparation to prevent lipid peroxidation and apo B cleavage by contaminating bacteria or proteinases. The LDL were dialysed against a 10 mM Tris HCl, Isotone, $100 \mu\text{M}$ DTPA, pH 7.40, sterile-filtered and stored at 4°C in the dark until use. The LDL concentration was measured by dry weight determination and the protein content by the Lowry method [55]. The freshly prepared LDL were dialysed against a 10 mM PBS without DTPA. Subsequently, the LDL was diluted with a 100 mM sodium acetate buffer, pH 4.50 to give a concentration of $0.2 \text{ mg LDL mL}^{-1}$. The nanoparticle suspensions (1 g L^{-1}) were added to the LDL to give a final concentration of $200 \mu\text{M}$. The formation of conjugated dienes was continuously monitored at 234 nm by a spectrophotometer (Hitachi U-2000) at 37°C for 240 min using 1 cm quartz cuvette [56].

Cytocompatibility was assessed following ISO-10993 guidelines. Human umbilical artery smooth muscle cells (HUASMCs, Promocell, passage 7) were used for the cytocompatibility assay. The cells were expanded in culture medium consisting of DMEM supplemented with 10% fetal calf serum (FCS, Gibco) and 1% antibiotic/antimycotic mix (ABM, Gibco). The different IONs were sterilized using H_2O_2 -low-temperature-plasma, resuspended in the phosphate-buffered saline, ultrasonicated (10 min), and transferred to the medium by magnetic separation. The samples were diluted to 0.1 g L^{-1} in culture medium. For the test, $10,000 \text{ cells cm}^{-2}$ were seeded in 96-well plates (Greiner Bio-One, Germany) and incubated at 37°C with 5% CO_2 for 24 h to allow for cell adhesion. Afterward, the different experimental samples were added to the cells. Culture medium served as the negative control, while culture medium supplemented with 2% Triton x-100 (Sigma) was used as the positive control. Cell proliferation was analyzed 24 and 72 h after adding IONs, by a commercial cell proliferation kit (XTT, Roche) following manufacturer's instructions. Briefly, $50 \mu\text{L}$ of the working solution (1:50 electron coupling reagent (ECR) with the XTT solution) were transferred to each well and incubated for 2 h. The optical density of formazan was measured at a wavelength of 450 nm and a reference wavelength of 630 nm using a plate reader (Spark, Tecan). An initial measurement at 0 h was used to exclude the effect of the IONs on the optical density. For better data visualization, all values were normalized to the absorbance of the NC.

The composition of PBS, AEF, ALF, and SBF can be found in the supplementary material (Tables S1–S3).

A 1.00 g L^{-1} particle solution in water (BIONs, ION@PVA, ION@Dex, ION@PLGA) was prepared and ultrasonicated (30 min). For each buffer, triplicates were prepared by exchanging the liquid phase through magnetic decantation. All samples are incubated at 37°C in an incubation shaker (Thermomixer comfort, Eppendorf) at 1000 rpm for 72 h. The hydrodynamic diameters were measured by DLS (Cuvette STD UV 4 clear side, KARTELL S.p.a.) using Zetasizer Ultra (Malvern Panalytical) at 37°C after 0, 1, 3, 5, 24, 48, and 72 h.

For each buffer, 2.00 mL of a 1.00 g L^{-1} for all particles were prepared as described above and incubated at 37°C in a thermoshaker at 1000 rpm. After 0, 1, 3, 5, 24, 48, and 72 h, $80 \mu\text{L}$ of the particle solution were taken and centrifuged at 17,000 rpm for 20 min to remove interfering particles. $60 \mu\text{L}$ of the supernatant were transferred to a new reaction tube, and $100 \mu\text{L}$ of 10% (w/v) ascorbic acid (Table S4) and $400 \mu\text{L}$ of acetate buffer (Table S5) were added. Fe^{3+} ions are reduced to Fe^{2+} by the added ascorbic acid. After incubation for 5 min at room temperature, $50 \mu\text{L}$ of 0.5% (v/v) phenanthroline solution (Table S6) were added and incubated for another 20 min. Subsequently, the volume is filled up to 1.00 mL with deionized water. Fe^{2+} ions form a red-orange chelate complex with 1,10-phenanthroline [57]. $300 \mu\text{L}$ of the sample were pipetted into a 96-well plate; then, the absorbance was measured at 510 nm using Tecan Infinite M200 microplate reader. The analysis was performed in triplicates. For the calibration curve, a 0.10 g L^{-1} Fe^{2+} stock solution was prepared from $\text{FeCl}_2 \times 4\text{H}_2\text{O}$ (Table S7). From the solution 0, 1, 2, 4, 6, 10, 20, 30, 50, 60, 80, 100, 120 and $160 \mu\text{L}$ were taken. The concentration of free iron ions was normalized to the initial concentration of the particulate stock solution. Therefore, $60 \mu\text{L}$ of the $300 \mu\text{L}$ remaining particle solutions were dissolved in $60 \mu\text{L}$ of concentrated hydrochloric acid (37%). The solution was filled to 1.00 mL with ddH_2O and mixed. From the diluted solution, $60 \mu\text{L}$ were treated in the acetate buffer-ascorbic acid mix analogous to the supernatants described above and then mixed with phenanthroline.

3. Results and discussion

The co-precipitation technique was used to synthesize BIONs, ION@PVA, and ION@Dex [50,51]. The PLGA coating was generated by the single emulsion method [53].

All particles were analyzed regarding their particle composition, size, surface properties, agglomeration, saturation magnetization, magnetophoretic behavior, and cytocompatibility. The detailed characterization of the used BIONs can be found in Turrina et al. [52].

The successful Dex, PVA, or PLGA coating is determined by FT-IR (Fig. S1). All particles show the characteristic Fe–O peak at 582 cm^{-1} [51,58–60]. For ION@Dex, the spectra showed $\nu\text{C-H}$ at 1622 cm^{-1} and $\nu\text{C-O}$ vibrations at around 1019 cm^{-1} and 1028 cm^{-1} [18, 61]. Between 765 cm^{-1} and 914 cm^{-1} , vibrations of the glucopyranose ring can be observed [62]. For PVA-coated IONs, a C–C stretching vibration at 1416 cm^{-1} and a Fe–O–C bond at 1092 cm^{-1} were observed [28]. At 850 cm^{-1} , the ρCH_2 vibration is visible, and adsorbed water was also detected at 1620 cm^{-1} [28]. For ION@Dex and ION@PVA, the intensity ratio of coating and ION is comparable, whereas ION@PLGA shows intense characteristic polymer peaks that overlay the distinct iron oxide peak. This ratio indicates a thicker polymer layer for ION@PLGA than the other two. The peak at 1754 cm^{-1} is attributed to the vibration of the carbonyl groups in the two monomers of PLGA. The bands between 1271 cm^{-1} to 1087 cm^{-1} are assigned to C–O vibrations [63].

The crystal structure of the different particles is determined by X-ray diffraction (XRD) analysis (Fig. 1D, Fig. S2) The measurements show the characteristic reflections corresponding to spinel structured iron oxide at 13.7° (220), 16.1° (311), 19.5° (400), 25.4° (511), and 27.7° (440) for all particles [11]. The coatings do not influence the crystal structure of the IONs.

The particle size is an essential criterion in nanomedicine [64]. A diameter between 10 and 100 nm is ideal for most applications in this field, avoiding rapid cleaning from the bloodstream and easy uptake through the blood-brain barrier [64,65]. Furthermore, small diameters lead to a large surface-to-volume ratio, giving the possibility of binding vast amounts of drugs or presenting many functional groups [11,12].

The Scherrer equation (Equation S1) uses XRD data to determine the iron oxide core size. Additionally, the morphology and particle diameter were determined with TEM. The diameters of BIONs coincide, $d_{\text{Scherrer}} = 8.8 \pm 0.9\text{ nm}$ and $d_{\text{TEM}} = 8.7 \pm 1.6\text{ nm}$ [52]. Therefore, the coating thickness was calculated by subtracting d_{Scherrer} from d_{TEM} . ION@Dex and ION@PLGA have comparable diameters with $d_{\text{Scherrer}} \sim 8.7\text{ nm}$ and $d_{\text{TEM}} \sim 10.5\text{ nm}$ (Table). The calculated coating thickness is, therefore, $\Delta d = \sim 1.8\text{ nm}$. Both particle types accumulate in small clusters (Fig. 2B, D). ION@Dex falls in the size range found in the literature between 3 nm and 13 nm [19,20,66]. According to Kayal et al., the average diameter of ION@PVA lies in the range of 10–15 nm, which can be compared with the synthesized particles [28]. ION@PLGA has a $d_{\text{TEM}} = 9.5\text{ nm}$. The Scherrer diameter could not be calculated because the thick coating leads to small reflexes even with intense measurement time (Equation S1). The PLGA-coated particles show smaller clusters and even some single ION@PLGA (Fig. 2F).

In the human body, multiple media with different pH values can be found, ranging from the acidic gastric system with a pH of 2 over pH 4–5 for the lysosomal or endosomal fluid up to the neutral pH of 7.4 of the cellular fluid or blood [35,36,67]. pH value and ionic strength can highly influence the colloidal stability of nanoparticles and therefore affect their hydrodynamic diameters [51]. DLS and zeta potential were used to analyze the surface charge and colloidal stability. Between a zeta potential range of -10 mV and $+10\text{ mV}$, nanoparticles are considered unstable and tend to agglomerate strongly [11].

For ION@Dex, ION@PVA, and ION@PLGA, the hydrodynamic diameters are analyzed in dependence on the pH in water.

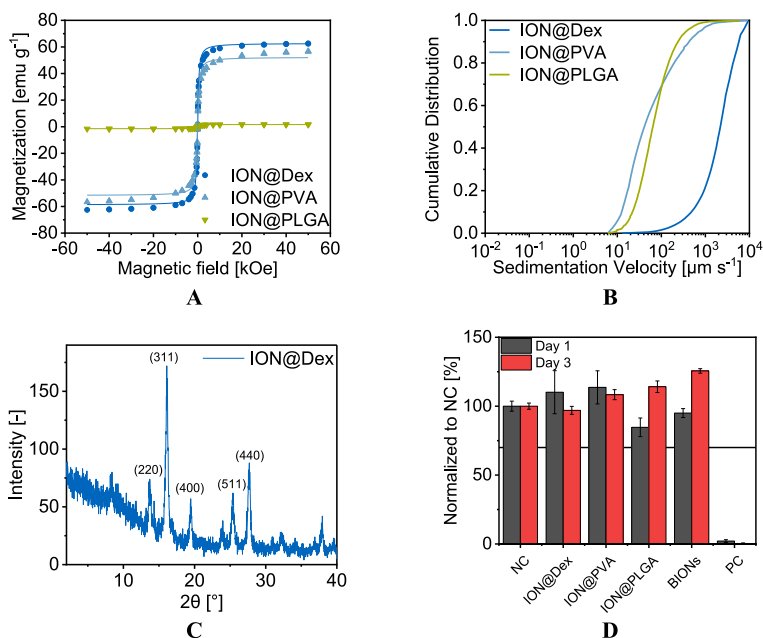


Fig. 1. SQUID analysis at 300 K, processed with the Langevin Mod fit (A). Cumulative velocity distribution at pH 7 in water, at room temperature (B). X-ray diffractogram of ION@Dex (C). Cytocompatibility over three days was analyzed by XTT assay with smooth muscle cells on the different particles, as well as a negative control (NC) and a positive control (PC). The results were normalized to NC (D).

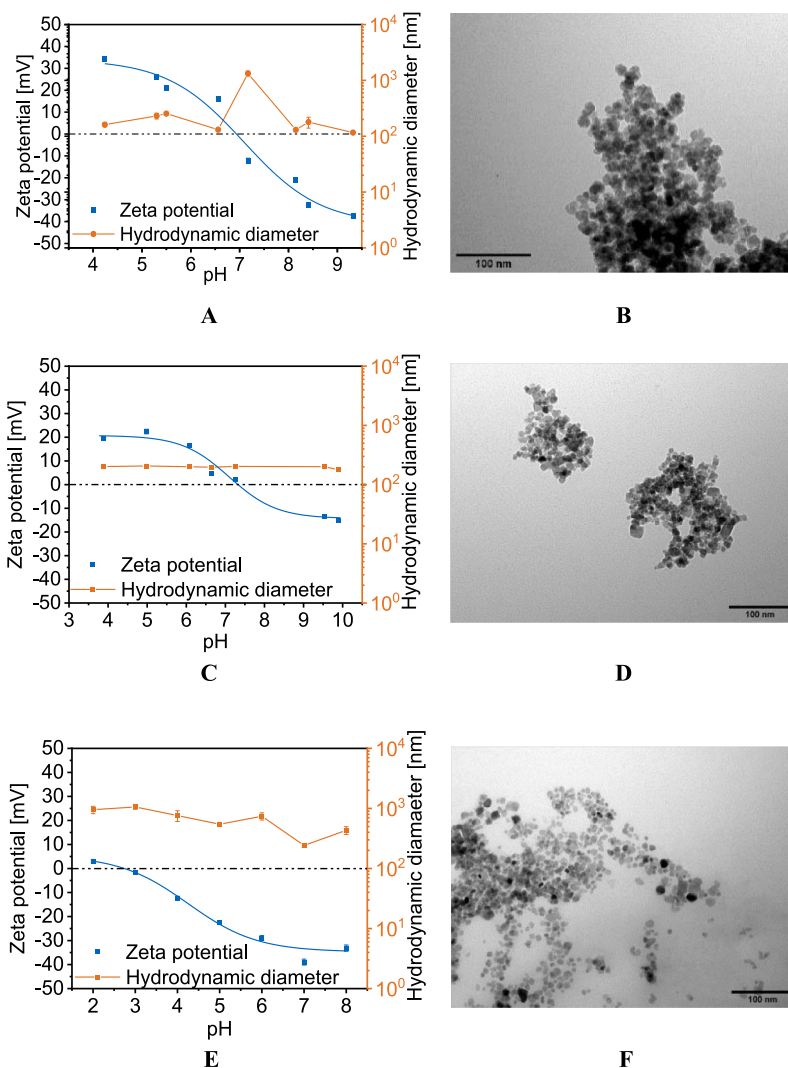


Fig. 2. IEP points of ION@Dex (A), ION@PVA (C), and ION@PLGA (E). TEM images of ION@Dex (B), ION@PVA (D), and ION@PLGA (F) at 120kx.

ION@Dex agglomerated around the IEP of 6.94 with a hydrodynamic diameter of 1330 nm (Table 1, Fig. 2A). Unterweger et al. determined an IEP of 4.60 for dextran-coated IONs. But it should be noted that significantly higher amounts of dextran were used to synthesize the particles [68]. At zeta potentials above and below ± 15 mV the ION@Dex had a Δd_{DLS} of 171 nm in water. Unterweger et al. also observed that ≥ 100 g L⁻¹ dextran could prevent the particles from forming agglomerates [62]. Nevertheless, compared to BIONs with an IEP at 7.10, the dextran-coating led to a shift of the IEP to a lower pH value and better stabilization around the IEP [52, 69]. ION@PLGA had an IEP at pH 2.88 (Fig. 2E, Table 1). The molecular weight of the lactic and glycolic chains, which influences the amount of carboxylic acid end groups, does affect the zeta potential [70]. Near the IEP, the particles formed agglomerates of 1061 nm.

Table 1

Mean diameter of ION@Dex, ION@PVA, and ION@PLGA determined via TEM and of XRD data with the Scherrer equation. For ION@PLGA the Scherrer diameter could not be calculated because the thick coating leads to small reflexes even with intense measurement time. IEPs of ION@Dex, ION@PVA, and ION@PLGA. Hydrodynamic diameters of BIONs, ION@Dex, ION@PVA, and ION@PLGA in SBF and human blood plasma at 37 °C.

Particles	TEM diameter d_{TEM} [nm]	Scherrer diameter d_{Scherrer} [nm]	Isoelectric point (IEP)	Hydrodynamic diameters in SBF [nm]	Hydrodynamic diameters in human blood plasma [nm]
BIONs				1905 ± 345	326 ± 17
ION@Dex	10.5 ± 2.1	8.6 ± 0.5	6.9	1416 ± 684	238 ± 18
ION@PVA	10.6 ± 2.1	8.8 ± 1.6	7.4	211 ± 7	238 ± 15
ION@PLGA	9.5 ± 2.1	–	2.9	841 ± 81	133 ± 1

pH values > 5 led to higher zeta potentials > -22.6 mV. The stabilizing effect led to a hydrodynamic diameter of 242 nm at pH 7. Similar d_{DLS} between 100 and 250 nm have been observed in the literature [23,71,72]. Liang et al. used similar PLGA-coated nanoparticles with a hydrodynamic diameter of 220 nm to create a drug delivery system for paclitaxel. These particles are already in preclinical studies [72]. ION@PVA showed an IEP of 7.35, a value comparable to the literature (Fig. 2C, Table 1) [40]. The PVA coating led to the best stabilization, with an $\Delta d_{DLS} = 198$ nm, independent of the zeta potential and stable at the IEP. This effect can be attributed to the hydrophilic PVA chains [73,74].

In addition to dynamic light scattering studies, we investigated small-angle X-ray scattering (SAXS) by taking BIONs and ION@Dex. By taking particles with and with coating we evaluate the agglomeration behavior and the primary particle size. SAXS profiles showed aggregation and primary particle sizes around 20 nm for all particles investigated (Fig. 3A and B). The highest aggregation is visible for BIONs at pH 7, which is in excellent agreement with DLS data and data from previous studies [52,75]. Even though this aggregation of nanomaterials is visible and makes it challenging to interpret the SAXS data, these results help to verify XRD data as well as TEM studies (Figs. 1C and 2). As complementary study ION@PVA are analyzed by a LDL assay.

Superparamagnetism is a crucial feature of IONs since it permits their application as a controllable drug delivery system, detection by MRI, or in hyperthermia therapy [11]. The saturation magnetization of the various coated particles was measured by superconducting quantum interference device (SQUID) and plotted against the applied magnetic field strength (Fig. 1A). All plotted curves showed the typical sigmoidal shape of superparamagnetic particles with no magnetization at a magnetic field strength of 0.0 Oe [11, 76]. The used BIONs have a saturation magnetization of ± 67.0 emu g^{-1} [52]. A slightly lower saturation magnetization of 62.0 emu g^{-1} can be seen for the dextran-coated particles. The Langevin Mod fit shows that the particles have an almost ideal profile. ION@PVA showed a saturation magnetization of ± 56.7 emu g^{-1} and a curve that differs from the ideal fit above a magnetic field strength of ± 20.0 kOe. Other studies with ION@PVA demonstrated superparamagnetic behavior and reported decreasing saturation magnetization with the increasing PVA coating [28]. For the ION@PLGA, only a saturation magnetization of ± 1.60 emu g^{-1} was reached. This data corresponds to the IR measurements where the high characteristic PLGA peaks indicated a thick polymer coating. In the literature, similar behavior of ION@PLGA can be found between Lee et al. with a saturation magnetization < 0.1 emu g^{-1} and Wang et al. with 4.00 emu g^{-1} [77,78]. The space- and time-resolved extinction profiles (STEP) technology was used to understand the particle's stability and magnetophoretic behavior at pH 7.4 (Fig. 1B). The sedimentation rates in a magnetic field increase with higher agglomeration and higher saturation magnetization of the particles [75]. In comparable conditions, BIONs sank with a sedimentation velocity of 1.2 mm s^{-1} [52]. As ION@Dex formed large agglomerates at physiological pH values, ION@Dex sank faster with a velocity of 2.2 mm s^{-1} . However, BIONs as well as ION@Dex particles show a significantly lower sedimentation velocity without magnetophoretic sedimentation. (Fig. S3). ION@PLGA had sedimentation rates at 64.1 $\mu m s^{-1}$, which fits the low saturation magnetization. PVA is known to stabilize the IONs highly, so even though it has a higher magnetization, its sedimentation velocity with 41.0 $\mu m s^{-1}$ was comparably low as IONs@PLGA [73]. The specific surface area of the BIONs as well as of the dextran coated particles is in the range of 100 $m^2 g^{-1}$ which corresponds to the particle size (Fig. S4).

FT-IR spectroscopy and XRD verified the successful synthesis. The coating material and thickness influenced the particles' size, surface properties, saturation magnetization, and magnetophoretic behavior of the IONs. PVA coating showed the best stabilization of the IONs in a broad pH range and around the IEP.

The cytocompatibility of BIONs ION@Dex, ION@PVA, and ION@PLGA was determined by XTT assay after direct contact with HUASMCs after one and three days (Fig. 1D). The particles did not influence the cell morphology (Fig. S5). All particles show more than 70% viability compared to the negative control. ISO-10993 suggests this threshold for cytocompatibility. BIONs have been previously analyzed under the same conditions for their cell viability at a lower concentration of 0.08 $g L^{-1}$ and show good cytocompatibility as well [52]. The cytocompatible behavior also fits other laboratory experiments for different coated ions with smooth muscle cells. E.g., Zhang et al. showed a minor decrease in cell viability for ION@DMSO, ION@APTS, or ION@Glu [79]. The cytocompatibility of BIONs and the different coated particles gives them the potential for application in nanomedicine.

To better understand the impact of coating materials on the IONs degradation and agglomeration profile, BIONs, ION@Dex, ION@PVA, and ION@PLGA were incubated in SBF, ALF, AEF, and PBS for 72 h at 37 °C (Fig. 4).

In contrast to Rabel et al., a faster protocol was used here, which shortens the protocol to three days (vs. 28 days) [36]. Faster shaking speeds (1000 rpm vs 110 rpm) ensure that the particles are kept in suspension and therefore have more contact with the

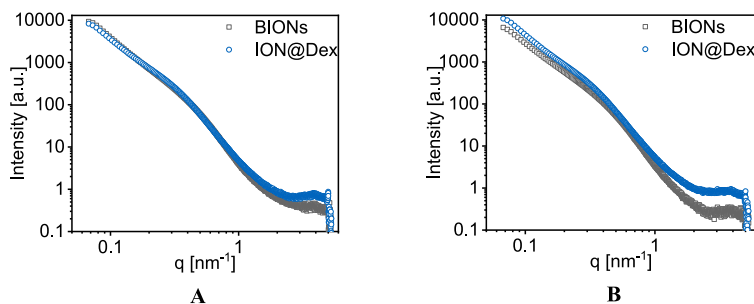


Fig. 3. Small-angle X-ray scattering (SAXS) profiles of ION@Dex and BIONs at pH 4 (A) and 7 (B).

medium.

The initial contact with the body after injection in the bloodstream was analyzed in SBF (Fig. 5A and B, Table S1). Over this period, regardless of particle composition, no iron release was detected in the supernatants of the particle solutions. This behavior was also observed in the literature and can be explained by the low solubility of the particles in physiological conditions [36]. Rabel et al. did not observe any dissolution of organic (Starch, Dextran, Chitosan) and inorganic (Silica) coated particles over 28 days [36]. Compared to the hydrodynamic diameter of BIONs (504 ± 10.5 nm) in d_{H_2O} (pH 7.4), in SBF, a 3.77 times higher agglomeration with an initial hydrodynamic diameter of 1905 ± 345.2 nm occurred. Over 72 h, hydrodynamic diameters of BIONs remained at $1.00 \mu\text{m}$ – $2.00 \mu\text{m}$, indicating constant agglomeration of the BIONs. At physiological pH, the BIONs with an IEP at 7.10 don't show a strong surface charge and form agglomerates accordingly [52]. Furthermore, high electrolyte concentrations in the medium, such as sodium, calcium, chloride, and hydrogen phosphate, increase the aggregation [36,80]. ION@Dex already showed large hydrodynamic diameters in water at pH 7.17 of 1330 nm and colloidal instability around its IEP of 6.94. In SBF, the particles demonstrated almost similar initial agglomeration with hydrodynamic diameters of 1416 nm compared to diameters in water. After 72 h, hydrodynamic diameters increased up to $>2.00 \mu\text{m}$. A thicker dextran coating could decrease the agglomeration [81]. ION@PLGA showed an agglomeration over time from 841 nm to 1311 nm after three days. Even though the particles had a stable colloidal behavior in water (242 nm) at comparable pH values because of its IEP at acidic pH values, the salts induce 5.4 times higher agglomeration. The hydrodynamic diameters of ION@PVA are minimally influenced by SBF, leading to agglomerates of 240 nm after 72 h. This agglomeration is comparable to water at 205 nm. The long polymer chains support the colloidal stability [36,73]. PVA is known to form hydrogen bonding between the polymer chains resulting in a hydrogel structure, embedding the particle, and responsible for steric stabilization [81]. SBF simulates the salt composition, concentration, and pH value, whereas proteins and viscosity of the blood were not considered. Human blood plasma contains proteins (Albumin, IgG, Transferrin), glucose, mineral ions, hormones, carbon dioxide, and blood cells [82]. To better understand the effect of those additional components, the hydrodynamic diameters in SBF and in human plasma were compared (Table 1, Fig. S6).

The agglomerates of BIONs, ION@Dex, and ION@PLGA highly decreased in human blood plasma. The hydrodynamic diameters of ION@PVA remained constant. All particles had diameters <350 nm, and all coatings led to a colloidal stabilization. This effect can be caused by the higher viscosity of around 1.44 mPa and the binding of plasma proteins [40,75,83]. Because no degradation takes place, the small hydrodynamic diameters of the coated IONs should ensure prolonged blood circulation times.

PBS buffer (pH 7.40) was used to simulate the cytoplasm of the cell (Fig. 5C and D, Table S2) [40]. The Fe^{2+} -release experiments showed identical results as in SBF. The IONs don't dissolve at physiological pH values. Congruent to SBF, BIONs agglomerate in larger hydrodynamic diameters, with a Δd of 2227 nm, than the coated particles. Hydrodynamic diameters of ION@Dex remained smaller (788 nm) for 5 h, whereas almost identical hydrodynamic diameters of $\geq 2.00 \mu\text{m}$ to BIONs occurred after 24 h. The effect can be attributed to the change in buffer composition since the pH value was not modified. Compared to SBF, an amount of potassium phosphate (1.20 g L^{-1}) and sodium phosphate (7.20 g L^{-1}) can be found in PBS. Therefore, it can be assumed that phosphate ions bind on the surface of ION@Dex and stabilize the particle in the first 5 h. Almasri et al. can verify the stabilizing effect of adsorbed phosphate ions [84]. ION@PVA starts with similar agglomerate sizes of 220 nm compared to SBF. After 5 h, the particles formed larger hydrodynamic diameters up to 588 nm. ION@PLGA was less influenced over time and showed sizes between 1120 and 1440 nm.

Both buffers at physiological pH values did not lead to ION degradation. The salt concentration, viscosity, and protein content influenced the agglomerate size; all coatings did decrease this size. At the same time, only the PVA coating showed distinct smaller hydrodynamic diameters than the other coatings. All particles experienced distinct smaller hydrodynamic diameters in human blood serum.

In the cell, the first stage of degradation of foreign material is found in endosomes and was simulated by AEF (Fig. 5) [41]. The pH of the endosome is decreased to 5.5 by proton pumps that influx the H^+ [85]. Here the first stage of degradation of foreign material from the cell occurs. Accordingly, the particles' initial degradation by released iron ions can be observed. BIONs experienced a constant iron ion release of up to 15.3% after 72 h. The thick PLGA coating can degrade to lactic acid and glycolic acid in acidic media [86–88]. Afterward, the IONs are dissolved. After 72 h, 9.56% of iron ions are released from ION@PLGA. ION@Dex and ION@PVA dissolve faster than BIONs. A dissolution of 20.4% and 21.9% is reached. Similar trends have been observed in the literature for

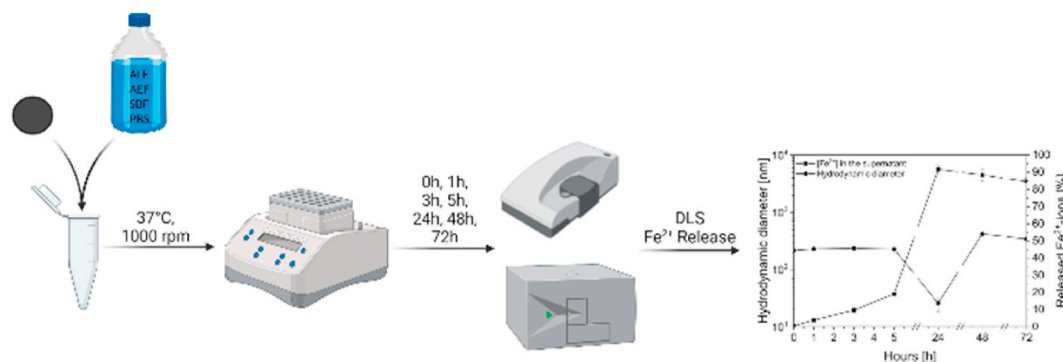


Fig. 4. Schematic overview of the agglomeration and Fe^{2+} -release study over 72 h with BIONs, ION@Dex, ION@PVA, and ION@PLGA.

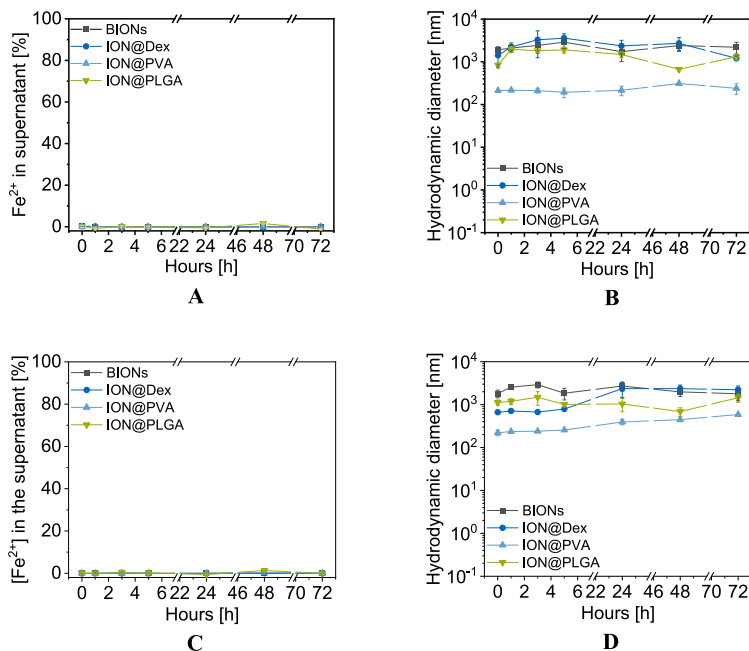


Fig. 5. Fe²⁺ release profiles in SBF (A) and PBS (C) and agglomeration in SBF (B) and PBS (D) for BIONs, ION@Dex, ION@PVA, and ION@PLGA for 72 h at 37 °C (1000 rpm).

DEAE-Dextran, and chitosan-coated IONs [36]. These particles protonated at acidic pH values and attracted more water and dissolution agents, leading to faster iron ion release [36]. Rabel et al. showed dissolution of ~20% after 14 days, indicating that the accelerated mixing (1000 rpm vs. 110 rpm [36]) speeds up the degradation 4.6 times in AEF. This effect can be attributed to the shear

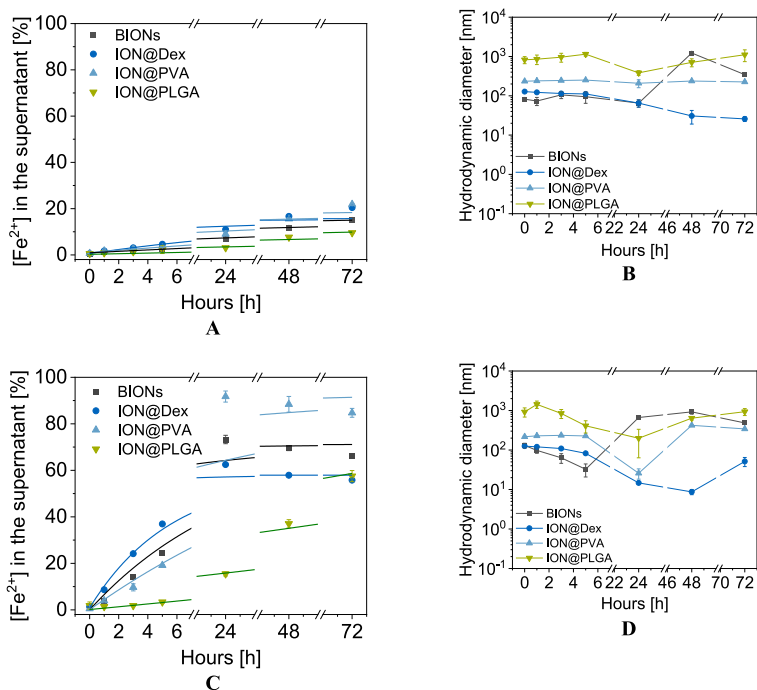


Fig. 6. Fe²⁺ release profiles in AEF (A) and ALF (C) described with a first order kinetic and agglomeration in AEF (B) and ALF (D) for BIONs, ION@Dex, ION@PVA, and ION@PLGA for 72 h at 37 °C (1000 rpm).

forces exerted by the shaking and the better mixing of the particles. At low mixing rates, the particles sediment to the bottom. As a result, the individual particles are more difficult to access and dissolve slowly because a larger agglomerate has a smaller accessible surface area. Lanzl et al. found that physicochemical properties such as morphology, size, and agglomeration behavior also influence the dissolution profile of the particles [89]. Thus, 40 nm-sized particles dissolve up to ten times slower than smaller particles in pH values between 1.00 and 7.00 [89]. In the first 24 h, the dissolution of BIONS can be followed by DLS. Hydrodynamic diameters decrease from 82.2 nm to 65.1 nm (6.80% Fe^{2+} -release). Afterward, the particle agglomerated to a size of 346 nm after 72 h. The large agglomerates were dissolved slower. Gutierrez et al. have shown that the degradation of BIONS increases with decreasing pH [35]. Furthermore, an acidic pH reduces the protection of organic shells against chelating components of AEF such as citrate and lactate [35, 36]. The dissolution of iron oxides in organic acids such as citrate is a multi-step process. By chemisorption, the acid adsorbs onto the iron oxide surface. Here, the particle surface's Lewis base/acid properties are involved. Then, non-reductive dissolution can occur. Thus, iron-ligand complexes dissolve from the surface as a whole. This process is characterized by high activation energy, achieved only at high temperatures [90]. In these experiments, at 37 °C, reductive dissolution is more dominant. Fe^{2+} ions of magnetite dissolve from the crystal and accumulate in the solution [90–92]. The carboxylic acids of citrate can complex with iron ions, similar to EDTA. The chelate complexes promote the dissolution of iron oxides [90]. ION@PLGA demonstrated initial agglomeration with hydrodynamic diameters of 824 nm, which is 3.4 times higher than in water. After 24 h, the size decreased to 384 nm. Similar to BIONS, the PLGA-coated particles started to agglomerate in the last two days (1108 nm). Without additional agglomeration, ION@Dex decreased its hydrodynamic diameters from 127 nm to 25.8 nm after 72 h.

The initial size is comparable to the agglomeration in water at acidic pH values. The results of ION@PVA revealed constant hydrodynamic diameters of 200 nm–300 nm. This behavior does not correspond to the degradation study. It can be assumed that larger agglomerated particles degraded slower and were detected in DLS.

ALF simulated the degradation of the particles in the lysosome with an acidic pH value of 4.5 (Fig. 6A and B). The initial size is comparable to agglomeration in water at acidic pH values. The results of ION@PVA revealed constant hydrodynamic diameters of 200 nm–300 nm. This behavior does not correspond to the degradation study. It can be assumed that larger agglomerated particles degraded slower and were detected in DLS (Fig. 6C and D, Table S5) [41]. BIONS experience a fast dissolution in the first 24 h, up to 73.3% iron ion release migrating into a plateau. The dissolution of ION@PVA starts slower in the first 5 h but then speeds up and reaches 91.0%. A plateau setting suggests that these particles are almost entirely degraded [36]. Due to the IEP of ION@PVA (7.35), the surface is positively charged and thus attracts more water and solubilizing agents [36]. In the beginning, ION@Dex experienced a faster dissolution than BIONS, slowing down after 5 h to a maximal degradation of 62.5% (24 h). ION@PLGA is dissolved up to 57.5% after 72 h. As the coating dissolved first, the curve experienced a smaller slope. In ALF, the particles dissolved four times faster than in AEF, which was also reported by Gutierrez et al. and Rabel et al. for differently coated IONs [35,36].

Hydrodynamic diameters of BIONS decreased rapidly from 130 nm to 32.6 nm after 5 h. Afterward, the diameters increased and stayed constant for the next days at a $\Delta d \sim 692$ nm. The data verify that the decrease in hydrodynamic diameters can visualize the degradation in the acidic surrounding. The remaining 26.7% of particles seem to form huge agglomerates. As larger particles take longer to dissolve, the Fe^{2+} release slowed down and reached a plateau. Comparable to AEF, ION@PLGA initially formed huge agglomerates of 922 nm. The hydrodynamic diameters constantly decreased until 199 nm at 24 h, congruent to the degradation profile. Afterward, the sizes increased again up to 932 nm. Compared to AEF (384 nm, 24 h), the hydrodynamic diameters of ION@PLGA showed a higher and faster decrease in ALF (198 nm, 24 h). ION@Dex showed an initial size of 125 nm. ION@Dex's hydrodynamic diameters decreased from 125 nm to 8.71 nm in 48 h. In the last hour, the remaining particles formed aggregates of 51.5 nm. Similar behavior was observed for the PVA-coated particles. The size decreased from 217 nm to 25.8 nm in the first 24 h, while afterward, the IONs showed agglomerates of 342 nm.

In summary, the organic coatings did stabilize the particles. The acidic environment did induce degradation. In ALF, the particles dissolved faster than in AEF. All particles except ION@PLGA reached a plateau in 72 h due to the formation of big agglomerates. ION@PVA experienced the fastest iron ion release. ION@PLGA had the highest initial agglomeration in the acidic media.

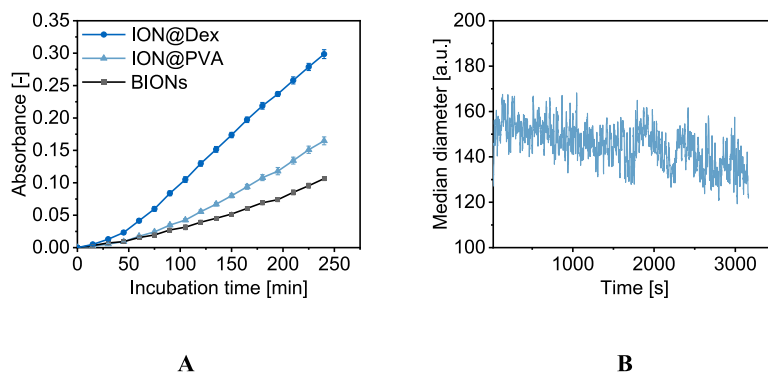


Fig. 7. Diene oxidation of dissolved nanoparticles (48 h at pH 4.5 in acetate buffer) in acetate buffer (pH 4.5) (A). Standard deviation derives from at least four independent experiments. Dissolution of ION@PVA particles in acetate buffer at pH 4.5 (B).

Oxidative stress induced by the dissolved particles after 48 h was emulated with an low-density lipoprotein (LDL) assay. Due to the thick coating of ION@PLGA that leads to different mass balance only BIONS and the thin coatings (PVA, Dex) were used. Here oxidation is fastest for dissolved ION@Dex particles and slowest for dissolved BION particles in an acetate buffer. Due to oxidative stress by reactive oxygen species (ROS) of the dienes, the oxidation was monitored over 240 min (Fig. 7A). The results indicate that the coating plays a role in the dissolution of the magnetic particles and in the oxidation state and therefore influences the oxidation behavior. Here, the dextran-coated particles, which also tend to be dissolved fastest in AEF, show the highest oxidation kinetic. Interestingly, the naked BIONS demonstrate the slowest kinetic, which is in good agreement with the dissolution of these particles.

The dissolution kinetic of ION@PVA shows slight aggregate size decreases with the optofluidic force induction measurements (Fig. 7B). These measurements indicate a direct size decrease even though the exact hydrodynamic diameter cannot be reflected (Fig. S5).

4. Conclusion

Three different commonly used organic coatings on IONs, PLGA, PVA, and Dex were successfully synthesized. The coatings influence the particles' properties. While all had similar d_{TEM} the IEP point influenced the colloidal stability. ION@PVA showed the least agglomeration over a pH range from 4 to 10. SAXS profiles, as an alternative method, could visualize aggregation and primary particle sizes around 20 nm for BIONS and ION@Dex. The coating thickness affected the saturation magnetization, whereas the agglomeration also influenced the sedimentation velocity in a magnetic field. All particles, including BIONS, showed good cytocompatibility (>70%) over three days in smooth muscle cells. The experimental setup for long-term agglomeration and degradation studies did speed up the process by a factor of 4.6, allowing fast screening of multiple candidates and thus can shorten the preclinical phase. Furthermore, it was ensured the particles didn't sediment during the experiment. The investigated particles all have different colloidal stability and dissolution profiles. In SBF and PBS, none of the investigated particles dissolved. ION@PVA showed the least agglomeration. A first degree of degradation of the particles is visible in AEF, which confirms the pH dependence of the dissolution. The IONs did dissolve faster in ALF, with the degradation rate decreasing with the shrinking size, leading to a plateau. The fastest Fe^{2+} release could be measured for ION@PVA in ALF, while ION@PLGA experienced the lowest degradation. The oxidation kinetic of BIONS was slower than ION@Dex and ION@PVA, fitting to the degradation results in AEF. This study provides essential insights into the agglomeration and degradation profile and the oxidative stress of IONs with standard coatings for medical applications. The used analytical setup combining DLS, phenanthroline assay, SAXS, and LDL assay is ideal for a fast preclinical study of new IONs, giving often neglected yet crucial information about the behavior and toxicity of nanoparticles in the human body. With this study we want to emphasize the dissolution of nanomaterials and the potential use of generally cytocompatible iron oxide particles for ferroptosis applications.

Author contribution statement

Chiara Turrina: Conceived and designed the experiments; Performed the experiments; Analyzed and interpreted the data; Wrote the paper.

Anna Klassen, Davide Milani, Diana Rojas-Gonzalez, Gerhard Ledinski, Doris Auer, Barbara Sartori: Performed the experiments; Analyzed and interpreted the data.

Gerhard Cvirn: Analyzed and interpreted the data; Wrote the paper.

Petra Mela, Sonja Berensmeier: Analyzed and interpreted the data; Contributed reagents, materials, analysis tools or data; Wrote the paper.

Sebastian Schwaminger: Conceived and designed the experiments; Performed the experiments; Analyzed and interpreted the data; Contributed reagents, materials, analysis tools or data; Wrote the paper.

Funding

We appreciate the support from TUM International Graduate School of Science and Engineering (IGSSE). The funders had no role in the design of the study, the collection, analysis, and interpretation of data, the writing of the manuscript, or the decision to publish the results.

Data availability statement

Data will be made available on request.

Declaration of competing interest

The authors declare that they have no known competing financial interests or personal relationships that could have appeared to influence the work reported in this paper.

Acknowledgements

We are thankful for Tom Nilges (Technical University of Munich) to provide the X-ray diffractometer and for the support of Carsten

Peters (Technical University of Munich) with TEM measurements. The graphical abstract and Fig. 2 were created with BioRender.com.

Appendix A. Supplementary data

Supplementary data to this article can be found online at <https://doi.org/10.1016/j.heliyon.2023.e16487>.

References

- [1] K. Riehemann, S.W. Schneider, T.A. Luger, B. Godin, M. Ferrari, H. Fuchs, Nanomedicine—challenge and perspectives, *Angew. Chem. Int. Ed.* 48 (2009) 872–897, <https://doi.org/10.1002/anie.200802585>.
- [2] S. Bamrungsap, Z. Zhao, T. Chen, L. Wang, C. Li, T. Fu, W. Tan, Nanotechnology in therapeutics: a focus on nanoparticles as a drug delivery system, *Nanomedicine* 7 (2012) 1253–1271, <https://doi.org/10.2217/nnm.12.87>.
- [3] V. Wagner, A. Dullaart, A.-K. Bock, A. Zweck, The emerging nanomedicine landscape, *Nat. Biotechnol.* 24 (2006) 1211–1217, <https://doi.org/10.1038/nbt1006-1211>.
- [4] S.-W. Cao, Y.-J. Zhu, M.-Y. Ma, L. Li, L. Zhang, Hierarchically nanostructured magnetic hollow spheres of Fe₃O₄ and γ-Fe₂O₃: preparation and potential application in drug delivery, *J. Phys. Chem. C* 112 (2008) 1851–1856, <https://doi.org/10.1021/jp077468>.
- [5] L.H. Reddy, J.L. Arias, J. Nicolas, P. Couvreur, Magnetic nanoparticles: design and characterization, toxicity and biocompatibility, pharmaceutical and biomedical applications, *Chem. Rev.* 112 (2012), <https://doi.org/10.1021/cr300068p>.
- [6] P.V. Devarajan, S.M. Dawre, R. Dutta, Infectious diseases: need for targeted drug delivery, in: *Targeted Drug Delivery Concepts and Design*, Springer, Cham, 2015, pp. 113–148.
- [7] W. Wu, Z. Wu, T. Yu, C. Jiang, W.S. Kim, Recent progress on magnetic iron oxide nanoparticles: synthesis, surface functional strategies and biomedical applications, *Sci. Technol. Adv. Mater.* 16 (2015), <https://doi.org/10.1088/1468-6996/16/2/023501>.
- [8] M.V. Yigit, A. Moore, Z. Medarova, Magnetic nanoparticles for cancer diagnosis and therapy, *Pharm. Res.* 29 (2012) 1180–1188, <https://doi.org/10.1007/s11095-012-0679-7>.
- [9] L. Josephson, J. Lewis, P. Jacobs, P.F. Hahn, D.D. Stark, The effects of iron oxides on proton relaxivity, *Magn. Reson. Imaging* 6 (1988), [https://doi.org/10.1016/0730-725x\(88\)90088-4](https://doi.org/10.1016/0730-725x(88)90088-4).
- [10] An-Hui Lu, E.L. Salabas, Ferdi Schüth, Magnetic nanoparticles: synthesis, protection, functionalization, and application, *Angew. Chem. Int. Ed.* 46 (2007) 1222–1244, <https://doi.org/10.1002/anie.200602866>.
- [11] S. Laurent, D. Forge, M. Port, A. Roch, C. Robic, L. Vander Elst, R.N. Muller, Magnetic iron oxide nanoparticles: synthesis, stabilization, vectorization, physicochemical Characterizations, and Biological Applications, *Chem. Rev.* 108 (2008) 2064–2110, <https://doi.org/10.1021/cr068445e>.
- [12] K. Mylikie, P. Nowak, P. Rybczynski, M. Ziegler-Borowska, Polymer-coated magnetite nanoparticles for protein immobilization, *Materials* 14 (2021), <https://doi.org/10.3390/ma14020248>.
- [13] S.C. McBain, H.H. Yiu, J. Dobson, Magnetic nanoparticles for gene and drug delivery, *Int. J. Nanomed.* 3 (2008), <https://doi.org/10.2147/ijn.s1608>.
- [14] N.A. Alcantar, E.S. Aydil, J.N. Israelachvili, Polyethylene glycol-coated biocompatible surfaces, *J. Biomed. Mater. Res.* 51 (2000) 343–351, [https://doi.org/10.1002/1097-4636\(20000905\)51:3<343::AID-JBM7>3.0.CO;2-D](https://doi.org/10.1002/1097-4636(20000905)51:3<343::AID-JBM7>3.0.CO;2-D).
- [15] K.E. Albinali, M.M. Zagho, Y. Deng, A.A. Elzatahy, A perspective on magnetic core-shell carriers for responsive and targeted drug delivery systems, *Int. J. Nanomed.* 14 (2019) 1707–1723, <https://doi.org/10.2147/IJN.S193981>.
- [16] C.S.N. de, J. Snir, C. Willert, R. Rohani, R. Foley, P.J. Foster, G.A. Dekaban, Labelling dendritic cells with SPIO has implications for their subsequent in vivo migration as assessed with cellular MRI, *Contrast Media Mol. Imaging* 6 (2011), <https://doi.org/10.1002/cmml.433>.
- [17] S. Santosh, P. Podaralla, B. Miller, Anaphylaxis with elevated serum tryptase after administration of intravenous ferumoxytol, *NDT Plus* 3 (2010) 341–342, <https://doi.org/10.1093/ndtplus/sfq084>.
- [18] M. Khalkhali, S. Sadighian, K. Rostamizadeh, F. Khoehi, M. Naghibi, N. Bayat, M. Habibzadeh, M. Hamidi, Synthesis and characterization of dextran coated magnetite nanoparticles for diagnostics and therapy, *Bioimpacts* 5 (2015) 141–150, <https://doi.org/10.15171/bi.2015.19>.
- [19] M. Peng, H. Li, Z. Luo, J. Kong, Y. Wan, L. Zheng, Q. Zhang, H. Niu, A. Vermorken, W. van de Ven, C. Chen, X. Zhang, F. Li, L. Guo, Y. Cui, Dextran-coated superparamagnetic nanoparticles as potential cancer drug carriers in vivo, *Nanoscale* 7 (2015) 11155–11162, <https://doi.org/10.1039/c5nr01382h>.
- [20] H. Unterwiesing, D. Subatzus, R. Tietze, C. Janko, C. Alexiou, Hypericin-bearing magnetic iron oxide nanoparticles for selective drug delivery in photodynamic therapy, *Int. J. Nanomed.* 10 (2015) 6985, <https://doi.org/10.2147/IJN.S92336>.
- [21] Mazaher Ahmadi, Iron oxide nanoparticles for delivery purposes, in: M. Mozafari (Ed.), *Nanoengineered Biomaterials for Advanced Drug Delivery*, Elsevier, San Diego, 2020, pp. 373–393.
- [22] F. Danhier, E. Ansorena, J.M. Silva, R. Coco, B.A. Le, V. Préat, PLGA-based nanoparticles: an overview of biomedical applications, *J. Contr. Release* 161 (2012), <https://doi.org/10.1016/j.jconrel.2012.01.043>.
- [23] C.V. Rocha, V. r Gonçalves, M. Costa da Costa da Silva, M. Bañobre-López, J. Gallo, PLGA-based composites for various biomedical applications, *Int. J. Mol. Sci.* 23 (2022) 2034, <https://doi.org/10.3390/ijms23042034>.
- [24] C. Saengruengrit, P. Ritprajak, S. Wanichwecharungruang, A. Sharma, G. Salvan, D.R.T. Zahn, N. Insin, The combined magnetic field and iron oxide-PLGA composite particles: effective protein antigen delivery and immune stimulation in dendritic cells, *J. Colloid Interface Sci.* 520 (2018), <https://doi.org/10.1016/j.jcis.2018.03.008>.
- [25] M.R. Ruggiero, S. Geninatti Crich, E. Sieni, P. Sgarbossa, E. Cavallari, R. Stefania, F. Dughiero, S. Aime, Iron oxide/PLGA nanoparticles for magnetically controlled drug release, *JAE* 53 (2017) S53–S60, <https://doi.org/10.3233/JAE-162246>.
- [26] A. Karimi, W.M.A. Wan Daud, Materials, preparation, and characterization of PVA/MMT nanocomposite hydrogels: a review, *Polym. Compos.* 38 (2017) 1086–1102, <https://doi.org/10.1002/pc.23671>.
- [27] Siow-Feng Chong, Anton A.A. Smith, Alexander N. Zelikin, Microstructured, functional PVA hydrogels through bioconjugation with oligopeptides under physiological conditions, *Small* 9 (2013), <https://doi.org/10.1002/smll.201201774>.
- [28] S. Kayal, R.V. Ramanujan, Doxorubicin loaded PVA coated iron oxide nanoparticles for targeted drug delivery, *Mater. Sci. Eng. C* 30 (2010) 484–490, <https://doi.org/10.1016/j.msec.2010.01.006>.
- [29] M. Ebad, S. Bullo, K. Buskara, M.Z. Hussein, S. Fakurazi, G. Pastorn, Release of a liver anticancer drug, sorafenib from its PVA/LDH- and PEG/LDH-coated iron oxide nanoparticles for drug delivery applications, *Sci. Rep.* 10 (2020) 1–19, <https://doi.org/10.1038/s41598-020-76504-5>.
- [30] A.L. Cortajarena, D. Ortega, S.M. Ocampo, A. Gonzalez-García, P. Couleaud, Rodolfo Miranda, C. Belda-Iniesta, A. Ayuso-Sacido, Engineering iron oxide nanoparticles for clinical settings, *Nanobiomedicine* 1 (2014) 2.
- [31] M. Levy, N. Luciani, D. Alloeyau, D. Elgrabli, V. Deveaux, C. Pechoux, S. Chat, G. Wang, N. Vats, F. Gendron, C. Factor, S. Lotersztajn, A. Luciani, C. Wilhelm, F. Gazeau, Long term in vivo biotransformation of iron oxide nanoparticles, *Biomaterials* 32 (2011), <https://doi.org/10.1016/j.biomaterials.2011.02.031>.
- [32] S.K. Misra, A. Dybowska, D. Berhanu, S.N. Luoma, E. Valsami-Jones, The complexity of nanoparticle dissolution and its importance in nanotoxicological studies, *Sci. Total Environ.* 438 (2012), <https://doi.org/10.1016/j.scitotenv.2012.08.066>.

- [33] Michael Lévy, Florence Lagarde, Valentin-Adrian Maraloiu, Marie-Geneviève Blanchin, François Gendron, Claire Wilhelm, Florence Gazeau, Degradability of superparamagnetic nanoparticles in a model of intracellular environment: follow-up of magnetic, structural and chemical properties, *Nanotechnology* 21 (2010), 395103, <https://doi.org/10.1088/0957-4484/21/39/395103>.
- [34] L.K. Limbach, Y. Li, R.N. Grass, T.J. Brunner, M.A. Hintermann, M. Muller, D. Gunther, W.J. Stark, Oxide nanoparticle uptake in human lung fibroblasts: effects of particle size, agglomeration, and diffusion at low concentrations, *Environ. Sci. Technol.* 39 (2005) 9370–9376, <https://doi.org/10.1021/es051043o>.
- [35] L. Gutiérrez, S. Romero, S.G.B. da, R. Costo, M.D. Vargas, C.M. Ronconi, C.J. Serna, S. Veintemillas-Verdaguer, P.M.M. Del, Degradation of magnetic nanoparticles mimicking lysosomal conditions followed by AC susceptibility, *Biomed. Eng.* 60 (2015), <https://doi.org/10.1515/bmt-2015-0043>.
- [36] M. Rabel, P. Warncke, C. Grüttnner, C. Bergemann, H.-D. Kurland, R. Müller, V. Dugandžić, J. Thamm, F.A. Müller, J. Popp, D. Cialla-May, D. Fischer, Simulation of the long-term fate of superparamagnetic iron oxide-based nanoparticles using simulated biological fluids, *Nanomedicine* 14 (2019) 1681–1706, <https://doi.org/10.2217/nmm-2018-0382>.
- [37] Erin Hopkins, Terrence Sanvictores, Sandeep Sharma, Physiology, acid base balance, in: E. Hopkins, T. Sanvictores, S. Sharma (Eds.), *Physiology, Acid Base Balance*, StatPearls Publishing, 2021.
- [38] L.V. Stebounova, E. Guio, V.H. Grassian, Silver nanoparticles in simulated biological media: a study of aggregation, sedimentation, and dissolution, *J. Nanoparticle Res.* 13 (2011) 233–244, <https://doi.org/10.1007/s11051-010-0022-3>.
- [39] Margareth R.C. Marques, R. Loebenberg, M. Almkainzi, Simulated biological fluids with possible application in dissolution testing, *Dissolution Technol.* (2011) 15–28, <https://doi.org/10.14227/DT180311P15>.
- [40] U. Sakulkhu, M. Mahmoudi, L. Maurizi, G. Coullerez, M. Hofmann-Antenbrink, M. Vries, M. Motazacker, F. Rezaee, H. Hofmann, Significance of surface charge and shell material of superparamagnetic iron oxide nanoparticle (SPION) based core/shell nanoparticles on the composition of the protein corona, *Biomater. Sci.* 3 (2014) 265–278, <https://doi.org/10.1039/C4BM00264D>.
- [41] A. MilosevicAc, J. Bourquin, D. Burnand, P. Lemal, B. Rothen-Rutishauser, Artificial lysosomal platform to study nanoparticle long-term stability, *CHIMIA Int. J. Chem.* 73 (2019) 55–58, <https://doi.org/10.2533/chimia.2019.55>.
- [42] J.A. Mindell, Lysosomal acidification mechanisms, *Annu. Rev. Physiol.* 74 (2012), <https://doi.org/10.1146/annurev-physiol-012110-142317>.
- [43] L. Lartigue, D. Alloeyau, J. Kolosnjaj-Tabi, Y. Javed, P. Guardia, A. Riedinger, C. Péchoux, T. Pellegrino, C. Wilhelm, F. Gazeau, Biodegradation of iron oxide nanocubes: high-resolution in situ monitoring, *ACS Nano* 7 (2013) 3939–3952, <https://doi.org/10.1021/nm305719y>.
- [44] R.M. Cornell, U. Schwertmann, *The Iron Oxides: Structure, Properties, Reactions, Occurrences and Uses*, vollst. überarb. u. erw. Auflage, second, Wiley-VCH, Weinheim, 2006.
- [45] P.'a. Ma, H. Xiao, C. Yu, J. Liu, Z. Cheng, H. Song, X. Zhang, C. Li, J. Wang, Z. Gu, J. Lin, Enhanced cisplatin chemotherapy by iron oxide nanocarrier-mediated generation of highly toxic reactive oxygen species, *Nano Lett.* 17 (2017) 928–937, <https://doi.org/10.1021/acs.nanolett.6b04269>.
- [46] H. Zhou, X. Lu, C. Du, Z. Zhou, J. Feng, Z. Liang, Y. Xu, X. Qiu, Z. Shen, Cycloacceleration of reactive oxygen species generation based on exceedingly small magnetic iron oxide nanoparticles for tumor ferroptosis therapy, *Small* 18 (2022), e2202705, <https://doi.org/10.1002/sml.202202705>.
- [47] H. He, L. Du, H. Guo, Y. An, L. Lu, Y. Chen, Y. Wang, H. Zhong, J. Shen, J. Wu, X. Shuai, Redox responsive metal organic framework nanoparticles induces ferroptosis for cancer therapy, *Small* 16 (2020), e2001251, <https://doi.org/10.1002/sml.202001251>.
- [48] C. Zhang, W. Bu, D. Ni, S. Zhang, Q. Li, Z. Yao, J. Zhang, H. Yao, Z. Wang, J. Shi, Synthesis of iron nanometallic glasses and their application in cancer therapy by a localized Fenton reaction, *Angew. Chem. Int. Ed.* 55 (2016) 2101–2106, <https://doi.org/10.1002/anie.201510031>.
- [49] S.J. Dixon, B.R. Stockwell, The role of iron and reactive oxygen species in cell death, *Nat. Chem. Biol.* 10 (2014) 9–17, <https://doi.org/10.1038/nchembio.1416>.
- [50] R. Massart, Preparation of aqueous magnetic liquids in alkaline and acidic media, *IEEE Trans. Magn.* 17 (1981) 1247–1248, <https://doi.org/10.1109/TMAG.1981.1061188>.
- [51] C. Turrina, S. Berensmeier, S.P. Schwaminger, Bare iron oxide nanoparticles as drug delivery carrier for the short cationic peptide lasioglossin, *Pharmaceuticals* 14 (2021), <https://doi.org/10.3390/ph14050405>.
- [52] C. Turrina, D. Milani, A. Klassen, D.M. Rojas-González, J. Cookman, M. Opel, P. Mela, S. Berensmeier, S.P. Schwaminger, Carboxymethyl-dextran coated superparamagnetic iron oxide nanoparticles for drug delivery: influence of coating thickness on the particle properties, *Int. J. Mol. Sci.* (2022), 14743.
- [53] R.A. Jain, The manufacturing techniques of various drug loaded biodegradable poly(lactide-co-glycolide) (PLGA) devices, *Biomaterials* 21 (2000) 2475–2490, [https://doi.org/10.1016/S0142-9612\(00\)00115-0](https://doi.org/10.1016/S0142-9612(00)00115-0).
- [54] M. Šimić, D. Auer, C. Neuper, N. Šimić, G. Prossliner, R. Prassl, C. Hill, U. Hohenester, Real-time nanoparticle characterization through optofluidic force induction, *Phys. Rev. Appl.* 18 (2022), 24056, <https://doi.org/10.1103/PhysRevApplied.18.024056>.
- [55] G. Jürgens, A. Ashy, H. Esterbauer, Detection of new epitopes formed upon oxidation of low-density lipoprotein, lipoprotein (a) and very-low-density lipoprotein. Use of an antiserum against 4-hydroxynonenal-modified low-density lipoprotein, *Biochem. J.* 265 (1990), <https://doi.org/10.1042/bj2650605>.
- [56] H. Esterbauer, G. Striegl, H. Puhl, M. Rotheneder, Continuous monitoring of in vitro oxidation of human low density lipoprotein, *Free Radic. Res. Commun.* 6 (1989) 67–75, <https://doi.org/10.3109/10715768909073429>.
- [57] J. Braunschweig, J. Bosch, K. Heister, C. Kuebeck, R.U. Meckenstock, Reevaluation of colorimetric iron determination methods commonly used in geomicrobiology, *J. Microbiol. Methods* 89 (2012) 41–48, <https://doi.org/10.1016/j.mimet.2012.01.021>.
- [58] A.K. Bordbar, A.A. Rastegari, R. Amiri, E. Ranjbakhsh, M. Abbasi, A.R. Khosropour, Characterization of modified magnetite nanoparticles for albumin immobilization, *Biotechnol. Res. Int.* 2014 (2014), <https://doi.org/10.1155/2014/705068>.
- [59] Issmat Al Kawni, Ricardo Garcia, S. Youssef, M. Abboud, J. Podlecki, R. Habchi, Stabilization and encapsulation of magnetite nanoparticles, *Mater. Res. Express* 16 (2016).
- [60] Sigma Aldrich, IR spectrum table & chart. <https://www.sigmaaldrich.com/DE/de/technical-documents/technical-article/analytical-chemistry/photometry-and-reflectometry/ir-spectrum-table>, 2022 (accessed 13 July 2022).
- [61] R.Z. Ahmed, K. Siddiqui, M. Arman, N. Ahmed, Characterization of high molecular weight dextran produced by *Weissella cibaria* CMGDEX3, *Carbohydr. Polym.* 90 (2012) 441–446, <https://doi.org/10.1016/j.carbpol.2012.05.063>.
- [62] H. Unterweger, R. Tietze, C. Janko, J. Zaloga, S. Lyer, S. Dürri, N. Taccardi, O.M. Goudouri, A. Hoppe, D. Eberbeck, D.W. Schubert, A.R. Boccaccini, C. Alexiou, Development and characterization of magnetic iron oxide nanoparticles with a cisplatin-bearing polymer coating for targeted drug delivery, *Int. J. Nanomed.* 9 (2014), <https://doi.org/10.2147/IJN.S63433>.
- [63] S. Gurpreet, K. Tanurajvir, K. Ravinder, K. Anudeep, Recent biomedical applications and patents on biodegradable polymer-PLGA, *Int. J. Pharm. Pharmaceut. Sci.* 1 (2014) 30–42.
- [64] S. Jain, P.V. Devarajan (Eds.), *Targeted Drug Delivery Concepts and Design*, Springer, Cham, 2015.
- [65] V. Ceña, P. Játiva, Nanoparticle crossing of blood-brain barrier: a road to new therapeutic approaches to central nervous system diseases, *Nanomedicine* 13 (2018) 1513–1516, <https://doi.org/10.2217/nmm-2018-0139>.
- [66] R.Y. Hong, B. Feng, L.L. Chen, G.H. Liu, H.Z. Li, Y. Zheng, D.G. Wei, Synthesis, characterization and MRI application of dextran-coated Fe3O4 magnetic nanoparticles, *Biochem. Eng. J.* 42 (2008) 290–300, <https://doi.org/10.1016/j.bej.2008.07.009>.
- [67] E. Hopkins, T. Sanvictores, S. Sharma (Eds.), *Physiology, Acid Base Balance*, StatPearls Publishing, 2021.
- [68] H. Unterweger, L. Dézsi, J. Matuszak, C. Janko, M. Poettler, J. Jordan, T. Bäuerle, J. Szebeni, T. Fey, A.R. Boccaccini, C. Alexiou, I. Cicha, Dextran-coated superparamagnetic iron oxide nanoparticles for magnetic resonance imaging: evaluation of size-dependent imaging properties, storage stability and safety, *Int. J. Nanomed.* 13 (2018), <https://doi.org/10.2147/IJN.S156528>.
- [69] V. Ayala, A.P. Herrera, M. Latorre-Esteves, M. Torres-Lugo, C. Rinaldi, Effect of surface charge on the colloidal stability and in vitro uptake of carboxymethyl dextran-coated iron oxide nanoparticles, *J. Nanoparticle Res.* 15 (2013) 1–14, <https://doi.org/10.1007/s11051-013-1874-0>.
- [70] C.E. Astete, C.M. Sabliov, Synthesis and characterization of PLGA nanoparticles, *J. Biomater. Sci. Polym. Ed.* 17 (2006) 247–289, <https://doi.org/10.1163/156856206775997322>.
- [71] C. Chittasupho, S.X. Xie, E. Baoum, T. Yakovleva, T.J. Siahaan, C.J. Berkland, ICAM-1 targeting of doxorubicin-loaded PLGA nanoparticles to lung epithelial cells, *Eur. J. Pharmaceut. Sci.* 37 (2009), <https://doi.org/10.1016/j.ejps.2009.02.008>.

- [72] C. Liang, Y. Yang, Y. Ling, Y. Huang, T. Li, X. Li, Improved therapeutic effect of folate-decorated PLGA-PEG nanoparticles for endometrial carcinoma, *Bioorg. Med. Chem.* 19 (2011), <https://doi.org/10.1016/j.bmc.2011.05.016>.
- [73] P.A. Tran, H. T. Nguyen, K. Fox, N. Tran, In vitro cytotoxicity of iron oxide nanoparticles: effects of chitosan and polyvinyl alcohol as stabilizing agents, *Mater. Res. Express* 5 (2018), 35051, <https://doi.org/10.1088/2053-1591/aab5f3>.
- [74] N. Tran, A. Mir, D. Mallik, A. Sinha, S. Nayyar, T. J. Webster, Bactericidal effect of iron oxide nanoparticles on *Staphylococcus aureus*, *Int. J. Nanomed.* 5 (2010) 277, <https://doi.org/10.2147/ijn.s9220>.
- [75] L. Wittmann, C. Turrina, S.P. Schwaminger, The effect of pH and viscosity on magnetophoretic separation of iron oxide nanoparticles, *Magnetochemistry* 7 (2021) 80, <https://doi.org/10.3390/magnetochemistry7060080>.
- [76] K.N. Koo, A.F. Ismail, M.H.D. Othman, N. Bidin, M. A. Rahman, Preparation and characterization of superparamagnetic magnetite (Fe₃O₄) nanoparticles: a short review, *Mal. J. Fund. Appl. Sci.* 15 (2019) 23–31, <https://doi.org/10.11113/mjfas.v15n2019.1224>.
- [77] S.-J. Lee, J.-R. Jeong, S.-C. Shin, J.-C. Kim, Y.-H. Chang, K.-H. Lee, J.-D. Kim, Magnetic enhancement of iron oxide nanoparticles encapsulated with poly(D,L-lactide-co-glycolide), *Colloids Surf. A Physicochem. Eng. Asp.* 255 (2005) 19–25, <https://doi.org/10.1016/j.colsurfa.2004.12.019>.
- [78] P.-C. Wang, C.-F. Lee, T.-H. Young, D.-T. Lin, W.-Y. Chiu, Preparation and clinical application of immunomagnetic latex, *J. Polym. Sci. Polym. Chem.* 43 (2005) 1342–1356, <https://doi.org/10.1002/pola.20601>.
- [79] S. Zhang, X. Chen, C. Gu, Y. Zhang, N. Gu, The effect of iron oxide magnetic nanoparticles on smooth muscle cells, *Nanoscale Res. Lett.* 4 (2009) 70–77, <https://doi.org/10.1007/s11671-008-9204-7>.
- [80] S.-C. Yang, S.-Y.-R. Paik, J. Ryu, K.-O. Choi, T.S. Kang, J.K. Lee, C.W. Song, S. Ko, Dynamic light scattering-based method to determine primary particle size of iron oxide nanoparticles in simulated gastrointestinal fluid, *Food Chem.* 161 (2014) 185–191, <https://doi.org/10.1016/j.foodchem.2014.04.022>.
- [81] A. Petri-Fink, B. Steitz, Andrija Finka, J. Salaklang, H. Hofmann, Effect of cell media on polymer coated superparamagnetic iron oxide nanoparticles (SPIONs): colloidal stability, cytotoxicity, and cellular uptake studies, *Eur. J. Pharm. Biopharm.* (2008) 129–137.
- [82] Y. Shen, J. Kim, E.F. Strittmatter, J.M. Jacobs, D.G. Camp, R. Fang, N. Tolié, R.J. Moore, R.D. Smith, Characterization of the human blood plasma proteome, *Proteomics* 5 (2005), <https://doi.org/10.1002/pmic.200401246>.
- [83] G. Késmárky, P. Kenyeres, M. Rábai, K. Tóth, Plasma viscosity: a forgotten variable, *Clin. Hemorheol. Microcirc.* 39 (2008) 243–246, <https://doi.org/10.3233/CH-2008-1088>.
- [84] D.A. Almasri, N.B. Saleh, M.A. Atieh, G. McKay, S. Ahzi, Adsorption of phosphate on iron oxide doped halloysite nanotubes, *Sci. Rep.* 9 (2019) 1–13, <https://doi.org/10.1038/s41598-019-39035-2>.
- [85] J. Bourquin, A. Milosevic, D. Hauser, R. Lehner, F. Blank, A. Petri-Fink, B. Rothen-Rutishauser, Biodistribution, clearance, and long-term fate of clinically relevant nanomaterials, *Adv. Mater.* 30 (2018), e1704307, <https://doi.org/10.1002/adma.201704307>.
- [86] K. Makino, M. Arakawa, T. Kondo, Preparation and in vitro degradation properties of polylactide microcapsules, *Chem. Pharm. Bull.* 33 (1985), <https://doi.org/10.1248/cpb.33.1195>.
- [87] L. Martín-Banderas, J. Alvarez-Fuentes, M. Durán-Lobato, J. Prados, C. Melguizo, M. Fernández-Arévalo, M.Á. Holgado, Cannabinoid derivate-loaded PLGA nanocarriers for oral administration: formulation, characterization, and cytotoxicity studies, *Int. J. Nanomed.* 7 (2012) 5793–5806, <https://doi.org/10.2147/IJN.S34633>.
- [88] M.D. Blanco, M.J. Alonso, Development and characterization of protein-loaded poly(lactide-co-glycolide) nanospheres, *Eur. J. Pharm. Biopharm.* 43 (1997) 287–294, [https://doi.org/10.1016/S0939-6411\(97\)00056-8](https://doi.org/10.1016/S0939-6411(97)00056-8).
- [89] C.A. Lanzl, J. Baltusaitis, D.M. Cwiertny, Dissolution of hematite nanoparticle aggregates: influence of primary particle size, dissolution mechanism, and solution pH, *Langmuir* 28 (2012) 15797–15808, <https://doi.org/10.1021/la3022497>.
- [90] D. Papias, M. Taxiarchou, I. Paspaliaris, A. Kontopoulos, Mechanisms of dissolution of iron oxides in aqueous oxalic acid solutions, *Hydrometallurgy* 42 (1996) 257–265, [https://doi.org/10.1016/0304-386X\(95\)00104-0](https://doi.org/10.1016/0304-386X(95)00104-0).
- [91] E. Baumgartner, M.A. Blesa, H. Marinovich, A.J.G. Maroto, Heterogeneous electron transfer as a pathway in the dissolution of magnetite in oxalic acid solutions, *Inorg. Chem.* 22 (1983) 2224–2226, <https://doi.org/10.1021/ic00158a002>.
- [92] M.A. Blesa, H.A. Marinovich, E.C. Baumgartner, A.J.G. Maroto, Mechanism of dissolution of magnetite by oxalic acid-ferrous ion solutions, *Inorg. Chem.* 26 (1987) 3713–3717, <https://doi.org/10.1021/ic00269a019>.

4. Discussion

Nanomedicine has great potential to improve medicine and healthcare, leading to better prevention, faster diagnosis, and efficient treatment of diseases like cancer or antibiotic-resistant infections [14,157]. IONs are especially the focus of research due to their superparamagnetic behavior, high saturation magnetization, low toxicity, easy and cost-efficient synthesis, and the high surface-to-volume ratio [22,25]. These properties make IONs a suitable drug carrier for targeted drug delivery. An external magnetic field can guide them to cancerous or infected tissue, where they accumulate, leading to a high local concentration while reducing the overall amount and toxicity of the drug to the healthy tissue [198]. Antimicrobial peptides like LL are promising new drug candidates. They have high antimicrobial activity against gram-positive and gram-negative bacteria without resistance formation and are highly active against various cancer cells [227].

4.1. Drug Delivery System

Combining IONs as drug carriers and LL as a drug could provide a new, engaging, efficient system that could treat intracellular infections and cancer. As this system was never studied before, this thesis aimed to synthesize and analyze various IONs with ideal properties as drug carriers. Here the focus was the particle composition, magnetic behavior, surface properties, and agglomeration. If the system was promising also, the cytocompatibility was determined. Furthermore, different binding types of LL to the surface of the particles were analyzed for their effectiveness, efficiency, and drug activity.

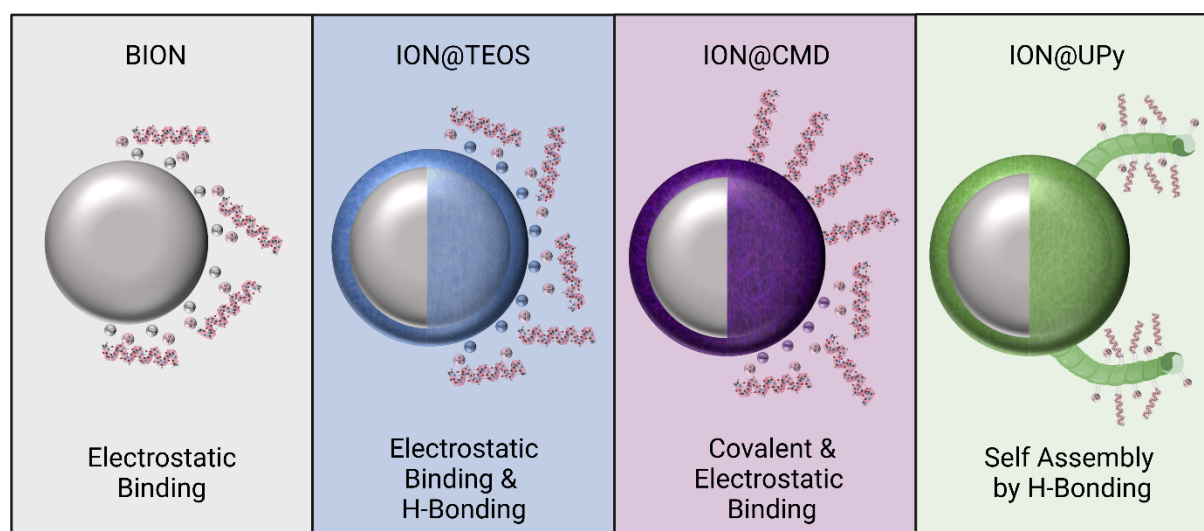


Figure 4.1: Schematic overview of the different particle types used as drug carriers with the analyzed binding types. It was created with BioRender.com.

Four different IONs were analyzed as potential drug carriers, covering four essential particle types (Figure 4.1). At first, this work focused on BIONs (Chapter 3.1, [232]). Without coating, these particles are particularly easy and cost-efficient to synthesize by co-precipitation [29]. The particle size of 9.9 nm is ideal for superparamagnetic behavior and a high BET area (Table 4.0.1), though they agglomerate in

water and form average diameters of 229 nm. This size could already lead to a raised clearance by the spleen [194].

Table 4.0.1: Summary of particle properties for BIONs, ION@TEOS, ION@Dex, ION@CMD, ION@UPy-NH₂, ION@PVA, and ION@PLGA. – indicates that the probes could not be measured with the analytic device. x indicates that it was not measured because the analytical data was not necessary for the respective study. The table is a summary of data from chapters 3.1-3.6 [232–237].

Particles	d_{TEM} (nm)	$d_{Scherrer}$ (nm)	IEP	d_{DLS} [Water] (nm)	Sat. Magnetization (emu g ⁻¹)	Magneto- phoresis ($\mu\text{m s}^{-1}$)	BET (m ² g ⁻¹)
BIONs	9.9	9.2	8.0	229	63.2	521	115
ION@TEOS0.98	8.7	8.8	1.9	88.2	66.0	1.79	115
ION@TEOS1.96	12	9.0	3.8	125	41.6	34.7	50.6
ION@TEOS3.91	23	9.0	4.2	223	28.6	72.8	27.9
ION@TEOS7.82	31	7.7	4.2	329	11.8	43.8	23.2
ION@Dex	11	8.6	6.9	254	62.0	2200	96.2
ION@CMD6.25	11	10	4.6	137	59.7	78.9	-
ION@CMD12.5	11	8.6	4.4	87.1	59.6	18.4	-
ION@CMD25.0	8.0	5.6	3.9	94.2	53.1	30.7	-
ION@CMD125	7.6	4.7	2.4	162	29.9	90.2	-
ION@CMD250	6.3	0.6	1.7	200	23.4	160	-
ION@UPy-NH ₂	x	x	x	177	31.3	x	x
ION@PVA	11	8.8	7.4	205	56.7	41.0	x
ION@PLGA	9.5	-	2.9	345	1.60	64.1	-

Different pH values and buffers influenced the zeta potential and colloidal stability of BIONs. The best adsorption of LL with 0.55 g g⁻¹ (22.7% drug loading) was generated within PBS at pH 7.4 by electrostatic interaction. The peptide has a cationic character at this pH, and the BIONs surface is predominantly positively charged with the negatively charged phosphate ION acting like a linker between the drug and carrier. Furthermore, the high ionic strength increases phosphate adsorption to the metal oxides [238]. The LL starting concentration and buffer composition generally influenced the electrostatic interaction, while the particle concentration did not affect the equilibrium. Even though the relatively high drug loading, the agglomeration behavior was negatively impacted by bound peptide ($d_{DLS} > 1000$ nm), and the electrostatic binding was influenced by particle washing, leading to a drug loss (0.23 g g⁻¹ after three washing steps, average loss of 35% peptide). The effect of LL on the hydrodynamic diameters and the particle size distribution can be explained by its multi-cationic character that can act as a binder agent. Furthermore, different pH values and physiological salt concentrations did highly increase the agglomeration of BIONs. Therefore, in the following studies, the

colloidal stability needed to be improved by coatings. A different surface charge or different binding mechanism could improve the efficiency of LL binding and decrease the loss through washing. The LL binding was temperature sensitive; therefore, hyperthermia conditions could start the drug elution. Bacterial growth experiments doubled the activity of bound LL (MIC: 0.53 μM) compared to the free drug (1.13 μM), making the elution of the peptide unnecessary. This effect of improved antimicrobial behavior could be explained by better exposure of the drug when being bound to the nanoparticles, which can interact with bacteria by themselves [239]. Even though LL could be bound quickly and in high amounts to the BION surface, and the system was highly antimicrobial, the big agglomerates dependent on the buffer composition, pH, temperature, and LL binding limited the application in the human body [194]. In the next step, biocompatible coatings were analyzed to enhance the particle's stability and tolerability of the human system [21,29]. Because this first study could show improved antimicrobial behavior of bound LL within the next studies, the focus was shifted from analyzing potential elution conditions to generating a more effective peptide binding. Inorganic, organic, and supramolecular coatings were investigated to cover a broad spectrum.

Silica is a bioinspired, non-toxic, acid-stable, negatively charged material and a widely used inorganic coating [21,31,51]. The inert silica stabilizes the particles from agglomeration at physiologic pH [29,45]. The Stöber process synthesized silica-coated IONs with a core-shell structure by hydrolysis of TEOS [50]. TEOS is a comparable cheap chemical with a price of 18.3 € per 25 mL (Sigma Aldrich, 78-10-4, 12.12.2022), which makes ION@TEOS still a low-cost drug carrier. Silica is negatively charged. The more negatively charged surface than the bare ION surface bears the potential for improved binding of the cationic LL. This study analyzed the influence of silica-coating thickness on the particle properties and the LL binding in Chapter 3.2 ([235]). While adding different TEOS equivalents did not influence the particle core size and crystallinity, the coating thickness increased with higher TEOS amounts. Four different ION@TEOS were synthesized, ranging from a diameter between 8.7 nm and 31 nm (Table 4.0.1). The silica surface consists of siloxane groups (Si–O–Si) that can form through dissociative chemisorption silanol groups (Si–OH) that can create depending on the pH deprotonated hydroxy groups (Si–O⁻) [240]. The IEP of the particles ranged from 1.9 to 4.2. The BET surface decreased with a thicker coating due to the rising particle size, highly affecting the stability of the particles and binding behavior. In contrast to a positive surface charge prone to induce toxicity, hemolysis, platelet aggregation, and faster clearance, negatively charged particles have a longer blood half-life [194]. While BIONs formed agglomerates of an average of 18.5 particles in water, the silica coating lowered this value to around 10.2 particles per agglomerate, independent of the coating thickness. Therefore d_{DLS} was between 88.2 nm and 329 nm. In PBS buffer (pH 7.4), all particles showed a different, concentration-dependent agglomeration. While BIONs were highly agglomerated, the silica shell could improve stability. The stabilizing effect can be explained through steric stabilization, reduced Van der Waals forces, and a stable surface [241,242]. The thicker the coating, the less the particles agglomerated. ION@TEOS formed the smallest agglomerates in PBS at around 657 nm. Even though this inorganic coating highly

improves the colloidal stability compared to BIONs, the agglomerate size was above 200 nm in a physiological medium, limiting their medical application [194]. ION@TEOS098, the particles with the thinnest silica layer, showed the smallest particle size, highest specific surface area, lowest IEP, and highest magnetization. Yet, STEP technology showed that they experience the slowest sedimentation in a magnetic field ($1.79 \mu\text{m s}^{-1}$), due to their electrostatic stabilization [243]. The drug loading was concentration-dependent. As thicker the coating was, as lower the maximal loading reached due to the decreased specific surface area. The highest drug loading of 0.28 g g^{-1} was reached with ION@TEOS0.98. In contrast to BIONs, where the peptide was continuously washed away, for ION@TEOS, the LL loading stayed constant after the second washing step. The negatively charged silica surface led to a stronger electrostatic interaction. The amine groups of lysine and the hydroxy groups on the silica surface formed hydrogen bonds [244]. The silica coating showed efficient LL binding and improved colloidal stability. Yet an optimal system for application in the human body was not reached; therefore, an alternative coating material was analyzed that had the potential to reduce agglomeration further and bind LL efficiently.

Organic polymers are usually biocompatible, non-toxic, and water-soluble [63,244]. The high density of free carboxyl groups gives CMD a negative charge, improving the blood circulation time and cellular uptake [84,85]. ION@CMD can be fast and easily synthesized by an in situ co-precipitation [30,89]. In contrast, the generation of silica-coated IONs takes two synthesis steps. While reducing one synthesis step decreases the overall cost, CMD sodium salt, with 112 € per 10 g (Sigma Aldrich, 39422-83-8, 12.12.2022), is more expensive than TEOS, but still comparably inexpensive. The targeted delivery allows low particle amounts per treatment, which makes the ION@CMD still affordable as a drug carrier. A broad rule for the medical costs of cancer treatment is that a disease-adjusted life year costs between 60.000 and 160.000 € (2007) [245]. This study analyzed the influence of the five CMD coating thicknesses on the particle properties and their applicability in drug delivery in Chapter 3.3 ([234]). Higher CMD equivalents led to a thicker coating and reduced core size with decreased magnetization (59.7 to 23.4 emu g^{-1}). This effect can be explained by the conventional nucleation theory [26,246]. The coating thickness ranged from 5.68 nm to 0.77 nm. A combination of HAADF-STEM and iDPC, and low-dose TEM could determine a core-shell character and visualize the coating for the first time. The coating did not influence the crystal structure but prevented the oxidation from magnetite to maghemite leading to Fe_3O_4 ratios of up to 47.5% while BIONs only showed 15.6%. Above a threshold range of 12.5-25 g L^{-1} CMD, the particles were colloidal stable over a broad pH spectrum (in water: 87.1 nm – 200 nm), independent of their IEP (Table 4.0.1). The negative surface charge of CMD leads to the repulsion of particles with the same net charge, which is responsible for the stabilizing effect. In contrast to silica, the number of particles that form agglomerates (around 8- 31) was not similar for the different CMD thicknesses. ION@CMD had a negative surface charge at physiological pH due to IEP between 4.6 and 1.7, decreasing with the coating thickness. This effect improved their stability in PBS and human plasma. For example, the diameters in PBS ranged from 165 nm ($1.2 \times$ the size compared to the

agglomeration in water) to 34.5 nm (0.2 x). Compared to BIONs and ION@TEOS, the colloidal stabilization of ION@CMD is superior. These small hydrodynamic diameters at physiological conditions make the CMD coating favorable for application in the human body. STEP analysis demonstrated the overall stability and significant impact of agglomeration on the magnetophoresis ($18.4\text{-}160 \mu\text{m s}^{-1}$). All ION@CMD showed good cytocompatibility (> 70%) over three days in smooth muscle cells, analyzed by XTT assay. Especially, ION@CMD12.5 showed ideal diameters, colloidal stability, and magnetization, overcoming the limitations of ION@TEOS and BIONs. However comparable to BIONs ION@CMD bound LL by only electrostatic interaction, showing a peptide loading of 0.32 g g^{-1} (24.3% drug loading) and a substantial decrease in loading with every washing step (1.30% after two washing steps). This fact made the ION@TEOS superior for the adsorption process of LL. In contrast to electrostatic binding, covalent binding is stronger and independent of pH or temperature [247]. The free carboxy groups of CMD and the free amine group of LL can form an amide bond by EDC/NHS coupling [248]. This method led to significantly higher drug loadings (up to 62%) and excellent efficiency of 82.3%. In comparison, the electrostatic interaction was less sufficient, with only 28% of the LL amount being bound. As already mentioned in chapter 3.1 with BIONs, increasing LL loading again promoted agglomeration. A 0.55 g g^{-1} LL loading formed hydrodynamic diameters of around 96 nm. This system showed high antimicrobial activity in growth experiments with *E.coli* (MIC 1.7 μM). The antimicrobial behavior of LL was not affected by covalent binding because the carboxy group of CMD reacts with the primary amine of LL. ION@CMD are easy to synthesize, cytocompatible, colloidally stable, and can bind LL effectively and efficiently, making this system a promising new candidate for treating cancer and intracellular infections. Compared to BIONs and ION@TEOS, ION@CMD had great potential for use in the human body.

In the last step, a supramolecular coating was analyzed. Supramolecular polymers find a minor application in drug delivery, mainly due to yet lower knowledge and higher production costs. However, they can induce tunable properties and increase flexibility in the system [91]. The UPy-units used in chapter 3.4 ([233]) were synthesized on demand; therefore, the price per gram cannot be calculated. The UPy units can form dimers by hydrogen bonding that can self-assemble into fibers with an amphiphilic supramolecular structure [249]. An extensive library of various functionalized UPy-units exists, allowing flexibility to mix and match different units by self-assembly into large networks [250]. ION@UPy were generated in a three-step process. At first, superparamagnetic BIONs synthesized by co-precipitation were functionalized with APTS, then an aldehyde group was introduced by the addition of PGA, and UPy-NH₂ could be bound by imine binding. FT-IR and TGA measurements could prove the successful coating, showing that the bound UPy amount was around 7wt%. The particles showed a saturation magnetization of $\pm 31 \text{ Am}^2 \text{ kg}^{-1}$. The positive zeta potential indicated that the UPy moieties built fibrous networks with a cationic outer charge. At pH 7 in water, the hydrodynamic diameter of ION@UPy-NH₂ was around 177 nm, making them applicable for drug delivery [194]. Nile Red assay determined a huge blue shift indicating the formation of fibers [251]. The study generated an innovative

magnetic drug delivery system that has the potential to bind UPy functionalized drugs flexibly. Though important characteristics and LL was not analyzed.

Therefore a follow-up study, shown in chapter 3.5 ([237]), focused on the UPy-coated IONs as a drug carrier for LL and their effect on cytocompatibility. Compared to the previous studies, more intense cytotoxicity studies with different analytical methods and internalization tests were used. The morphology of ION@UPy could be analyzed by HAADF-STEM combined with iDPC and Cryo-TEM. The system was assembled by a magnetic core with a UPy shell and UPy fibers. The micrographs could prove the data from the preceding Nile Red assay. The cytocompatibility of ION@UPy and its precursors was analyzed with a metabolic resazurin assay and live dead fluorescent staining [252,253]. The system showed high cytocompatibility with human kidney cells (HK-2) and a concentration-dependent reduction of the metabolic activity to 53% for macrophagic THP-1 cells. Both cell types internalized ION@UPy-NH₂ within 24 hours, making them promising candidates for intracellular drug delivery. While the macrophagic cells internalized most of the particles within 2 hours, the HK-2 cells only adsorbed the particles at this time. Champion et al. showed that worm-like structures are slower internalized compared to spherical ones [254]. Therefore the particles would might get internalized even faster with shorter fibers. UPy functionalized LL was used to generate a drug delivery system. The conjugation of AMPs to polymers or nanoparticles and supramolecular engineering could improve their toxicity to human cells yet often limit their application [255–257]. The binding of UPy-LL to the drug carrier was realized by easy and fast self-assembly with high efficiency of 99%. This process reassembled the UPy-moieties forming slightly more and shorter fibers. Comparable to the experiments with BIONs, binding of UPy-LL to the nanoparticles improved its antimicrobial activity against *E.coli* from a MIC of 3.5 μ M to 1.8 μ M. The supramolecular engineering improved the cytocompatibility in HK-2 cells from 5.4 μ M to 11 μ M, while the cytotoxicity against macrophages was higher at 5.4 μ M. The experiments proved that combining supramolecular engineering and IONs is a great tool to increase antimicrobial activity while reducing the cytotoxicity of LL. The facile and fast self-assembly makes the system interesting for other UPy functionalized AMPs or drugs.

The studies described in chapters 3.1 to 3.5 showed that an ideal design of IONs and their coatings could overcome common issues, including agglomeration, magnetophoresis, effective and efficient drug binding, and cytocompatibility. Although BIONs and ION@TEOS did not fulfill all the required expectations for medical applications, ION@CMD@LL and ION@UPy-NH₂@UPy-LL are innovative and promising systems for the magnetic delivery of AMPs.

4.2. Stability and Agglomeration

For the application of nanoparticles in medicine, it is essential to generate knowledge about their degradation, colloidal stability, and toxicity in preclinical studies [258]. Even though massive research has been done on the design, characterization, and application of various IONs, long-term agglomeration, and degradation studies in body fluids are often missing. The second part of this thesis

analyzed the effect of common coating materials of IONs on their behavior in human body fluids. After injection into the human body, IONs meet different body fluids like blood, endosomal fluid, lysosomal fluid, and cytosol (Figure 4.2). Each fluid has a different composition and pH. Simulated fluids are a cost-efficient alternative to in vivo experiments [259,260]. The study in chapter 3.6 analyzed the influence of surface properties, using BIONs, ION@PVA, ION@PLGA, and ION@Dex, on the behavior inside the human body ([236]). The focus lay on their cytocompatibility, agglomeration, degradation, and oxidative stress. Beforehand the particles were characterized and compared. While all IONs had a comparable d_{TEM} (9.5 nm - 11 nm), the IEP varied from 2.9 for the PLGA, 6.9 for Dex, and 7.4 for PVA coating. ION@PVA had the best colloidal stability over a wide pH range (pH 4-10) in water (Table 4.1). This low agglomeration behavior is comparable to ION@CMD in chapter 3.3. Unterweger et al. showed that the usage of higher Dex equivalents during co-precipitation could reduce the IEP and improve the colloidal stability of these particles [168].

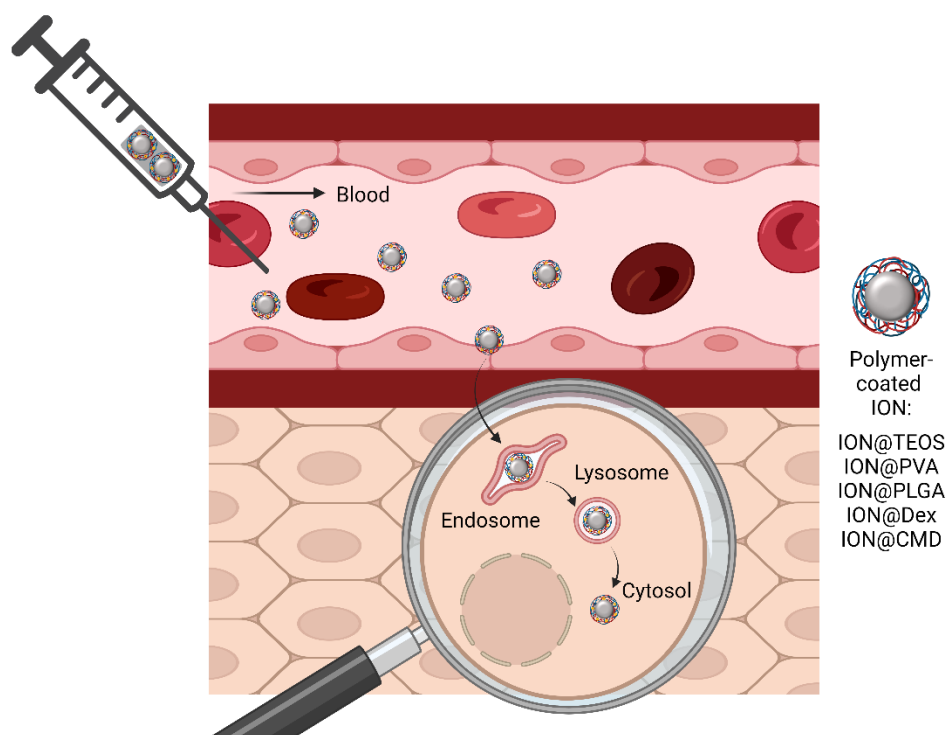


Figure 4.2: Schematic illustration of the cycle of polymer-coated IONs in the human body after injection. The nanoparticles are dispersed in different body fluids like blood, endosomal, lysosomal fluid, and cytosol. It was created with BioRender.com.

The coating thickness, surface charge, agglomeration, and saturation magnetization affected the magnetophoretic behavior. SAXS measurements determined aggregation and primary particle sizes around 20 nm for ION@Dex and BIONs and are, therefore, an attractive alternative method. All four particle types showed no cytotoxicity (>70%) in smooth muscle cells over three days. The study provided a new experimental setup for long-term agglomeration and degradation analysis of IONs. A combination of DLS and phenanthroline assay was used to get reliable and easy-to-measure data. In contrast to a protocol by Rabel et al. in which the particles were incubated at 110 rpm, faster-shaking speeds of 1000 rpm ensured that the particles stayed in suspension during incubation and shortened the

preclinical tests from around 28 days to three days [260]. Therefore our protocol allows for the fast screening of many candidates, hopefully closing this knowledge gap in the future. All particles showed different agglomeration and dissolution profiles. At pH 7.4 in SBF and PBS, none of the investigated IONs dissolved, while ION@PVA experienced the lowest hydrodynamic diameters, comparable to water (240 nm). The long polymer chains of PVA and potential hydrogen bonding between the polymer chains improved steric stabilization, independent of high salt concentrations [261,262]. In dependence of the acidic pH IONs did dissolve in AEF and even faster in ALF. The iron ion release decreased with shrinking particle size forming a plateau. ION@PVA (91%) experienced the highest and ION@PLGA (58%) lowest degradation within three days. The hydrodynamic diameters decreased congruent to the degradation profile in the first 24 hours. Afterward, the particles agglomerated. Comparable to the dissolution profile in AEF, the oxidation kinetics of ION@PVA and ION@Dex was faster than that of BIONs. The more rapid iron ion release can be explained by the protonation of the coatings at acidic pH values, leading to the attraction of water and dissolution agents [260]. This study showed a great analytical setup of DLS, phenanthroline assay, SAXS, and LDL assay that can generate fast essential knowledge within a preclinical study. Of course, a complete characterization of IONs is necessary to understand the data fully. A good preclinical study combining short and long-term analytics, cytocompatibility experiments, and a detailed description can enhance, accelerate, and cheapen the design of nanoparticles for application in nanomedicine.

5. Summary & Outlook

Magnetic drug delivery can bring drugs directly to the target, leading to a high local drug dose and high efficiency while avoiding toxic side effects. IONs are superparamagnetic, non-toxic, have a high surface-to-volume ratio, and are fast and easy to synthesize. They can be designed specifically regarding their size, shape, surface functionalization, and magnetic properties to generate a magnetic drug carrier system. The surface properties can be influenced by various coatings, often forming a core-shell structure. AMPs are highly antimicrobial without showing resistance formation and can be active against different cancer cells. Therefore, they are a promising new drug against cancer and intracellular infections that have yet been only limited by their concentration-dependent potential toxicity to human cells.

This study analyzed four different drug carriers, BIONs, ION@TEOS as an inorganic coating, ION@CMD as an organic coating, and ION@UPy as a supramolecular coating. A multi-analytical approach (TEM, XRD, FT-IR, SQUID, Raman, TGA, STEP, BET, DLS, Zeta potential, and Nile Red assay) was used to characterize the particles in detail and analyze their applicability in the human body. Depending on the coating, different binding methods were used, including electrostatic binding, H-bonding, covalent binding, or supramolecular self-assembly. The activity of the bound drug was studied by growth experiments with *E.coli*, which determined the MIC.

Though BIONs were the cheapest nanoparticles, could bind high amounts of LL, and improved the antimicrobial behavior of the peptide, their usability as a drug carrier was limited by the weak electrostatic peptide binding and uncontrolled buffer, temperature, pH, and loading-dependent agglomeration. The inorganic silica coating improved the strength of LL binding and the colloidal stability in water. However, especially in physiological media, the hydrodynamic sizes were above a reasonable range for application in the human body. Even though both systems are not ideal for drug delivery, the studies provided new trends and insights into the behavior of a BION surface and different thicknesses of a silica coating on the binding of a short cationic peptide, agglomeration, and magnetophoresis. The new knowledge could be used to design IONs with individual properties or custom peptide-based tags for bioseparation.

The organic CMD coating was able to overcome the agglomeration issues and reduced the oxidation of magnetite. The coating thickness influenced the core size, colloidal stability, IEP, and magnetophoresis. For this study, special TEM techniques like HAADF-STEM combined with iDPC and low-dose TEM were necessary to visualize the coating. A comparison of electrostatic and covalent binding revealed that amide formation has distinct better effectivity and efficiency. Also, the covalent binding did not reduce the antimicrobial activity of LL. Since ION@CMD showed good cytocompatibility in human cells, high drug loading, and ideal colloidal stability, they are a promising new drug carrier system for AMPs that can be synthesized in one step. To further analyze their suitability as a drug delivery system,

the following steps could be long-term agglomeration and degradation experiments, internalization experiments in human cells, analysis of the cytotoxicity of ION@CMD@LL, and tests with infected tissue or cancerous cells. Moreover, it would be interesting to analyze the antimicrobial behavior with other clinical-relevant strands like *S. aureus*. If the results are promising, the next step should be *in vitro* studies.

The supramolecular UPy coating strongly differs from the previously analyzed coatings. The potential high production costs make it only interesting for diseases that conventional treatments can not cure or lead to highly toxic side effects. The study provided an entirely new synthesis approach for an efficient UPy shell with fibers. The morphology of the drug carrier could be visualized with a combination of HAADF-STEM and Cryo-TEM. The system's good cytocompatibility was analyzed by live/dead staining and a metabolic assay. Fluorescent microscopy showed that the particles could be internalized in both HK-2 and THP-1 cells. UPy functionalized LL was bound easily and highly efficiently by self-assembly. ION@UPy@UPy-LL has the potential to overcome the toxicity of LL not only by concentration reduction due to magnetic targeting but also through supramolecular engineering. The cytocompatibility tests proved this assumption. This system already shows high potential as a new, innovative drug delivery system. However, additional experiments that lead to a reduction of fiber length could accelerate the internalization into cells. Again it would be interesting to proceed with this work with other clinical-relevant strands and *in vitro* tests. Furthermore, ION@UPy have the capability to bind various UPy-functionalized AMPs or other drugs by self-assembly flexibly.

For the application of IONs in nanomedicine, not only a complete characterization of the particles is necessary, but it is also crucial to determine their long-term behavior in body fluids in preclinical studies. Therefore in the second part of the study, an experimental setup was shown that could analyze the effects of coatings on the IONs' stability and agglomeration within three days. The central part of this study was a combination of phenanthroline assay and DLS measurements, supported by an LDL assay that analyzed oxidative stress and SAXS measurements. Incubation in simulated body fluids was used as a low-cost, easy-to-get alternative to animal studies. Three common coated IONs, ION@PVA, ION@Dex, and ION@PLGA, were examined in this study. Clear coherences of the surface properties and the agglomeration and degradation profile were shown. In comparison, ION@PVA showed the lowest agglomeration and fastest degradation profile of all analyzed particles, which makes them the most promising candidate for an application in nanomedicine. In the future, this experimental setup can be used to explore more coated IONs for their long-term behavior and usability in the human body. It has the potential to close a knowledge gap in this field and shorten the preclinical phase. As the CMD and UPy-coated IONs showed the most promising results, it would be especially interesting to analyze them with this experimental setup and determine their potential long-term behavior in human body fluids. The systems should be analyzed with and without the drug LL. Additional tests about the

thrombogenic behavior, heating efficiency, and activity in magnetic resonance measurements could help to classify coated IONs and improve their design for a safe and efficient medical application.

6. References

- [1] B.Y.S. Kim, J.T. Rutka, W.C.W. Chan, *Nanomedicine*, *N. Engl. J. Med.* 363 (2010) 2434–2443. <https://doi.org/10.1056/NEJMra0912273>.
- [2] R. P. Feynman, There's plenty of room at the bottom, *Eng. Sci. (CalTech)* (1960) 22–36.
- [3] R.A. Freitas, What is nanomedicine?, *Nanomedicine* 1 (2005) 2–9. <https://doi.org/10.1016/j.nano.2004.11.003>.
- [4] K.E. Drexler, *Engines of creation: The coming area of nanotechnology*, Anchor Books, New York, 1990.
- [5] R.A. Freitas, *Nanomedicine Volume I*, Landes Bioscience, Georgetown, 1999.
- [6] M. Bensharada, R. Telford, B. Stern, V. Gaffney, Loss on ignition vs. thermogravimetric analysis: a comparative study to determine organic matter and carbonate content in sediments, *J Paleolimnol* 67 (2022) 191–197. <https://doi.org/10.1007/s10933-021-00209-6>.
- [7] M. Krstić, S. Ražić, Analytical Approaches to the Characterization of Solid Drug Delivery Systems with Porous Adsorbent Carriers, *Curr. Med. Chem.* 25 (2018) 3956–3972. <https://doi.org/10.2174/0929867325666180212120908>.
- [8] S.P. Schwaminger, D. Bauer, P. Fraga-García, F.E. Wagner, S. Berensmeier, Oxidation of magnetite nanoparticles: impact on surface and crystal properties, *CrystEngComm* 19 (2017) 246–255. <https://doi.org/10.1039/C6CE02421A>.
- [9] R. Bleul, A. Baki, C. Freese, H. Paysen, O. Kosch, F. Wiekhorst, Continuously manufactured single-core iron oxide nanoparticles for cancer theranostics as valuable contribution in translational research, *Nanoscale Adv.* 2 (2020) 4510–4521. <https://doi.org/10.1039/d0na00343c>.
- [10] S. Brunauer, P.H. Emmett, E. Teller, Adsorption of Gases in Multimolecular Layers, *J. Am. Chem. Soc.* 60 (1938) 309–319. <https://doi.org/10.1021/ja01269a023>.
- [11] J. Clarke, A. I. Braginski (Eds.), *The SQUID Handbook: Fundamentals and Technology of SQUIDS and SQUID Systems*, Wiley-VCH, Weinheim, 2004.
- [12] O. Mykhaylyk, D. Lerche, D. Vlaskou, V. Schoemig, T. Detloff, D. Krause, M. Wolff, T. Joas, S. Berensmeier, C. Plank, Magnetophoretic Velocity Determined by Space- and Time-Resolved Extinction Profiles, *IEEE Magn. Lett.* 6 (2015) 1–4. <https://doi.org/10.1109/LMAG.2015.2474306>.
- [13] Stanford Magnets, An Introduction to Vibrating Sample Magnetometer. <https://www.stanfordmagnets.com/an-introduction-to-vibrating-sample-magnetometer.html> (accessed 12 January 2023).
- [14] S.K. Saxena, *NanoBioMedicine*, Springer Singapore Pte. Limited, Singapore, 2020.
- [15] M. Rahman, *Nanomaterials*, BoD – Books on Demand, 2011.
- [16] R.M. Cornell, U. Schwertmann, *The Iron Oxides: Structure, Properties, Reactions, Occurrences and Uses*, second. vollst. überarb. u. erw. Auflage, Wiley-VCH, Weinheim, 2006.
- [17] C. Buzea, I. Pacheco, Nanomaterial and Nanoparticle: Origin and Activity, in: M. Ghorbanpour, K. Manika, A. Varma (Eds.), *Nanoscience and Plant–Soil Systems*, Springer International Publishing, Cham, 2017, pp. 71–112.
- [18] C. Boxall, G. Kelsall, Z. Zhang, Photoelectrophoresis of colloidal iron oxides. Part 2.—Magnetite (Fe₃O₄), *J. Chem. Soc., Faraday Trans.* 92 (1996) 791–802. <https://doi.org/10.1039/FT9969200791>.

- [19] B. Li, Q. Sun, H. Fan, M. Cheng, A. Shan, Y. Cui, R. Wang, Morphology-Controlled Synthesis of Hematite Nanocrystals and Their Optical, Magnetic and Electrochemical Performance, *Nanomaterials (Basel)* 8 (2018). <https://doi.org/10.3390/nano8010041>.
- [20] Z. Zhang, C. Boxall, G.H. Kelsall, Photoelectrophoresis of colloidal iron oxides 1. Hematite (α -Fe₂O₃), *Colloids Surf. A Physicochem. Eng. Asp.* 73 (1993) 145–163. [https://doi.org/10.1016/0927-7757\(93\)80013-5](https://doi.org/10.1016/0927-7757(93)80013-5).
- [21] W. Wu, Z. Wu, T. Yu, C. Jiang, W.-S. Kim, Recent progress on magnetic iron oxide nanoparticles: synthesis, surface functional strategies and biomedical applications, *Sci. Technol. Adv. Mater.* 16 (2015) 23501. <https://doi.org/10.1088/1468-6996/16/2/023501>.
- [22] A.-H. Lu, E.L. Salabas, F. Schüth, Magnetic nanoparticles: synthesis, protection, functionalization, and application, *Angew. Chem. Int. Ed.* 46 (2007) 1222–1244. <https://doi.org/10.1002/anie.200602866>.
- [23] M. Yamaura, R.L. Camilo, L.C. Sampaio, M.A. Macêdo, M. Nakamura, H.E. Toma, Preparation and characterization of (3-aminopropyl)triethoxysilane-coated magnetite nanoparticles, *J. Magn. Magn. Mater.* 279 (2004) 210–217. <https://doi.org/10.1016/j.jmmm.2004.01.094>.
- [24] K.N. Koo, A.F. Ismail, M.H.D. Othman, N. Bidin, M. A R., Preparation and characterization of superparamagnetic magnetite (Fe₃O₄) nanoparticles: A short review, *Mal. J. Fund. Appl. Sci.* 15 (2019) 23–31. <https://doi.org/10.11113/mjfas.v15n2019.1224>.
- [25] A. Ali, H. Zafar, M. Zia, I. Ul Haq, A.R. Phull, J.S. Ali, A. Hussain, Synthesis, characterization, applications, and challenges of iron oxide nanoparticles, *Nanotechnol. Sci. Appl.* 9 (2016) 49–67. <https://doi.org/10.2147/NSA.S99986>.
- [26] H.-C. Roth, S.P. Schwaminger, M. Schindler, F.E. Wagner, S. Berensmeier, Influencing factors in the CO-precipitation process of superparamagnetic iron oxide nano particles: A model based study, *J. Magn. Magn. Mater.* 377 (2015) 81–89. <https://doi.org/10.1016/j.jmmm.2014.10.074>.
- [27] I. Martínez-Mera, M.E. Espinosa-Pesqueira, R. Pérez-Hernández, J. Arenas-Alatorre, Synthesis of magnetite (Fe₃O₄) nanoparticles without surfactants at room temperature, *Mater. Lett.* 61 (2007) 4447–4451. <https://doi.org/10.1016/j.matlet.2007.02.018>.
- [28] Babes, D., Tanguy, J.J. Le Jeune, Jallet, Synthesis of Iron Oxide Nanoparticles Used as MRI Contrast Agents: A Parametric Study, *J. Colloid Interface Sci.* 212 (1999) 474–482. <https://doi.org/10.1006/jcis.1998.6053>.
- [29] S. Laurent, D. Forge, M. Port, A. Roch, C. Robic, L. Vander E., R.N. Muller, Magnetic iron oxide nanoparticles: synthesis, stabilization, vectorization, physicochemical characterizations, and biological applications, *Chem. Rev.* 108 (2008) 2064–2110. <https://doi.org/10.1021/cr068445e>.
- [30] R. Massart, Preparation of aqueous magnetic liquids in alkaline and acidic media, *IEEE Trans. Magn.* 17 (1981) 1247–1248. <https://doi.org/10.1109/TMAG.1981.1061188>.
- [31] K. Mylkie, P. Nowak, P. Rybczynski, M. Ziegler-Borowska, Polymer-Coated Magnetite Nanoparticles for Protein Immobilization, *Materials (Basel)* 14 (2021). <https://doi.org/10.3390/ma14020248>.
- [32] V.K. LaMer, R.H. Dinegar, Theory, Production and Mechanism of Formation of Monodispersed Hydrosols, *J. Am. Chem. Soc.* 72 (1950) 4847–4854. <https://doi.org/10.1021/ja01167a001>.
- [33] J. Baumgartner, A. Dey, P.H.H. Bomans, C. Le Coadou, P. Fratzl, Sommerdijk, N. A. J. M., D. Faivre, Nucleation and growth of magnetite from solution, *Nat. Mater.* 12 (2013) 310–314. <https://doi.org/10.1038/nmat3558>.

- [34] S. Schwaminger, C. Syhr, S. Berensmeier, Controlled Synthesis of Magnetic Iron Oxide Nanoparticles: Magnetite or Maghemite?, *Crystals* 10 (2020) 214. <https://doi.org/10.3390/cryst10030214>.
- [35] D. Forge, A. Roch, S. Laurent, H. Tellez, Y. Gossein, F. Renaux, L. Vander E., R.N. Muller, Optimization of the Synthesis of Superparamagnetic Contrast Agents by the Design of Experiments Method, *J. Phys. Chem. C* 112 (2008) 19178–19185. <https://doi.org/10.1021/jp803832k>.
- [36] S. Jain, P.V. Devarajan (Eds.), *Targeted Drug Delivery Concepts and Design*, Springer, Cham, 2015.
- [37] F.M. Kievit, M. Zhang, Surface engineering of iron oxide nanoparticles for targeted cancer therapy, *Acc. Chem. Res.* 44 (2011) 853–862. <https://doi.org/10.1021/ar2000277>.
- [38] M. Muthiah, I.-K. Park, C.-S. Cho, Surface modification of iron oxide nanoparticles by biocompatible polymers for tissue imaging and targeting, *Biotechnol. Adv.* 31 (2013) 1224–1236. <https://doi.org/10.1016/j.biotechadv.2013.03.005>.
- [39] J. Wolfram, Y. Yang, J. Shen, A. Moten, C. Chen, H. Shen, M. Ferrari, Y. Zhao, The nano-plasma interface: Implications of the protein corona, *Colloids Surf. B: Biointerfaces* 124 (2014) 17–24. <https://doi.org/10.1016/j.colsurfb.2014.02.035>.
- [40] S. Tenzer, D. Docter, J. Kuharev, A. Musyanovych, V. Fetz, R. Hecht, F. Schlenk, D. Fischer, K. Kiouptsi, C. Reinhardt, K. Landfester, H. Schild, M. Maskos, S.K. Knauer, R.H. Stauber, Rapid formation of plasma protein corona critically affects nanoparticle pathophysiology, *Nat. Nanotechnol.* 8 (2013) 772–781. <https://doi.org/10.1038/nnano.2013.181>.
- [41] H.-C. Roth, S. Schwaminger, P. Fraga García, J. Ritscher, S. Berensmeier, Oleate coating of iron oxide nanoparticles in aqueous systems: the role of temperature and surfactant concentration, *J Nanopart Res* 18 (2016). <https://doi.org/10.1007/s11051-016-3405-2>.
- [42] Yong W., Jian F. W., Xiaowei T., Xue Z. L., Hong Y., "Pulling" Nanoparticles into Water: Phase Transfer of Oleic Acid Stabilized Monodisperse Nanoparticles into Aqueous Solutions of α -Cyclodextrin, *Nano Lett* 3 (2003) 1555–1559. <https://doi.org/10.1021/nl034731j>.
- [43] M. von Smoluchowski, Zur kinetischen Theorie der Brownschen Molekularbewegung und der Suspensionen, *Ann. Phys.* 326 (1906) 756–780. <https://doi.org/10.1002/andp.19063261405>.
- [44] J. Xu, J. Sun, Y. Wang, J. Sheng, F. Wang, M. Sun, Application of iron magnetic nanoparticles in protein immobilization, *Molecules (Basel)* 19 (2014) 11465–11486. <https://doi.org/10.3390/molecules190811465>.
- [45] D. Couto, M. Freitas, F. Carvalho, E. Fernandes, Iron Oxide Nanoparticles: An Insight into their Biomedical Applications, *Curr. Med. Chem.* 22 (2015) 1808–1828. <https://doi.org/10.2174/0929867322666150311151403>.
- [46] A. Jahanban-Esfahlan, S. Dastmalchi, S. Davaran, A simple improved desolvation method for the rapid preparation of albumin nanoparticles, *Int. J. Biol. Macromol.* 91 (2016) 703–709. <https://doi.org/10.1016/j.ijbiomac.2016.05.032>.
- [47] H. Nosrati, N. Sefidi, A. Sharafi, H. Danafar, H. Kheiri Manjili, Bovine Serum Albumin (BSA) coated iron oxide magnetic nanoparticles as biocompatible carriers for curcumin-anticancer drug, *Bioorg. Chem.* 76 (2018) 501–509. <https://doi.org/10.1016/j.bioorg.2017.12.033>.
- [48] A.K. Gupta, M. Gupta, Synthesis and surface engineering of iron oxide nanoparticles for biomedical applications, *Biomaterials* 26 (2005) 3995–4021. <https://doi.org/10.1016/j.biomaterials.2004.10.012>.

- [49] J. Wagner, T. Autenrieth, R. Hempelmann, Core shell particles consisting of cobalt ferrite and silica as model ferrofluids [CoFe₂O₄-SiO₂ core shell particles], *J. Magn. Magn. Mater.* 252 (2002) 4–6. [https://doi.org/10.1016/S0304-8853\(02\)00729-1](https://doi.org/10.1016/S0304-8853(02)00729-1).
- [50] W. Stöber, A. Fink, E. Bohn, Controlled growth of monodisperse silica spheres in the micron size range, *J. Colloid Interface Sci.* 26 (1968) 62–69. [https://doi.org/10.1016/0021-9797\(68\)90272-5](https://doi.org/10.1016/0021-9797(68)90272-5).
- [51] C. Costa, F. Brandão, M.J. Bessa, S. C., V. Valdiglesias, G. Kiliç, N. Fernandez.-Bertolez, P. Quaresma, E. Pereira, E. Pásaro, B. Laffon, J.P. Teixeira, In vitro cytotoxicity of superparamagnetic iron oxide nanoparticles on neuronal and glial cells. Evaluation of nanoparticle interference with viability tests, *J. Appl. Toxicol.* 36 (2016) 361–372. <https://doi.org/10.1002/jat.3213>.
- [52] A. Raghunath, E. Perumal, Metal oxide nanoparticles as antimicrobial agents: a promise for the future, *Int. J. Antimicrob. Agents* 49 (2017) 137–152. <https://doi.org/10.1016/j.ijantimicag.2016.11.011>.
- [53] L.S. Arias, J.P. Pessan, A.P.M. Vieira, Lima, T. M. Toito de, A.C.B. Delbem, D.R. Monteiro, Iron Oxide Nanoparticles for Biomedical Applications: A Perspective on Synthesis, Drugs, Antimicrobial Activity, and Toxicity, *Antibiotics (Basel)* 7 (2018). <https://doi.org/10.3390/antibiotics7020046>.
- [54] X.-M. Zhu, Y.-X.J. Wang, K.C.-F. Leung, S.-F. Lee, F. Zhao, D.-W. Wang, J.M.Y. Lai, C. Wan, C.H.K. Cheng, A.T. Ahuja, Enhanced cellular uptake of aminosilane-coated superparamagnetic iron oxide nanoparticles in mammalian cell lines, *Int. J. Nanomed.* 7 (2012) 953–964. <https://doi.org/10.2147/IJN.S28316>.
- [55] L. Nalbandian, E. Patrikiadou, V. Zaspalis, A. Patrikidou, E. Hatzidaki, C. N. Papandreou, Magnetic Nanoparticles in Medical Diagnostic Applications: Synthesis, Characterization and Proteins Conjugation, *Curr. Nanosci.* (2016) 455–468.
- [56] M. Kermanian, S. Sadighian, M. Naghibi, M. Khoshkam, PVP Surface-protected silica coated iron oxide nanoparticles for MR imaging application, *J. Biomater. Sci. Polym. Ed.* 32 (2021) 1356–1369. <https://doi.org/10.1080/09205063.2021.1916869>.
- [57] Y.-H. Lien, T.-M. Wu, J.-H. Wu, J.-W. Liao, Cytotoxicity and drug release behavior of PNIPAM grafted on silica-coated iron oxide nanoparticles, *J. Nanopart. Res.* 13 (2011) 5065–5075. <https://doi.org/10.1007/s11051-011-0487-8>.
- [58] A. Taufiq, A. Nikmah, A. Hidayat, S. Sunaryono, N. Mufti, N. Hidayat, H. Susanto, Synthesis of magnetite/silica nanocomposites from natural sand to create a drug delivery vehicle, *Heliyon* 6 (2020) e03784. <https://doi.org/10.1016/j.heliyon.2020.e03784>.
- [59] J. Hwang, E. Lee, J. Kim, Y. Seo, K.H. Lee, J.W. Hong, A.A. Gilad, H. Park, J. Choi, Effective delivery of immunosuppressive drug molecules by silica coated iron oxide nanoparticles, *Colloids Surf. B: Biointerfaces* 142 (2016). <https://doi.org/10.1016/j.colsurfb.2016.01.040>.
- [60] C.H. Yu, A. Al-Saadi, S.-J. Shih, L. Qiu, K.Y. Tam, S.C. Tsang, Immobilization of BSA on Silica-Coated Magnetic Iron Oxide Nanoparticle, *J. Phys. Chem. C* 113 (2009) 537–543. <https://doi.org/10.1021/jp809662a>.
- [61] Mendonça, E. S. D. T. de, Faria, A. C. B. de, S.C.L. Dias, F.F.H. Aragón, J.C. Mantilla, J.A.H. Coaquira, J.A. Dias, Effects of silica coating on the magnetic properties of magnetite nanoparticles, *Surf. Interfaces* 14 (2019) 34–43. <https://doi.org/10.1016/j.surfin.2018.11.005>.
- [62] Z. Gao, H.L. Ring, A. Sharma, B. Namsrai, N. Tran, E.B. Finger, M. Garwood, C.L. Haynes, J.C. Bischof, Preparation of Scalable Silica-Coated Iron Oxide Nanoparticles for Nanowarming, *Adv. Sci. (Weinh.)* 7 (2020) 1901624. <https://doi.org/10.1002/advs.201901624>.

- [63] S.C. McBain, H.H. Yiu, J. Dobson, Magnetic nanoparticles for gene and drug delivery, *Int. J. Nanomedicine* 3 (2008). <https://doi.org/10.2147/ijn.s1608>.
- [64] N. A. Alcantar, E. S. Aydil, J. N. Israelachvili, Polyethylene glycol-coated biocompatible surfaces, *J. Biomed. Mater. Res.* 51 (2000) 343–351. [https://doi.org/10.1002/1097-4636\(20000905\)51:3<343:AID-JBM7>3.0.CO;2-D](https://doi.org/10.1002/1097-4636(20000905)51:3<343:AID-JBM7>3.0.CO;2-D).
- [65] B. Pelaz, P. del Pino, P. Maffre, R. Hartmann, M. Gallego, S. Rivera-Fernández, de la Fuente, J. M., G.U. Nienhaus, W.J. Parak, Surface Functionalization of Nanoparticles with Polyethylene Glycol: Effects on Protein Adsorption and Cellular Uptake, *ACS Nano* 9 (2015) 6996–7008. <https://doi.org/10.1021/acsnano.5b01326>.
- [66] K.E. Albinali, M.M. Zagho, Y. Deng, A.A. Elzatahry, A perspective on magnetic core-shell carriers for responsive and targeted drug delivery systems, *Int. J. Nonomed.* 14 (2019) 1707–1723. <https://doi.org/10.2147/IJN.S193981>.
- [67] F. Haaf, A. Sanner, F. Straub, Polymers of N-Vinylpyrrolidone: Synthesis, Characterization and Uses, *Polym J* 17 (1985) 143–152. <https://doi.org/10.1295/polymj.17.143>.
- [68] A. Karimi, Wan D., Wan M. A., Materials, preparation, and characterization of PVA/MMT nanocomposite hydrogels: A review, *Polym. Compos.* 38 (2017) 1086–1102. <https://doi.org/10.1002/pc.23671>.
- [69] M. Aslam, M.A. Kalyar, Z.A. Raza, Polyvinyl alcohol: A review of research status and use of polyvinyl alcohol based nanocomposites, *Polym Eng Sci* 58 (2018) 2119–2132. <https://doi.org/10.1002/pen.24855>.
- [70] S. Bamrungsap, Z. Zhao, T. Chen, L. Wang, Li, T. Fu, W. Tan, Nanotechnology in therapeutics: a focus on nanoparticles as a drug delivery system, *Nanomedicine (Lond.)* 7 (2012) 1253–1271. <https://doi.org/10.2217/nmm.12.87>.
- [71] S.-F. Chong, A.A.A. Smith, A.N. Zelikin, Microstructured, functional PVA hydrogels through bioconjugation with oligopeptides under physiological conditions, *Small (Weinheim)* 9 (2013) 942–950. <https://doi.org/10.1002/sml.201201774>.
- [72] G. Pandey, S. Singh, G. Hitkari, Synthesis and characterization of polyvinyl pyrrolidone (PVP)-coated Fe₃O₄ nanoparticles by chemical co-precipitation method and removal of Congo red dye by adsorption process, *Int Nano Lett* 8 (2018) 111–121. <https://doi.org/10.1007/s40089-018-0234-6>.
- [73] A. Petri-Fink, M. Chastellain, L. Juillerat-Jeanneret, A. Ferrari, H. Hofmann, Development of functionalized superparamagnetic iron oxide nanoparticles for interaction with human cancer cells, *Biomaterials* 26 (2005) 2685–2694. <https://doi.org/10.1016/j.biomaterials.2004.07.023>.
- [74] N.S. LABIDI, A. DJEBAILI, N.S. LABIDI, A. DJEBAILI, Studies of The Mechanism of Polyvinyl Alcohol Adsorption on The Calcite/Water Interface in The Presence of Sodium Oleate, *J. Met. Mater. Miner.* 7 (2008) 147–161. <https://doi.org/10.4236/jmmce.2008.72012>.
- [75] S. Kayal, R.V. Ramanujan, Doxorubicin loaded PVA coated iron oxide nanoparticles for targeted drug delivery, *Mater. Sci. Eng. C* 30 (2010) 484–490. <https://doi.org/10.1016/j.msec.2010.01.006>.
- [76] M. Ebadi, S. Bullo, K. Buskara, M.Z. Hussein, S. Fakurazi, G. Pastorin, Release of a liver anticancer drug, sorafenib from its PVA/LDH- and PEG/LDH-coated iron oxide nanoparticles for drug delivery applications, *Sci Rep* 10 (2020) 1–19. <https://doi.org/10.1038/s41598-020-76504-5>.
- [77] M. Khalkhali, S. Sadighian, K. Rostamizadeh, F. Khoeini, M. Naghibi, N. Bayat, M. Habibzadeh, M. Hamidi, Synthesis and characterization of dextran coated magnetite nanoparticles for diagnostics and therapy, *Bioimpacts* 5 (2015) 141–150. <https://doi.org/10.15171/bi.2015.19>.

- [78] Mazaher A., Iron oxide nanoparticles for delivery purposes, in: M. Mozafari (Ed.), *Nanoengineered Biomaterials for Advanced Drug Delivery*, Elsevier, San Diego, 2020, pp. 373–393.
- [79] C.S.N. de, J. Snir, C. Willert, R. Rohani, R. Foley, P.J. Foster, G.A. Dekaban, Labelling dendritic cells with SPIO has implications for their subsequent in vivo migration as assessed with cellular MRI, *Contrast Media Mol. Imaging* 6 (2011). <https://doi.org/10.1002/cmml.433>.
- [80] S. Santosh, P. Podaralla, B. Miller, Anaphylaxis with elevated serum tryptase after administration of intravenous ferumoxytol, *NDT plus* 3 (2010). <https://doi.org/10.1093/ndtplus/sfq084>.
- [81] Pharmacosmos, Carboxymethyl-Dextran, 2022. <https://www.dextran.com/about-dextran/dextran-chemistry/carboxymethyl-dextran> (accessed 14 September 2022).
- [82] M. Peng, H. Li, Z. Luo, J. Kong, Y. Wan, L. Zheng, Q. Zhang, H. Niu, A. Vermorken, W. van de Ven, C. Chen, X. Zhang, F. Li, L. Guo, Y. Cui, Dextran-coated superparamagnetic nanoparticles as potential cancer drug carriers in vivo, *Nanoscale* 7 (2015) 11155–11162. <https://doi.org/10.1039/c5nr01382h>.
- [83] H. Unterweger, D. Subatzus, R. Tietze, C. Janko, C. Alexiou, Hypericin-bearing magnetic iron oxide nanoparticles for selective drug delivery in photodynamic therapy, *Int. J. Nanomed.* 10 (2015) 6985. <https://doi.org/10.2147/IJN.S92336>.
- [84] V. Ayala, A.P. Herrera, M. Latorre-Esteves, M. Torres-Lugo, C. Rinaldi, Effect of surface charge on the colloidal stability and in vitro uptake of carboxymethyl dextran-coated iron oxide nanoparticles, *J Nanopart Res* 15 (2013) 1874–. <https://doi.org/10.1007/s11051-013-1874-0>.
- [85] S. Ning, Q. Huang, X. Sun, C. Li, Y. Zhang, J. Li, Y.-N. Liu, Carboxymethyl dextran-coated liposomes: Toward a robust drug delivery platform, *Soft Matter* 7 (2011) 9394. <https://doi.org/10.1039/c1sm05814b>.
- [86] J.W. Lee, D.K. Kim, Carboxymethyl group activation of dextran cross-linked superparamagnetic iron oxide nanoparticles, *J. Korean Ceram. Soc.* 58 (2021) 106–115. <https://doi.org/10.1007/s43207-020-00077-2>.
- [87] E.A. Dubiel, C. Kuehn, R. Wang, P. Vermette, In vitro morphogenesis of PANC-1 cells into islet-like aggregates using RGD-covered dextran derivative surfaces, *Colloids Surf. B: Biointerfaces* 89 (2012). <https://doi.org/10.1016/j.colsurfb.2011.09.003>.
- [88] J. Li, Y. Zhou, M. Li, N. Xia, Q. Huang, H. Do, Y.N. Liu, F. Zhou, Carboxymethylated dextran-coated magnetic iron oxide nanoparticles for regenerable bioseparation, *J. Nanosci. Nanotechnol* 11 (2011). <https://doi.org/10.1166/jnn.2011.5002>.
- [89] K. Vasić, Ž. Knez, E.A. Konstantinova, A.I. Kokorin, S. Gyergyek, M. Leitgeb, Structural and magnetic characteristics of carboxymethyl dextran coated magnetic nanoparticles: From characterization to immobilization application, *React. Funct. Polym.* 148 (2020) 104481. <https://doi.org/10.1016/j.reactfunctpolym.2020.104481>.
- [90] M. Das, E.A. Oyarzabal, L. Chen, S.-H. Lee, N. Shah, G. Gerlach, W. Zhang, T.-H.H. Chao, N. van den Berge, C. Liu, C. Donley, S.A. Montgomery, Y.-Y.I. Shih, One-pot synthesis of carboxymethyl-dextran coated iron oxide nanoparticles (CION) for preclinical fMRI and MRA applications, *Neuroimage* 238 (2021) 118213. <https://doi.org/10.1016/j.neuroimage.2021.118213>.
- [91] X. Jiang, C. He, W. Lin, Supramolecular metal-based nanoparticles for drug delivery and cancer therapy, *Curr. Opin. Chem. Biol.* 61 (2021) 143–153. <https://doi.org/10.1016/j.cbpa.2021.01.005>.

- [92] H. Li, E. Peng, F. Zhao, J. Li, J. Xue, Supramolecular Surface Functionalization of Iron Oxide Nanoparticles with α -Cyclodextrin-Based Cationic Star Polymer for Magnetically-Enhanced Gene Delivery, *Pharmaceutics* 13 (2021). <https://doi.org/10.3390/pharmaceutics13111884>.
- [93] S. Philip, S. Kuriakose, Synthesis of Superparamagnetic Iron Oxide Nanoparticles Stabilized by Biocompatible Supramolecular β -Cyclodextrin for Biomedical Applications, *Mater. Today: Proc.* 11 (2019) 1030–1035. <https://doi.org/10.1016/j.matpr.2018.12.034>.
- [94] J. Li, D.J. Mooney, Designing hydrogels for controlled drug delivery, *Nat Rev Mater* 1 (2016) 1–17. <https://doi.org/10.1038/natrevmats.2016.71>.
- [95] A.M. Butt, Amin, M. C. I. M., H. Katas, N. Sarisuta, W. Witoonsaridsilp, R. Benjakul, In Vitro Characterization of Pluronic F127 and D--Tocopheryl Polyethylene Glycol 1000 Succinate Mixed Micelles as Nanocarriers for Targeted Anticancer-Drug Delivery, *J. Nanomater.* 2012 (2012) 1–11. <https://doi.org/10.1155/2012/916573>.
- [96] Y. Zhang, Y. Sun, X. Yang, J. Hilborn, D. A Ossipov, Injectable In Situ Forming Hybrid Iron Oxide-Hyaluronic Acid Hydrogel for Magnetic Resonance Imaging and Drug Delivery, *Macromol. Biosci.* 14 (2014). <https://doi.org/10.1002/mabi.201400117>.
- [97] M. Schenone, V. Dančik, B.K. Wagner, P.A. Clemons, Target identification and mechanism of action in chemical biology and drug discovery, *Nat. Chem. Biol* 9 (2013) 232–240. <https://doi.org/10.1038/nchembio.1199>.
- [98] Ahmad N., M.R. Zakaria, Oligosaccharide From Hemicellulose, in: H.M. Ali, H. Ariffin, S.M. Sapuan (Eds.), *Lignocellulose for future bioeconomy*, Elsevier, Amsterdam, 2019, pp. 135–152.
- [99] Z. Sun, C. Song, C. Wang, Y. Hu, J. Wu, Hydrogel-Based Controlled Drug Delivery for Cancer Treatment: A Review, *Mol. Pharm.* 17 (2020) 373–391. <https://doi.org/10.1021/acs.molpharmaceut.9b01020>.
- [100] P. Thoniyot, M.J. Tan, A.A. Karim, D.J. Young, X.J. Loh, Nanoparticle-Hydrogel Composites: Concept, Design, and Applications of These Promising, Multi-Functional Materials, *Adv. Sci. (Weinh.)* 2 (2015) 1400010. <https://doi.org/10.1002/advs.201400010>.
- [101] L.C. Gonçalves, A.B. Seabra, M.T. Pelegrino, D.R. de Araujo, J.S. Bernardes, P.S. Haddad, Superparamagnetic iron oxide nanoparticles dispersed in Pluronic F127 hydrogel: potential uses in topical applications, *RSC Adv.* 7 (2017) 14496–14503. <https://doi.org/10.1039/C6RA28633J>.
- [102] W. Zhao, K. Odelius, U. Edlund, C. Zhao, A.-C. Albertsson, In Situ Synthesis of Magnetic Field-Responsive Hemicellulose Hydrogels for Drug Delivery, *Biomacromolecules* 16 (2015) 2522–2528. <https://doi.org/10.1021/acs.biomac.5b00801>.
- [103] N.V. Mdlovu, F.A. Mavuso, K.-S. Lin, T.-W. Chang, Y. Chen, S.S.-S. Wang, C.-M. Wu, N.B. Mdlovu, Y.-S. Lin, Iron oxide-pluronic F127 polymer nanocomposites as carriers for a doxorubicin drug delivery system, *Colloids Surf. A Physicochem. Eng. Asp.* 562 (2019) 361–369. <https://doi.org/10.1016/j.colsurfa.2018.11.052>.
- [104] W. Gonciarz, Ł. Lechowicz, M. Urbaniak, W. Kaca, M. Chmiela, Use of Fourier-Transform Infrared Spectroscopy (FT-IR) for Monitoring Experimental *Helicobacter pylori* Infection and Related Inflammatory Response in Guinea Pig Model, *Int. J. Mol. Sci.* 22 (2021) 281. <https://doi.org/10.3390/ijms22010281>.
- [105] K. Sato, M. Seimiya, Y. Kodera, A. Kitamura, F. Nomura, Application of Fourier-transform infrared (FT-IR) spectroscopy for simple and easy determination of chylomicron-triglyceride and very low density lipoprotein-triglyceride, *Clinica Chimica Acta* 411 (2010). <https://doi.org/10.1016/j.cca.2009.11.026>.

- [106] H. Günzler, IR-Spektroskopie: Eine Einführung, fourth., vollständig überarbeitete und aktualisierte Aufl (Online-Ausg.), Wiley-VCH GmbH & Co. KGaA, Weinheim, 2003.
- [107] T. Hecht, Physikalische Grundlagen der IR-Spektroskopie: Von Mechanischen Schwingungen Zur Vorhersage und Interpretation Von IR-Spektren, Springer Vieweg. in Springer Fachmedien Wiesbaden GmbH, Wiesbaden, 2019.
- [108] A. Bartošová, L. Blinová, M. Sirotiak, A. Michalíková, Usage of FTIR-ATR as Non-Destructive Analysis of Selected Toxic Dyes, Res. Papers Faculty of Mater. Sci. Technol. Slovak University of Technology 25 (2017) 103–111. <https://doi.org/10.1515/rput-2017-0012>.
- [109] D.J. Gardiner (Ed.), Practical Raman spectroscopy: With 11 tables, Springer, Berlin, Heidelberg, 1989.
- [110] G.G. Hammes, Spectroscopy for the biological sciences, Wiley-Interscience, Hoboken, N.J., 2005.
- [111] D.A. Long, The Raman Effect, John Wiley & Sons, Ltd, Chichester, UK, 2002.
- [112] N. Saadatkah, A. Carillo Garcia, S. Ackermann, P. Leclerc, M. Latifi, S. Samih, G.S. Patience, J. Chaouki, Experimental methods in chemical engineering: Thermogravimetric analysis—TGA, Can J Chem Eng 98 (2020) 34–43. <https://doi.org/10.1002/cjce.23673>.
- [113] A.A. Dongargaonkar, J.D. Clogston, Quantitation of Surface Coating on Nanoparticles Using Thermogravimetric Analysis, Methods Mol. Biol. 1682 (2018). https://doi.org/10.1007/978-1-4939-7352-1_6.
- [114] Zaitsev, Filimonov, Presnyakov, Gambino, Chu, Physical and Chemical Properties of Magnetite and Magnetite-Polymer Nanoparticles and Their Colloidal Dispersions, J. Colloid Interface Sci. 212 (1999) 49–57. <https://doi.org/10.1006/jcis.1998.5993>.
- [115] Friedrich W, Knipping P, von Laue M, Interferenz-Erscheinungen bei Röntgenstrahlen: Sitzungsberichte der Mathematisch-Physikalischen Classe der Königlich-Bayerischen Akademie der Wissenschaften zu München, first ed., Verl. d. Königl. Byer. Akad. d Wiss., München, 1912.
- [116] A.W. Nicol, X-ray Diffraction, in: A.W. Nicol (Ed.), Physicochemical Methods of Mineral Analysis, Springer US, Boston, MA, 1975, pp. 249–320.
- [117] W.L. BRAGG, The Specular Reflection of X-rays, Nature 90 (1912) 410. <https://doi.org/10.1038/090410b0>.
- [118] W. L. Bragg, The structure of some crystals as indicated by their diffraction of X-rays, Proc. R. Soc. Lond. A 89 (1913) 248–277. <https://doi.org/10.1098/rspa.1913.0083>.
- [119] B.D. Cullity, S.R. Stock, Elements of X-ray diffraction, third. ed., internat. ed., Pearson/Prentice Hall, Upper Saddle River, NJ, 2001.
- [120] R. Jenkins, Introduction to X-Ray Powder Diffractometry, Wiley, New York, 2012.
- [121] B.J. Inkson, Scanning electron microscopy (SEM) and transmission electron microscopy (TEM) for materials characterization, in: G. Hübschen, H.-G. Herrmann, I. Altpeter, R. Tschuncky (Eds.), Materials characterization using nondestructive evaluation (NDE) methods, Elsevier/WP Woodhead Publishing, Amsterdam, Boston, Cambridge, 2016, pp. 17–43.
- [122] L. Reimer, Transmission Electron Microscopy: Physics of Image Formation, fifthth ed., Springer New York, New York, NY, 2008.
- [123] J. Wagner, Teilchengrößen-Bestimmung mittels dynamischer Lichtstreuung, Chem. Ing. Tech. 58 (1986) 578–583. <https://doi.org/10.1002/cite.330580708>.

- [124] K.A. Dill, S. Bromberg, *Molecular driving forces: Statistical thermodynamics in chemistry and biology*, Garland, New York, London, 2003.
- [125] W. Sutherland, LXXV. A dynamical theory of diffusion for non-electrolytes and the molecular mass of albumin, *London Edinburgh Philos. Mag. J. Sci.* 9 (1905) 781–785. <https://doi.org/10.1080/14786440509463331>.
- [126] A. Bootz, V. Vogel, D. Schubert, J. Kreuter, Comparison of scanning electron microscopy, dynamic light scattering and analytical ultracentrifugation for the sizing of poly(butyl cyanoacrylate) nanoparticles, *Eur. J. Pharm. Biopharm.* 57 (2004) 369–375. [https://doi.org/10.1016/S0939-6411\(03\)00193-0](https://doi.org/10.1016/S0939-6411(03)00193-0).
- [127] A. Kumar, C.K. Dixit, Methods for characterization of nanoparticles, in: N. Gupta, R. Chan, S. Nimesh (Eds.), *Advances in nanomedicine for the delivery of therapeutic nucleic acids*, Woodhead Publishing, Duxford, 2017, pp. 43–58.
- [128] Sieu-nhan-kem-xoi, Unknow (14 April 2018).
- [129] O. Stern, ZUR THEORIE DER ELEKTROLYTISCHEN DOPPELSCHICHT, *Z. Elektrochem. angew. phys. Chem.* 30 (1924) 508–516. <https://doi.org/10.1002/bbpc.192400182>.
- [130] D.L. Chapman, LI. A contribution to the theory of electrocapillarity, *Lond. Edinb. Dublin Philos. Mag.* 25 (1913) 475–481. <https://doi.org/10.1080/14786440408634187>.
- [131] C.N. Lunardi, A.J. Gomes, F.S. Rocha, J.d. T., G.S. Patience, Experimental methods in chemical engineering: Zeta potential, *Can J Chem Eng* 99 (2021) 627–639. <https://doi.org/10.1002/cjce.23914>.
- [132] E.J.W. VERWEY, Theory of the stability of lyophobic colloids, *J Phys Colloid Chem* 51 (1947) 631–636. <https://doi.org/10.1021/j150453a001>.
- [133] B. Derjaguin, L. Landau, Theory of the stability of strongly charged lyophobic sols and of the adhesion of strongly charged particles in solutions of electrolytes, *Prog. Surf. Sci.* 43 (1993) 30–59. [https://doi.org/10.1016/0079-6816\(93\)90013-L](https://doi.org/10.1016/0079-6816(93)90013-L).
- [134] T. Hiemstra, W.H. van Riemsdijk, A Surface Structural Approach to Ion Adsorption: The Charge Distribution (CD) Model, *J. Colloid Interface Sci.* 179 (1996) 488–508. <https://doi.org/10.1006/jcis.1996.0242>.
- [135] J.J. Spitzer, A consistent alternative to the dlvo theory, *The Journal of Adhesion* 79 (2003) 893–903. <https://doi.org/10.1080/714906147>.
- [136] N. Hwang, A. R. Barron, BET surface area analysis of nanoparticles, OpenStax-CNX (2011).
- [137] S. Lowell, J.E. Shields, M.A. Thomas, M. Thommes, Surface Area Analysis from the Langmuir and BET Theories, in: W. L. Bragg (Ed.), *Characterization of Porous Solids and Powders: Surface Area, Pore Size and Density*, Springer, Dordrecht, 2004, pp. 58–81.
- [138] W. Buckel, *Supraleitung: Grundlagen und Anwendungen*, fifth., überarb. und. erg. Aufl., VCH, Weinheim, 1994.
- [139] C.M. Thiele, Magnetische Resonanz im Erdmagnetfeld oder darunter, *Angew. Chem.* 119 (2007) 4904–4909. <https://doi.org/10.1002/ange.200700730>.
- [140] S. Foner, Versatile and Sensitive Vibrating-Sample Magnetometer, *Review of Scientific Instruments* 30 (1959) 548–557. <https://doi.org/10.1063/1.1716679>.
- [141] L. Wittmann, C. Turrina, S.P. Schwaminger, The Effect of pH and Viscosity on Magnetophoretic Separation of Iron Oxide Nanoparticles, *Magnetochemistry* 7 (2021) 80. <https://doi.org/10.3390/magnetochemistry7060080>.

- [142] D.M. Kuhn, M. Balkis, J. Chandra, P.K. Mukherjee, M.A. Ghannoum, Uses and limitations of the XTT assay in studies of *Candida* growth and metabolism, *J. Clin. Microbiol.* 41 (2003) 506–508. <https://doi.org/10.1128/JCM.41.1.506-508.2003>.
- [143] F.P. Altman, Tetrazolium salts and formazans, *Progress in histochemistry and cytochemistry* 9 (1976). [https://doi.org/10.1016/s0079-6336\(76\)80015-0](https://doi.org/10.1016/s0079-6336(76)80015-0).
- [144] D.M. Kuhn, T. George, J. Chandra, P.K. Mukherjee, M.A. Ghannoum, Antifungal susceptibility of *Candida* biofilms: unique efficacy of amphotericin B lipid formulations and echinocandins, *Antimicrob. Agents Chemother.* 46 (2002) 1773–1780. <https://doi.org/10.1128/AAC.46.6.1773-1780.2002>.
- [145] T. L. Riss, R. A. Moravec, A. L. Niles, S. Duellman, H. A. Benink, T. J. Worzella, L. Minor, Cell Viability Assays, in: T.L. Riss, R.A. Moravec, A.L. Niles, S. Duellman, H. A. Benink, T.J. Worzella, L. Minor (Eds.), *Assay Guidance Manual* [Internet], Eli Lilly & Company and the National Center for Advancing Translational Sciences, 2016.
- [146] M. J. Stoddart (Ed.), *Mammalian Cell Viability: Methods and Protocols*, Humana Press, 2011.
- [147] P. Stiefel, S. Schmidt-Emrich, K. Maniura-Weber, Q. Ren, Critical aspects of using bacterial cell viability assays with the fluorophores SYTO9 and propidium iodide, *BMC Microbiol.* 15 (2015) 36. <https://doi.org/10.1186/s12866-015-0376-x>.
- [148] D.J. Arndt-Jovin, T.M. Jovin, Chapter 16 Fluorescence Labeling and Microscopy of DNA, in: Y.-l. Wang, D.L. Taylor (Eds.), *Fluorescence microscopy of living cells in culture*, Academic Press, San Diego, 2011, pp. 417–448.
- [149] R.W. Foley, A. Wiek, Scenarios of nanotechnology innovation vis-à-vis sustainability challenges, *Futures* 64 (2014) 1–14. <https://doi.org/10.1016/j.futures.2014.09.005>.
- [150] A. Drenkova-Tuhtan, K. Mandel, A. Paulus, C. Meyer, F. Hutter, C. Gellermann, G. SEXTL, M. Franzreb, H. Steinmetz, Phosphate recovery from wastewater using engineered superparamagnetic particles modified with layered double hydroxide ion exchangers, *Water Res.* 47 (2013) 5670–5677. <https://doi.org/10.1016/j.watres.2013.06.039>.
- [151] M. Takafuji, S. Ide, H. Ihara, Z. Xu, Preparation of Poly(1-vinylimidazole)-Grafted Magnetic Nanoparticles and Their Application for Removal of Metal Ions, *Chem. Mater.* 16 (2004) 1977–1983. <https://doi.org/10.1021/cm030334y>.
- [152] P.V. Nidheesh, Heterogeneous Fenton catalysts for the abatement of organic pollutants from aqueous solution: a review, *RSC Adv.* 5 (2015) 40552–40577. <https://doi.org/10.1039/C5RA02023A>.
- [153] M.B. Gawande, P.S. Branco, R.S. Varma, Nano-magnetite (Fe₃O₄) as a support for recyclable catalysts in the development of sustainable methodologies, *Chem. Soc. Rev.* 42 (2013) 3371–3393. <https://doi.org/10.1039/c3cs35480f>.
- [154] A. Csáki, M. Thiele, J. Jatschka, A. Dathe, D. Zopf, O. Stranik, W. Fritzsche, Plasmonic nanoparticle synthesis and bioconjugation for bioanalytical sensing, *Eng. Life Sci.* 15 (2015) 266–275. <https://doi.org/10.1002/elsc.201400075>.
- [155] B. Li, H. Cao, J. Shao, M. Qu, J.H. Warner, Superparamagnetic Fe₃O₄ nanocrystals@graphene composites for energy storage devices, *J. Mater. Chem.* 21 (2011) 5069. <https://doi.org/10.1039/c0jm03717f>.
- [156] P. Tartaj, M.P. Morales, T. Gonzalez-Carreño, S. Veintemillas-Verdaguer, C.J. Serna, The iron oxides strike back: from biomedical applications to energy storage devices and photoelectrochemical water splitting, *Adv. Mater.* 23 (2011) 5243–5249. <https://doi.org/10.1002/adma.201101368>.

- [157] R. Bayford, T. Rademacher, I. Roitt, S.X. Wang, Emerging applications of nanotechnology for diagnosis and therapy of disease: a review, *Physiol. Meas.* 38 (2017) R183-R203. <https://doi.org/10.1088/1361-6579/aa7182>.
- [158] A.I. Archakov, Nanobiotechnologies in medicine: Nanodiagnostics and nanodrugs, *Biochem. Moscow Suppl. Ser. B* 4 (2010) 2–14. <https://doi.org/10.1134/S1990750810010026>.
- [159] O. Zitka, M. Ryvolova, J. Hubalek, T. Eckschlager, V. Adam, R. Kizek, From amino acids to proteins as targets for metal-based drugs, *Curr. Drug Metab.* 13 (2012) 306–320. <https://doi.org/10.2174/138920012799320437>.
- [160] P.V. Baptista, Nanodiagnostics: leaving the research lab to enter the clinics?, *Diagnosis (Berl)* 1 (2014) 305–309. <https://doi.org/10.1515/dx-2014-0055>.
- [161] N. Naseri, E. Ajarlou, F. Asghari, Y. Pilehvar-Soltanahmadi, An update on nanoparticle-based contrast agents in medical imaging, *Artif. Cells Nanomed. Biotechnol.* 46 (2018) 1111–1121. <https://doi.org/10.1080/21691401.2017.1379014>.
- [162] M.J. Sands, A. Levitin, Basics of magnetic resonance imaging, *Semin Vasc Surg* 17 (2004) 66–82. <https://doi.org/10.1053/j.semvascsurg.2004.03.011>.
- [163] J.M. Tognarelli, M. Dawood, M.I.F. Shariff, V.P.B. Grover, M.M.E. Crossey, I.J. Cox, S.D. Taylor-Robinson, M.J.W. McPhail, Magnetic Resonance Spectroscopy: Principles and Techniques: Lessons for Clinicians, *J Clin Exp Hepatol* 5 (2015) 320–328. <https://doi.org/10.1016/j.jceh.2015.10.006>.
- [164] D.H. Lee, Mechanisms of contrast enhancement in magnetic resonance imaging, *Can. Assoc. Radiol* 42 (1991) 6–12.
- [165] M. Rogosnitzky, S. Branch, Gadolinium-based contrast agent toxicity: a review of known and proposed mechanisms, *Biomaterials* 29 (2016) 365–376. <https://doi.org/10.1007/s10534-016-9931-7>.
- [166] M.J. Akhtar, M. Ahamed, H.A. Alhadlaq, Immunotoxic potential of nanoparticles of cerium oxide and gadolinium oxide in human monocyte (THP-1) cells, *J. King Saud Univ. Sci.* 34 (2022) 102291. <https://doi.org/10.1016/j.jksus.2022.102291>.
- [167] European Medicine Agency (Ed.), EMA/457616/2017, European Medicine Agency, London, 2017.
- [168] H. Unterweger, L. Dézsi, J. Matuszak, C. Janko, M. Poettler, J. Jordan, T. Bäuerle, J. Szebeni, T. Fey, A.R. Boccaccini, C. Alexiou, I. Cicha, Dextran-coated superparamagnetic iron oxide nanoparticles for magnetic resonance imaging: evaluation of size-dependent imaging properties, storage stability and safety, *Int. J. Nanomed.* 13 (2018) 1899–1915. <https://doi.org/10.2147/IJN.S156528>.
- [169] Philips, Forschungsinitiative Magnetic Particle Imaging - Erstes industriell gefertigtes System am UKE installiert, 2014. https://www.philips.de/a-w/about/news/archive/standard/news/healthcare/20140710_Forschungsinitiative_Magnetic_Particle_Imaging.html (accessed 19 October 2022).
- [170] J. Haegele, T. Sattel, M. Erbe, K. Luedtke-Buzug, M. Taupitz, J. Borgert, T.M. Buzug, J. Barkhausen, F.M. Vogt, Magnetic Particle Imaging (MPI), *Rofo* 184 (2012) 420–426. <https://doi.org/10.1055/s-0031-1281981>.
- [171] T. Knopp, N. Gdaniec, M. Möddel, Magnetic particle imaging: from proof of principle to preclinical applications, *Phys. Med. Biol.* 62 (2017) R124-R178. <https://doi.org/10.1088/1361-6560/aa6c99>.
- [172] P. Vogel, M.A. Rückert, T. Kampf, V.C. Behr, Highly Flexible and Modular Simulation Framework for Magnetic Particle Imaging, 2022.

- [173] E.Y. Yu, M. Bishop, B. Zheng, R.M. Ferguson, A.P. Khandhar, S.J. Kemp, K.M. Krishnan, P.W. Goodwill, S.M. Conolly, Magnetic Particle Imaging: A Novel in Vivo Imaging Platform for Cancer Detection, *Nano Lett* 17 (2017) 1648–1654. <https://doi.org/10.1021/acs.nanolett.6b04865>.
- [174] F. Ludwig, E. Heim, S. Mäuselein, D. Eberbeck, M. Schilling, Magnetorelaxometry of magnetic nanoparticles with fluxgate magnetometers for the analysis of biological targets, *J. Magn. Magn. Mater.* 293 (2005) 690–695. <https://doi.org/10.1016/j.jmmm.2005.02.045>.
- [175] R.W. Chantrell, S.R. Hoon, B.K. Tanner, Time-dependent magnetization in fine-particle ferromagnetic systems, *J. Magn. Magn. Mater.* 38 (1983) 133–141. [https://doi.org/10.1016/0304-8853\(83\)90037-9](https://doi.org/10.1016/0304-8853(83)90037-9).
- [176] S. Knappe, T.H. Sander, O. Kosch, F. Wiekhorst, J. Kitching, L. Trahms, Cross-validation of microfabricated atomic magnetometers with superconducting quantum interference devices for biomagnetic applications, *Appl. Phys. Lett.* 97 (2010) 133703. <https://doi.org/10.1063/1.3491548>.
- [177] A. Jaufenthaler, P. Schier, T. Middelmann, M. Liebl, F. Wiekhorst, D. Baumgarten, Quantitative 2D Magnetorelaxometry Imaging of Magnetic Nanoparticles using Optically Pumped Magnetometers, *Sensors (Basel)* 20 (2020). <https://doi.org/10.3390/s20030753>.
- [178] L.E. Cole, R.D. Ross, J. Tilley, T. Vargo-Gogola, R.K. Roeder, Gold nanoparticles as contrast agents in x-ray imaging and computed tomography, *Nanomedicine (Lond.)* 10 (2015) 321–341. <https://doi.org/10.2217/nnm.14.171>.
- [179] A.J. Mieszawska, W.J.M. Mulder, Z.A. Fayad, D.P. Cormode, Multifunctional gold nanoparticles for diagnosis and therapy of disease, *Mol. Pharm.* 10 (2013) 831–847. <https://doi.org/10.1021/mp3005885>.
- [180] T. Jones, D. Townsend, History and future technical innovation in positron emission tomography, *J. Med. Imaging* 4 (2017) 11013. <https://doi.org/10.1117/1.JMI.4.1.011013>.
- [181] S. Goel, C.G. England, F. Chen, W. Cai, Positron emission tomography and nanotechnology: A dynamic duo for cancer theranostics, *Adv. Drug Deliv. Rev.* 113 (2017) 157–176. <https://doi.org/10.1016/j.addr.2016.08.001>.
- [182] D.L.J. Thorek, D. Ulmert, N.-F.M. Diop, M.E. Lupu, M.G. Doran, R. Huang, D.S. Abou, S.M. Larson, J. Grimm, Non-invasive mapping of deep-tissue lymph nodes in live animals using a multimodal PET/MRI nanoparticle, *Nat Commun* 5 (2014) 1–9. <https://doi.org/10.1038/ncomms4097>.
- [183] M. Silindir, A.Y. Özer, S. Erdoğan, The use and importance of liposomes in positron emission tomography, *Drug Deliv.* 19 (2012) 68–80. <https://doi.org/10.3109/10717544.2011.635721>.
- [184] L.S. Biswaro, da Costa Sousa, M. G., T.M.B. Rezende, S.C. Dias, O.L. Franco, Antimicrobial Peptides and Nanotechnology, Recent Advances and Challenges, *Front. Microbiol.* 9 (2018) 855. <https://doi.org/10.3389/fmicb.2018.00855>.
- [185] I.X. Yin, J. Zhang, I.S. Zhao, M.L. Mei, Q. Li, C.H. Chu, The Antibacterial Mechanism of Silver Nanoparticles and Its Application in Dentistry, *Int. J. Nanomed.* 15 (2020) 2555–2562. <https://doi.org/10.2147/IJN.S246764>.
- [186] P.K. Deb, H.M.A. Odetallah, B. Al-Jaidi, R.R. Akkinepalli, A. Al-Aboudi, R.K. Tekade, Biomaterials and Nanoparticles for Hyperthermia Therapy, in: R.K. Tekade (Ed.), *Biomaterials and Bio-Nanotechnology*, Elsevier Science & Technology, San Diego, 2019, pp. 375–413.
- [187] L.C. Kennedy, L.R. Bickford, N.A. Lewinski, A.J. Coughlin, Y. Hu, E.S. Day, J.L. West, R.A. Drezek, A new era for cancer treatment: gold-nanoparticle-mediated thermal therapies, *Small (Weinheim)* 7 (2011) 169–183. <https://doi.org/10.1002/sml.201000134>.

- [188] K. McNamara, S.A.M. Tofail, Nanosystems: the use of nanoalloys, metallic, bimetallic, and magnetic nanoparticles in biomedical applications, *Phys. Chem. Chem. Phys.* 17 (2015) 27981–27995. <https://doi.org/10.1039/c5cp00831j>.
- [189] G.v. Maltzahn, J.-H. Park, A. Agrawal, N.K. Bandaru, S.K. Das, M.J. Sailor, S.N. Bhatia, Computationally guided photothermal tumor therapy using long-circulating gold nanorod antennas, *Cancer Res.* 69 (2009) 3892–3900. <https://doi.org/10.1158/0008-5472.CAN-08-4242>.
- [190] J.-T. Jang, J. Lee, J. Seon, E. Ju, M. Kim, Y.I. Kim, M.G. Kim, Y. Takemura, A.S. Arbab, K.W. Kang, K.H. Park, S.H. Paek, S. Bae, Giant Magnetic Heat Induction of Magnesium-Doped γ -Fe₂O₃ Superparamagnetic Nanoparticles for Completely Killing Tumors, *Adv. Mater.* 30 (2018). <https://doi.org/10.1002/adma.201704362>.
- [191] G. Hemery, C. Genevois, F. Couillaud, S. Lacomme, E. Gontier, E. Ibarboure, S. Lecommandoux, E. Garanger, O. Sandre, Monocore vs. multicore magnetic iron oxide nanoparticles: uptake by glioblastoma cells and efficiency for magnetic hyperthermia, *Mol. Syst. Des. Eng.* 2 (2017) 629–639. <https://doi.org/10.1039/C7ME00061H>.
- [192] A. Tewabe, A. Abate, M. Tamrie, A. Seyfu, E. Abdela Siraj, Targeted Drug Delivery - From Magic Bullet to Nanomedicine: Principles, Challenges, and Future Perspectives, *J. Multidiscip. Healthc* 14 (2021) 1711–1724. <https://doi.org/10.2147/JMDH.S313968>.
- [193] A. Kumar, Nanomedicine in drug delivery, CRC Press/Taylor & Francis Group, Boca Raton, Fla., 2013.
- [194] T. Sun, Y.S. Zhang, B. Pang, D.C. Hyun, M. Yang, Y. Xia, Engineered nanoparticles for drug delivery in cancer therapy, *Angew. Chem. Int. Ed.* 53 (2014) 12320–12364. <https://doi.org/10.1002/anie.201403036>.
- [195] K. Cheng, S. Peng, C. Xu, S. Sun, Porous hollow Fe₃O₄ nanoparticles for targeted delivery and controlled release of cisplatin, *J. Am. Chem. Soc.* 131 (2009) 10637–10644. <https://doi.org/10.1021/ja903300f>.
- [196] J. Kost, R. Langer, Responsive polymeric delivery systems, *Adv. Drug Deliv. Rev.* 46 (2001) 125–148. [https://doi.org/10.1016/S0169-409X\(00\)00136-8](https://doi.org/10.1016/S0169-409X(00)00136-8).
- [197] J. Yoo, C. Park, G. Yi, D. Lee, H. Koo, Active Targeting Strategies Using Biological Ligands for Nanoparticle Drug Delivery Systems, *Cancers (Basel)* 11 (2019). <https://doi.org/10.3390/cancers11050640>.
- [198] Y.-L. Liu, D. Chen, P. Shang, D.-C. Yin, A review of magnet systems for targeted drug delivery, *J. Control Release* 302 (2019) 90–104. <https://doi.org/10.1016/j.jconrel.2019.03.031>.
- [199] P.H. MEYERS, F. CRONIC, C.M. NICE, Experimental approach in the use and magnetic control of metallic iron particles in the lymphatic and vascular system of dogs as a contrast and isotopic agent, *Am. J. Roentgenol. Radium Ther. Nucl. Med.* 90 (1963) 1068–1077.
- [200] Y.-P. Wang, Y.-T. Liao, C.-H. Liu, J. Yu, H.R. Alamri, Z.A. Alothman, M.S.A. Hossain, Y. Yamauchi, K.C.-W. Wu, Trifunctional Fe₃O₄/CaP/Alginate Core-Shell-Corona Nanoparticles for Magnetically Guided, pH-Responsive, and Chemically Targeted Chemotherapy, *ACS Biomater. Sci. Eng.* 3 (2017) 2366–2374. <https://doi.org/10.1021/acsbomaterials.7b00230>.
- [201] Y. Qu, J. Li, J. Ren, J. Leng, C. Lin, D. Shi, Enhanced synergism of thermo-chemotherapy by combining highly efficient magnetic hyperthermia with magnetothermally-facilitated drug release, *Nanoscale* 6 (2014) 12408–12413. <https://doi.org/10.1039/c4nr03384a>.
- [202] D. Chenthamara, S. Subramaniam, S.G. Ramakrishnan, S. Krishnaswamy, M.M. Essa, F.-H. Lin, M.W. Qoronfleh, Therapeutic efficacy of nanoparticles and routes of administration, *Biomater. Res.* 23 (2019) 20. <https://doi.org/10.1186/s40824-019-0166-x>.

- [203] H.A. Krebs, Chemical Composition of Blood Plasma and Serum, *Annu. Rev. Biochem.* 19 (1950) 409–430. <https://doi.org/10.1146/annurev.bi.19.070150.002205>.
- [204] W. Xue, Y. Liu, N. Zhang, Y. Yao, P. Ma, H. Wen, S. Huang, Y. Luo, H. Fan, Effects of core size and PEG coating layer of iron oxide nanoparticles on the distribution and metabolism in mice, *Int. J. Nanomed.* 13 (2018) 5719–5731. <https://doi.org/10.2147/IJN.S165451>.
- [205] H. S. Choi, W. Liu, P. Misra, E. Tanaka, J. P. Zimmer, B. I. Ipe, M. G. Bawendi, J. V. Frangioni, Renal clearance of quantum dots, *Nat. Biotechnol.* (2007) 1165–1170.
- [206] H. Maeda, H. Nakamura, J. Fang, The EPR effect for macromolecular drug delivery to solid tumors: Improvement of tumor uptake, lowering of systemic toxicity, and distinct tumor imaging in vivo, *Adv. Drug Deliv. Rev.* 65 (2013) 71–79. <https://doi.org/10.1016/j.addr.2012.10.002>.
- [207] S.D. Conner, S.L. Schmid, Regulated portals of entry into the cell, *Nature* 422 (2003) 37–44. <https://doi.org/10.1038/nature01451>.
- [208] M. Podinovskaia, C. Prescianotto-Baschong, D.P. Buser, A. Spang, A novel live-cell imaging assay reveals regulation of endosome maturation, *Elife* 10 (2021). <https://doi.org/10.7554/eLife.70982>.
- [209] J. Volatron, F. Carn, J. Kolosnjaj-Tabi, Y. Javed, Q.L. Vuong, Y. Gossuin, C. Ménager, N. Luciani, G. Charron, M. Hémadi, D. Alloyeau, F. Gazeau, Ferritin Protein Regulates the Degradation of Iron Oxide Nanoparticles, *Small (Weinheim)* 13 (2017). <https://doi.org/10.1002/sml.201602030>.
- [210] S. Nie, Understanding and overcoming major barriers in cancer nanomedicine, *Nanomedicine (Lond.)* 5 (2010) 523–528. <https://doi.org/10.2217/nmm.10.23>.
- [211] R.A. Revia, M. Zhang, Magnetite nanoparticles for cancer diagnosis, treatment, and treatment monitoring: recent advances, *Mater. Today (Kidlington)* 19 (2016) 157–168. <https://doi.org/10.1016/j.mattod.2015.08.022>.
- [212] M.I. Hutchings, A.W. Truman, B. Wilkinson, Antibiotics: past, present and future, *Curr. Opin. Microbiol.* 51 (2019) 72–80. <https://doi.org/10.1016/j.mib.2019.10.008>.
- [213] WHO Scientific work group, Antimicrobial resistance*, *Bull. World Health Organ.* 61 (1983) 383–394.
- [214] C.J.L. Murray, K.S. Ikuta, F. Sharara, L. Swetschinski, G. Robles A., A. Gray, C. Han, C. Bisignano, P. Rao, E. Wool, S.C. Johnson, et al., Global burden of bacterial antimicrobial resistance in 2019: a systematic analysis, *The Lancet* 399 (2022) 629–655. [https://doi.org/10.1016/S0140-6736\(21\)02724-0](https://doi.org/10.1016/S0140-6736(21)02724-0).
- [215] U. Hofer, The cost of antimicrobial resistance, *Nat. Rev. Microbiol.* 17 (2019) 3. <https://doi.org/10.1038/s41579-018-0125-x>.
- [216] Y. Huan, Q. Kong, H. Mou, H. Yi, Antimicrobial Peptides: Classification, Design, Application and Research Progress in Multiple Fields, *Front. Microbiol.* 11 (2020) 582779. <https://doi.org/10.3389/fmicb.2020.582779>.
- [217] Ferlay J, Ervik M, Lam F, Colombet M, Mery L, Piñeros M, et al., Global Cancer Observatory: Cancer Today., 2020 (accessed 4 November 2022).
- [218] B.A. Chabner, T.G. Roberts, Timeline: Chemotherapy and the war on cancer, *Nat. Rev. Cancer* 5 (2005) 65–72. <https://doi.org/10.1038/nrc1529>.
- [219] V.T. DeVita, E. Chu, A history of cancer chemotherapy, *Cancer Res.* 68 (2008) 8643–8653. <https://doi.org/10.1158/0008-5472.CAN-07-6611>.

- [220] C. Lindley, J.S. McCune, T.E. Thomason, D. Lauder, A. Sauls, S. Adkins, W.T. Sawyer, Perception of chemotherapy side effects cancer versus noncancer patients, *Cancer Pract.* 7 (1999) 59–65. <https://doi.org/10.1046/j.1523-5394.1999.07205.x>.
- [221] Q.-Y. Zhang, Z.-B. Yan, Y.-M. Meng, X.-Y. Hong, G. Shao, J.-J. Ma, X.-R. Cheng, J. Liu, J. Kang, C.-Y. Fu, Antimicrobial peptides: mechanism of action, activity and clinical potential, *Mil. Med. Res.* 8 (2021) 48. <https://doi.org/10.1186/s40779-021-00343-2>.
- [222] University of Nebraska Medical Center, Antimicrobial Peptide Database: APD3, 2022 (accessed 3 November 2022).
- [223] A.A. Baxter, F.T. Lay, I.K.H. Poon, M. Kvensakul, M.D. Hulett, Tumor cell membrane-targeting cationic antimicrobial peptides: novel insights into mechanisms of action and therapeutic prospects, *Cell. Mol. Life Sci.* 74 (2017) 3809–3825. <https://doi.org/10.1007/s00018-017-2604-z>.
- [224] J. Diosa, F. Guzman, C. Bernal, M. Mesa, Formation mechanisms of chitosan-silica hybrid materials and its performance as solid support for KR-12 peptide adsorption: Impact on KR-12 antimicrobial activity and proteolytic stability, *J. Mater. Res. Technol.* 9 (2020) 890–901. <https://doi.org/10.1016/j.jmrt.2019.11.029>.
- [225] F. Costa, C. Teixeira, P. Gomes, M.C.L. Martins, Clinical Application of AMPs, in: K. Matsuzaki (Ed.), *Antimicrobial Peptides: Book Subtitle Basics for Clinical Application*, Springer, Singapore, 2019, pp. 281–298.
- [226] K. Matsuzaki (Ed.), *Antimicrobial Peptides: Book Subtitle Basics for Clinical Application*, Springer, Singapore, 2019.
- [227] V. Cerovský, M. Budesínský, O. Hovorka, J. Cvacka, Z. Voburka, J. Slaninová, L. Borovicková, V. Fucík, L. Bednářová, I. Votruba, J. Straka, Lasioglossins: three novel antimicrobial peptides from the venom of the eusocial bee *Lasioglossum laticeps* (Hymenoptera: Halictidae), *Chembiochem* 10 (2009) 2089–2099. <https://doi.org/10.1002/cbic.200900133>.
- [228] L. Packer, The nesting biology and social organisation of *Lasioglossum (evylaeus) laticeps* (Hymenoptera, Halictidae) in England, *Ins. Soc* 30 (1983) 367–375. <https://doi.org/10.1007/BF02223968>.
- [229] B. Mishra, A. Basu, R. Saravanan, L. Xiang, L.K. Yang, S.S.J. Leong, Lasioglossin-III: antimicrobial characterization and feasibility study for immobilization applications, *RSC Adv.* 3 (2013) 9534. <https://doi.org/10.1039/c3ra40887f>.
- [230] F. Battista, R. O., P. Del Vecchio, R. Winter, L. Petraccone, Insights into the Action Mechanism of the Antimicrobial Peptide Lasioglossin III, *Int. J. Mol. Sci.* 22 (2021). <https://doi.org/10.3390/ijms22062857>.
- [231] S. Saha, P. Ratrey, A. Mishra, Association of Lasioglossin-III Antimicrobial Peptide with Model Lipid Bilayers, *BIOPHYSICS* 67 (2022) 188–199. <https://doi.org/10.1134/S0006350922020178>.
- [232] C. Turrina, S. Berensmeier, S.P. Schwaminger, Bare Iron Oxide Nanoparticles as Drug Delivery Carrier for the Short Cationic Peptide Lasioglossin, *Pharmaceuticals* 14 (2021) 405. <https://doi.org/10.3390/ph14050405>.
- [233] C. Turrina, P.Y.W. Dankers, S. Berensmeier, S. Schwaminger, Iron oxide nanoparticles with supramolecular ureidopyrimidinone coating, *Current Directions in Biomedical Engineering* 8 (2022) 13–16. <https://doi.org/10.1515/cdbme-2022-1004>.
- [234] C. Turrina, D. Milani, A. Klassen, D.M. Rojas-González, J. Cookman, M. Opel, B. Sartori, P. Mela, S. Berensmeier, S.P. Schwaminger, Carboxymethyl-Dextran-Coated Superparamagnetic Iron Oxide Nanoparticles for Drug Delivery: Influence of the Coating Thickness on the Particle Properties, *International Journal of Molecular Sciences* 23 (2022) 14743. <https://doi.org/10.3390/ijms232314743>.

- [235] C. Turrina, A. Oppelt, M. Mitzkus, S. Berensmeier, S.P. Schwaminger, Silica-coated superparamagnetic iron oxide nanoparticles: New insights into the influence of coating thickness on the particle properties and lasioglossin binding, *MRS Communications* 12 (2022) 632–639. <https://doi.org/10.1557/s43579-022-00228-y>.
- [236] C. Turrina, A. Klassen, D. Milani, D. M. Rojas-González, G. Ledinski, D. Auer, B. Sartori, G. Cvirn, P. Mela, S. Berensmeier, S. P. Schwaminger, Screening of superparamagnetic iron oxide nanoparticles for their application in the human body: Influence of various coatings (2023). <https://doi.org/10.26434/chemrxiv-2023-wx78h>.
- [237] C. Turrina, J. Cookman, R. Bellan, P. Y. W. Dankers, S. Berensmeier, S. Schwaminger, Iron oxide nanoparticles with supramolecular ureidopyrimidinone coating for drug delivery: Improved cytocompatibility of the antimicrobial peptide lasioglossin, *Journal of Drug Delivery Science and Technology* (2023).
- [238] D.A. Almasri, N.B. Saleh, M.A. Atich, G. McKay, S. Ahzi, Adsorption of phosphate on iron oxide doped halloysite nanotubes, *Sci. Rep.* 9 (2019) 3232. <https://doi.org/10.1038/s41598-019-39035-2>.
- [239] J.A. Thomas, F. Schnell, Y. Kaveh-Baghbaderani, S. Berensmeier, S.P. Schwaminger, Immunomagnetic Separation of Microorganisms with Iron Oxide Nanoparticles, *Chemosensors* 8 (2020) 17. <https://doi.org/10.3390/chemosensors8010017>.
- [240] S.E. Favela-Camacho, E.J. Samaniego-Benítez, A. Godínez-García, L.M. Avilés-Arellano, J.F. Pérez-Robles, How to decrease the agglomeration of magnetite nanoparticles and increase their stability using surface properties, *Colloids and Surfaces A: Physicochemical and Engineering Aspects* 574 (2019) 29–35. <https://doi.org/10.1016/j.colsurfa.2019.04.016>.
- [241] T.K. Jain, M.A. Morales, S.K. Sahoo, D.L. Leslie-Pelecky, V. Labhasetwar, Iron oxide nanoparticles for sustained delivery of anticancer agents, *Mol. Pharm.* 2 (2005) 194–205. <https://doi.org/10.1021/mp0500014>.
- [242] S.G. Kwon, T. Hyeon, Colloidal chemical synthesis and formation kinetics of uniformly sized nanocrystals of metals, oxides, and chalcogenides, *Acc. Chem. Res.* 41 (2008) 1696–1709. <https://doi.org/10.1021/ar8000537>.
- [243] I.A. Bakhteeva, I.V. Medvedeva, M.A. Uimin, I.V. Byzov, S.V. Zhakov, A.E. Yermakov, N.N. Shchegoleva, Magnetic sedimentation and aggregation of Fe₃O₄@SiO₂ nanoparticles in water medium, *Separation and Purification Technology* 159 (2016) 35–42. <https://doi.org/10.1016/j.seppur.2015.12.043>.
- [244] C. Guo, G.P. Holland, Investigating Lysine Adsorption on Fumed Silica Nanoparticles, *J. Phys. Chem. C* 118 (2014) 25792–25801. <https://doi.org/10.1021/jp508627h>.
- [245] A. Müller-Lissner, Krebsbehandlung: 160.000 Euro pro Lebensjahr, 2007. <https://www.tagesspiegel.de/wissen/160000-euro-pro-lebensjahr-1549435.html> (accessed 12 December 2022).
- [246] V. Sebastian, M. Arruebo, J. Santamaria, Reaction engineering strategies for the production of inorganic nanomaterials, *Small* 10 (2014) 835–853. <https://doi.org/10.1002/sml.201301641>.
- [247] L. Abarca-Cabrera, P. Fraga-García, S. Berensmeier, Bio-nano interactions: binding proteins, polysaccharides, lipids and nucleic acids onto magnetic nanoparticles, *Biomater. Res.* 25 (2021) 12. <https://doi.org/10.1186/s40824-021-00212-y>.
- [248] Millipore, Microsphere Coupling—Two-step EDC/Sulfo NHS Covalent Coupling Procedure for Estapor® Carboxyl-modified Dyed Microspheres. EMD Millipore Corporation: Burlington, Sigma-Aldrich, Application Note (2015).
- [249] P.Y.W. Dankers, T.M. Hermans, T.W. Baughman, Y. Kamikawa, R.E. Kieltyka, M.M.C. Bastings, H.M. Janssen, N.A.J.M. Sommerdijk, A. Larsen, M.J.A. van Luyn, A.W. Bosman, E.R. Popa, G. Fytas, E.W. Meijer, Hierarchical

- formation of supramolecular transient networks in water: a modular injectable delivery system, *Adv. Mater.* 24 (2012) 2703–2709. <https://doi.org/10.1002/adma.201104072>.
- [250] P.J. Besseling, T. Mes, A.W. Bosman, J.W. Peeters, H.M. Janssen, M.H. Bakker, J.O. Fledderus, M. Teraa, M.C. Verhaar, H. Gremmels, P.Y.W. Dankers, The in-vitro biocompatibility of ureido-pyrimidinone compounds and polymer degradation products, *Journal of Polymer Science* 59 (2021) 1267–1277. <https://doi.org/10.1002/pol.20210072>.
- [251] D.L. Sackett, J. Wolff, Nile red as a polarity-sensitive fluorescent probe of hydrophobic protein surfaces, *Anal. Biochem.* 167 (1987) 228–234. [https://doi.org/10.1016/0003-2697\(87\)90157-6](https://doi.org/10.1016/0003-2697(87)90157-6).
- [252] K. Präbst, H. Engelhardt, S. Ringgeler, H. Hübner, Basic Colorimetric Proliferation Assays: MTT, WST, and Resazurin, *Methods in molecular biology* (Clifton, N.J.) 1601 (2017) 1–17. https://doi.org/10.1007/978-1-4939-6960-9_1.
- [253] A.M. Collins, A.M. Donoghue, Viability assessment of honey bee, *Apis mellifera*, sperm using dual fluorescent staining, *Theriogenology* 51 (1999) 1513–1523. [https://doi.org/10.1016/s0093-691x\(99\)00094-1](https://doi.org/10.1016/s0093-691x(99)00094-1).
- [254] J.A. Champion, S. Mitragotri, Shape induced inhibition of phagocytosis of polymer particles, *Pharm. Res.* 26 (2009) 244–249. <https://doi.org/10.1007/s11095-008-9626-z>.
- [255] S.J. Lam, N.M. O'Brien-Simpson, N. Pantarat, A. Sulistio, E.H.H. Wong, Y.-Y. Chen, J.C. Lenzo, J.A. Holden, A. Blencowe, E.C. Reynolds, G.G. Qiao, Combating multidrug-resistant Gram-negative bacteria with structurally nanoengineered antimicrobial peptide polymers, *Nat. Microbiol.* 1 (2016) 16162. <https://doi.org/10.1038/nmicrobiol.2016.162>.
- [256] Dicky Pranantyo, L. Xu, E. Kang, M. Mya, M. Chan-Park, Conjugation of Polyphosphoester and Antimicrobial Peptide for Enhanced Bactericidal Activity and Biocompatibility, undefined (2016).
- [257] S. Zaccaria, R.C. van Gaal, M. Riool, S.A.J. Zaat, P.Y.W. Dankers, Antimicrobial peptide modification of biomaterials using supramolecular additives, *J. Polym. Sci. A Polym. Chem.* 56 (2018) 1926–1934. <https://doi.org/10.1002/pola.29078>.
- [258] A.L. Cortajarena, D. Ortega, S.M. Ocampo, A. Gonzalez-García, P. Couleaud, R. Miranda, C. Belda-Iniesta, A. Ayuso-Sacido, Engineering Iron Oxide Nanoparticles for Clinical Settings, *Nanobiomedicine (Rij)* 1 (2014) 2. <https://doi.org/10.5772/58841>.
- [259] L. Gutiérrez, S. Romero, G.B. da Silva, R. Costo, M.D. Vargas, C.M. Ronconi, C.J. Serna, S. Veintemillas-Verdaguer, M. Del Puerto Morales, Degradation of magnetic nanoparticles mimicking lysosomal conditions followed by AC susceptibility, *Biomed. Tech. (Berl)* 60 (2015) 417–425. <https://doi.org/10.1515/bmt-2015-0043>.
- [260] M. Rabel, P. Warncke, C. Grüttner, C. Bergemann, H.-D. Kurland, R. Müller, V. Dugandžić, J. Thamm, F.A. Müller, J. Popp, D. Cialla-May, D. Fischer, Simulation of the long-term fate of superparamagnetic iron oxide-based nanoparticles using simulated biological fluids, *Nanomedicine (Lond)* 14 (2019) 1681–1706. <https://doi.org/10.2217/nmm-2018-0382>.
- [261] E. Hopkins, T. Sanvictores, S. Sharma (Eds.), *StatPearls* [Internet], StatPearls Publishing, 2022.
- [262] A. Petri-Fink, B. Steitz, A. Finka, J. Salaklang, H. Hofmann, Effect of cell media on polymer coated superparamagnetic iron oxide nanoparticles (SPIONs): colloidal stability, cytotoxicity, and cellular uptake studies, *Eur. J. Pharm. Biopharm.* 68 (2008) 129–137. <https://doi.org/10.1016/j.ejpb.2007.02.024>.

7. Appendix

7.1. Supporting information

7.1.1. Bare iron oxide nanoparticles as drug delivery carrier for the short cationic peptide lasioglossin



Supporting Materials

Bare iron oxide nanoparticles as drug delivery carrier for the short cationic peptide lasioglossin

Chiara Turrina ¹, Sonja Berensmeier ¹ and Sebastian P. Schwaminger ^{1,*}

¹ Bioseparation Engineering Group, Department of Mechanical Engineering, Technical University of Munich

* Correspondence: s.schwaminger@tum.de

Particle characterization

Table S1: BION Size calculation with the Scherrer equation from XRD data, measured with Mo K α . The lattice constant is calculated from the Bragg equation.

2θ	16.01	13.72	19.40	Average
Size	9.07 nm	8.71 nm	9.74 nm	9.17 nm

Scherrer equation:

$$L = \frac{0.89 \cdot 0.07093 \text{ nm}}{42\theta \cdot \cos(\theta)} \tag{S2}$$

Table S2: Modified Langevin fit for SQUID Analysis

	y0	xc	C	s
Magnetization	0.13902±0.66446	2.96189±25.77472	58.02718±0.79117	352.84062±22.54824

Boltzmann fit for Zeta Potential Analysis:

$$y = -39.61 + (15.46 - (-39.61)) / (1 + (e^{x-8.21})^{0.25}) \tag{S1}$$

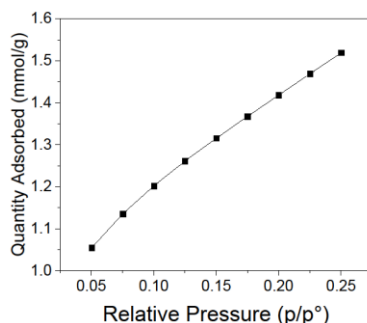
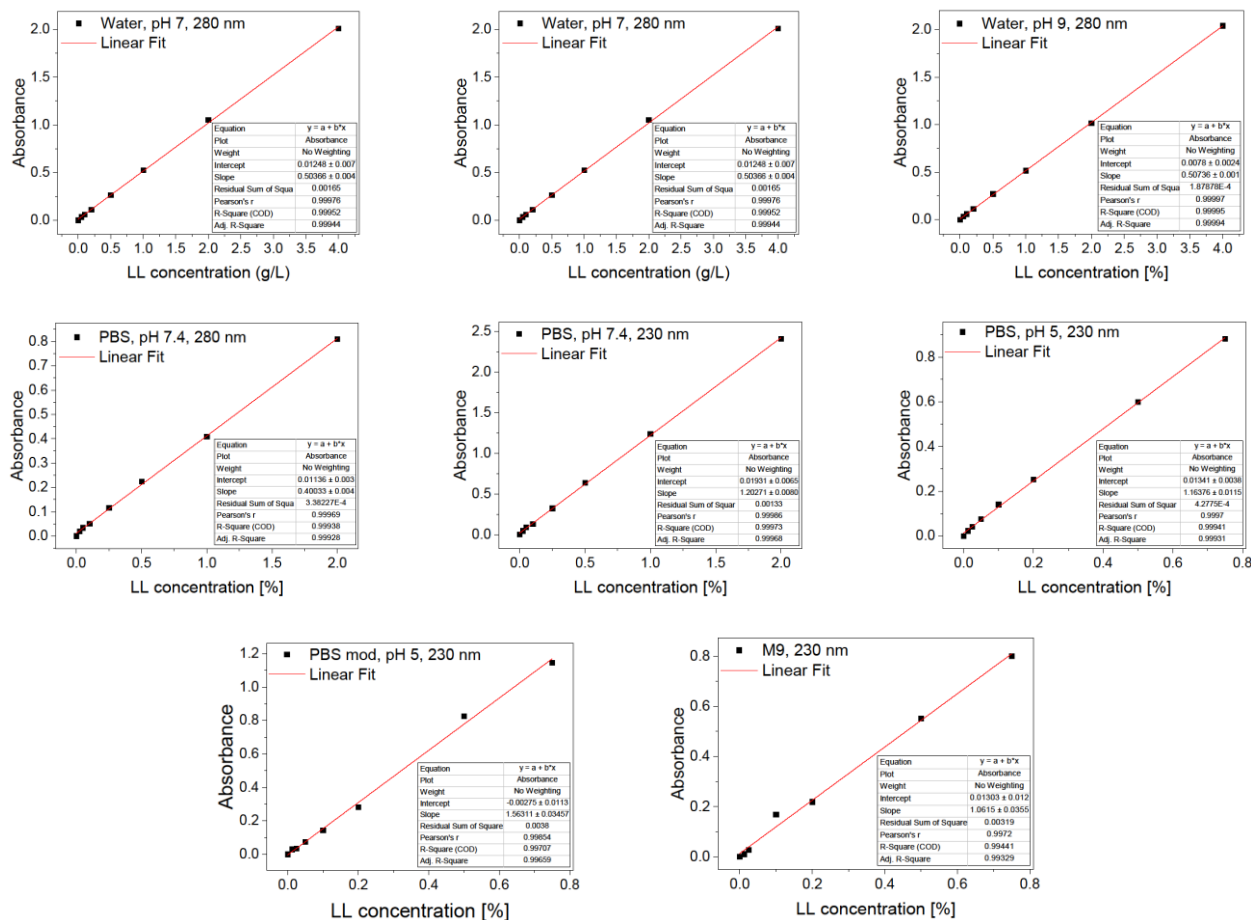


Figure S1: BET measurement: Adsorbed nitrogen to relative pressure.

Drug loading

$$\text{Drug loading} = \frac{m(\text{drug})}{m(\text{drug}) + m(\text{nanocarrier})} \tag{S3}$$

Figure S2: Exemplary calibration curves for the photometric measurements for the adsorption and release experiments.



A new calibration curve was generated for each measurement, so these curves are exemplary for all the used conditions.

Table S3: Data of Adsorption and release experiments.

LL Conc.	Adsorption: Water, pH 7, 280 nm			Washing 1: Water, pH 7, 280 nm			Adsorption: Water, pH 9, 280 nm			Washing 1: Water, pH 9, 280 nm		
	Absorbance	Absorbance	Absorbance	Absorbance	Absorbance	Absorbance	Absorbance	Absorbance	Absorbance	Absorbance	Absorbance	Absorbance
[g/L]	Value 1	Value 2	Value 3	Value 1	Value 2	Value 3	Value 1	Value 2	Value 3	Value 1	Value 2	Value 3
0	0.0727	0.059	0.0773	0.0414	0.0427	0.0414	0.0409	0.0432	0.0414	0.0403	0.0401	0.0403
0.025	0.0558	0.0972	0.127	0.0422	0.0426	0.0815	0.0656	0.0756	0.0555	0.0938	0.0767	0.0593
0.05	0.0839	0.0622	0.0822	0.0532	0.045	0.0452	0.0816	0.0698	0.0819	0.052	0.056	0.0496
0.1	0.107	0.103	0.162	0.0429	0.0478	0.0465	0.062	0.073	0.101	0.0441	0.046	0.0558
0.25	0.163	0.155	0.156	0.0496	0.0499	0.0455	0.113	0.0975	0.114	0.0423	0.0422	0.0465
0.5	0.262	0.274	0.237	0.0478	0.0496	0.0497	0.223	0.224	0.235	0.0501	0.0565	0.071
1	0.505	0.459	0.487	0.0648	0.0574	0.0739	0.452	0.444	0.427	0.0842	0.0744	0.0845
2	1	1.01	1.01	0.124	0.0969	0.11	0.834	0.892	0.93	0.127	0.136	0.15

LL Conc.	Adsorption: PBS, pH 7.4, 280 nm			Washing 1: PBS, pH 7.4, 280 nm			Adsorption: PBS, pH 7.4, 230 nm			Washing 1: PBS, pH 7.4, 230 nm		
	Absorbance			Absorbance			Absorbance			Absorbance		
[g/L]	Value 1	Value 2	Value 3	Value 1	Value 2	Value 3	Value 1	Value 2	Value 3	Value 1	Value 2	Value 3
0	0.0446	0.0429	0.0439	0.0456	0.0456	0.0455	0.082	0.0794	0.0803	0.0809	0.0809	0.0814
2	0.581	0.683	0.648	0.141	0.161	0.171	1.74	2.01	1.93	0.349	0.387	0.418
1	0.261	0.241	0.25	0.123	0.126	0.136	0.688	0.637	0.641	0.293	0.297	0.305
0.5	0.121	0.113	0.12	0.097	0.0943	0.105	0.274	0.263	0.214	0.209	0.194	0.199
0.25	0.0794	0.0849	0.0989	0.0833	0.12	0.0863	0.148	0.17	0.216	0.147	0.194	0.159
0.1	0.0642	0.0873	0.0895	0.0781	0.0855	0.0968	0.118	0.148	0.15	0.131	0.139	0.152
0.05	0.0693	0.0628	0.0921	0.0643	0.073	0.0915	0.119	0.114	0.148	0.114	0.122	0.144
0.025	0.0571	0.0532	0.0593	0.054	0.0601	0.0786	0.102	0.0958	0.104	0.0942	0.0992	0.125

Elution	LL Start Concentration	Absorbance: 1 h			Absorbance: 17 h			Absorbance: 27 h		
		Value 1	Value 2	Value 3	Value 1	Value 2	Value 3	Value 1	Value 2	Value 3
230 nm	[g/L]									
PBS, pH 5, 25 °C	1	0.18	0.159	0.164						
	0	0.0801	0.0807	0.08						
PBS, pH 5, 40 °C	1	0.167	0.159	0.168	0.171	0.164	0.181	0.189	0.177	0.196
	0	0.085	0.0859	0.0853	0.0842	0.0842	0.0844	0.0861	0.086	0.0861
PBS, pH 5, 60 °C	1	0.33	0.268	0.205						
	0	0.088	0.0879	0.0888						
PBS mod, pH 5, 25 °C	1	0.23	0.221	0.234						
	0	0.088	0.0889	0.0905						
PBS mod, pH 5, 60 °C	1	0.24	0.245	0.22						
	0	0.0905	0.0909	0.0907						
M9, 37 °C	1	0.2	0.199	0.199	0.219	0.214	0.207	0.236	0.232	0.218
	0	0.185	0.189	0.182	0.201	0.215	0.218	0.211	0.211	0.212

Elution kinetic	LL Start Concentration							
		[g/L]	1 min	5 min	15 min	30 min	60 min	180 min
230 nm	1	0.23	0.226	0.227	0.233	0.225	0.232	0.264
PBS, pH 5, 25 °C	1	0.24	0.247	0.221	0.228	0.226	0.238	0.343
	1	0.234	0.234	0.229	0.262	0.227	0.222	0.26
	0	0.113	0.112	0.102	0.106	0.102	0.103	0.107

Adsorption kinetic	LL Starting Concentration							
	[g/L]	1 min	6 min	16 min	31 min	61 min	181 min	1441 min
230 nm	1	0.316	0.287	0.259	0.287	0.27	0.275	0.263
PBS, pH 5, 25 °C	1	0.324	0.267	0.229	0.26	0.276	0.278	0.278
	0	0.0453	0.0461	0.0453				

For the calculation of all experiments the blank is subtracted from the adsorption or desorption data.

Table S4: Influence of Washing on the peptide loading in PBS buffer.

Starting peptide concentration [g/L]	Equilibrium peptide concentration [g/L]	Loading Adsorption [g/g]	Loading Washing 1 [g/g]	Loss 1 [%]	Loading Washing 2 [g/g]	Loss 2 [%]	Loading Washing 3 [g/g]	Loss 3 [%]
2.00	1.45	0.55	0.29	46.1	0.24	17.7	0.20	15.5
1.00	0.49	0.51	0.33	34.8	0.27	20.2	0.21	22.2
0.50	0.17	0.34	0.24	30.4	0.15	37.7	0.06	58.4

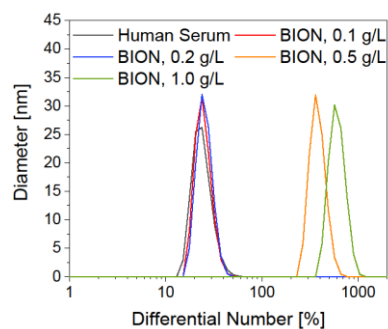


Figure S3: Agglomeration behavior of BIONs in Human Serum depending on the concentration.

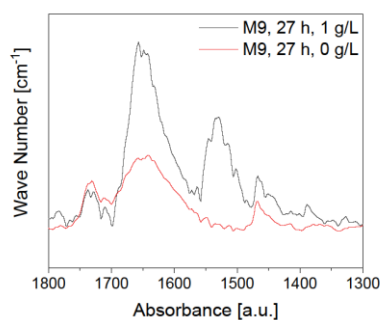


Figure S4: IR spectra of BION@LL and only BIONs after 27 h desorption in M9 medium.

Growth studies

Table S5: Components of M9 Medium for 1 L (867 ml sterile water).

Solution	Composition	Amount of substances	Volume
M9 salt solution (10x)	Na ₂ HPO ₄	33.7 mM	100 mL
	KH ₂ PO ₄	22.0 mM	
	NaCl	8.55 mM	
	NH ₄ Cl	9.35 mM	
20% glucose solution	Glucose monohydrate	0.40%	20 mL
1 M MgSO ₄ solution	MgSO ₄ ·7 H ₂ O	1.00 mM	1 mL
1 M CaCl ₂ solution	CaCl ₂ ·2 H ₂ O	0.30 mM	0.3 mL
1 M mg/mL biotin solution	Biotin	1.00 µg	1 mL
1 M mg/mL thiamin solution	Thiamin	1.00 µg	1 mL
	EDTA	13.4 mM	10 mL (1x)
Trace elements solution (100x)	FeCl ₃ ·6 H ₂ O	3.10 mM	
	ZnCl ₂	0.62 mM	
	CuCl ₂ ·2 H ₂ O	76.0 µM	
	CoCl ₂ ·2 H ₂ O	42.0 µM	
	H ₃ BO ₃	162 µM	
	MNCl ₂ · 4 H ₂ O	8.10 µM	

Microscopy

For each measurement, five group squares of biological triplicates are counted.

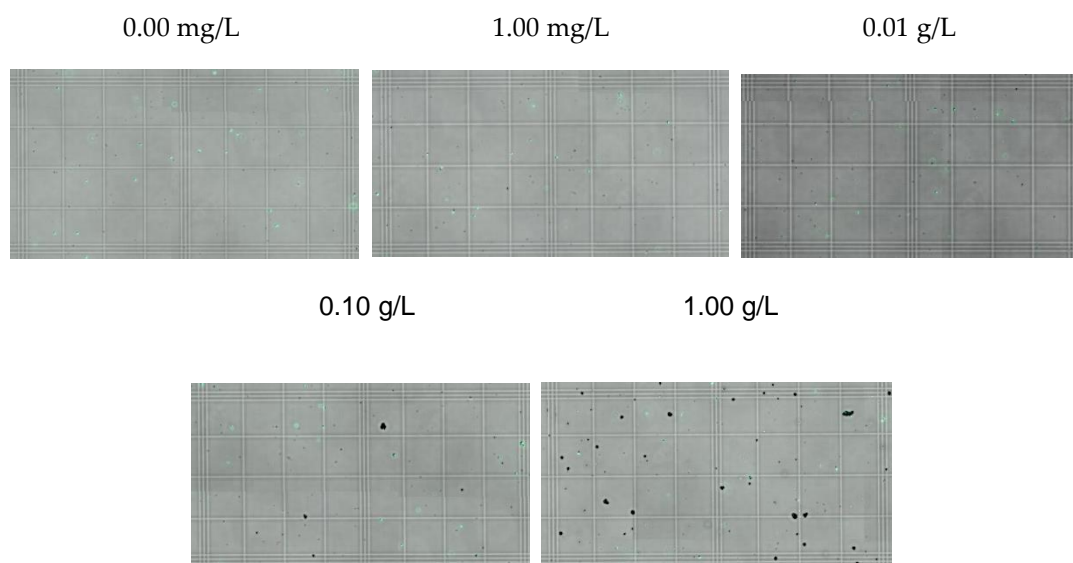


Figure S5: *E. coli* colony grown in M9 media with ampicillin, incubated with different concentrations of BIONs (37 °C, addition of IPTG after 5 h).

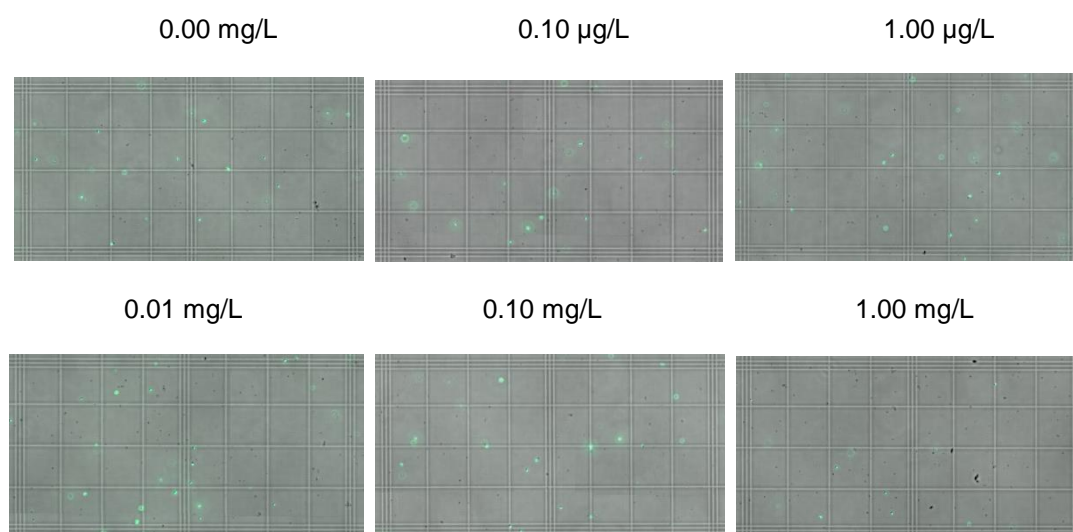
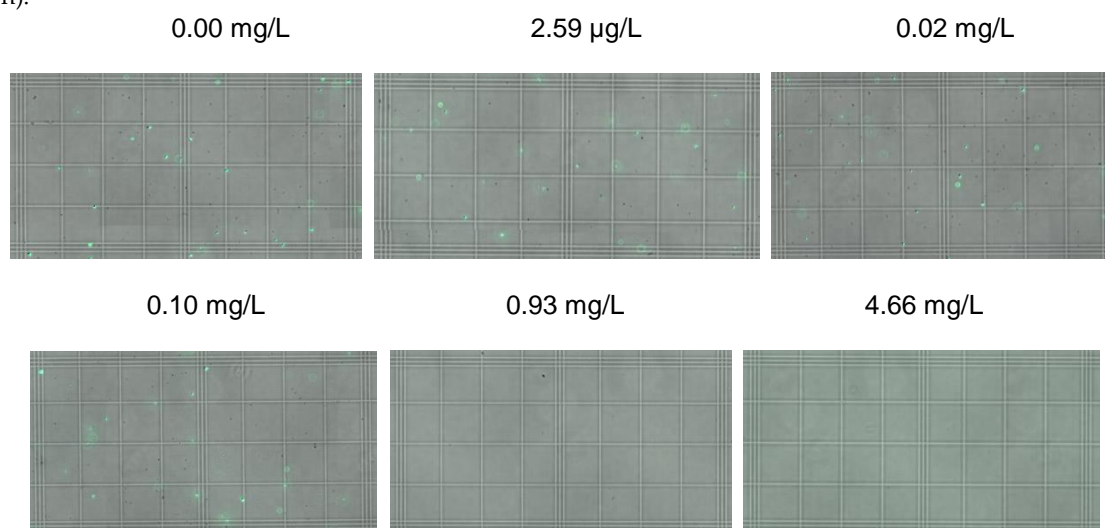


Figure S6: *E. coli* colony grown in M9 media with ampicillin, incubated with different concentrations of LL (37 °C, addition of IPTG after 5 h).



OD₆₀₀

Figure S7: *E. coli* colony grown in M9 media with ampicillin, incubated with different concentrations of BION@LL (37 °C, addition of IPTG after 5 h).

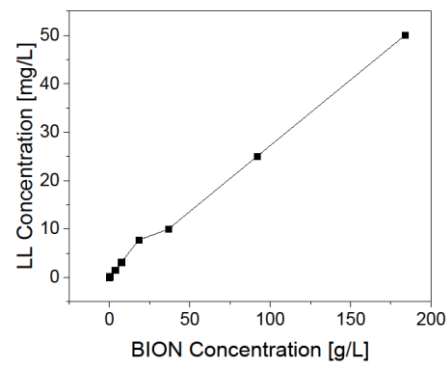


Figure S8: Amount of LL loaded on BIONs.

7.1.2. Silica-coated superparamagnetic iron oxide nanoparticles: New insights into the influence of coating thickness on the particle properties and lasioglossin binding

Silica-coated superparamagnetic iron oxide nanoparticles: New insights into the influence of coating thickness on the particle properties and lasioglossin binding

Chiara Turrina¹, Anne Oppelt¹, Michaela Mitzkus¹, Sonja Berensmeier¹ and Sebastian P. Schwaminger^{1,2*}

¹ Bioseparation Engineering Group, TUM School of Engineering and Design, Technical University of Munich, Boltzmannstraße 15, Garching, 85748, Germany

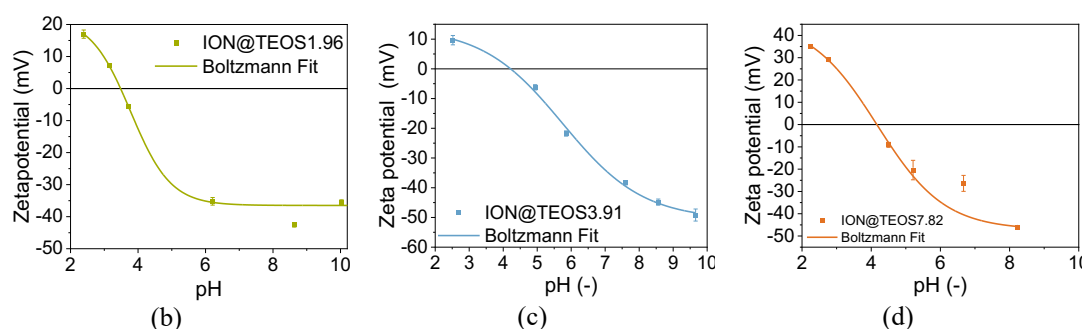
² Otto Loewi Research Center, Division of Physiological Chemistry, Medical University of Graz, Neue Stiftingtalstraße 6 HBK M1/D3, Graz, 8010, Austria

* sebastian.schwaminger@medunigraz.at

Supporting Information

SI-Table 1: Overview ION@Silica particles, synthesized by different techniques, with different sizes and applications.

Particle	Size	Synthesis	Application	Reference
PVP protected ION@Silica	11.8 nm	Sol-gel/surface protection	MR imaging	[1]
PNIPAM grafted ION@Silica	18.8	Reverse microemulsion	Adsorption of BSA	[2]
ION@Silica	21.3-30 nm	Sol-gel	Drug delivery of Doxorubicin	[3]
ION@Silica	15 nm	Sodium metasilicate	Drug delivery of Doxorubicin	[3]
ION@Silica	40.5 nm	Reverse microemulsion	Drug carrier for immunosuppressive Mycophenolic acid	[4]
ION@Silica	7.69 nm	Microemulsion	Immobilization of BSA	[5]
ION@Silica	15.6-17.0 nm	Stöber	Pyridine adsorption	[6]
Mesoporous ION@Silica	5.5-45 nm	Modified Stöber	Nanowarming	[7]
ION@Silica	8.67-31.2 nm	Stöber	Adsorption of antimicrobial peptide	Turrina et al.



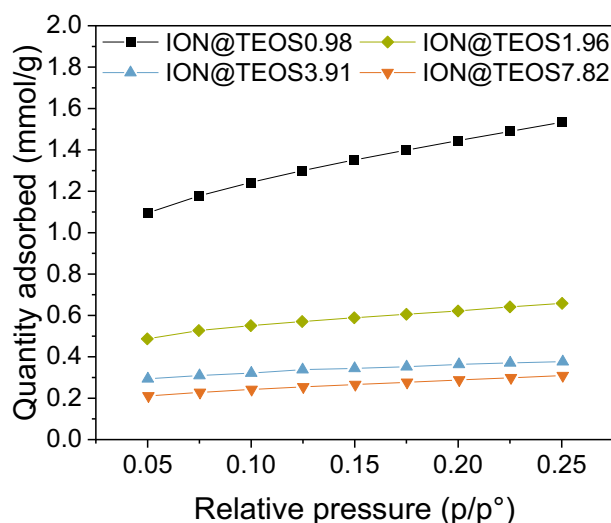
SI-Figure 1: IEP of different ION@TEOS by zeta potential measurements at different pH values in water at 25 °C.

SI-Table 2: Comparison of different ION@TEOS, regarding the particle and coating size, the magnetic properties, the agglomeration behavior and IEP in water and the BET surface.

Ref.	Synthesis	Size Core	Size Shell	ION@Silica	Magnetic properties	Agglomeration in water	IEP in water	BET
[8]	Modified polyol process	10 nm	20 nm		± 15 kOe			
[9]	Sol Gel			7-10 nm	65.67 emu/g	117.2 nm	2.5	
[10]	Sol Gel	5-15 nm	2-100 nm					
[3]	Sol-Gel	8.9-13.2		21.3-30 nm	21.6-9.2 emu/g			
[3]	Sodium metasilicate			15 nm	64.24 emu/g	1209.5 nm	3.5	
[11]	Stöber	10 nm	10 nm	30 nm	32 emu/ g	170 nm		
[12]	Stöber	56 nm		62 nm			3.5	
[6]	Stöber			15.6 -17 nm	(330 K) 72-87 emu/g			84-45 m ² /g
Turrina et al.	Stöber	9 nm	0.42-23.1	8.67-31.2	66.1-11.8 emu/g	88.2-329 nm	1.87-4.17	115-23.2

SI-Table 3: Harmonic average values of the sedimentation speed measured by STEP-technology of BIONs and ION@TEOS in water at 870 nm.

Particle	Harmonic average value [$\mu\text{m s}^{-1}$]
BION	521
ION@TEOS0.98	1.79
ION@TEOS1.96	34.7
ION@TEOS3.91	72.8
ION@TEOS7.82	43.8



SI-Figure 1: BET measurement: Adsorbed nitrogen to relative pressure.

Scherrer Equation:

(1)

$$L = \frac{0.89 * 0.07093 \text{ nm}}{FWHM * \cos(\theta)}$$

SI-Table 4: Peakcenters and full width at half maximum (FWHM) of the reflexes of BIONs and IONs@TEOS analyzed by XRD. The data is used to calculate the diameter of the ION core with the Scherrer equation.

BIONs		ION@TEOS0.98		ION@TEOS1.96		ION@TEOS3.91		ION@TEOS7.82	
Peak center [2θ °]	FWHM	Peak center [2θ °]	FWHM	Peak center [2θ °]	FWHM	Peak center [2θ °]	FWHM	Peak center [2θ °]	FWHM
16.2	0.46	16.2	0.46	16.1	0.44	16.1	0.40	16.1	0.51
19.5	0.32	19.3	0.47	19.5	0.48	19.5	0.51	19.6	0.64
25.5	0.54	25.5	0.40	25.4	0.44	25.4	0.43	25.3	0.46
27.8	0.39	27.7	0.36	27.7	0.37	27.7	0.41	27.7	0.48

References

- [1] M. Kermanian, S. Sadighian, M. Naghibi, M. Khoshkam, PVP Surface-protected silica coated iron oxide nanoparticles for MR imaging application, *J. Biomater. Sci. Polym. Ed.* 32 (2021) 1356–1369. <https://doi.org/10.1080/09205063.2021.1916869>.
- [2] Y.-H. Lien, T.-M. Wu, J.-H. Wu, J.-W. Liao, Cytotoxicity and drug release behavior of PNIPAM grafted on silica-coated iron oxide nanoparticles, *J Nanopart Res* 13 (2011) 5065–5075. <https://doi.org/10.1007/s11051-011-0487-8>.
- [3] A. Taufiq, A. Nikmah, A. Hidayat, S. Sunaryono, N. Mufti, N. Hidayat, H. Susanto, Synthesis of magnetite/silica nanocomposites from natural sand to create a drug delivery vehicle, *Heliyon* 6 (2020) e03784. <https://doi.org/10.1016/j.heliyon.2020.e03784>.
- [4] J. Hwang, E. Lee, J. Kim, Y. Seo, K.H. Lee, J.W. Hong, A.A. Gilad, H. Park, J. Choi, Effective delivery of immunosuppressive drug molecules by silica coated iron oxide nanoparticles, *Colloids Surf. B Biointerfaces* 142 (2016) 290–296. <https://doi.org/10.1016/j.colsurfb.2016.01.040>.
- [5] C.H. Yu, A. Al-Saadi, S.-J. Shih, L. Qiu, K.Y. Tam, S.C. Tsang, Immobilization of BSA on Silica-Coated Magnetic Iron Oxide Nanoparticle, *J. Phys. Chem. C* 113 (2009) 537–543. <https://doi.org/10.1021/jp809662a>.

- [6] E.S.D.T. de Mendonça, A.C.B. de Faria, S.C.L. Dias, F.F.H. Aragón, J.C. Mantilla, J.A.H. Coaquira, J.A. Dias, Effects of silica coating on the magnetic properties of magnetite nanoparticles, *Surf. Interfaces* 14 (2019) 34–43. <https://doi.org/10.1016/j.surfin.2018.11.005>.
- [7] Zhe Gao, Hattie L. Ring, Anirudh Sharma, Baterdene Namsrai, Nam Tran, Erik B. Finger, Michael Garwood, Christy L. Haynes, John C. Bischof, Preparation of Scalable Silica-Coated Iron Oxide Nanoparticles for Nanowarming, *Advanced Science* 7 (2020) 1901624. <https://doi.org/10.1002/advs.201901624>.
- [8] M. Abbas, B. Parvatheeswara Rao, M. Nazrul Islam, S.M. Naga, M. Takahashi, C. Kim, Highly stable-silica encapsulating magnetite nanoparticles (Fe₃O₄/SiO₂) synthesized using single surfactantless- polyol process, *Ceram. Int.* 40 (2014) 1379–1385. <https://doi.org/10.1016/j.ceramint.2013.07.019>.
- [9] S.E. Favela-Camacho, E.J. Samaniego-Benítez, A. Godínez-García, L.M. Avilés-Arellano, J.F. Pérez-Robles, How to decrease the agglomeration of magnetite nanoparticles and increase their stability using surface properties, *Colloids Surf., A* 574 (2019) 29–35. <https://doi.org/10.1016/j.colsurfa.2019.04.016>.
- [10] Y. Lu, Y. Yin, B.T. Mayers, Y. Xia, Modifying the surface properties of superparamagnetic iron oxide nanoparticles through a sol–gel approach, *Nano Lett.* 2 (2002) 183–186. <https://doi.org/10.1021/nl015681q>.
- [11] I.A. Bakhteeva, I.V. Medvedeva, M.A. Uimin, I.V. Byzov, S.V. Zhakov, A.E. Yermakov, N.N. Shchegoleva, Magnetic sedimentation and aggregation of Fe₃O₄@SiO₂ nanoparticles in water medium, *Sep. Purif. Technol.* 159 (2016) 35–42. <https://doi.org/10.1016/j.seppur.2015.12.043>.
- [12] K. Gdula, A. Dąbrowski, E. Skwarek, Synthesis, surface characterization and electrokinetic properties of colloidal silica nanoparticles with magnetic core, *Adsorption* 22 (2016) 681–688. <https://doi.org/10.1007/s10450-015-9755-8>.

7.1.3. Carboxymethyl-dextran coated superparamagnetic iron oxide nanoparticles for drug delivery: Influence of coating thickness on the particle properties

Carboxymethyl-dextran coated superparamagnetic iron oxide nanoparticles for drug delivery: Influence of coating thickness on the particle properties

Chiara Turrina^a, Davide Milani^a, Anna Klassen^a, Diana M. Rojas-González^b, Jennifer Cookman^c, Matthias Opel^d, Barbara Sartori^c, Petra Mela^b, Sonja Berensmeier^a and Sebastian P. Schwaminger^{a,f*}

^a Bioseparation Engineering Group, Department for Engineering and Design, Technical University of Munich

^b Chair of Medical Materials and Implants, Department of mechanical engineering, Munich Institute of Biomedical Engineering, TUM School of Engineering and Design, Technical University of Munich

^c Department of Chemical Sciences, Bernal Institute, University of Limerick, Castletroy, University of Limerick, V94 T9PX

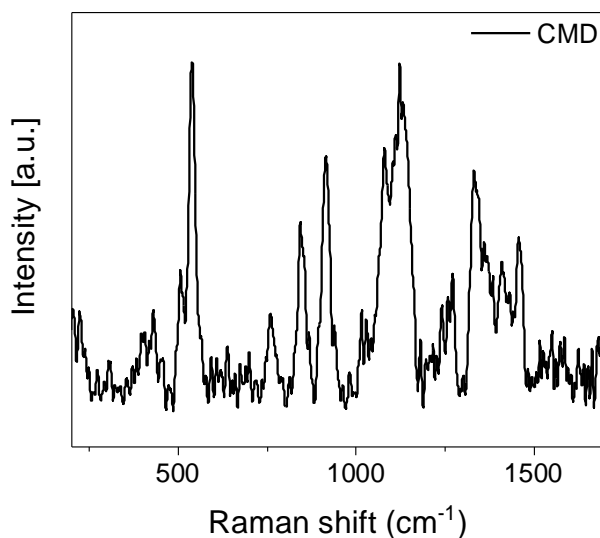
^d Walther-Meißner-Institut, Bayerische Akademie der Wissenschaften, Garching, Germany

^e Institute of Inorganic Chemistry, Graz University of Technology, Stremayrgasse 9/IV, Graz, 8010, Austria

^f Division of Medicinal Chemistry, Otto Loewi Research Center, Medical University of Graz, Neue Stiftingtalstraße 6, Graz, 8010, Austria

* sebastian.schwaminger@medunigraz.at

Electronic Supplementary Information



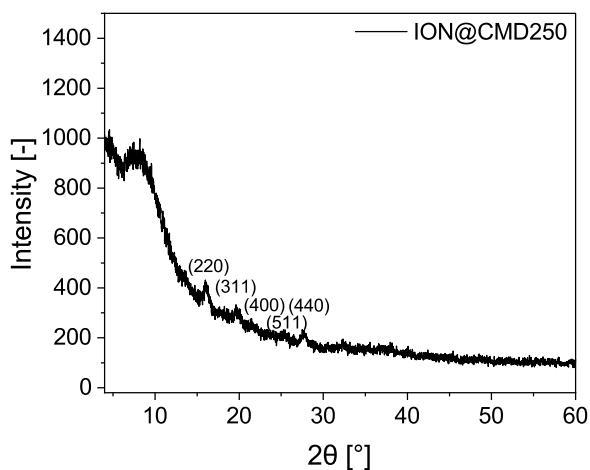
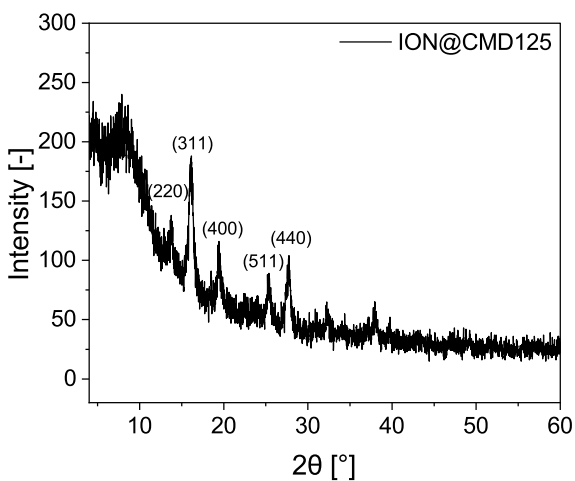
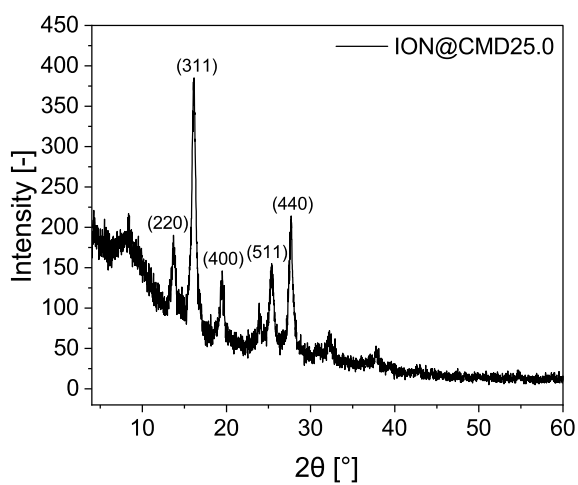
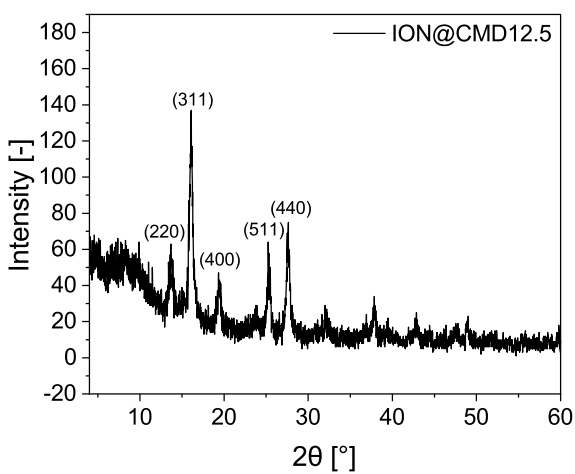
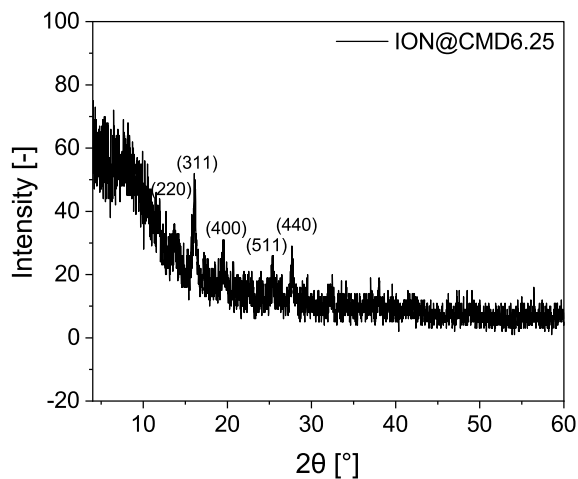
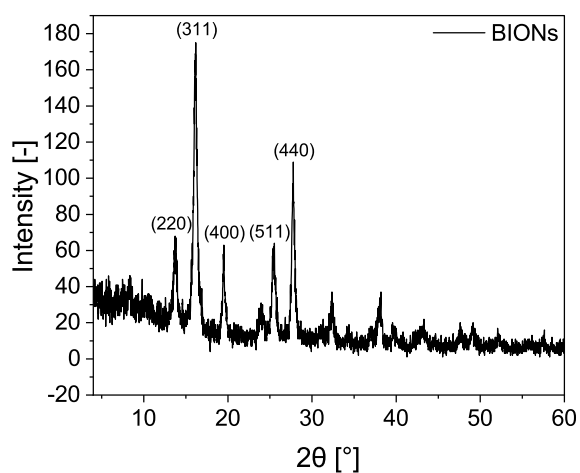
SI-Figure S1: Raman Spectra of CMD measured using a 488 nm laser, the laser power was reduced to 1 mW for each measurement by optical filters (Exposure: 10 s, Co-Ad. 2).

Magnetite content was calculated using the formula determined by Schwaminger et al. [1].

$$\text{Magnetite (\%)} = 100 * \left(1 - \frac{A(710)}{A(660)}\right) \quad (1)$$

SI-Table S1: Magnetite contents of the particles BIONs, ION@CMD6.25 to 125 determined by comparing the magnetite peak area (660) and maghemite peak area. The magnetite content could not be determined for ION@CMD250 because no peak was visible in the Raman spectrum. Peak areas were determined using the Voigt fit at 660 cm^{-1} and 710 cm^{-1} .

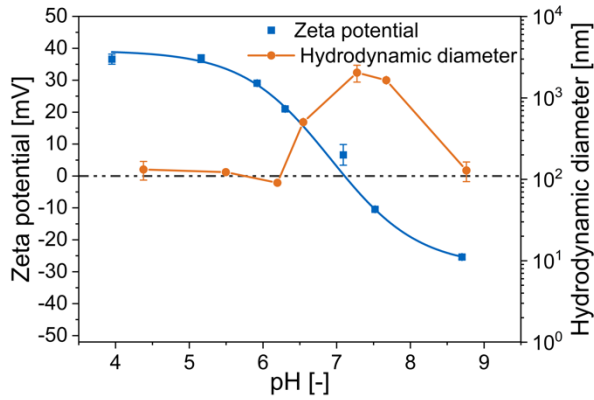
Particles	A(660 cm^{-1})	A(710 cm^{-1})	Magnetite [%]
BIONs	961.8	811.4	15.6
ION@CMD6.26	550.1	434.5	21.0
ION@CMD12.5	805.2	531.8	33.9
ION@CMD25.0	566.6	297.6	47.5
ION@CMD125	418.5	245.2	41.6
ION@CMD250	-	-	-



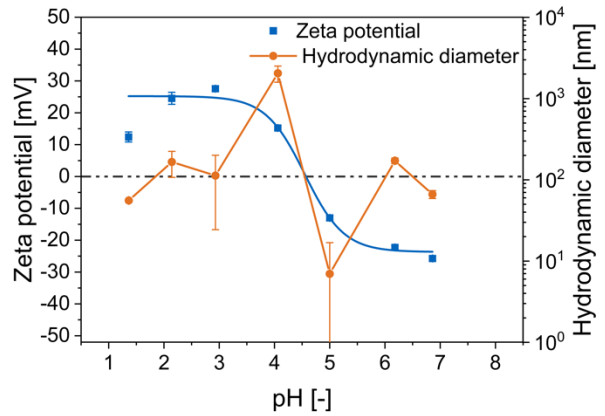
SI-Figure S2: Diffractograms of BIONs, ION@CMD6.25, ION@CMD12.5, ION@CMD25.0, ION@CMD125, and ION@CMD250. The intensities of the X-ray beam scattered by the sample are plotted as a function of the 2θ diffraction angle.

Hydrodynamic diameter d_H was calculated using the Einstein-Stokes-Law for spheres. (Hydrodynamic diameter d_H , diffusion coefficient D , Boltzmann constant k_B , temperature T , viscosity η)

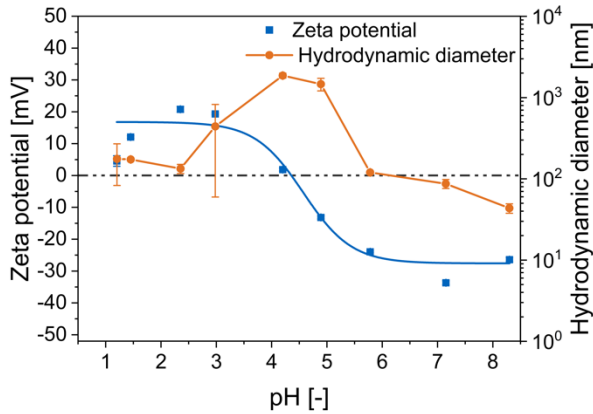
$$D = \frac{k_B * T}{6 * \pi * \eta * d_H} \quad (2)$$



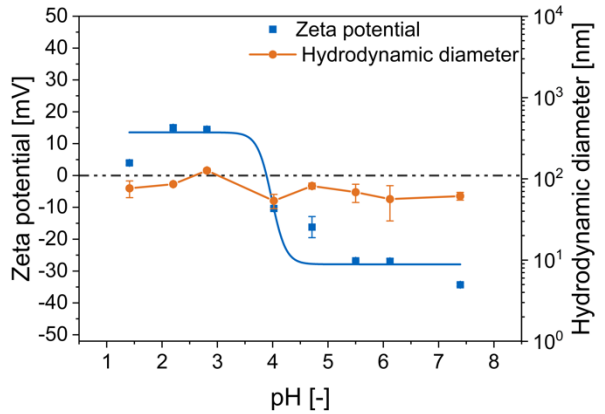
(a)



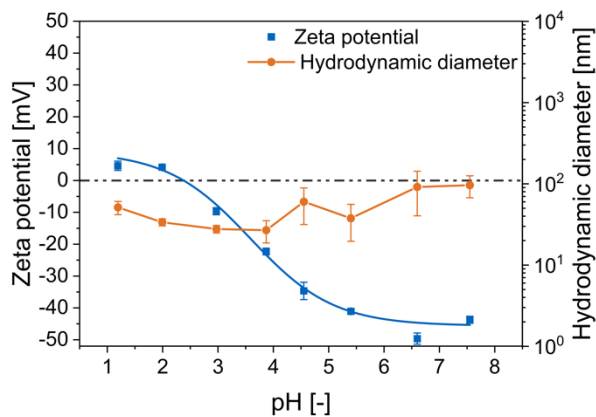
(b)



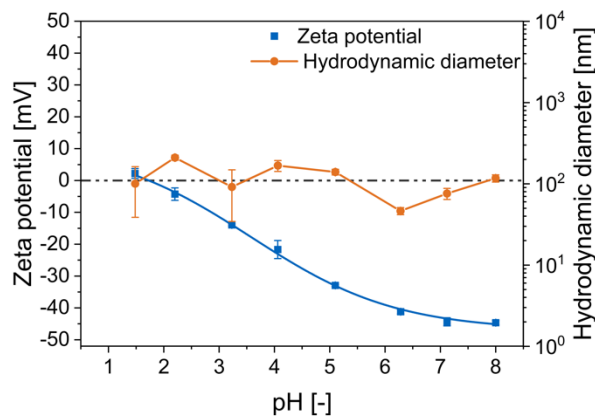
(c)



(d)



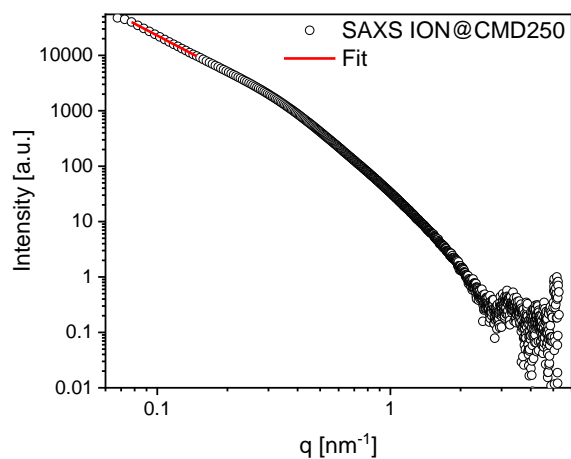
(e)



(f)

SI-Figure S3: Increasing CMD coating thickness shifts the IEP in the acidic. IEPs and d_H through different pH values of a) BIONs, b) ION@CMD6.25, c) ION@CMD12.5, d) ION@CMD25, e) ION@CMD125, and f) ION@CMD250.

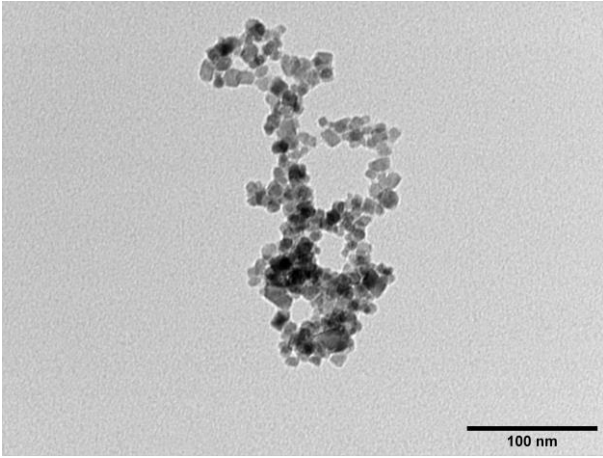
Small Angle X-Ray Scattering data were acquired at the Austrian SAXS beamline at the Elettra Synchrotron in Trieste; the beamline length was set to 1386.101 mm, corresponding to a q range of 0.07 nm^{-1} - 5.3 nm^{-1} , where $q = 4\pi \sin\theta/\lambda$, λ is the wavelength of the incident X-rays, and 2θ is the scattering angle. The photon energy was set to 8 keV corresponding to a wavelength of 0.154 nm. The sample was loaded in a quartz capillary with 1.5 mm diameter and exposed to X-Rays. 10 images of 10 s each were collected by a Pilatus 3 1M detector (Dectris Ltd., Baden, Switzerland). The angular scale of the diffraction pattern was calibrated with silver behenate (d-spacing 5.8376 nm). The acquired images were azimuthally integrated by SAXSDog, the automatic data integration pipeline available at the SAXS outstation, normalized on transmission and fluctuation of the primary beam intensity, and background subtracted.



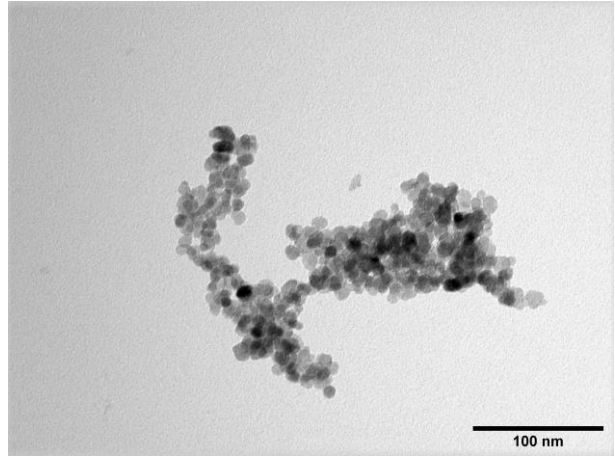
SI-Figure S4: SAXS profiles of ION@CMD250 and fit at pH 7.

The Scherrer equation was used to calculate the particle size L of the magnetite crystal. The Scherrer shape factor K has a constant value of 0.89. The X-ray wavelength λ is 0.07093 nm. The Bragg angle θ_0 and the full half-width of the reflection $\Delta 2\theta$ are calculated using Origin software. The two largest reflections of the plane (311) and (440) were used

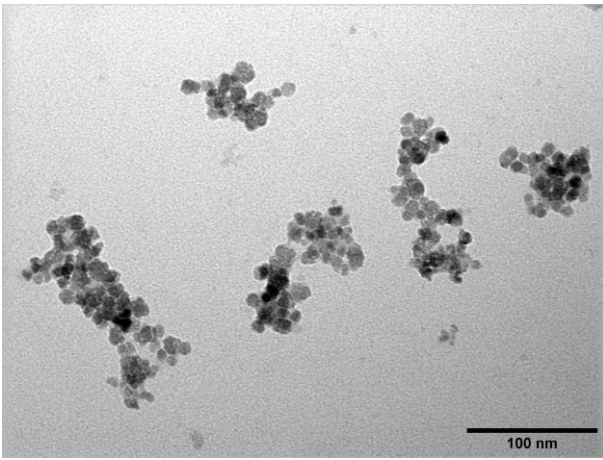
$$D = \frac{K * \lambda}{\beta * \cos(\theta)} \quad (3)$$



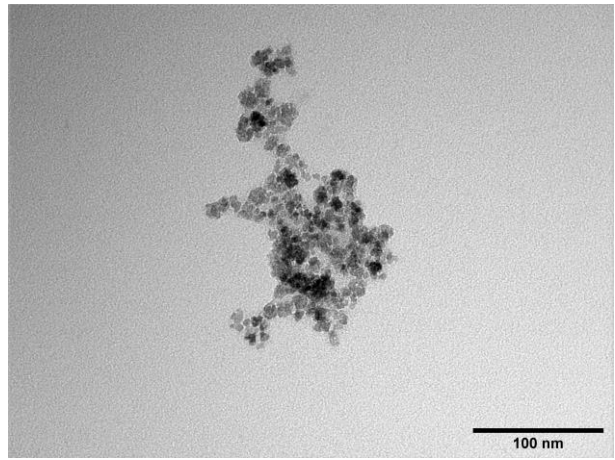
A



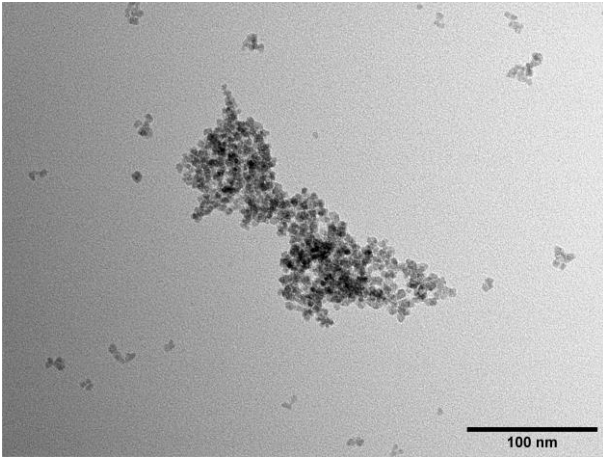
B



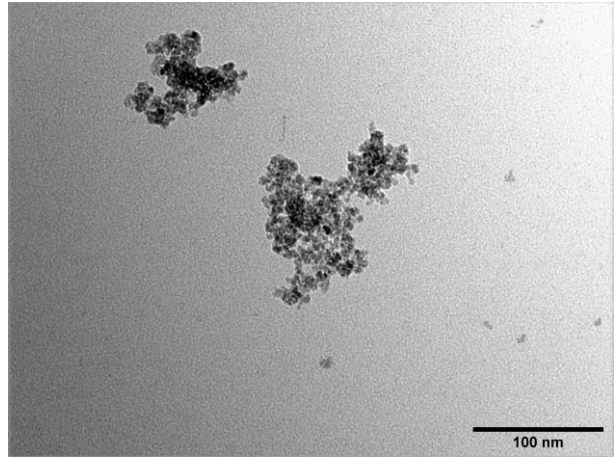
C



D

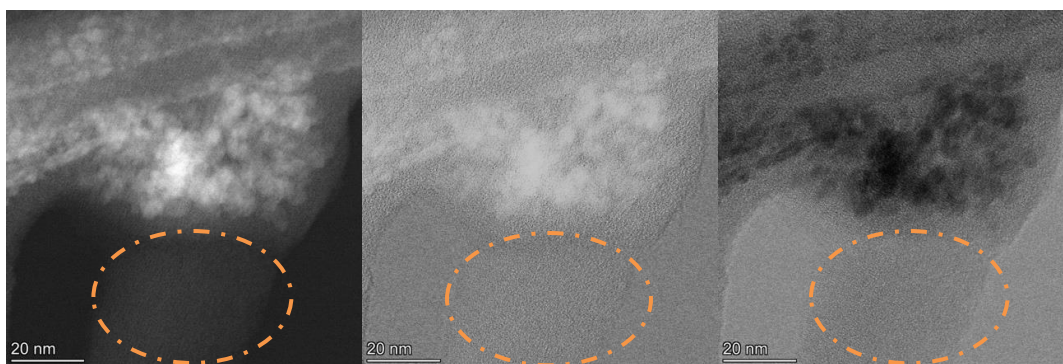


E

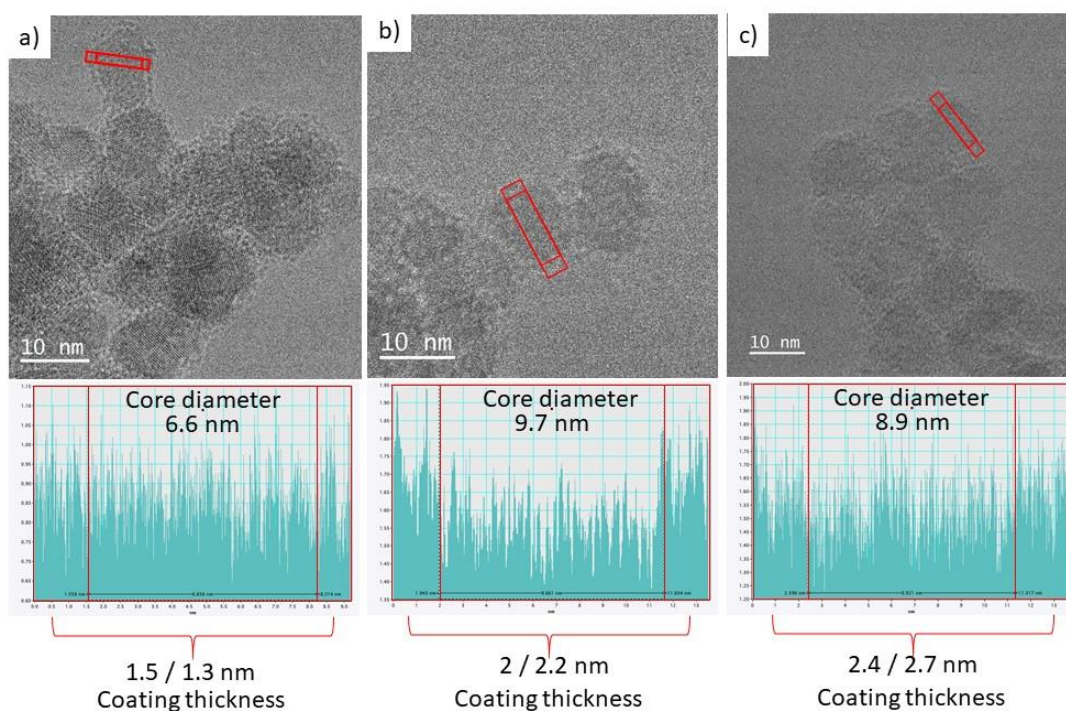


F

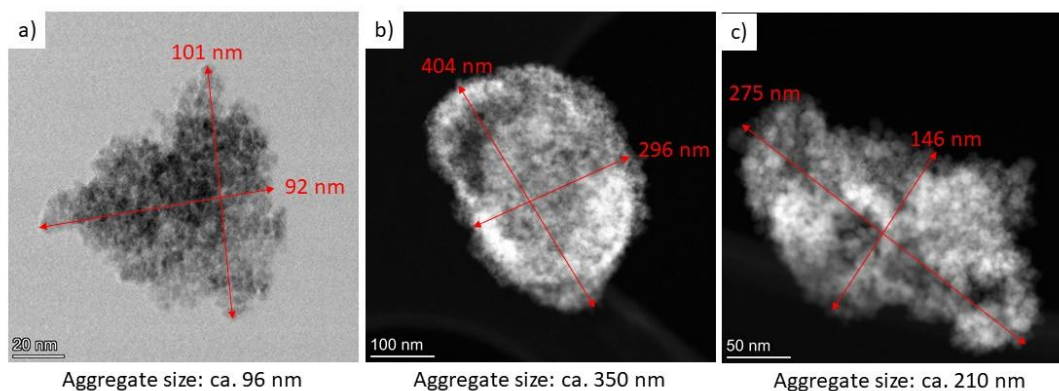
SI-Figure S5: TEM micrographs at a magnification of 120k of (A) BIONs, (B) ION@CMD6.25, (C) ION@CMD12.5, (D) ION@CMD25, (E) ION@CMD125 and (F) ION@CMD250. Images were processed with ImageJ.



SI-Figure S6: HAADF-STEM micrographs indicating where the nanoparticle core with an amorphous coating for ION@CMD12.5 on the left. The picture in the middle shows DPCx (A-C) and the right one DPCy (B-D). The orange markers show artifacts created by the rastering electron beam. Scale bars shown inset.



SI-Figure S7: Low-dose TEM micrographs analyzed for core size and coating thickness for A) ION@CMD250, B) ION@CMD12.5, and C) ION@CMD6.25.



SI-Figure S8: Low-dose TEM micrographs analyzed for their agglomerate size for A) ION@CMD250, B) ION@CMD12.5, and C) ION@CMD6.25.

SI-Table S2: Mean hydrodynamic diameters of BIONs and IONs@CMD in water, 50 mM PBS and human Plasma. For d_H in water, the amount of particles per agglomerate is calculated based on d_{TEM} . For PBS and Human plasma, the stabilization is calculated by dividing through the agglomerates in water.

Particles	d_H in dH_2O [nm]	Amount of particles (d_{TEM})	d_H in			
			50 mM PBS (pH 7.4) [nm]	d_H , PBS/ d_H , H_2O	d_H in Human Plasma [nm]	d_H , HP/ d_H , H_2O
BIONs	503 ± 10.5	57.3x	1902 ± 360	3.78x	442 ± 9.63	0.87x
ION@CMD6.26	137 ± 0.33	12.6x	165 ± 12.83	1.21x	50.6 ± 2.46	0.37x
ION@CMD12.5	87.1 ± 10.9	7.99x	158 ± 5.47	1.81x	41.5 ± 9.47	0.48x
ION@CMD25.0	94.2 ± 8.07	11.8x	73.6 ± 9.59	0.78x	79.3 ± 39.0	0.84x
ION@CMD125	162 ± 101	21.5x	34.5 ± 0.81	0.21x	51.6 ± 15.6	0.32x
ION@CMD250	200 ± 32.3	31.6x	69.3 ± 12.3	0.35x	25.8 ± 3.34	0.13x

LangevinMod Fit

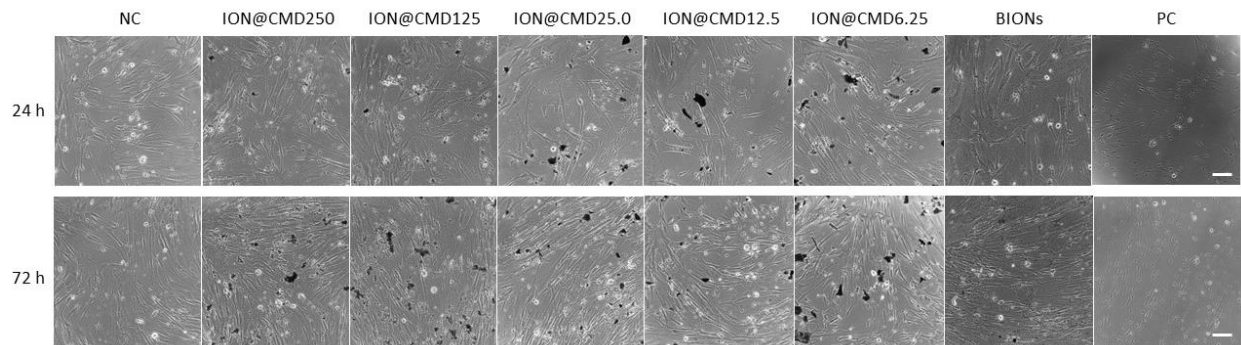
$$y = y_0 + C \left(\coth \left(\frac{x - x_c}{s} \right) - \frac{s}{x - x_c} \right)$$

$$\coth z = \frac{e^z + e^{-z}}{e^z - e^{-z}}$$

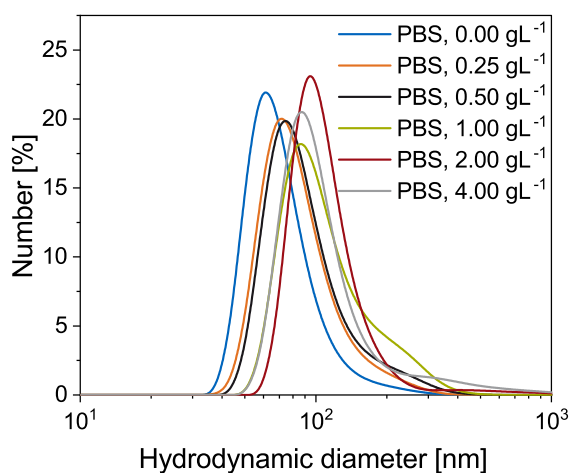
SI-Equation 4: Modified Langevin function by OriginLab, with y_0 = offset, x_c = center, C = Amplitude, s = Scale. Lower and upper bounds: none.

SI-Table S3: Sedimentation velocity of BIONs and ION@CMDs in dH₂O (pH = 7 – 7.4). Measurements were taken at wavelengths of 870 nm, 630 nm, and 420 nm (Profile: 1000; Interval: 1s; Angle: 0°; Light factor: 1.00; Temperature: 25 °C).

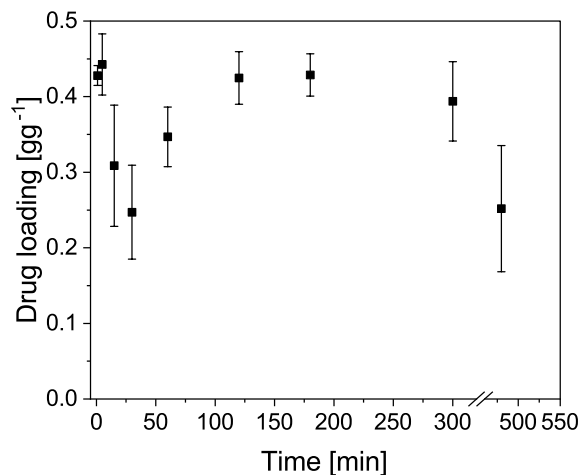
Particles	Sedimentation velocity [$\mu\text{m s}^{-1}$]
BIONs	1152
ION@CMD6.25	78.95
ION@CMD12.5	18.39
ION@CMD25.0	30.72
ION@CMD125	90.24
ION@CMD250	160.6



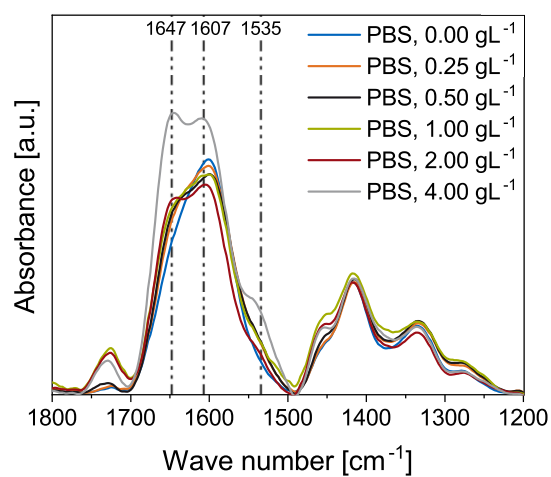
SI-Figure S9: Phase contrast images of the cells incubated with IONs@CMD and BIONs after 24 and 72 hours for the cytocompatibility assay. Scale bar: 100 μm .



(a)

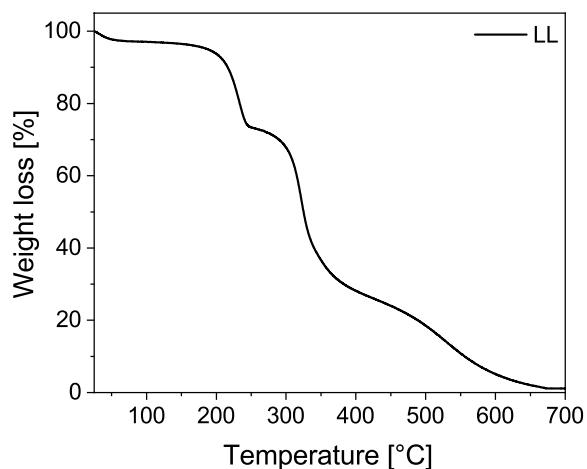


(b)



(c)

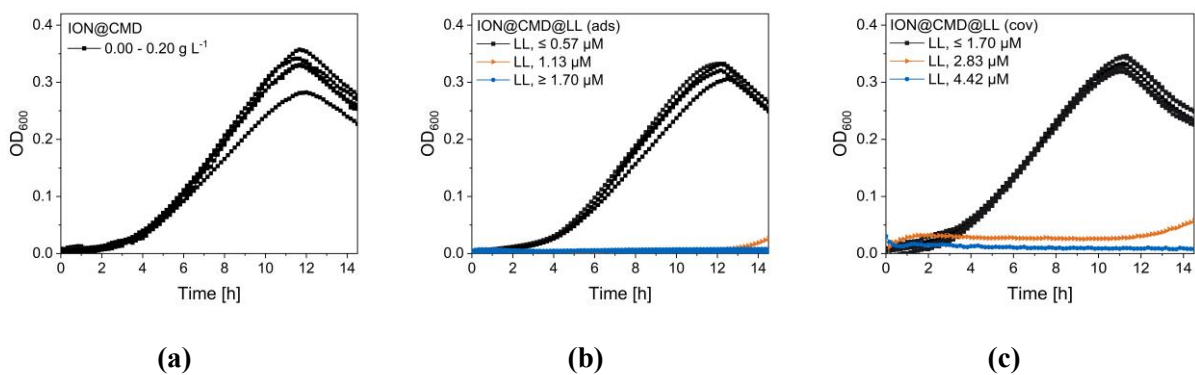
SI-Figure S10: Adsorption of LL onto the surface of ION@CMD12.5 in 50 mM PBS buffer at pH 7.4. : a) Hydrodynamic diameters of particles after LL adsorption at pH 7.4 in 50 mM PBS buffer. b) Adsorption kinetics of 4.00 g L⁻¹ LL onto the surface of ION@CMD12.5 (1 gL⁻¹) were measured over 8 hours. c) FT-IR spectrum of adsorbed LL (0.00 g L⁻¹ to 4.00 g L⁻¹ used) on ION@CMD12.5 (24 scans).



SI-Figure S2: Weight loss (%) of LL II plotted against Temperature (°C).

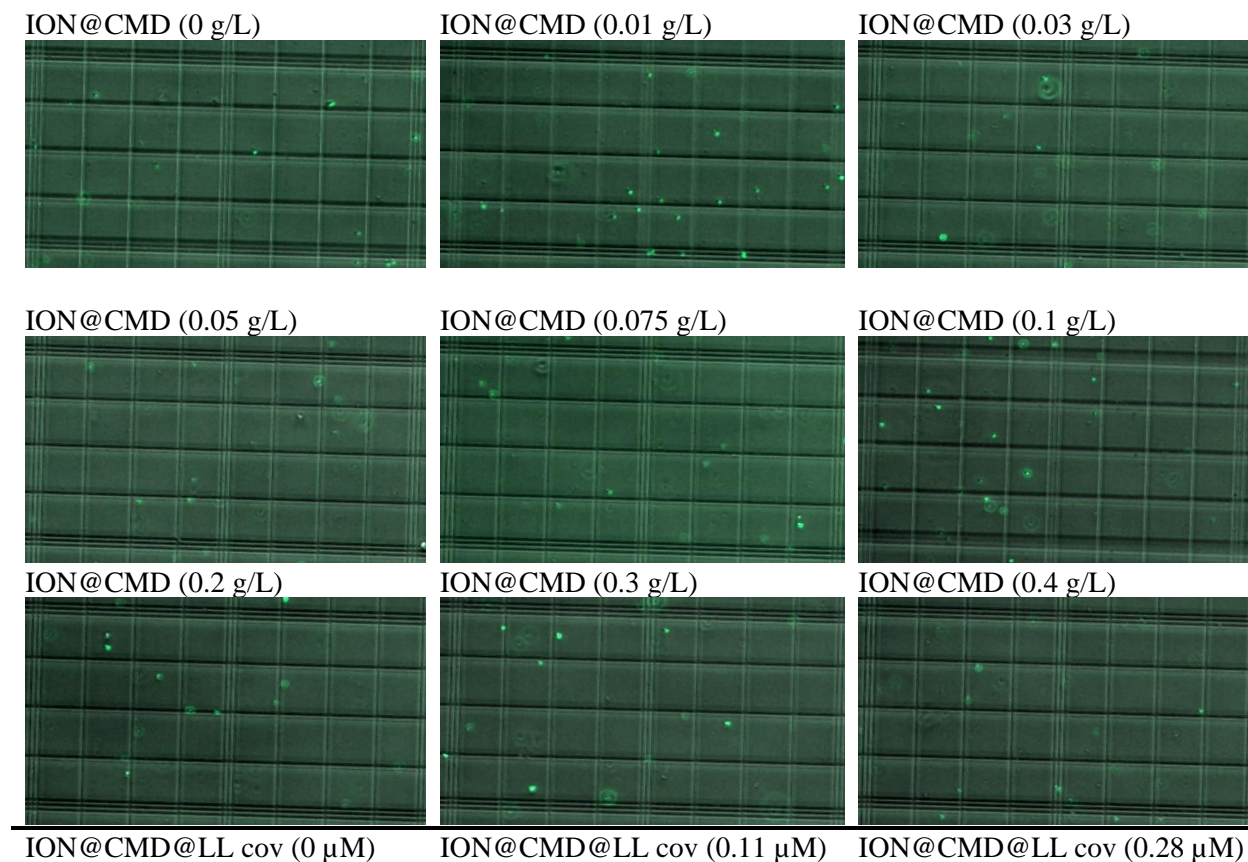
SI-Table S4: Efficiency of the protocols used to bind LL to the particle surface of ION@CMD12.5. Values were calculated by dividing the amount of LL bound by the amount of LL used. The calculation for Adsorptions are referred to the loadings reached with adsorption. Washing steps were not included.

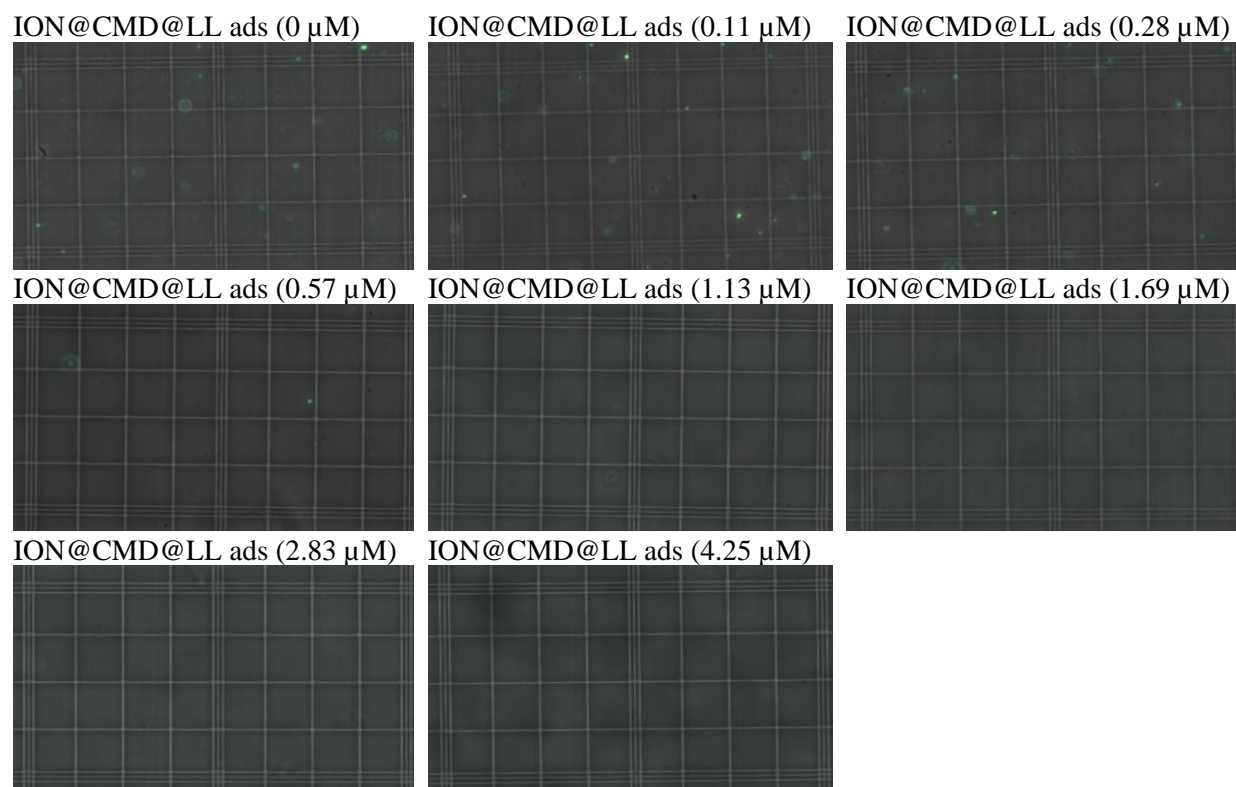
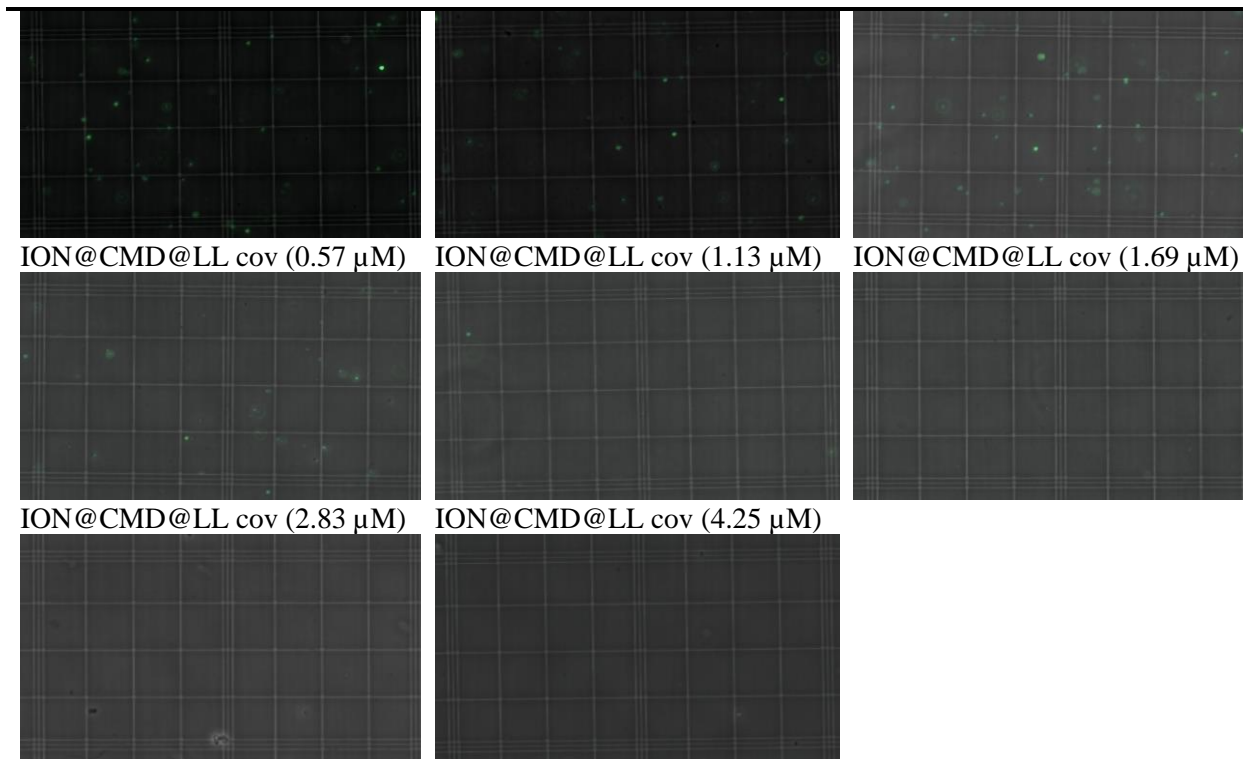
LL used in adsorption [g L ⁻¹]	Efficiency [%]	LL used in covalent binding [g L ⁻¹]	Efficiency [%]
0.00	0.00	0.00	0.00
0.25	28.4 ± 1.09	0.80	82.2 ± 0.11
0.50	25.9 ± 1.07	1.00	77.6 ± 0.18
1.00	13.5 ± 3.86	1.50	74.9 ± 0.18
2.00	12.4 ± 0.93	2.00	79.4 ± 0.08
4.00	8.07 ± 1.43	2.50	79.2 ± 0.19



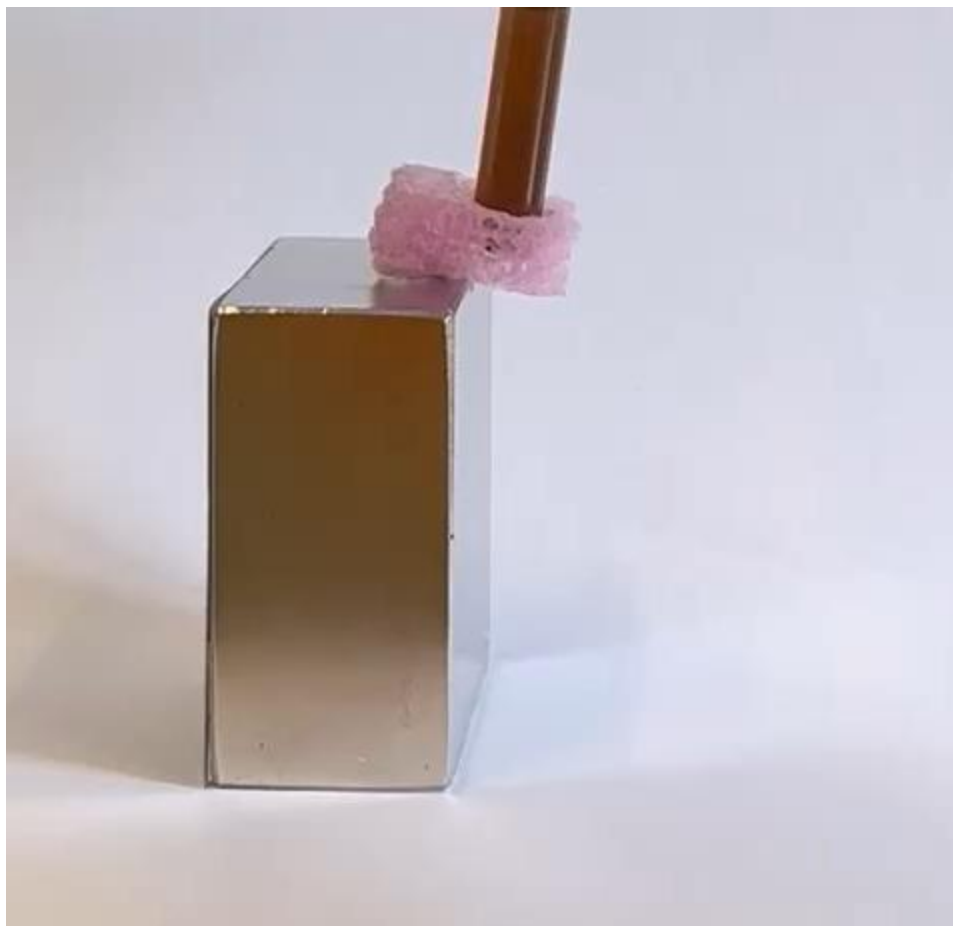
SI-Figure S3: OD₆₀₀ measurement of *E. coli* growth of different a) ION@CMD12.5 concentrations and different amounts of ION@CMD@LL obtained by b) adsorption or c) covalent binding.

After a short lag phase of about two and a half hours, the exponential phase starts about ten hours after the beginning of the experiment. At an OD₆₀₀ of 0.35, *E. coli* reaches its stationary phase, followed by the death phase. Both measurements at OD₆₀₀ and the cell counting showed no or negligible influence on cell growth of the ION@CMD12.5.





SI-Figure S4: *E. coli* colony grown in M9 media with ampicillin, incubated with different ION@CMD12.5, ION@CMD@LL (cov), and ION@CMD@LL (ads) concentrations (37 °C, addition of IPTG after 5 h).



SI-Movie 1: *A_{1g}L⁻¹ solution of ION@CMD12.5 with 0.55 g g⁻¹ LL contacted to a rectangular magnet (50.8 x 50.8 x 25.4 mm, adhesion force 100 kg, placement force 20 kg, obtained from Supermagnete).*

References

- [1] S. Schwaminger, C. Syhr, S. Berensmeier, Controlled Synthesis of Magnetic Iron Oxide Nanoparticles: Magnetite or Maghemite?, *Crystals* 10 (2020) 214. <https://doi.org/10.3390/cryst10030214>.

7.1.4. Iron Oxide Nanoparticles with Supramolecular Ureido-Pyrimidinone Coating for Antimicrobial Peptide Delivery

Iron Oxide Nanoparticles with Supramolecular Ureido-Pyrimidinone Coating for Antimicrobial Peptide Delivery

Chiara Turrina ¹, Jennifer Cookman ², Riccardo Bellan ³, Jiankang Song ³, Margret Paar ⁴, Patricia Y. W. Dankers ³, Sonja Berensmeier ¹ and Sebastian P. Schwaminger ^{1,4,5,*}

¹ Chair of Bioseparation Engineering, School of Engineering and Design, Technical University of Munich, Boltzmannstr. 15, 85748 Garching, Germany; c.turrina@tum.de (C.T.)

² Department of Chemical Sciences, Bernal Institute, University of Limerick, V94 T9PX Castletroy, Ireland; jennifer.cookman@ul.ie

³ Department of Biomedical Engineering, Institute for Complex Molecular Systems, Eindhoven University of Technology, 5600 MB Eindhoven, The Netherlands; r.bellan@tue.nl (R.B.)

⁴ Division of Medicinal Chemistry, Otto Loewi Research Center, Medical University of Graz, Neue Stiftingtalstraße 6, 8010 Graz, Austria

⁵ BioTechMed-Graz, Mozartgasse 12, 8010 Graz, Austria

* Correspondence: sebastian.schwaminger@medunigraz.at; Tel.: +43-3163-8572-125

Supporting information

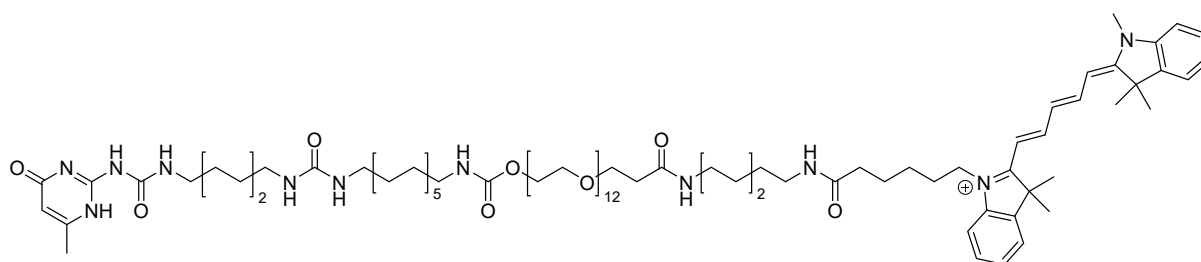


Figure S1: Structure of UPy-Cy5.

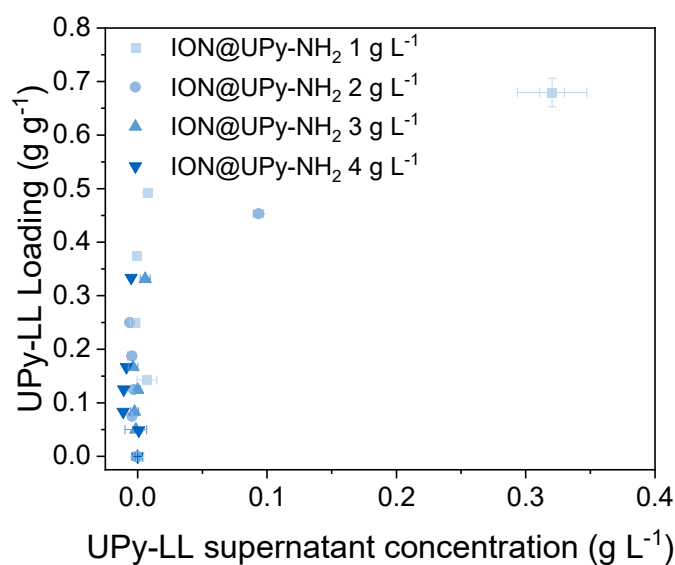


Figure S2: UPy-LL loading on different ION@UPy-NH₂ concentrations.

Table S1: Amount of bound UPy-LL on ION@UPy-NH₂ after dilution to different particle concentrations.

ION@UPy-NH ₂ @UPy-LL concentration [g L ⁻¹]	0 g L ⁻¹	0.005 g L ⁻¹	0.01 g L ⁻¹	0.015 g L ⁻¹	0.03 g L ⁻¹	0.04 g L ⁻¹	0.05 g L ⁻¹	0.075 g L ⁻¹	0.1 g L ⁻¹
UPy-LL concentration bound to ION@UPy-NH ₂	0 μM	1.77 μM	3.53 μM	5.40 μM	10.6 μM	14.1 μM	17.7 μM	26.5 μM	35.3 μM

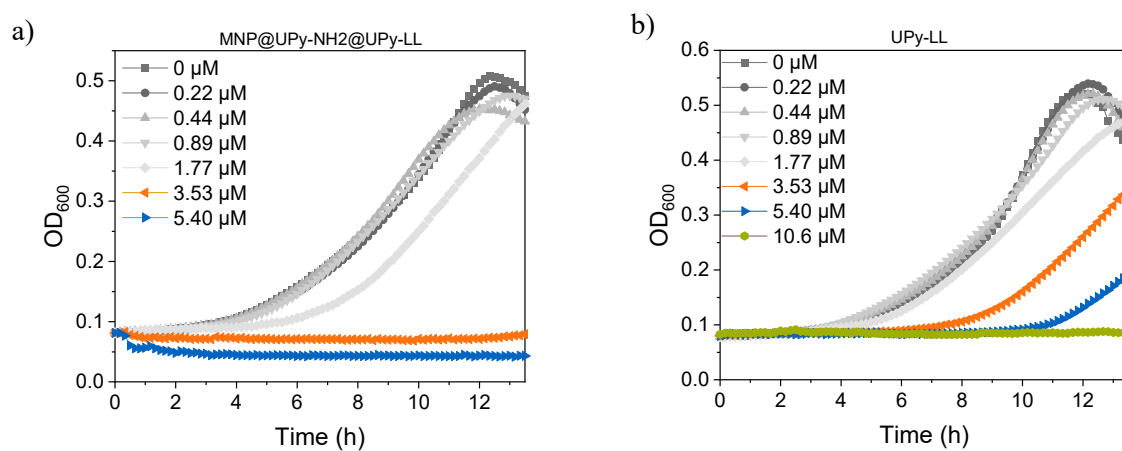


Figure S3: OD₆₀₀ measurements of *E. coli* growth contacted with (a) ION@UPy-NH₂@UPy-LL and (b) free UPy-LL.

7.1.5. Superparamagnetic iron oxide nanoparticles for their application in the human body: Influence of the surface

Chiara Turrina,^a Anna Klassen,^a Davide Milani,^a Diana M. Rojas-González,^b Gerhard Ledinski,^c Doris Auer,^d Barbara Sartori,^e Gerhard Cvirn,^c Petra Mela,^b Sonja Berensmeier,^a and Sebastian P. Schwaminger^{a,c,f,*}

^aChair of Bioseparation Engineering, Department for Engineering and Design, Technical University of Munich, Germany

^bChair of Medical Materials and Implants, Department for Engineering and Design, Technical University of Munich, Germany

^cDivision of Medicinal Chemistry, Otto Loewi Research Center, Medical University of Graz, Austria

^dDivision of Medical Physics and Biophysics, Gottfried Schatz Research Center, Medical University of Graz, Austria

^eInstitute of Inorganic Chemistry, Graz University of Technology, Stremayrgasse 9/IV, Graz, 8010, Austria

^fBioTechMed-Graz, Austria

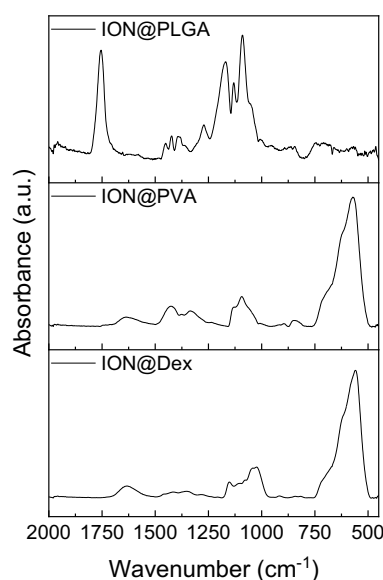


Figure S1: IR spectra of ION@PLGA, ION@PVA, and ION@Dex.

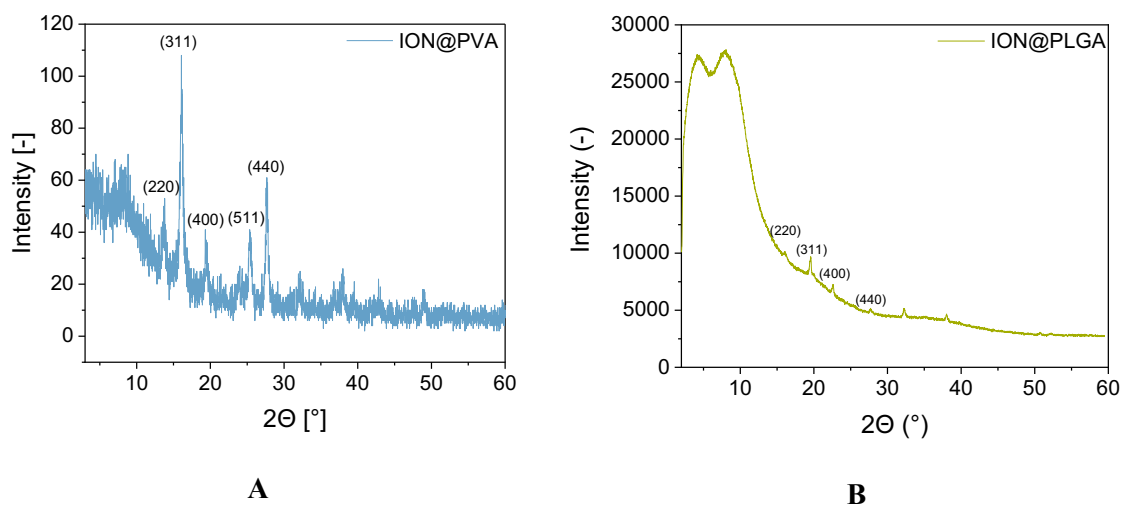


Figure S2: X-ray diffractogram of A) ION@PVA and B) ION@PLGA.

$$L = \frac{K * \lambda}{\beta * \cos(\theta)}$$

Equation S1: Scherrer equation was used to calculate the particle size L of the magnetite crystal. The Scherrer shape factor K has a constant value of 0.89. The X-ray wavelength λ is 0.07093 nm. The Bragg angle θ_0 and the full half-width of the reflection $\Delta 2\theta$ are calculated using Origin software. The two largest reflections of the plane (311) and (440) were used

Table S1: Composition of 1 L 50 mM PBS buffer (pH 7.4).

Component	Mass
NaCl	40.0 g
KCl	1.00 g
NaH ₂ PO ₄	7.20 g
KH ₂ PO ₄	1.20 g

Table S2: Composition of ALF and AEF per liter according to Marques et al. [1] pH adjusted to 4.5 for ALF and 5.5 for AEF.

Component	Mass
Calcium chloride dihydrate	0.13 g
Citric acid	20.8 g
Glycerol	0.06 g
Magnesium chloride	0.05 g
Sodium citrate dihydrate	0.08 g
Sodium chloride	3.21 g

Sodium phosphate heptahydrate	0.18 g
Sodium lactate	0.09 g
Sodium hydroxide	6.00 g
Sodium pyruvate	0.09 g
Sodium sulfate	0.04 g
Sodium tartrate dihydrate	0.09 g
Formaldehyde 37%	2.70 mL

Table S3: Composition of SBF per liter according to Marques et al. [1] pH adjusted to 7.4.

Component	Mass
Calcium chloride dihydrate	0.38 g
Magnesium chloride	0.15 g
Potassium chloride	0.23 g
Potassium phosphate	0.14 g
Sodium chloride	8.04 g
Sodium bicarbonate	0.36 g
Sodium sulfate	0.07 g
Tris(hydroxymethyl)aminomethane	6.12 g
1M hydrochloric acid	39.0 mL

Table S4: Phenanthroline assay: Fe²⁺-stock solution.

Component	Mass
FeCl ₂ (H ₂ O) ₄	35.5 mg
dH ₂ O	100 mL

Table S5: Phenanthroline assay: 10% ascorbic acid solution.

Component	Mass
L-ascorbic acid	5.01 mg
dH ₂ O	50.0 mL

Table S6: Phenanthroline assay: Acetic acid buffer (pH 4.5).

Component	Mass
Acetic acid	15.0 mL

1M NaOH	130 mL
dH ₂ O	115 mL

Table S7: Phenanthroline assay: Phenanthroline solution.

Component	Mass
Phenanthroline	2.50 mL
dH ₂ O	50.0 mL

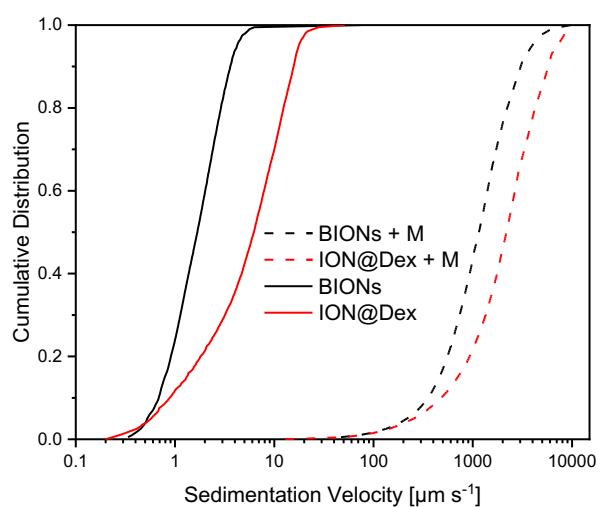


Figure S3: Cumulative velocity distribution at pH 7 in water, at room temperature with (M) and without magnetopheretic sedimentation.

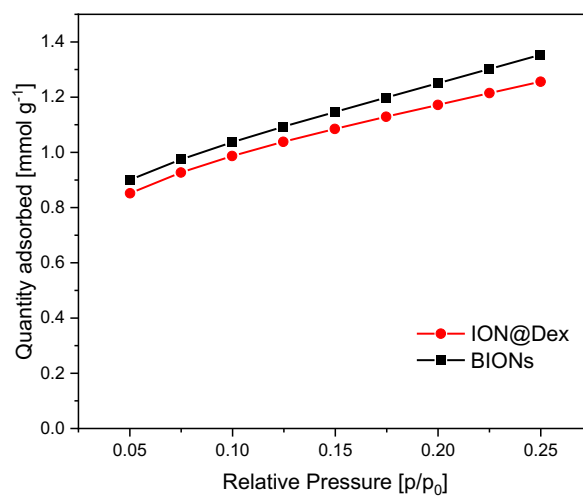


Figure S4: Nitrogen adsorption isotherm on BION and ION@Dex particles at 77 K.

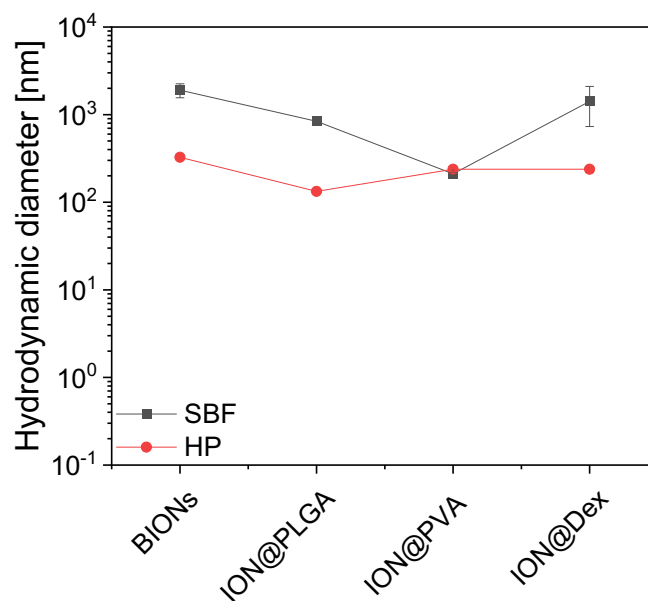


Figure S5: Hydrodynamic diameters of BIONs, ION@PLGA, ION@PVA, and ION@Dex in SBF and human blood plasma (HP).

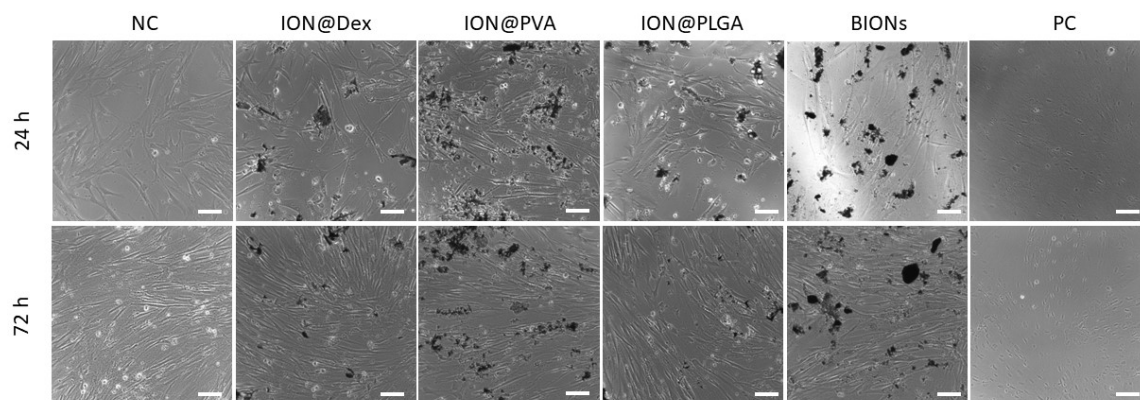


Figure S6: Phase contrast images of the cells incubated with IONs@CMD and BIONs after 24 and 72 hours for the cytocompatibility assay. Scale bar: 100 μm .

References

- [1] Margareth R. C. Marques, R. Loebenberg, M. Almukainzi, Simulated Biological Fluids with Possible Application in Dissolution Testing, *Dissolution Technologies* (2011) 15–28. <https://doi.org/10.14227/DT180311P15>.

7.2. List of publications

Authors	Titel	Reference	Category
Chiara Turrina, Sonja Berensmeier, Sebastian P. Schwaminger	Bare iron oxide nanoparticles as drug delivery carrier for the short cationic peptide lasioglossin	Pharmaceuticals, 2021, 14 (5), 405 DOI: 10.3390/ph14050405	Article
Leonie Wittmann, Chiara Turrina, Sebastian P. Schwaminger	The effect of pH and viscosity on magnetophoretic separation or iron oxide nanoparticles	Magnetochemistry, 2021, 7 (6), 80 DOI: 10.3390/magnetochemistry7060080	Article
Alexander A. Zanker, Patrick Stargardt, Sophie C. Kurxbach, Chiara Turrina, Juergen Mairhofer, Sebastian P. Schwaminger, Sonja Berensmeier	Direct capture and selective elution of a secreted polyglutamate-tagged nanobody using bare magnetic nanoparticles	Biotechnology Journal, 2022, 17 (5), 2100577 DOI: 10.1002/biot.202100577	Article
Chiara Turrina, Patricia Y. W. Dankers, Sonja Berensmeier, Sebastian Schwaminger	Iron oxide nanoparticles with supramolecular ureidopyrimidinone coating	Current Directions in Biomedical Engineering, 2022, 8 (2), 13-16 DOI: 10.1515/cdbme-2022-1004	Conference Paper
Chiara Turrina, Anne Oppelt, Michaela Mitzkus, Sonja Berensmeier, Sebastian P. Schwaminger	Silica-coated superparamagnetic iron oxide nanoparticles: New insights into the influence of coating thickness on the particle properties and lasioglossin binding	MRS Communications, 2022, 12 (5), 632-639 DOI: 10.1557/s43579-022-00228-y	Communication
Mikhail Suetin, Stefan Rauwolf, Sebastian P. Schwaminger, Chiara Turrina, Leonie Wittmann, Saientan Bag, Sonja Berensmeier, Wolfgang Wenzel	Peptide adsorption on silica surfaces: Simulation and experimental insights	Colloids and Surfaces B: BioInterfaces, 2022, 218, 112759 DOI: 10.1016/j.colsurfb.2022.112759	Article
Chiara Turrina, Davide Milani, Anna Klassen, Diana	Carboxymethyl-Dextran-Coated Superparamagnetic	International Journal of Molecular	Article

M. Rojas-González, Jennifer Cookman, Matthias Opel, Barbara Sartori, Petra Mela, Sonja Berensmeier, Sebastian P. Schwaminger	Iron Oxide Nanoparticles for Drug Delivery: Influence of the Coating Thickness on the Particle Properties	Sciences, 2022, 23 (23), 14743, DOI: https://doi.org/10.3390/ijms232314743	
Chiara Turrina, Anna Klassen, Davide Milani, Diana M. Rojas-González, Gerhard Ledinski, Doris Auer, Barbara Sartori, Gerhard Cvirn, Petra Mela, Sonja Berensmeier, Sebastian P. Schwaminger	Superparamagnetic iron oxide nanoparticles for their application in the human body: Influence of the surface	Heliyon, 2023, 9 (6), e16487 DOI: https://doi.org/10.1016/j.heliyon.2023.e16487	Article
Chiara Turrina, Jennifer Cookman, Riccardo Bellan, Patricia Y. W. Dankers, Sonja Berensmeier, Sebastian P. Schwmainger	Iron oxide nanoparticles with supramolecular ureido-pyrimidinone coating for antimicrobial peptide delivery	Int. J. Mol. Sci. 2023, 24(19), 14649, DOI: https://doi.org/10.3390/ijms241914649	Article

7.3. Permissions

7.3.1. Bare iron oxide nanoparticles as drug delivery carrier for the short cationic peptide lasioglossin

All articles published by MDPI are immediately available worldwide under an open access license. This means:

- everyone has free and unlimited access to the full text of *all* articles published in MDPI journals;
- everyone is free to re-use the published material if proper accreditation/citation of the original publication is given;
- open access publication is supported by the authors' institutes or research funding agencies by payment of a comparatively low Article Processing Charge (APC) for accepted articles.

No special permission is required to reuse all or part of article published by MDPI, including figures and tables. For articles published under an open access Creative Common CC BY license, any part of the article may be reused without permission provided that the original article is clearly cited. Reuse of an article does not imply endorsement by the authors or MDPI.

7.3.2. Silica-coated superparamagnetic iron oxide nanoparticles: New insights into the influence of coating thickness on the particle properties and lasioglossin binding

Open access articles in Springer Nature journals are published under Creative Commons licences. These provide an industry-standard framework to support easy re-use of open access material. Under Creative Commons licences, authors retain copyright of their articles.

MRS Communications articles are published open access under a CC BY licence (Creative Commons Attribution 4.0 International licence). The CC BY licence is the most open licence available and considered the industry 'gold standard' for open access; it is also preferred by many funders. This licence allows readers to copy and redistribute the material in any medium or format, and to alter, transform, or build upon the material, including for commercial use, providing the original author is credited.

[CC BY 4.0](#)

You are free to:

Share - copy and redistribute the material in any medium or format

Adapt - remix, transform, and build upon the material for any purpose, even commercially.

Under the following terms:

Attribution — You must give [appropriate credit](#), provide a link to the license, and [indicate if changes were made](#). You may do so in any reasonable manner, but not in any way that suggests the licensor endorses you or your use.

No additional restrictions — You may not apply legal terms or [technological measures](#) that legally restrict others from doing anything the license permits.

7.3.3. Carboxymethyl-dextran coated superparamagnetic iron oxide nanoparticles for drug delivery: Influence of coating thickness on the particle properties

All articles published by MDPI are immediately available worldwide under an open access license. This means:

- everyone has free and unlimited access to the full text of *all* articles published in MDPI journals;
- everyone is free to re-use the published material if proper accreditation/citation of the original publication is given;
- open access publication is supported by the authors' institutes or research funding agencies by payment of a comparatively low Article Processing Charge (APC) for accepted articles.

No special permission is required to reuse all or part of article published by MDPI, including figures and tables. For articles published under an open access Creative Common CC BY license, any part of the article may be reused without permission provided that the original article is clearly cited. Reuse of an article does not imply endorsement by the authors or MDPI.

7.3.4. Iron oxide nanoparticles with supramolecular ureidopyrimidinone coating

[CC BY 4.0](#)

You are free to:

Share - copy and redistribute the material in any medium or format

Adapt - remix, transform, and build upon the material for any purpose, even commercially.

Under the following terms:

Attribution — You must give [appropriate credit](#), provide a link to the license, and [indicate if changes were made](#). You may do so in any reasonable manner, but not in any way that suggests the licensor endorses you or your use.

No additional restrictions — You may not apply legal terms or [technological measures](#) that legally restrict others from doing anything the license permits.

7.3.5. Superparamagnetic iron oxide nanoparticles for their application in the human body: Influence of the surface

Heliyon is a fully [open access](#) journal. Once published, your article will be immediately and permanently available for readers to read, download, and share. Readers will be able to access your article freely on both Heliyon.com and ScienceDirect.

This is an open access article distributed under the terms of the [Creative Commons CC-BY](#) license, which permits unrestricted use, distribution, and reproduction in any medium, provided the original work is properly cited.

You are not required to obtain permission to reuse this article.

7.3.6. Iron oxide nanoparticles with supramolecular ureido-pyrimidinone coating for antimicrobial peptide delivery

All articles published by MDPI are immediately available worldwide under an open access license. This means:

- everyone has free and unlimited access to the full text of *all* articles published in MDPI journals;
- everyone is free to re-use the published material if proper accreditation/citation of the original publication is given;
- open access publication is supported by the authors' institutes or research funding agencies by payment of a comparatively low Article Processing Charge (APC) for accepted articles.

No special permission is required to reuse all or part of article published by MDPI, including figures and tables. For articles published under an open access Creative Common CC BY license, any part of the article may be reused without permission provided that the original article is clearly cited. Reuse of an article does not imply endorsement by the authors or MDPI.